

**Semi-mechanistic, data-based, and hybrid models:
A comprehensive comparison on the example of the
direct DME synthesis from CO₂-rich synthesis gas**

zur Erlangung des akademischen Grades einer
DOKTORIN DER INGENIEURWISSENSCHAFTEN (DR.-ING.)

von der KIT-Fakultät für Chemieingenieurwesen und Verfahrenstechnik des
Karlsruher Instituts für Technologie (KIT)
genehmigte

DISSERTATION

von
Nirvana Delgado Otalvaro, M. Sc.
aus Medellin/Kolumbien

Tag der mündlichen Prüfung: 18. Januar 2023

Erstgutachter: Prof. Dr.-Ing. Jörg Sauer

Zweitgutachter: Prof. Dr.-Ing. habil. Roland Dittmeyer

TABLE OF CONTENTS

	Page
LIST OF TABLES	iv
LIST OF FIGURES	vi
PREAMBLE	ix
CHAPTER 1. INTRODUCTION	1
1.1 Background and Motivation	1
1.2 Objectives and Outline	3
CHAPTER 2. SEMI-MECHANISTIC MODEL	6
2.1 Introduction	6
2.2 Experimental Setup and Procedures	8
2.2.1 Reactor and periphery	8
2.2.2 Materials	9
2.2.3 Kinetic measurements	9
2.2.4 Estimation of model-specific parameters	10
2.3 Mathematical model	11
2.3.1 Reactor model	11
2.3.2 Reaction kinetic model	13
2.4 Results and discussion	16
2.4.1 Experimental results	16
2.4.2 Modeling Results	21
2.5 Summary and conclusions	32
CHAPTER 3. DATA-BASED MODEL	34
3.1 Introduction	34
3.2 Artificial Neural Networks - Key Design Parameters and Modeling	35
3.2.1 Features and Functional Principles	35
3.2.2 Generalization	37
3.3 Data and Methodology for the ANN's Design	38
3.3.1 Activation Function	40
3.3.2 Training Algorithm	40
3.3.3 Data Division Scheme and Training Strategy	41
3.3.4 Network's Architecture	42
3.3.5 Evaluation of the Selected ANN	42
3.4 Results and Discussion	43
3.4.1 Network Design and Training	43
3.4.2 Best Network's Evaluation	45
3.5 Summary and Conclusions	51

CHAPTER 4. HYBRID MODEL	53
4.1 Introduction	53
4.2 Available models for the direct synthesis of DME - an overview	54
4.2.1 Semi-mechanistic (lumped) models	54
4.2.2 Data-based models	57
4.2.3 Hybrid models	58
4.3 Models' structures, modeling and experimental methodology	58
4.3.1 Lumped model	59
4.3.2 Data-based model and ANN training strategy	62
4.3.3 Hybrid model	63
4.3.4 Experimental equipment and procedures	65
4.4 Hybrid model results	66
4.4.1 ANN-HM training results	66
4.4.2 Hybrid model's performance and interpolation ability	67
4.4.3 Models' extrapolation ability	70
4.5 Summary and conclusions	77
CHAPTER 5. SUMMARY	79
BIBLIOGRAPHY	92
APPENDIX A. Additional Results on Semi-mechanistic Model	111
A.1 Reduction procedure and conditioning.	111
A.2 A priori Criteria.	111
A.3 Model Discrimination.	112
A.4 Selectivity	116
A.5 Mole percentage profiles including CO and CO ₂	117
A.6 Non re-parametrized model specific parameters	118
A.7 Overview of selected studies conducted at different CZA-to- γ -Al ₂ O ₃ ratios	119
APPENDIX B. Additional Results on Data-based Model	122
B.1 Selected ANN and model specific parameters	122
B.2 Evaluation of the Selected ANN	122
APPENDIX C. Additional Results on Hybrid Model	126
C.1 ANN of hybrid model	126
C.2 Interpolation of hybrid model at complementary feed compositions	126
C.3 Complementary Figures	132
C.4 A priori Criteria	134
C.5 Experimental values	134
C.6 Catalyst conditioning and deactivation	134
APPENDIX D. Published Manuscripts	137

LIST OF TABLES

		Page
Table 2.1	Selected properties of the commercial catalysts.	9
Table 2.2	Conditions for kinetic measurements.	10
Table 2.3	Parameters for the calculation of fitted equilibrium constants. . .	15
Table 2.4	Parameter estimates and 95 % confidence intervals.	24
Table 2.5	Adsorption constants at different temperatures.	24
Table 2.6	Binary correlation coefficients of parameter estimates.	24
Table 3.1	Conditions of kinetic data.	39
Table 3.2	Tested activation functions	40
Table 3.3	Tested training algorithms	41
Table 3.4	Adjusted coefficients of determination R_{adj}^2 for lumped model and ANN.	47
Table 4.1	Model specific parameters for the lumped model used for the comparative evaluation of the hybrid model.	61
Table 4.2	Mean relative errors between the experiments and the predictions of the lumped and hybrid model.	68
Table A.1	Calculated criteria for the verification of assumptions.	111
Table A.2	Compilation of tested reaction kinetic models during model discrimination.	113
Table A.3	Parameter estimates in non re-parametrized form.	118
Table A.4	Overview of selected studies conducted at different CZA-to- γ - Al_2O_3 ratios	120
Table B.1	Model specific parameters of the chosen ANN (Part 1).	122
Table B.2	Model specific parameters of the chosen ANN (Part 2).	123
Table C.1	Model specific parameters of the ANN-HM with 5 HNs.	126
Table C.2	Model specific parameters of the ANN-HM with 5 HNs (Part 2).	127
Table C.3	Model specific parameters of the chosen ANN-HM with 26 HNs	127
Table C.4	Model specific parameters of the chosen ANN-HM with 26 HNs (Part 2).	128
Table C.5	Model specific parameters of the ANN-HM with 28 HNs.	129
Table C.6	Model specific parameters of the ANN-HM with 28 HNs (Part 2).	130
Table C.7	Calculated a priori criteria.	135

Table C.8	Experimental values measured for validation of simulation results at extrapolated conditions.	136
-----------	--	-----

LIST OF FIGURES

		Page
Figure 2.1	CO _x conversion determined experimentally.	17
Figure 2.2	DME yield determined experimentally.	18
Figure 2.3	CO _x conversion determined experimentally and plotted at exemplary conditions.	19
Figure 2.4	DME and methanol yield determined experimentally and plotted at exemplary conditions.	21
Figure 2.5	Parity plots for main components, simulations with semi-mechanistic model.	23
Figure 2.6	Reaction rates at different CORs.	27
Figure 2.7	Reaction rates at different temperatures and low COR.	28
Figure 2.8	Reaction rates at different temperatures and high COR.	30
Figure 2.9	Reaction rates at different CZA-to- γ -Al ₂ O ₃ weight ratios.	31
Figure 2.10	CO ₂ and CO conversion for all evaluated CORs and temperatures.	32
Figure 3.1	Classification of artificial neural networks.	35
Figure 3.2	ANN structure and functionality of the artificial neuron.	36
Figure 3.3	Schematic representation of early stopping.	38
Figure 3.4	Data division scheme and training strategy.	42
Figure 3.5	Performance of activation functions and training algorithms.	44
Figure 3.6	Effect of the hidden layer size on the predictive accuracy of the ANN.	45
Figure 3.7	Parity plots for main components, simulations with ANN.	46
Figure 3.8	Mean relative error of prediction for the lumped model and ANN.	47
Figure 3.9	Measured concentrations in the product gas and 95% confidence intervals (CI) of the Data-based (ANN) and lumped model.	49
Figure 3.10	Components mole fraction in the product gas within and beyond the model's validity range regarding the temperature.	50
Figure 4.1	Overview of the validity ranges of lumped models from the open literature.	56
Figure 4.2	Schematic representation of the lumped, hybrid and data-based models.	60
Figure 4.3	Representation of the data-based model used for the comparative evaluation of the hybrid model.	62

Figure 4.4	Schematic representation of ANN's architecture for the hybrid model.	64
Figure 4.5	Schematic representation of the axial domain discretization. . . .	65
Figure 4.6	Training results for different architectures of the hybrid model's artificial neural network.	68
Figure 4.7	Surface response for the hybrid model predictions within the validity range of temperature and total gas flow.	69
Figure 4.8	Experimental validation of dimensional extrapolation of the pressure.	71
Figure 4.9	Dimension extrapolation of the catalyst bed composition.	73
Figure 4.10	Evaluation of range extrapolation of the temperature at low total volume flow.	74
Figure 4.11	Evaluation of range extrapolation of the temperature at high total volume flow.	76
Figure A.1	Total sum of squared errors for the implemented models.	112
Figure A.2	DME selectivity determined experimentally.	116
Figure A.3	Selectivity of methanol and DME at exemplary conditions.	116
Figure A.4	Mole percentage profiles at different CORs.	117
Figure A.5	Mole percentage profiles at different temperatures and low COR.	117
Figure A.6	Mole percentage profiles at different temperatures and high COR.	117
Figure A.7	Mole percentage profiles at different CZA-to- γ -Al ₂ O ₃	118
Figure B.1	Schematic representation of selected network architecture.	122
Figure B.2	Components mole fraction in the product gas at complementary feed composition.	123
Figure B.3	Components mole fraction in the product gas at complementary feed composition.	123
Figure B.4	Components mole fraction in the product gas at complementary feed composition.	124
Figure B.5	Components mole fraction in the product gas at complementary feed composition.	124
Figure B.6	Components mole fraction in the product gas at complementary feed composition.	125
Figure C.2	Surface response for the hybrid model predictions at complementary feed compositions	131
Figure C.3	Surface response for the hybrid model predictions at complementary feed compositions	131
Figure C.4	Range extrapolation of the temperature with complementary ANN-HM	132

Figure C.5	Range extrapolation of the temperature with complementary ANN-HM	133
Figure C.6	Range extrapolation of the temperature with complementary ANN-HM	133
Figure C.7	Range extrapolation of the temperature with complementary ANN-HM	134

PREAMBLE

The investigations presented in this doctoral dissertation were carried out at the Institute of Catalysis Research and Technology (IKFT) of the Karlsruhe Institute of Technology (KIT) in the period from March 2019 to March 2022. During this time a total of four peer reviewed research articles have been published. While the first publication,

- Delgado Otalvaro, N., Kaiser, M., Herrera Delgado, K., Wild, S., Sauer, J. and Freund, H., Optimization of the direct synthesis of dimethyl ether from CO₂ rich synthesis gas: closing the loop between experimental investigations and model-based reactor design. *Reaction Chemistry & Engineering*, 2020, 5, 949-960 [1],

is not explicitly a part of this dissertation, it represents the basis of the investigations conducted here, and it is used as an important reference in every chapter. The contents of the following three publications *i.e.*,

- Delgado Otalvaro, N., Sogne, G., Herrera Delgado, K., Pitter, S. and Sauer, J., Kinetics of the direct DME synthesis from CO₂ rich syngas under variation of the CZA-to- γ -Al₂O₃ ratio of a mixed catalyst bed. *RSC Advances*, 2021, 11 (40), 24556-24569 [2]
- Delgado Otalvaro, N., Gül Bilir, P., Herrera Delgado, K., Pitter, S. and Sauer, J., Modeling the Direct Synthesis of Dimethyl Ether using Artificial Neural Networks. *Chemie Ingenieur Technik*, 2021, 93, 754-761 [3]
- Delgado Otalvaro, N., Gül Bilir, P., Herrera Delgado, K., Pitter, S. and Sauer, J., Kinetics of the direct DME synthesis: state of the art and comprehensive comparison of semi-mechanistic, data-based and hybrid modeling approaches. *Catalyst*, 2022, 12(3), 347 [4]

are included in Chapters 2 to 4 respectively with changes in formatting, layout, citation style, and structure. Tables and figures have been adapted to the style of this dissertation, and the original articles are attached at the end of this thesis in Appendix D.

1. INTRODUCTION

The context and motivation for this thesis as well as the objectives, the scientific questions and the outline are presented in this chapter.

1.1 Background and Motivation

The focus of this work is the modeling of the direct synthesis of Dimethyl ether from CO₂-enriched synthesis gas using different modeling approaches. Dimethyl ether (DME) is of general interest due to its extensive range of applications. It has been widely used as an environmentally friendly aerosol propellant [5], as a solvent [6], as feedstock for the production of lower olefins [7], and other chemicals such as acetic acid [8], methyl acetate [9], and aromatics [10]. It can also be used for power generation in gas turbines, boilers, and fuel cells [6, 7, 11], or as an alternative to liquefied petroleum gas [7, 12] and diesel [5, 7, 13]. In regards to emissions, the combustion of DME produces no particulate matter, half the NO_x, and significantly less noise than diesel combustion [14]. Another attractive feature of DME is its multi-source nature. DME is derived from syngas (CO/H₂) produced from a variety of carbon-containing feedstocks including fossil sources, but more importantly, also a variety of renewable resources such as wood and biomass [6, 7]. Furthermore, DME can also be produced from captured CO₂ using green hydrogen obtained by electrolysis [15]. Considering these aspects, implementing DME as part of an industrial defossilisation strategy contributes to sustainability goals not only by reducing emissions, but also by reducing the depletion of natural energy resources.

The commercially established process for DME production is the indirect synthesis. In this process, the syngas is first transformed to methanol, which is subsequently dehydrated to DME. The state of the art for the initial process step is the low-pressure methanol synthesis, which is typically performed with copper composite catalysts [16]. Among these, CuO/ZnO/Al₂O₃ (CZA) is most commonly used for industrial applications [17]. This process step is traditionally conducted at pressures up to 10 MPa, and temperatures between 473 and 573 K [18]. The subsequent methanol dehydration to DME is conducted in tube reactors at pressures above 1 MPa and temperatures between 523 and 673 K [19, 20], over solid acidic catalysts such as γ -Al₂O₃, silicium modified γ -Al₂O₃ and zeolites [21]. Due to its low cost, high surface area, good thermal and mechanical stability, and high selectivity towards DME, the γ -Al₂O₃ catalyst is the most widely used [15, 22].

The alternative production route for DME is the direct synthesis over dual catalyst systems. In this process, both steps are coupled to produce DME from syngas in one step. Therefore, only one reactor is needed in the direct route. Additionally, the consumption of methanol by the dehydration reaction leads to a shift of the thermodynamic equilibrium of methanol synthesis towards the products. As a result, higher one-pass conversions of the syngas can be achieved with the coupled process under comparable conditions [6, 23]. The technical feasibility of the direct route has been demonstrated at pilot scale [24–27]. However, this process is still under development [27], and further reactor and process optimization are still necessary for commercial application at industrial scale [6].

A powerful design and optimization tool are mathematical models. These act as a representation of the real world and can be employed for the development of new technologies, scale-up, technical and economic evaluation of novel process alternatives, monitoring and control, and many others [28–30]. Hence, reliable predictive models are essential, especially for a system at the development stage such as the direct DME synthesis. However, the modeling of this process is challenging and the detailed reaction mechanism has not yet been fully understood [31].

In the lack of mechanistic knowledge, the most common model type for the direct DME synthesis is semi-mechanistic or *lumped*. I.e., models built based on mechanistic assumptions and kinetic data, that enable a system representation within a specific operating window [1, 2, 32–41]. Semi-mechanistic models provide some extrapolation capability within a reasonable range, and extrapolation is a common practice. However, the range of validity of these models is strictly speaking limited by the operational window in which the kinetic data were measured, and by the validity of the assumptions made. Moreover, specifically for DME, dynamic structural changes of the metallic catalyst [42], the variation of the dominant pathway of the methanol synthesis [43], and catalyst deactivation [23, 44], make it almost impossible to correlate a vast array of experiments at different working conditions using a single lumped model [45].

A promising modeling approach when the detailed reaction mechanism is unknown is using machine learning to extract and predict input-output relationships in large data sets. These methods have been used successfully in various areas of the chemical and process industry, especially as predictive tools [46–48]. The most widespread machine learning approach for modeling complex phenomena is the use of artificial neural networks (ANNs) [49]. Due to their simple formulation, flexibility and robustness, ANNs have shown to be remarkable predictors for complex processes [50, 51]. Unlike semi-

mechanistic models, ANNs can be easily adapted to large amounts of multidimensional data in broad operational windows [48, 52]. One of the main drawbacks of ANNs is that their predictions are only reliable in the range in which the training data were measured, and extrapolation is only possible in a narrow range, under a high level of uncertainty [52, 53]. In general, ANN applications are strictly system specific and the characteristics of ANNs e.g., activation function, backpropagation algorithm, network architecture, etc., have to be determined for the individual application [53].

Another promising alternative for the modeling the behavior of chemical reactors are hybrid models that combine the features of both (semi-)mechanistic and data-based approaches [54]. It has been stated that these models have a simpler mathematical structure, provide a higher accuracy than lumped models in a much wider range, and a better extrapolation ability than data-based models [28, 53, 55]. Some studies on the individual steps of the DME synthesis have shown the potential of hybrid modeling for related systems [56–58].

Even though machine learning approaches have proven to have a high potential for modeling chemical reactors, recent works have highlighted that the adoption of these methods is still limited in chemical synthesis [49, 59, 60]. This could be confirmed with an extensive literature search on models for direct DME synthesis, that revealed that most models for this system are semi-mechanistic, while only a few models are data-based, and none of the models are hybrid in nature.

1.2 Objectives and Outline

The main objective of this work is the modeling of the direct DME synthesis from CO₂-enriched synthesis gas over the commercial CZA/ γ -Al₂O₃ catalyst system at an industrially relevant pressure level using semi-mechanistic, data-based and hybrid modeling approaches.

Three models, each expanding the scope of available models in their categories, are derived and systematically evaluated with respect to the critical features of each model type e.g., accuracy, computational burden, interpolation and extrapolation ability and capability. Numerical simulations are conducted with the three models for the assessment of each model type with regards to these aspects, and experiments are conducted for the validation of simulation results. Under consideration of the mentioned challenges and knowledge gaps for each modeling approach, the structure and outline of this work is described in the following.

- **Chapter 2:** In this chapter, a mechanistically sound lumped model is developed to predict product gas concentrations in a larger range than already modelled in the literature. As it was shown in a previous work [1], a mixed catalyst bed composition with an increased CZA-to- γ -Al₂O₃ ratio intensifies the thermodynamic synergetic effects of the direct DME synthesis and leads to a higher conversion and product yield. However, most works investigating the influence of the catalyst bed composition are experimental in scope. Hence, in this work, catalyst beds with different CZA-to- γ -Al₂O₃ ratios higher than one are evaluated and used for modeling. Additionally, a wide range of carbon oxide ratio (CO₂/CO_x) is investigated to evaluate the influence of high CO₂ concentrations in the feed on the process performance. A systematic model discrimination procedure is used to establish what is the most appropriate model structure i.e., which mechanistic approach is most suitable for the system description within the evaluated operating window. Furthermore, intrinsic kinetic data is used to determine which model-specific parameters enable accurate predictions in this range and the statistical and physico-chemical significance of the parameters is analysed and discussed, along with the mechanistic insights obtained with the model.
- **Chapter 3:** This chapter presents an ANN designed and trained to predict the product gas composition measured during integral experiments of the direct DME synthesis over the commercial CZA/ γ -Al₂O₃ catalyst system at high pressure. First, the questions regarding the ANN design such as what is a suitable activation function, backpropagation algorithm, network architecture, data division, and training strategy? are addressed. Additionally, one of the most frequently asked questions in the framework of data-based modeling is how much data is necessary to build a reliable predictive model? This question is addressed by training ANNs with the same set of data used for parameter estimation of a conventional lumped model [1] to show whether or not relatively small data sets are sufficient to meet the data requirements of a simple ANN. After having trained the two models to the same data, the models' predictions are compared, assessing their interpolation ability and extrapolation capability. One of the main questions to answer thereby, is to what extent, if at all, the data-based model can be extrapolated.
- **Chapter 4:** A hybrid model is derived and presented in this chapter. The first question to be answered here is what is a suitable hybrid structure to integrate available system knowledge with data-based approaches to fill knowledge gaps?. Since this model is the first of this type for the direct DME synthesis, the performance is evaluated in comparison to experimental values and to the predictions of

the other model types. For the later, the hybrid model was designed to have the same validity as the data-based and the lumped models evaluated in Chapter 3. Therefore, the observed discrepancies between model predictions are only due to the structural differences between the different model types, and the question what are the advantages of a hybrid model over conventional semi-mechanistic and/or data-based models in terms of computational burden, extrapolation capability, and other critical properties of predictive models? is addressed quantitatively on the example of the direct DME synthesis.

- **Chapter 5:** This chapter provides a comprehensive summary and discussion of the results of this work in its entirety. It also highlights the answers to the questions stated in this section, and it provides an overview of the limitations of this work, as well as possible future challenges and potentials.

2. SEMI-MECHANISTIC MODEL

The one-step synthesis of dimethyl ether over mechanical mixtures of Cu/ZnO/Al₂O₃ (CZA) and γ -Al₂O₃ was studied in a wide range of process conditions. Experiments were performed at an industrially relevant pressure of 5 MPa varying the carbon oxide ratio in the feed (CO₂ in CO_x from 20 to 80 %), temperature (503 – 533 K), space-time (240 – 400 kg_{cat} s/m_{gas}³), and the CZA-to- γ -Al₂O₃ weight ratio (from 1 to 5). Factors favoring the DME production in the investigated range of conditions, are an elevated temperature, a low CO₂ content in the feed, and a CZA-to- γ -Al₂O₃ weight ratio of 2. A lumped kinetic model was parametrized to fit the experimental data, resulting in one of the predictive models with the broadest range of validity in the open literature for the CZA/ γ -Al₂O₃ system.

2.1 Introduction

Dimethyl ether (DME) has many uses in industries. Applications include its use as a coolant or a propellant, and as an important commodity for the production of lower olefins. [61] Other potential applications include its use as a diesel substitute or fuel additive. [62, 63] Compared with fossil diesel fuels, the combustion of DME produces less NO_x, CO, and particulate emissions, while still achieving a high performance with only minor modifications of the fuel storage and supply. [21, 64] DME is produced from synthesis gas, which originates from different sources such as coal, natural gas, and waste materials like biomass. [21, 64, 65] Depending on the raw material and syngas production process, the composition of the syngas may change in a wide range, resulting in a variable feedstock for the DME synthesis.

The commercially established production route of DME involves two steps. The first step is methanol synthesis from syngas, followed by the methanol dehydration step in a second reactor. An alternative route is the direct or single-step synthesis, where DME is produced directly from syngas in a single reactor. [21] Potential advantages of a single reactor are reduced complexity and investment costs. Also, the direct synthesis is thermodynamically advantageous compared to the conventional route. [23] The in situ conversion of methanol by the dehydration reaction shifts the thermodynamic equilibrium of methanol synthesis towards the products. As a result, a higher conversion of the

synthesis gas can be achieved under comparable conditions. [23]

Many dual catalyst systems have been proposed in the scientific literature for the direct DME synthesis. [66–68] These combine the properties of metallic catalysts for the methanol synthesis (typically copper-based) [18], and a solid acid catalyst for the selective methanol dehydration to DME (such as γ -Al₂O₃, zeolites, and silica-modified alumina) [17]. In this chapter, mechanical mixtures of the two commercial catalysts of each step i.e., Cu/ZnO/Al₂O₃ (CZA) and γ -Al₂O₃ are considered.

Identifying and quantifying dependencies between process parameters and performance is essential for efficient, economically viable and safe process design and operation. Hence, numerous studies have been conducted investigating the influence of different variables on the performance of the direct DME synthesis from CO₂ rich synthesis gas.

CO₂ content in the synthesis gas. Ateka et al. [69] investigated the effect of CO₂ content in the feed gas on the thermodynamics of the methanol and DME synthesis. Ng et al. [41] studied the influence of CO₂-to-CO_x ratios and catalyst bed compositions on the kinetics of the DME synthesis at 523 K and 5 MPa. Peláez et al. [32] described the effects of different feed gas compositions on the process performance at a pressure of 3 MPa. These and other works, [15, 23, 70–72] have shown that increasing CO₂ content in the feed decreases the process performance, and that water plays an important role, not only affecting the reaction kinetics, but also the catalyst structure by deactivation of the dehydration component γ -Al₂O₃.

Catalyst bed composition and configuration. With regard to the composition of the catalyst bed, previous investigations [1, 37, 41, 73, 74] have shown on the basis of simulated and experimental data that optimization can lead to significant enhancement of the process performance. For instance, in the studies of Peláez et al. [32] and Peinado et al. [75] the authors showed that for CO₂ rich synthesis gas a significant increase in the performance is achieved by increasing the CZA-to- γ -Al₂O₃ ratio. In a previous study [1], applying a dynamic optimization scheme and experimental validation it has been shown that these effects hold true also for high pressure (5 MPa) and different compositions of CO₂ rich syngas, including a hydrogen-lean feed. Other studies [1, 73, 76] on the loading and arrangement of physical catalyst mixtures have shown that homogeneously mixed catalyst beds achieve similarly good process performance compared to more complex configurations.

Quantification and prediction of system behavior. Reliable models able to predict the process performance in different operating windows are necessary to enable the optimal reactor and process design, especially if DME synthesis is to be conducted at dynamic conditions or changing feed compositions. Therefore, several kinetic models have been proposed in the open literature to quantitatively describe and predict the effects of process variables on process performance. A widely used modelling approach is the combination of available models for the methanol synthesis, [77, 78] and its dehydration. [79] Models derived for the direct DME synthesis under mechanistic assumptions include the works of Lu et al. [80], Aguayo et al. [39], Ereña et al. [33], and Peláez et al. [32].

Although so many studies have been carried out for the direct DME synthesis from CO₂ rich synthesis gas, the detail reaction mechanism is still controversial. [31] Therefore, reliable kinetic models valid in a wide range of conditions at industrially relevant process conditions are still necessary. In this chapter, a reaction kinetic model is developed, that is applicable for an extended range of catalyst bed compositions, and process parameters (CO₂ content in the synthesis gas, temperature and space time). Hence, the scope of available reaction kinetic models is extended, and an useful tool for model-based reactor and process design and optimization is provided.

2.2 Experimental Setup and Procedures

In this chapter the equipment and methodology for the experimental kinetic investigations are described. First, the laboratory setup is described, then the materials used are listed, followed by a brief description of the experimental procedures and conditions at which the kinetic measurements were conducted.

2.2.1 Reactor and periphery

The reactor setup used in this work is presented in detail elsewhere. [71] It consists of a laboratory tube reactor made of the stainless steel with an internal diameter of 12 mm, and a total length of 460 mm. The reactor is divided in four independent heating zones, each of which is surrounded by brass jaws equipped with heating cartridges (Horst GmbH) to set the temperature at the reactor outer wall. The gas supply is regulated via mass flow controller (Bronkhorst High-Tech B.V.) by using proportional integral derivative control. The system pressure is set by using a mechanical pressure regulator (Emerson Electric Co.). A gas chromatograph G1530A (Agilent Technologies) was used to analyse the composition of the feed gas and product gas.

2.2.2 Materials

Commercial catalysts, i.e., Cu/ZnO/Al₂O₃ (CZA) and γ -Al₂O₃ (Alfa Aesar) were used as hydrogenation catalyst for the methanol synthesis and methanol dehydration to DME, respectively. Relevant properties of the used catalysts are provided in Table 2.1. The catalysts were ground and sieved to a particle size between 250 and 500 μm . To avoid hot spot formation, the catalytic bed was diluted with silicon carbide (SiC, Hausen Mineraliengroßhandel GmbH) of the same size distribution.

Table 2.1: Selected properties of the commercial catalysts.

Properties of the CZA Catalyst [68]	
Metal Composition (Cu/Zn/Al) / wt.%	64/29/6
Specific surface area S _{BET} / m ² g ⁻¹	98
Pore Volume / cm ³ g ⁻¹	0.332
Maximum pore diameter / nm	11
Pore size range / nm	5-26
Properties of the γ -Al ₂ O ₃ Catalyst [81]	
Specific surface area S _{BET} / m ² g ⁻¹	213
NH ₃ -TPD peak position in low and high temperature regions / K	512 and 624
Total acidity / mmol NH ₃ / g _{cat} (desorbed NH ₃ in NH ₃ -TPD)	0.37
Acidity in low and high temperature regions / mmol NH ₃ / g _{cat}	0.18 and 0.19

The feed gases, carbon monoxide (CO, 99.97 %), nitrogen (N₂, 99.9999 %), hydrogen (H₂, 99.9999 %) and a mixture carbon dioxide/nitrogen (CO₂/N₂, 50:50 \pm 1.0 %) were purchased by Air Liquid Germany GmbH.

2.2.3 Kinetic measurements

Before performing the kinetic measurements, the CZA share of the catalytic bed was reduced at atmospheric pressure (5% H₂ in N₂, at temperatures between 393 and 513 K). Following the reduction procedure, the catalyst was conditioned until stable catalyst activity was achieved, in order to decouple the kinetic measurements from deactivation effects. The reduction and conditioning procedures are described in detail elsewhere [71] and summarized in the electronic supplementary information (ESI). The kinetic measurements were performed at a pressure of 5 MPa under variation of the CZA-to- γ -Al₂O₃ weight ratio (μ), temperature (T), space time (τ), and carbon oxide ratio (COR),

$$\text{COR} = 100 \% \frac{y_{\text{CO}_2, \text{in}}}{y_{\text{CO}_2, \text{in}} + y_{\text{CO}, \text{in}}}. \quad (2.1)$$

The experimental conditions as summarized in Table 2.2 were chosen in order to measure intrinsic kinetics i.e., by minimizing heat and mass transport limitations. The total catalyst mass in all experiments was 2 g, while the mass of each catalyst was distributed in different ratios ($\mu = m_{\text{CZA}}/m_{\gamma\text{-Al}_2\text{O}_3}$). The mole fraction of H_2 in the feed ($y_{\text{H}_2,\text{in}}$) was set to 46.5 % to avoid a stoichiometric limitation in all cases. The mole fraction of carbon oxides in the feed, i.e., $y_{\text{CO}_x,\text{in}} = y_{\text{CO}_2,\text{in}} + y_{\text{CO},\text{in}}$ was at 15 %, and the fraction of N_2 ($y_{\text{N}_2,\text{in}}$) was set accordingly to 38.5 %. The concentrations used for the model parametrization were determined from the mean value of at least 4 chromatograms per operating point. Each set point was held for at least 3 hours enabling multiple readings, and confirmation of stability.

Table 2.2: Conditions for kinetic measurements.

Variable	Values
Temperature (T), K	503, 513, 523, 533
Space-time* (τ), $\text{kg}_{\text{cat}} \text{ s m}_{\text{gas}}^{-3}$	240, 300, 400
Carbon Oxide Ratio (COR), %	20, 40, 60, 80
Catalyst ratio (μ), $\text{g}_{\text{CZA}}/\text{g}_{\gamma\text{-Al}_2\text{O}_3}$	1, 2, 3, 5

*at standard conditions: $p = 101325 \text{ Pa}$, $T = 293.15 \text{ K}$

2.2.4 Estimation of model-specific parameters

The Matlab® (Version R2019a) built-in solver *ode45* was used to integrate the system of differential equations (Section 2.3.1) along the reactor axial coordinate. The model-specific parameters were fitted to experimental data using the nonlinear least-squares solver *lsqcurvefit* and the algorithm *trust-region-reflective*. The model-specific parameters were estimated such as to minimize the weighted sum of squared errors,

$$SSE = \sum_{n=1}^{\text{No.Exps}} w_n [y_n - f(x_n, \theta)]^2. \quad (2.2)$$

Where y_i represent the response values (measured quantities), $f(x_n, \theta)$ the predicted values with the nonlinear model function, x_n are the predictor values of observation n , θ the model-specific parameters, and w_n the estimated weight for observation n , which indicates the specific contribution of the information contained in the associated observation to the final parameter estimates.

The parameter estimation took place based on the measured mole fractions of the components in the product gas, excluding water and methanol since it was not possible to detect these species accurately over the wide range of conditions shown in Table 2.2.

Reported values for water and methanol correspond to those calculated based on the component balances (C, H and O balance). Additionally, experimental data for which the component balances exhibited a relative error higher than 8 % were excluded from the parameter estimation ($w_n = 0$). Due to the strong influence of initial parameter values, and in order to avoid local optimality, the fitting procedure was iteratively repeated until the relative difference between the parameters obtained in two consecutive iterations was lower than 5 %. The Matlab built-in function *nlparci* was used to calculate the 95 % confidence intervals of the parameter estimates using the residuals and the Jacobian matrix of the fitted model, which are both output arguments of *lsqcurvefit*. Additionally, correlation coefficients were computed using Equation 2.3,[82]

$$\rho_{i,j} = \frac{v_{i,j}}{\sqrt{v_{i,i} v_{j,j}}}. \quad (2.3)$$

Here, $v_{i,j}$ represents the elements of the covariance matrix of the parameters of the fitted model. The covariance matrix V_θ is calculated with the variance of the experimental fluctuations s^2 (assumed to be constant over all experiments) and the Jacobian matrix J by,

$$V_\theta = s^2(J^T J)^{-1}. \quad (2.4)$$

Correlation coefficients $|\rho_{i,j}| \geq 0.95$ are assessed to indicate a strong parameter correlation. [83]

2.3 Mathematical model

In this section, the mathematical model consisting of the reactor model (balance equations) and the reaction kinetic model (rate expressions) is presented.

2.3.1 Reactor model

The change of the mole fraction of the components along the reactor's axial coordinate can be described by the balance equation of an ideal plug flow reactor (Equation 2.5). This simplified form of the general material balance of a fixed-bed reactor is admissible for the characteristics of the lab-scale reactor, and the conditions at which it was operated. Isothermal operation was achieved by diluting the catalyst bed with silicon carbide (SiC), and diluting the feed gas with inert N_2 . Temperature gradients did not exceed 2 K in any of the measurements. Hence, the assumption of isothermal operation applies and the energy balance can be omitted. All measurements took place under steady state conditions, which was verified experimentally. Furthermore, it was proven by the means of *a priori* criteria, that no significant influence of mass or heat transport processes took place, and that the assumption of plug flow applies. Finally, the pressure drop in the

fixed bed was determined to be negligible by the means of correlations. Values to support the mentioned assumptions are reported in Table A.1 in the ESI. It can be concluded that the intrinsic reaction rates were measured in all experiments and that the reactor can be described by the balance equations of an ideal plug flow reactor. Furthermore, the volume contraction caused by reaction can be accounted for by Equation 2.6.

$$\frac{dy_i}{dz} = \frac{RTZ}{up} \left(R_i - y_i \sum_k^N R_k \right), \quad (2.5)$$

$$\frac{du}{dz} = \frac{RTZ}{p} \sum_i^N R_i. \quad (2.6)$$

In Equations 2.5 and 2.6, y_i is the mole fraction of component i , z represents the position in the axial coordinate, R is the universal gas constant in $\text{J mol}^{-1} \text{K}^{-1}$, T is the temperature in K, p is the pressure in Pa, u is the gas velocity in m s^{-1} , $\vartheta_{i,j}$ is the stoichiometric coefficient of component i in reaction j , and N is the number of components in the system. Z is the compressibility factor of the mixture, which takes into account possible deviations from the ideal gas behavior at the high pressure (5 MPa) considered in this investigation. The Peng-Robinson equation of state (PR-EoS) [84] was chosen to calculate Z , since it has already been successfully applied to the system under consideration, [1, 85] and it provides accurate calculations for light gases, alcohols and hydrocarbons. [86] In addition, van der Waals mixing rules [84] were used to account for inter-molecule interactions. The molar rate of depletion or formation of component i due to chemical reaction (R_i in $\text{mol m}^{-3} \text{s}^{-1}$) is defined by:

$$R_i = \sum_j^J \vartheta_{i,j} r_j^\nu, \quad (2.7)$$

with

$$r_j^\nu = (1 - \epsilon_{\text{bed}}) \rho_{\text{cat},j} \zeta_{\text{cat},j} r_j^m. \quad (2.8)$$

In the above equations, r_j^ν and r_j^m are the volume and mass specific rates of reaction j in $\text{mol m}^{-3} \text{s}^{-1}$ and $\text{mol kg}^{-1} \text{s}^{-1}$, ϵ_{bed} is the porosity of the catalyst bed estimated to be 0.39, $\rho_{\text{cat},j}$ is the density of the catalyst that promotes reaction j , i.e., the densities of the CZA and the $\gamma\text{-Al}_2\text{O}_3$ catalysts with the respective values of 1761.3 kg m^{-3} and 667.9 kg m^{-3} , and J is the number of reactions. Finally, $\zeta_{\text{cat},j}$ stands for the volume fraction of the catalyst that promotes reaction j calculated by,

$$\zeta_{\text{CZA}} = \frac{V_{\text{CZA}}}{V_{\text{CZA}} + V_{\gamma\text{-Al}_2\text{O}_3} + V_{\text{SiC}}}, \quad (2.9)$$

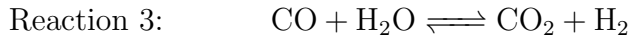
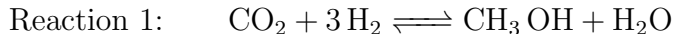
$$\zeta_{\gamma\text{-Al}_2\text{O}_3} = \frac{V_{\gamma\text{-Al}_2\text{O}_3}}{V_{\text{CZA}} + V_{\gamma\text{-Al}_2\text{O}_3} + V_{\text{SiC}}}. \quad (2.10)$$

Where V_{CZA} , $V_{\gamma\text{-Al}_2\text{O}_3}$ and V_{SiC} are the volumes of CZA, $\gamma\text{-Al}_2\text{O}_3$ and SiC respectively.

2.3.2 Reaction kinetic model

For the initial model discrimination, the available experimental data were simulated using eight different kinetic models from the open literature. [1, 32, 33, 36, 37, 39, 40, 87] Subsequently, the five models with the lower residual squared sum were parametrized to fit the data. The previous model [1] exhibited the best agreement with the experimental data acquired for this contribution, which can be attributed to similar operating conditions, and to the fact that in both contributions the same catalysts (same supplier), and pre-treatment procedures were employed. The mechanistic assumptions and model structure were chosen for fine-tuning, and the model structure that enabled the best fit is presented in the following. Further information on the initial model discrimination is presented in the ESI, along with a compilation of the rate expressions and specific parameters of the tested models (Table A.2). The new estimated model parameters are presented in Section 2.4.2.1 followed by the statistical evaluation of the estimates.

The reaction network considered in this model consists of the CO₂ hydrogenation (Reaction 1), the methanol dehydration to DME (Reaction 2), and the water gas shift reaction (Reaction 3). Reactions 1 and 3 are assumed to be promoted by the CZA catalyst, while reaction 2 is promoted by γ -Al₂O₃.



The reaction rate expressions were postulated based on the general Hougen-Watson formulation,

$$r = \frac{(\text{Kinetic Term})(\text{Potential Term})}{\text{Adsorption Term}}. \quad (2.11)$$

The kinetic term equals the rate constant of each reaction j (k_j). The potential term, describing the driving force of the reaction i.e., the distance from thermodynamic equilibrium, is defined for each reaction j as follows,

$$\text{Potential Term}_j = \prod_{i,j,\nu<0} f_i^{|\nu_{i,j}|} - \frac{1}{K_{f,j}} \prod_{i,j,\nu>0} f_i^{|\nu_{i,j}|}. \quad (2.12)$$

The adsorption term is generally defined by,

$$\text{Adsorption Term} = \left(1 + \sum_i K_{\text{ads},i} f_i \right)^n. \quad (2.13)$$

It accounts for the inhibition caused by adsorbed species on the catalytically active surface, and hence it must be defined for each component of the catalyst mixture.

The postulated model includes the adsorption of CO₂, CO and dissociated H₂ on the CZA (Equation 2.14), whereas no adsorption on the dehydration catalyst was considered (Equation 2.15). Furthermore, the adsorption term has a different influence on the rates of the CO₂ hydrogenation and the WGSR, with $n=3$ and 1 respectively. [1, 80] In Equations 2.12 and 2.13, f_i is the fugacity of component i in bar, $K_{f,j}$ is the equilibrium constant of the same reaction, $\nu_{i,j}$ is the stoichiometric coefficient of component i in reaction j , and K_i is the adsorption constant of component i .

$$\text{Ads. Term}_{\text{CZA}} = 1 + \sqrt{K_{\text{H}_2} f_{\text{H}_2}} + K_{\text{CO}_2} f_{\text{CO}_2} + K_{\text{CO}} f_{\text{CO}} \quad (2.14)$$

$$\text{Ads. Term}_{\gamma\text{-Al}_2\text{O}_3} = 1 \quad (2.15)$$

The resulting rate expressions for the three reactions are presented in Equations 2.16 to 2.18.

$$r_1^m = \frac{k_1 \left[f_{\text{CO}_2} f_{\text{H}_2}^3 - \frac{1}{K_{f,1}} f_{\text{MeOH}} f_{\text{H}_2\text{O}} \right]}{(1 + \sqrt{K_{\text{H}_2} f_{\text{H}_2}} + K_{\text{CO}_2} f_{\text{CO}_2} + K_{\text{CO}} f_{\text{CO}})^3} \quad (2.16)$$

$$r_2^m = k_2 \left[f_{\text{MeOH}}^2 - \frac{1}{K_{f,2}} f_{\text{DME}} f_{\text{H}_2\text{O}} \right] \quad (2.17)$$

$$r_3^m = \frac{k_3 \left[f_{\text{CO}} f_{\text{H}_2\text{O}} - \frac{1}{K_{f,3}} f_{\text{CO}_2} f_{\text{H}_2} \right]}{(1 + \sqrt{K_{\text{H}_2} f_{\text{H}_2}} + K_{\text{CO}_2} f_{\text{CO}_2} + K_{\text{CO}} f_{\text{CO}})} \quad (2.18)$$

The reaction rate and adsorption constants (k_j and K_i) are each calculated using modified Arrhenius and the Van't-Hoff equations (Equations 2.19 and 2.20). This re-parametrization reduces the correlation between the frequency factor and the activation energy, as well as between the sticking coefficients and the enthalpy of adsorption. [88] Other advantages of using re-parametrized expressions are lower computational costs and higher robustness in parameter estimation with the least squares algorithm. [89] These are particularly relevant for the fitting of large data sets, as used in this work.

$$k_j = \exp \left[k_{0,j}^* + E_{A,j}^* \left(\frac{T - T_R}{T} \right) \right] \quad (2.19)$$

$$K_i = \exp \left[K_i^* + \Delta H_{\text{ads},i}^* \left(\frac{T - T_R}{T} \right) \right] \quad (2.20)$$

The modified parameters are related to the parameters of the traditional Arrhenius equation according to Equation 2.21 and Equation 2.22. [82]

$$k_{0,j}^* = \ln(k_{0,j}) - \frac{E_{A,j}}{R T_R} \quad (2.21)$$

$$E_{A,j}^* = \frac{E_{A,j}}{R T_R} \quad (2.22)$$

the same applies to the Van't-Hoff equation as follows,

$$K_i^* = \ln(K_i) - \frac{\Delta H_{\text{ads},i}}{R T_R}, \quad (2.23)$$

$$\Delta H_{\text{ads},i}^* = \frac{\Delta H_{\text{ads},i}}{R T_R}. \quad (2.24)$$

The reference temperature (T_R) was calculated with Equation 2.25 based on the temperature of each experiment n . [90]

$$T_R = \left(\frac{1}{\text{No.Exps}} \sum_n \frac{1}{T_n} \right)^{-1} \quad (2.25)$$

The equilibrium constants $K_{f,j}$ of each reaction j are calculated using Equation 2.26, [91] the temperature T in K, and the parameters in Table 2.3.

$$K_{f,j} = 10^{\left(\frac{A_j}{T} - B_j \right)} \quad (2.26)$$

Table 2.3: Parameters for the calculation equilibrium constants fitted to Equation 2.26 [1].

Parameter	Reaction 1	Reaction 2	Reaction 3
A	3014.4029	1143.9494	2076.2131
B	10.3856	0.9925	2.0101

The equilibrium constants are dimensionless for reactions 2 and 3 (methanol dehydration to DME, and WGSR), while $K_{f,1}$ (the equilibrium constant of CO₂ hydrogenation to methanol) has the units bar⁻², in accordance with the law of mass action.

For performance evaluation, the conversion of component i (X_i), and the carbon-normalized yield and selectivity of component i from CO_x (Y_i and S_i) were computed based using Equations 2.27 to 2.29, respectively.

$$X_i = \frac{\dot{n}_{i,\text{in}} - \dot{n}_{i,\text{out}}}{\dot{n}_{i,\text{in}}} \quad (2.27)$$

$$Y_i = \frac{(\dot{n}_{i,\text{out}} - \dot{n}_{i,\text{in}})\eta_{c,i}}{(\dot{n}_{\text{CO}} + \dot{n}_{\text{CO}_2})_{\text{in}}} \quad (2.28)$$

$$S_i = \frac{(\dot{n}_{i,\text{out}} - \dot{n}_{i,\text{in}})\eta_{c,i}}{(\dot{n}_{\text{CO}} + \dot{n}_{\text{CO}_2})_{\text{in}} - (\dot{n}_{\text{CO}} + \dot{n}_{\text{CO}_2})_{\text{out}}} \quad (2.29)$$

In these equations, \dot{n}_i is the molar flow of component i , $\eta_{c,i}$ is the number of carbon atoms in the same component, and the subscripts “in” and “out” refer to the respective quantities at the reactor inlet and outlet.

2.4 Results and discussion

In this section, experimental results will be presented (Section 2.4.1), followed by the modelling results and mechanistic analysis (Section 2.4.2). Since most of the studies for the direct DME synthesis have been carried out with a catalyst weight ratio of one ($\mu=1$), this catalyst ratio is treated here as the reference composition for the evaluation of experimental and simulations results. The results are presented for the highest space-time (at which the effects are more pronounced) unless otherwise stated.

2.4.1 Experimental results

This section presents an overview of the effects observed experimentally. To determine causality and for a comprehensive understanding of the phenomena, the reactions kinetics are studied and analyzed in Section 2.4.2 in the light of the derived kinetic model and further kinetic studies from the literature.

For an initial qualitative analysis of the experimental results, the measured conversion of CO_x (X_{CO_x}) and DME yield (Y_{DME}) are shown in Figure 2.1 and 2.2 as a function of the temperature and the CZA-to- γ - Al_2O_3 ratio (μ) for the four investigated COR levels (20, 40, 60 and 80 %). To create this graphical representation, the values between the experiments were calculated using lowpass interpolation with the Matlab® function *interp*. The maximal conversion attained for the different inlet feed composition varies from 19.8 % (COR=80 %, $T=523$ K, $\mu=2$) to 42.6 % (COR=20 %, $T=533$ K, $\mu=2$). In general, low CORs, i.e., low CO_2 contents in the feed, lead to higher conversions at all temperatures. The highest conversions were reached in all cases with $\mu=2$, whereas the conversions attained with the reference catalyst bed composition ($\mu=1$) are the lowest. Even at high temperatures relatively low conversions are attained with the reference $\mu=1$ in comparison to those reached with the other catalyst beds. It is obvious that the temperature at which the maximal conversion was measured, decreases with increasing CORs.

The DME yield, displayed in Figure 2.1, exhibits a strong temperature dependency. The maximal Y_{DME} varies between 4.6 % (COR=80 %, $T=533$ K, $\mu=2$) and 27.9 % (COR=20 %, $T=533$ K, $\mu=2$). Overall, lower CORs lead to higher yields of DME, and analogous to the conversion of CO_x , the highest yields were attained with a CZA-to- γ - Al_2O_3 ratio $\mu=2$. The response surfaces are very similar for all CORs, however, it can be observed that with increasing COR, the region at which the highest yields are reached migrates towards the upper left corner i.e., towards high temperatures and low μ . At 533 K and 20 % COR for example, high yields are attained with all the catalyst beds, whereas at 80 % COR, the yields reached at this temperature are high with μ up to two,

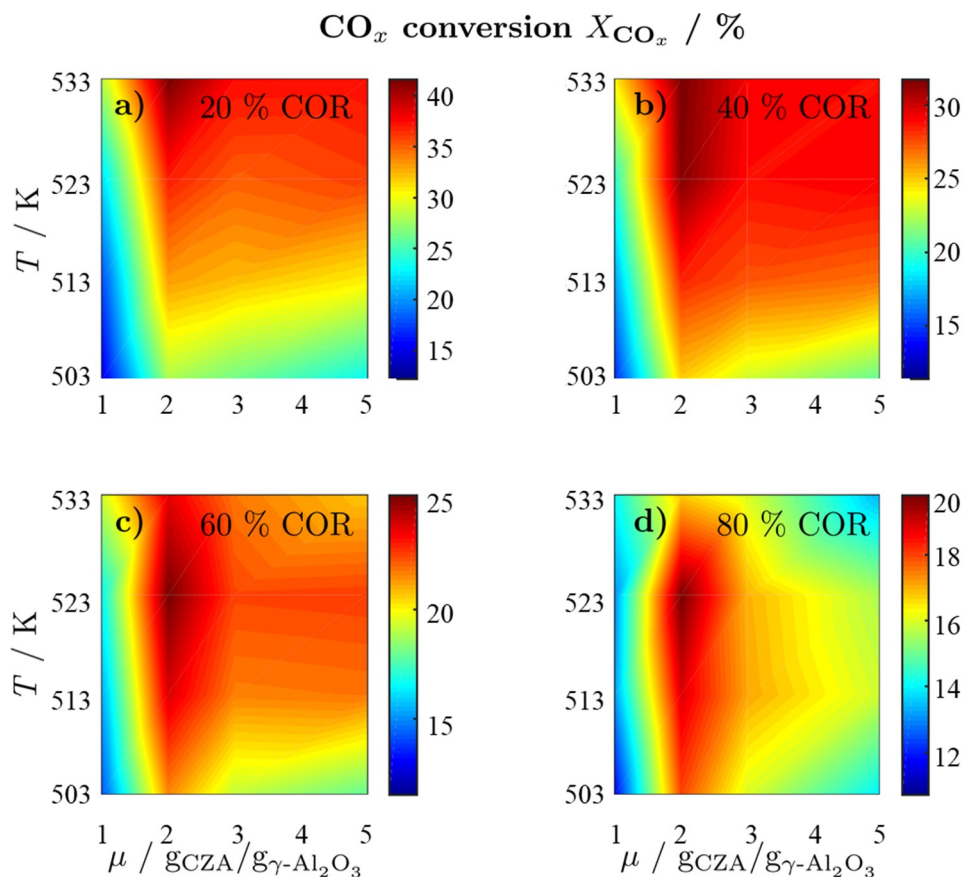


Figure 2.1: Conversion of CO_x determined experimentally and plotted as a function of the temperature (T) and the CZA-to- γ -Al₂O₃ ratio (μ) for nominal CORs of **a)** 20 % **b)** 40 % **c)** 60 % **d)** 80 %. Experimental conditions summarized in Table 2.2.

and significantly lower with μ of three and higher.

To enable a quantitative analysis of the observed effects, representative results at the minimal and maximal temperature are investigated more in detail in the following. The CO_x conversion is depicted in Figure 2.3 for the investigated CORs as a function of the CZA-to- γ -Al₂O₃ ratio, at the maximal and minimal temperature of 533 K and 503 K (Figure 2.3a and 2.3b). At 533 K, the CO_x conversion increased for all measured feeds when increasing μ up to a value of 2. This effect was most pronounced for a COR of 20 % where the relative enhancement of the conversion was of 47 %. For a COR of 80 % the relative enhancement amounted 19 %. A further increase of the CZA-to- γ -Al₂O₃-ratio had a negative effect on the conversion compared to the conversion obtained with $\mu=2$, but in all cases, the attained values were still higher than in the reference case ($\mu=1$). The only exception to this observation was for COR=80 % and $\mu=5$, where the conversion decreases from 14 % ($\mu=1$) to 13 % ($\mu=5$).

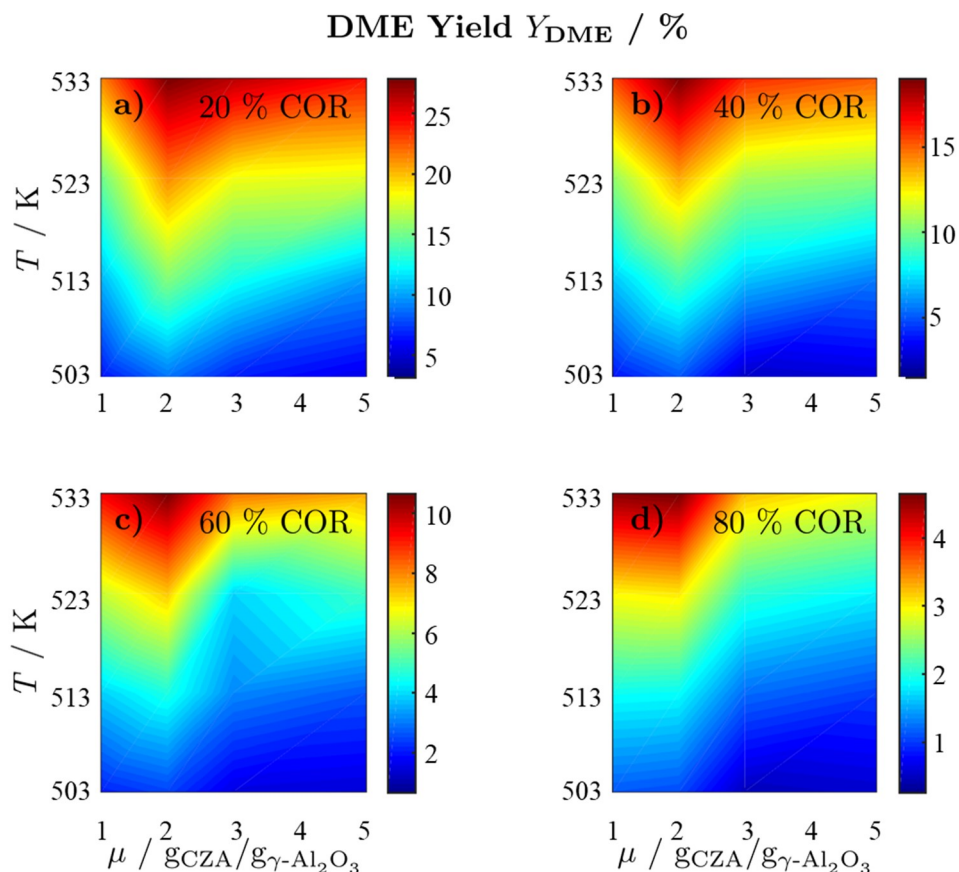


Figure 2.2: Yield of DME determined experimentally and plotted as a function of the temperature (T) and the CZA-to- γ - Al_2O_3 ratio (μ) for nominal CORs of **a)** 20 % **b)** 40 % **c)** 60 % **d)** 80 %. Experimental conditions summarized in Table 2.2.

At a temperature of 503 K, the conversion of CO_x shown in Figure 2.3b for all bed compositions and CORs is lower than for the corresponding values attained at 533 K, which can be attributed to the general dependency of the reaction rates on the temperature. For all CORs, a maximum at $\mu=2$ was detected. With this CZA-to- γ - Al_2O_3 -ratio, a relative conversion enhancement of 88 % and 52 % was obtained compared to $\mu=1$ at the minimal and maximal COR levels of 20 % and 80 % respectively. Comparable to the observations made at 533 K, the effect of the catalyst bed composition on the conversion is more pronounced at lower CORs. Furthermore, it can be observed that with the reference catalyst ratio $\mu=1$, the attained CO_x conversion is at a close value of approx. 14 % regardless of the CO_2 content in the inlet feed, in contrast to the other experiments with increasing CO_x conversion as the COR is decreased.

In general it was observed that decreasing amounts of CO_2 in the feed gas (i.e., decreasing CORs) lead to higher conversions, and to more pronounced effects of the cat-

alyst bed composition. The beneficial effect of low CO_2 concentration in the synthesis gas has been observed in other kinetic studies of both the methanol and the DME synthesis. [32, 41, 44, 77, 92, 93] Regarding the surface chemistry, low CO_2 concentration prevents sintering of the CZA catalyst, and promotes catalyst morphology that enhances the catalytic activity. [42, 44] From a thermodynamic perspective, high CO_2 feed concentration shifts the equilibrium of the WGSR towards the educts (H_2O and CO), resulting in increased water formation and subsequently in decrease of the methanol dehydration rate. [32, 41] This explanation is in accordance with the findings in this work and is further confirmed by increased methanol selectivity at high CORs discussed in the following. In Addition, this effect is explained on the basis of mechanistic considerations in Section 2.4.2.2.

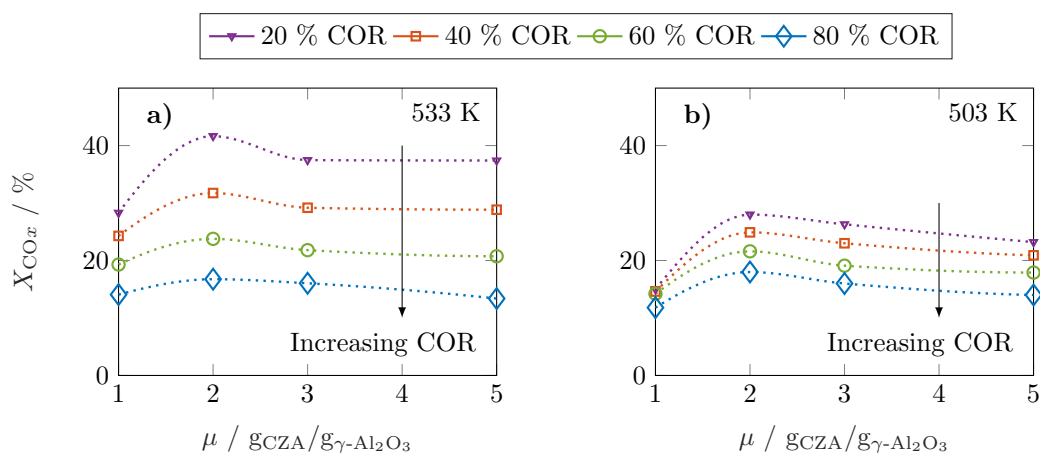


Figure 2.3: CO_x conversion as a function of the CZA-to- $\gamma\text{-Al}_2\text{O}_3$ ratio (μ) for CORs from 20 % to 80 %. a) $T=533\text{ K}$ b) $T=503\text{ K}$.

In Figure 2.4 the DME and methanol yields are shown for the minimal and maximal CORs 20 % and 80 %, and for the minimal and maximal temperatures 503 K and 533 K. Since the yield is calculated based on the reacted CO_x , and no other carbon-containing compounds were detected in a significant amount during the experiments, the yield is calculated only for methanol and DME. However, as discussed further in Section 2.4.2, CO and CO_2 formation was evidenced at some specific conditions.

At 533 K and a COR of 20 % (Figure 2.4a), the converted CO_x in the feed gas reacted to form mainly DME. In general, at this temperature and COR, an increased amount of the CZA catalyst led to a higher DME production than that attained with the reference catalyst bed ($\mu=1$). The highest relative enhancement of the DME yield was 30.3 % with $\mu=2$. A further increase of $\mu=3$ and 5 also enhanced the yield of DME but to a lower

extent (enhancement of 22.8 % and 13.2 % respectively compared to the yield attained with the reference $\mu=1$). At the same temperature and a COR of 80 % (Figure 4b), the methanol yield was at least twice as high as that of DME. An increased μ did not increase the DME yield which amounts 4.6 % at $\mu=1$ and 2, and was lower otherwise. Comparing the results shown in Figure 2.4a and 2.4b (and also Figures A.3a and A.3b), a shift of the selectivity from DME to methanol is observed when increasing the COR from 20 to 80 %. The water concentration is low at high CO contents in the feed (water removal via WGSR), and high at a high level of CO₂. [41] Obviously, presence of water is thermodynamically unfavorable for the dehydration, explaining the observed methanol concentration at high CORs. This conclusion is supported by the mechanistic analysis provided in Section 2.4.2.2.

In Figure 2.4c and 2.4d it is observable that for a temperature of 503 K, the yield of methanol is higher than that of DME for both COR levels. An enhancement of the DME yield compared to the reference case is still observable at a COR of 20 % (38.2 % and 4.3 % with $\mu=2$ and 3), whereas at 80 % COR, an increase of the μ proved to be disadvantageous for the DME yield. The lowest DME yields were observed at 503 K, a COR of 80 % and $\mu=3$ and 5.

The catalytic activity of the CZA/ γ -Al₂O₃ system is a function of combined physicochemical characteristics such as Cu surface area, dispersion, and acidity. [94–96] Furthermore, the setup of reaction conditions have also shown to be a key factor. [75] While the study of the catalysts properties was out of the scope of this work, a wide range of conditions was covered during the experimental program. The improvement observed by increasing the CZA-to- γ -Al₂O₃ ratio reveals that the number of required acid sites has already been significantly exceeded when equivalent catalyst masses are used. [1, 32] Therefore, an increase of the catalyst ratio leads to an overall enhancement of the synergistic effects of the direct DME synthesis i.e., the faster methanol formation due to an increased amount of CZA catalyst has a positive effect on the methanol dehydration even though the amount of the catalyst that promotes this reaction is reduced. Overall, it was observed that the highest enhancement of the DME yield was attained at a CZA-to- γ -Al₂O₃ ratio of $\mu=2$, and that higher ratios lead to a minor improvement, or even to a decrease of the DME production. Additionally, it was observed that the methanol yield increased with increasing CZA-to- γ -Al₂O₃ ratio at all conditions (Figure 2.4a to 2.4d) as also described in other kinetic studies. [32, 75, 94] Hence, the evidenced enhancement of the DME yield is associated to the higher conversion, i.e., the conversion of CO_x increased more than the DME selectivity decreased, leading to higher DME yields than with the reference catalyst bed.

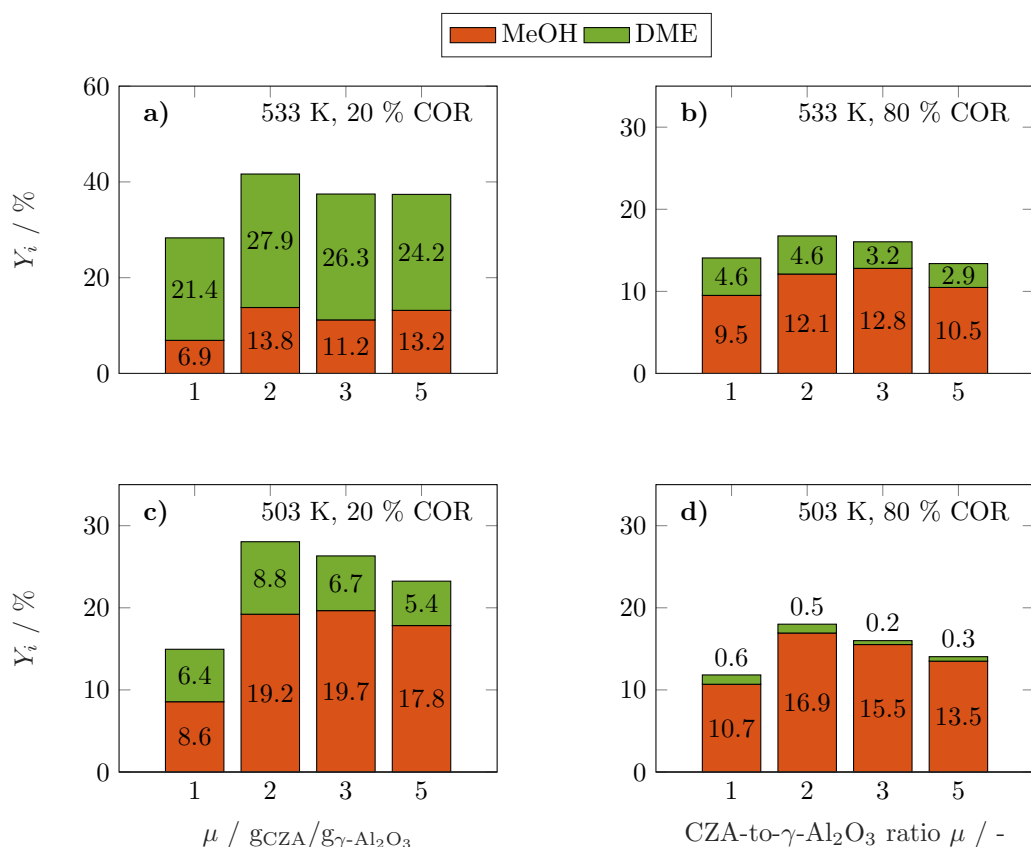


Figure 2.4: Yield of methanol and DME at specific exemplary conditions: **a)** 533 K, 20 % COR, **b)** 533 K, 80 % COR, **c)** 492 K, 20 % COR **d)** 492 K, 80 % COR.

2.4.2 Modeling Results

Predictive models able to make accurate predictions over a wide range of conditions are of considerable importance as a basis for model-based optimization and for the design of novel reactor concepts. The respective contribution of this chapter is a reaction kinetic model for direct DME synthesis suitable these purposes. In Section 2.4.2.1., the results of the parameter estimation are presented together with an analysis of the achieved goodness of fit and statistical significance of the parameter estimates. In Section 2.4.2.2, the phenomena experimentally observed (Section 2.4.1) are explained taking into account the derived kinetic model. In addition, it is described to what extent these findings are consistent with the results and new mechanistic insights of other studies.

2.4.2.1 Reaction kinetic model

In this section, the resulting kinetic model, i.e., the parameter estimates and model evaluation are discussed. As mentioned briefly in Section 2.3.2, the presented model was the one that enabled the best fit of the experimental data within the entire range of

conditions investigated in this work. The derived model chosen after a discrimination procedure agrees with the one derived from mechanistic assumptions by Lu et al. [80] and used in a previous work. [1] It considers the linearly independent reactions CO₂ hydrogenation and WGSR, along with the methanol dehydration to DME. In agreement with the mentioned studies, including no adsorption term for the dehydration catalyst, and the adsorption of CO, CO₂ and dissociated H₂ on the CZA catalyst led to the best representation of the experimental data. Considering the adsorption of water and methanol as done in other kinetic studies of the direct DME synthesis [32, 35, 39] worsen the quality of fit, and was therefore discounted from the model structure. The goodness of fit for CO, CO₂, H₂ and DME with the resulting model is represented by the parity diagrams in Figure 2.5 with the measured quantities plotted against the numerically predicted ones.

The model-specific parameters were estimated based on 186 experimental data points. The mean relative error between the predicted and measured molar fractions over all data amount to 2.7 % for CO₂, 7.2 % for CO, 1.0 % for H₂, and 22.3 % for DME. The deviation of the DME predictions is mostly attributed to an over-prediction of the data measured with $\mu=5$. The data taken with this catalyst bed exhibits the lowest DME production and low DME mole fractions in the product gas as shown in Figure 2.2. Hence, these measurements have a high signal-to-noise ratio, and a lower measurement accuracy, to which the larger deviations can be attributed to. Nonetheless, the deviation of the DME predictions is considered acceptable, especially regarding the extensive range in which the experiments were measured. Furthermore, the predictions lie with a clear tendency and a weak scattering along the bisector ($y = x$), and no systematic deviations are identifiable for any of the species.

The resulting parameter estimates are shown in Table 2.4 along with the respective 95 % confidence intervals. The adsorption parameters were fixed. Hence, no statistical information is available on these estimates. In regards to the rate constants, the confidence intervals demonstrate that all re-parametrized pre-exponential factors and activation energies are statistically significant. Moreover, the width of the confidence intervals is less than 13 % of the respective estimates for five out of six parameters. The widest confidence interval was that of the re-parametrized activation energy of the CO₂ hydrogenation, with a width of 29 % of the estimated value, which underlines the high statistical significance of the estimated kinetic parameters.

The reference temperature was calculated as $T_R = 517.43$ K using Equation 2.25 for the 186 experiments used for fitting.

According to Equations 2.22 and 2.24 $E_{A,j}^*$ and $\Delta H_{ads,i}^*$ are dimensionless, and $k_{0,j}^*$ is based on the mass of the catalyst that promotes each reaction, i.e., CZA for the CO₂

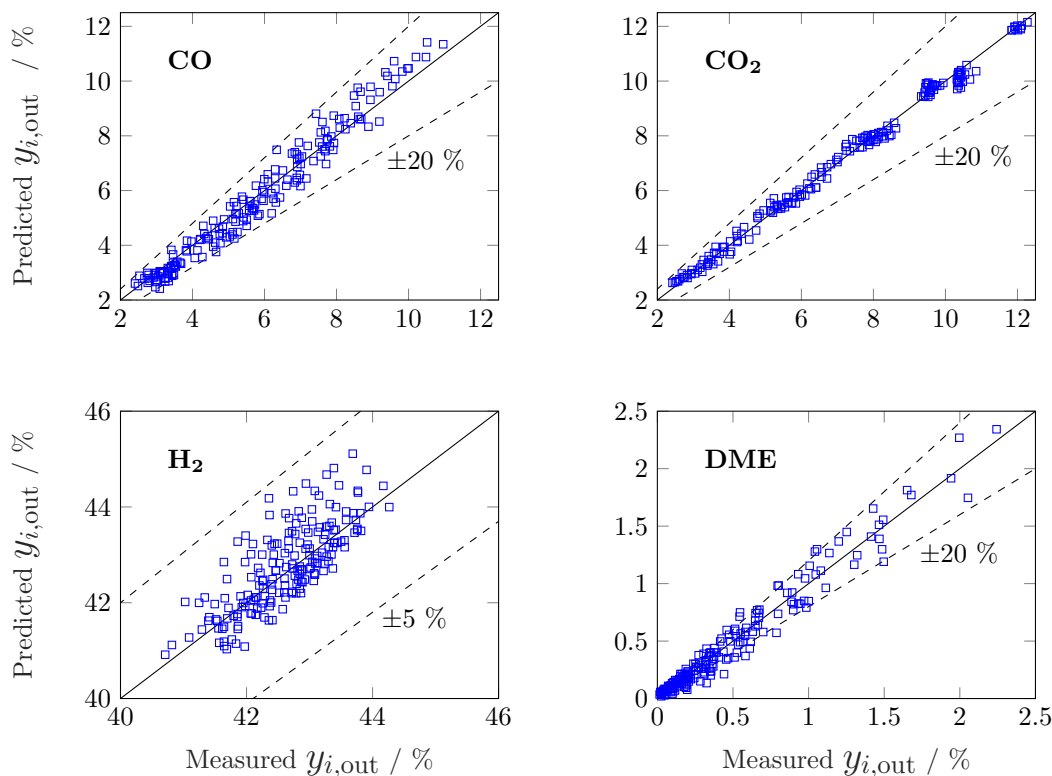


Figure 2.5: Parity plots for mole percent of CO, CO₂, H₂ and DME in the product gas for all data (186 experiments) and simulations conducted with the semi-mechanistic model.

hydrogenation and the WGSR, and γ -Al₂O₃ for the methanol dehydration to DME.

The adsorption constants K_i were calculated with Equation 2.20 at the different temperature levels to determine the influence of the adsorption of each species on the adsorption term (the reported value for H₂ corresponds to $\sqrt{K_{H_2}}$ according to Equation 2.14. The calculated values are shown in Table 2.5. The CO adsorption has clearly the lowest adsorption constant, in agreement with the studies of Lu et al. [80] and Delgado Otalvaro et al. [1] where the same adsorption term was employed. The constant of CO₂ adsorption exhibited both in Delgado Otalvaro et al. [1] and in the present work the highest value. This is also consistent with the investigations of Klier et al., [93] where a strong CO₂ adsorption on the metallic catalyst was observed. All adsorption constants shown in Table 2.5 decrease with increasing temperature due to the exothermal nature of adsorption.

Binary correlation coefficients ($\rho_{i,j}$) were computed to assess the correlation between the parameter estimates (Table 2.6). The absolute values of all the non-trivial correlations coefficients confirm that using the re-parametrized Arrhenius and Van't-Hoff equations

Table 2.4: Estimated parameters in re-parametrized form according to Equations 2.19 and 2.20, and 95 % confidence intervals. The non re-parametrized parameters are reported in the appendix, in Table A.3.

Reaction	$k_{0,j}^*$	$E_{A,j}^*$
CO ₂ hydrogenation	3.19 (\pm 0.04) $\frac{\text{mol}}{\text{kg s bar}^4}$	7.60 (\pm 2.20)
MeOH dehydration	-5.72 (\pm 0.07) $\frac{\text{mol}}{\text{kg s bar}^2}$	24.58 (\pm 3.22)
WGSR	1.74 (\pm 0.11) $\frac{\text{mol}}{\text{kg s bar}^2}$	40.77 (\pm 4.96)

Adsorbate	K_i^*	$\Delta H_{\text{ads},i}^*$
CO ₂	4.68 bar ⁻¹	-1.25
CO	-34.04 bar ⁻¹	-79.81
H ₂	7.13 bar ⁻¹	-5.04

Table 2.5: Adsorption constants at different temperatures.

	$T = 503$ K	$T = 513$ K	$T = 523$ K	$T = 533$ K
$K_{\text{CO}_2}/\text{bar}^{-1}$	111.9	109.2	106.6	104.1
$K_{\text{CO}}/\text{bar}^{-1}$	1.6E-14	3.2E-15	6.9E-16	1.6E-16
$\sqrt{K_{\text{H}_2}}/\text{bar}^{-0.5}$	37.9	36.0	34.3	32.8

(Equations 2.19 and 2.20) led successfully to a weak correlation between the parameter estimates. In addition, the convergence time of the fitting was reduced by about 60 % after applying re-parameterization.

Table 2.6: Binary correlation coefficients of parameter estimates.

$\rho_{i,j}$	$k_{0,1}^*$	$E_{A,1}^*$	$k_{0,2}^*$	$E_{A,2}^*$	$k_{0,3}^*$	$E_{A,3}^*$
$k_{0,1}^*$	1	-0,53	-0,83	0,40	-0,39	0,28
$E_{A,1}^*$		1	0,38	-0,85	0,31	-0,36
$k_{0,2}^*$			1	-0,44	-0,07	-0,11
$E_{A,2}^*$				1	-0,11	-0,03
$k_{0,3}^*$					1	-0,28
$E_{A,3}^*$						1

2.4.2.2 Mechanistic analysis

Using the derived model, the proposed reaction mechanism is elucidated in the following based on representative results. The influence of the COR, the temperature, and the CZA-to- γ -Al₂O₃ ratio on the reactions rates is discussed, as well as the observed CO and CO₂ formation during reaction.

Effect of the COR. In Section 2.4.1 it has been shown that high conversions and yields of DME are attained at the lowest COR levels. This was observed at all conditions in the investigated operating range, although at differing extent. This is in accordance with former kinetic studies of the methanol, [44, 77, 93] and DME synthesis [32, 41] which have shown that an optimal CO₂ feed concentration exists, at which both the methanol formation and subsequently the DME formation are favored, while exceeding this concentration leads to reduced conversions and yields. Sintering of Cu crystallites in the CZA catalyst takes place with CO/H₂ and CO₂/H₂ feeds due to Cu segregation from ZnO, and due to the presence of water respectively. However, sintering is prevented at the optimal CO₂ feed concentration. [44] Since no optimal value for the COR within the investigated operating range was observed, it can be concluded, in agreement with other studies, [32, 41, 44, 93] that the optimal value is probably less than or equal to 3 %, which was the lowest CO₂ concentration considered in this chapter (at 20 % COR).

To elucidate the effect of the COR on the reactions rates, these have been depicted in Figure 2.6a to 2.6c at exemplary conditions for the minimal and maximal CORs of 20 % and 80 %. Additionally, the mole percentage profiles of water, methanol and DME are displayed in Figure 2.6d (Figure S4 in the ESI includes the profiles of CO and CO₂, which were left out here for better visualisation). It is shown that the rates of the three reactions, i.e., CO₂ hydrogenation, methanol dehydration and WGSR, are higher at 20 % COR than at 80 % COR. This effect is straight forward for the WGSR where CO₂ is a product, and an increased product concentration shifts the equilibrium towards the educts according to the Le Chatelier's principle. For the CO₂ hydrogenation on the other hand, it may appear contradictory that the rate is lower at higher CORs since CO₂ is a reactant in this reaction. This has been attributed to several factors in the literature such as to the presence of water in high concentrations leading to sintering of the Cu particles, [44] to thermodynamic limitation of the methanol formation, [6] or to strong CO₂ adsorption on the metallic catalyst. [93] CO₂ adsorption is also believed to be important in this study, which is accounted for in the model by the strong influence of CO₂ concentration on the adsorption term (Equation 2.14) and Section 2.4.2.1), and by the considerable influence of the adsorption term on the CO₂ hydrogenation (Equation 2.16). The strong influence of the adsorption term leads to an overall decrease of the reaction rate with increasing CO₂ in the feed, even though the potential term of the forward reaction is indeed higher at higher CORs.

The rate of the WGSR (Figure 6c) takes on negative values at the reactor entrance at both CORs, indicating that the reverse water gas shift reaction (rWGSR) is faster than the WGSR at the inlet conditions. At 80 % COR the rWGSR is particularly fast (high

negative values, min. $r_3^v = -3.7 \text{ mol m}^3 \text{ s}^{-1}$ at $z=0$), which can be attributed to the high concentrations of CO_2 and H_2 in the feed. Although a high hydrogen feed concentration is necessary to avoid the stoichiometric limitation of CO_2 hydrogenation to methanol, the high feed concentration of both, CO_2 and H_2 , accelerates the rWGSR instead of the CO_2 hydrogenation as evidenced, leading to water and CO production. [70, 97] The simulations show that the rWGSR prevails over the WGSR for the initial 10 % bed length, resulting in a pronounced increase of water concentration (Figure 2.6d, blue dashed line). From a bed length beyond 10 %, the water gas shift equilibrium (reaction 3) shifts to the right side and r_3^v takes on nearly constant positive values over the entire following bed length, accompanied by reduced overall water formation as water is partially consumed by the WGSR. The widely accepted mechanism of methanol formation by CO_2 hydrogenation over copper-based catalysts was disputed by Gaikwad et al. [43] It was shown by means of space-resolved experiments that the main carbon source for methanol formation from CO_2 rich feeds depends on the reaction conditions, in particular on the temperature. The authors concluded that at 533 K and CO_2/H_2 feeds, methanol formation takes place via CO hydrogenation formed by the rWGSR at the reactor inlet. The simulation results are in accordance with that conclusion. i.e., the rWGSR takes place at the reactor inlet, followed by the CO hydrogenation, in the model described by the WGSR and the subsequent CO_2 hydrogenation. Which also explains the higher conversions and yields at high CO feed concentration. At this COR, the rWGSR prevails only at the reactor entrance (up to 0.8 % reactor length), and the rate does not reach such high negative values (min. $r_3^v = -2.2 \text{ mol m}^3 \text{ s}^{-1}$ at $z = 0$). As a result, the water concentration at the reactor entrance rises steeply, but does not reach such a high level as at 80 % COR. Although water has shown to limit the catalyst deactivation by coke deposition [33, 98] high water concentration in is indisputably detrimental for direct DME synthesis, especially when using $\gamma\text{-Al}_2\text{O}_3$ as the dehydration component. [64, 99] This underlines the importance of water removal, e.g., by permselective membranes [100, 101] which could also be axially tailored to counteract the observed steep water increase at the reactor entrance shown here as well as in other kinetic studies. [102, 103]

Clearly, the methanol dehydration to DME is also affected strongly by the COR, as shown in Figure 2.6b. At 20 % COR the concentration of methanol is higher than the concentration of water for the largest portion of the reactor (solid lines in Figure 2.6d). Conversely, at 80 % COR the water concentration is higher than the concentration of methanol (dashed lines in Figure 2.6d). Reduced methanol dehydration rate at high CORs has been explained in the literature by deactivation phenomena of the $\gamma\text{-Al}_2\text{O}_3$, and by a strong adsorption of methanol and/or water on the surface of the dehydration catalyst. [39, 41, 79, 80, 104] In the experiments in this work, no activity drop was observed and, as mentioned in Section 2.3.1, the model that enabled the best fit to the

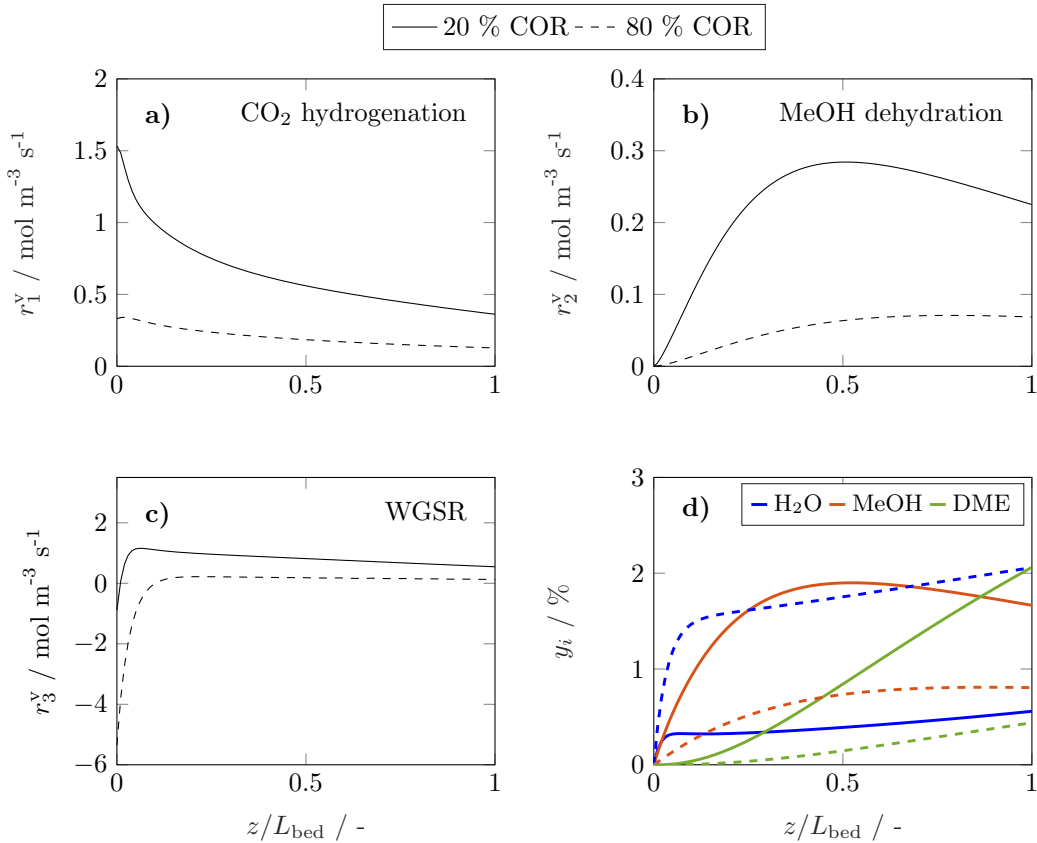


Figure 2.6: Reaction rates **a)** CO₂ hydrogenation, **b)** MeOH dehydration, **c)** WGSR and **d)** mole percentage profiles of water, methanol and DME at $T = 533$ K, $\mu = 2$.
 (—) Solid lines: 20 % COR, (---) Dashed lines: 80 % COR.

experimental data is based on the assumption that no adsorption on the dehydration catalyst takes place. [1, 80, 99] Hence, the influence of the COR on the dehydration rate is accounted for by thermodynamics only. I.e., considering the stoichiometry of the dehydration reaction it is clear that high methanol and low water concentrations as evidenced at 20 % COR are thermodynamically favorable for DME formation, while low methanol and high water concentrations as exhibited at 80 % COR are disadvantageous. As a result, the methanol dehydration is significantly slower at 80 % COR than at 20 % COR explaining the decreasing DME formation with increasing CORs observed experimentally (Figs. 2.2, 2.4a and 2.4b).

Effect of the temperature. The reaction rates, and the mole fractions of DME, water and methanol are depicted in Figure 2.7 at the minimal and maximal evaluated temperatures, i.e., at 503 K and 533 K for a COR of 20 %. Due to the general temperature dependence of the reaction rate constants, all reactions proceed faster at 533 K

than at 503 K (Figure 2.7a to 2.7c). In addition to the temperature dependence of the rate constants, the dependence of the adsorption rates is also relevant when assessing the influence of temperature based on the proposed model. Adsorption constants decrease with increasing temperatures due to the exothermal nature of adsorption processes (Table 2.5). Since the adsorption terms have an indirect proportional effect on the reaction rates (Equation 2.11), the slower adsorption also contributes to the higher rates of the CO₂ hydrogenation and WGSR evidenced at higher temperatures.

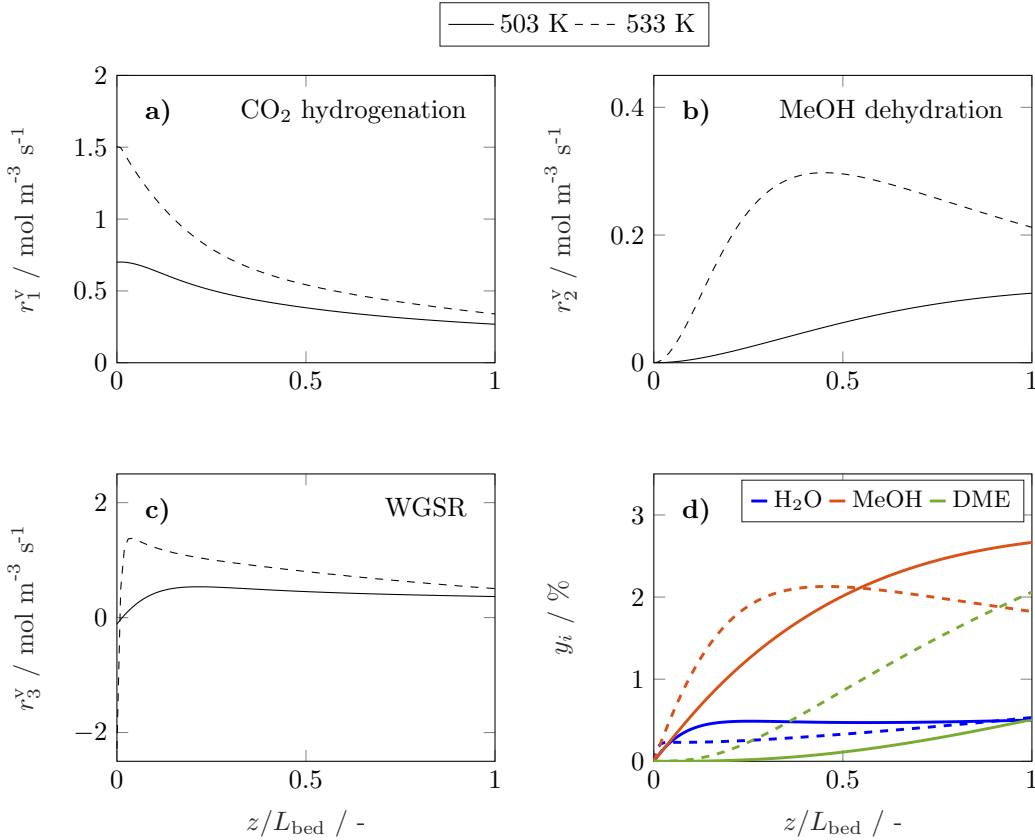


Figure 2.7: Reaction rates **a)** CO₂ hydrogenation, **b)** MeOH dehydration, **c)** WGSR and **d)** mole percentage profiles of water, methanol and DME at $\mu = 2$ and COR = 20 %.
(—) Solid lines: $T = 503$ K, (- - -) Dashed lines: $T = 533$ K.

A factor not considered by the model but potentially favors methanol dehydration at elevated temperature is enhanced water desorption from the dehydration catalyst surface, [105] leading to an increased number of available active centres for the dehydration reaction. The effect of the temperature on the concentrations profiles is shown in Figure 2.7d. Compared to 503 K (solid lines), at 533 K (dashed lines) the methanol concentration is higher for 55 % of the reactor length, while the water concentration is lower for almost the entire reactor. Hence it is obvious that at 533 K, the driving force of

the dehydration reaction is increased, leading to significantly higher DME concentrations and DME yields, as also determined experimentally (Figs. 2.4a and 2.4c). Furthermore, the concentration increase for DME is significantly higher than for methanol, confirming that higher temperatures have a positive effect on DME selectivity [75] (Figures A.2 and A.3).

In the study of Gaikwad et al., [43] for methanol synthesis at 453, 533 and 613 K, the authors concluded that at 533 K the main reaction mechanism takes place via rWGSR and CO hydrogenation, while at lower temperature, direct CO₂ hydrogenation is the dominant pathway. In Figure 2.8, simulation results at the highest COR considered (80 %) and at 503 and 533 K show that the developed lumped kinetic model is mechanistically sound according to these new insights. The respective reaction rates of the WGSR (Figure 2.8c) are of particular interest: at 533 K, the phenomenon described in Section 2.4.2.2 takes place; i.e., the rWGSR dominates at the reactor inlet, followed by both, WGSR and CO₂ hydrogenation, in combination representing a descriptor for CO hydrogenation; at 503 K, the WGSR rate is nearly zero and shows a nearly constant profile along the reactor length. This leads us to the conclusion that at 503 K, methanol formation takes place via direct CO₂ hydrogenation. From the findings of Gaikwad et al. [43], it cannot be concluded exactly at which temperature the mechanism shifts, although from the findings in this work it seems plausible that at 503 K, both reaction pathways are contributing.

Effect of the catalyst bed composition. There are several studies concerning the catalyst bed composition for the direct DME synthesis. A literature overview recently provided by Peinado et al. [75] summarizes that most studies have been performed for CO₂ lean feeds and, with high CZA proportions in the catalyst bed. Some of the studies cited state that the optimal catalyst bed composition consists of 50 % CZA [75, 94, 106] while other authors, like us, came to the conclusion that higher CZA-to-acid catalyst ratios are advantageous for the DME productivity. [1, 32, 92] To demonstrate the influence of higher CZA-to- γ -Al₂O₃ ratios on the reaction rates, these are depicted in Figure 2.9 for the reference CZA-to- γ -Al₂O₃ weight ratio $\mu = 1$, and for $\mu = 2$, which exhibited the best performance with regard to the DME yield in the experiments. The increased μ is clearly advantageous for all the reactions rates, as assumed in Section 2.4.1. The effect of the catalyst bed composition is less pronounced than that of the COR and the temperature, and no significant changes on the shapes of the reaction rate profiles is observed. With regard to the concentration profiles, an increased μ leads to higher methanol and DME concentrations, whereas the concentration of water is virtually unchanged. Moreover, the relative increase in methanol concentration is higher than the relative increase in DME, indicating a decrease of the selectivity towards DME, consistent with experimental ob-

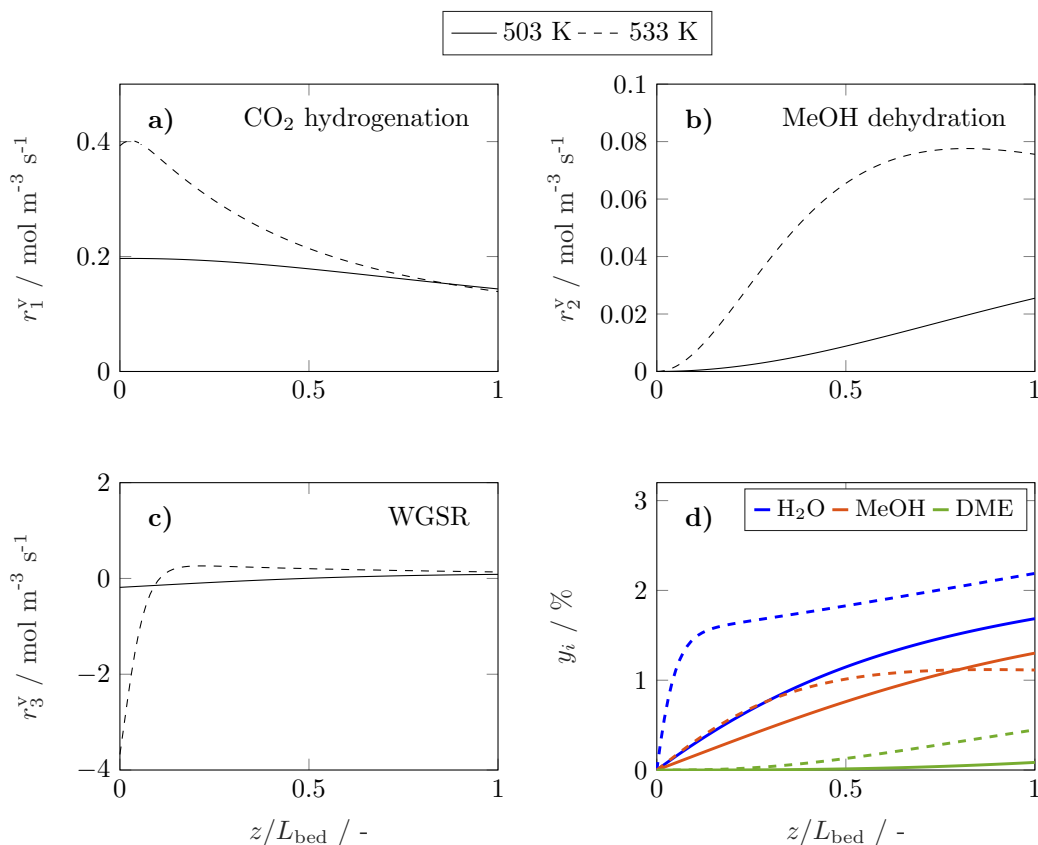


Figure 2.8: Reaction rates **a)** CO₂ hydrogenation, **b)** MeOH dehydration, **c)** WGSR and **d)** mole percentage profiles of water, methanol and DME at $\mu = 2$ and COR = 80 %.

(—) Solid lines: $T = 503 \text{ K}$, (---) Dashed lines: $T = 533 \text{ K}$.

servations described in Section 2.4.1.

Table A.4 in Appendix A provides an overview on studies with different CZA-to- $\gamma\text{-Al}_2\text{O}_3$ ratios. A direct comparison with other works regarding this variable is not comprehensively possible, due to the wide range of process parameters evaluated in literature studies, [75] and also due to more or less widespread catalyst properties, reactor types and configurations, and finally the respective methodology followed in each study. Commonly drawn conclusions in accordance with this work are as follows: (1) DME selectivity increases with decreasing CZA-to- $\gamma\text{-Al}_2\text{O}_3$ ratios when CO₂ is present in the feed. [75, 94] (2) However, decreasing CZA-to- $\gamma\text{-Al}_2\text{O}_3$ ratio especially below a value of 1, is detrimental for the DME production. [32, 75, 106] (3) Hence, increased DME yield attained with increasing CZA-to- $\gamma\text{-Al}_2\text{O}_3$ ratios is attributed to a significant enhancement of the CO_x conversion, that makes up for the selectivity loss. Higher amounts of the CZA catalyst, evidently lead to higher rates of CO₂ hydrogenation and water gas

shift reaction (Figure 2.9a and 2.9c), which are both promoted by this catalyst. On the other hand, increased methanol formation and water depletion rates are contributing to methanol dehydration to DME. Hence, explaining the higher rate of the dehydration reaction (Figure 2.9b), even though compared to the reference case ($\mu = 1$), the fraction of the dehydration catalyst at $\mu = 2$ is reduced. It should also be noted that most of the studies mentioned are experimental in scope. This emphasizes the general importance and necessity of models valid for a broader range of catalyst bed compositions (especially also for a wide range of CO_2/CO_x feed ratios) to enable model-based evaluation of optimization strategies and/or reactor designs under consideration of this variables.

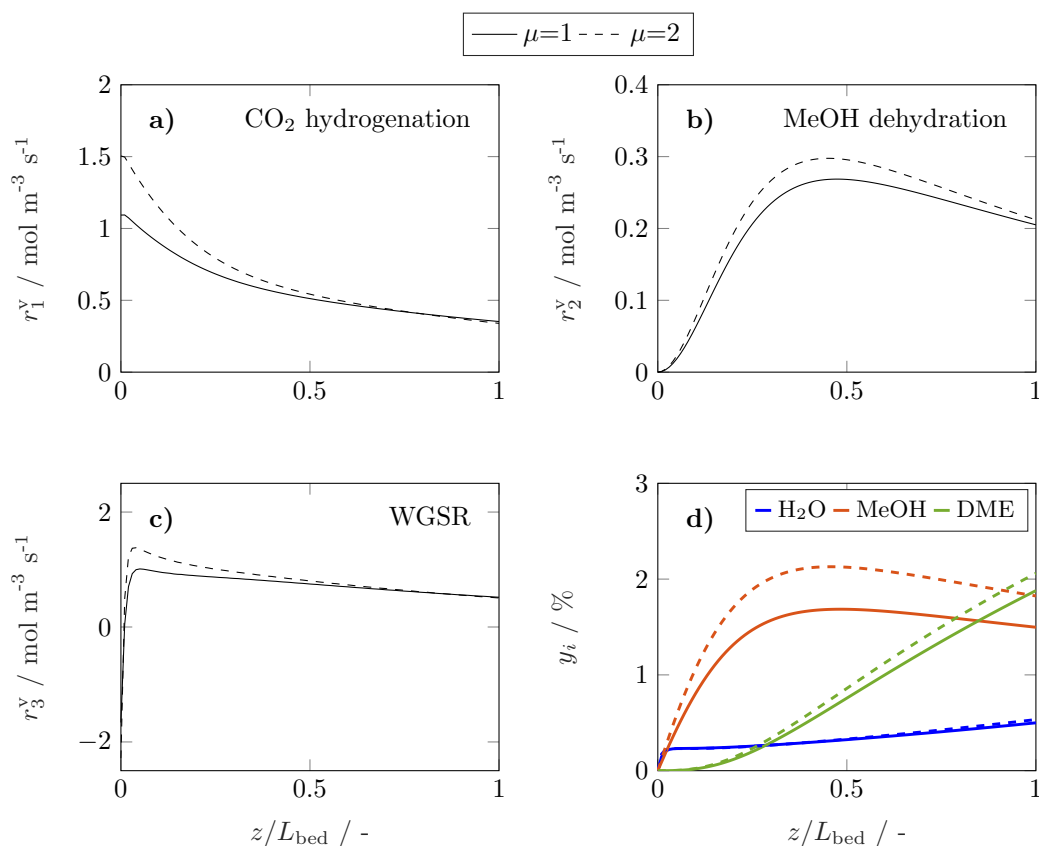


Figure 2.9: Reaction rates **a)** CO_2 hydrogenation, **b)** MeOH dehydration, **c)** WGSR and **d)** mole percentage profiles of water, methanol and DME at $T = 533$ K, $\text{COR} = 20$ %.

(—) Solid lines: $\mu = 1$, (- - -) Dashed lines: $\mu = 2$.

CO_2 and CO formation during reaction. According to Equation 2.27, a negative conversion (X_i) indicates that the amount of the respective species i is higher at the reactor outlet than at the reactor inlet i.e., that the species was formed during reaction. Within the wide operational windows studied in this work, CO_2 and CO formation was

observed at specific conditions. As depicted in Figure 2.10a, CO₂ formation was evidenced at high temperatures and low CORs. The highest CO₂ formation, i.e., the lowest CO₂ conversion, was observed at 20 % COR and 533 K. At these conditions, the WGSR is faster than the CO₂ hydrogenation for most of the reactor length. Hence, more CO₂ is produced than consumed, explaining the negative CO₂ conversions. Contrary to the results at higher temperatures, CO₂ formation does not take place at 503 K. CO formation on the other hand, was evidenced at low temperatures and high CORs (Figure 2.10b). The minimal CO conversion took place at 80 % COR and 503 K, caused by a relatively late shift of the rWGSR to WGSR. At these conditions, the rWGSR prevailed over the WGSR for approx. half of the reactor length. The CO produced in the first half of the reactor, is not completely consumed in the second half, leading to the slight overall CO production shown in Figure 2.10b. In agreement with the mechanistic analysis presented before, CO₂ and CO conversion show opposite trends, with the CO conversion increasing with temperature, as methanol formation takes place via CO hydrogenation. [43] CO conversion is also increasing with decreasing COR, due to WGSR that is favored at high CO feed concentration, and decreases respectively with increasing COR according to an increased participation of the rWGSR.

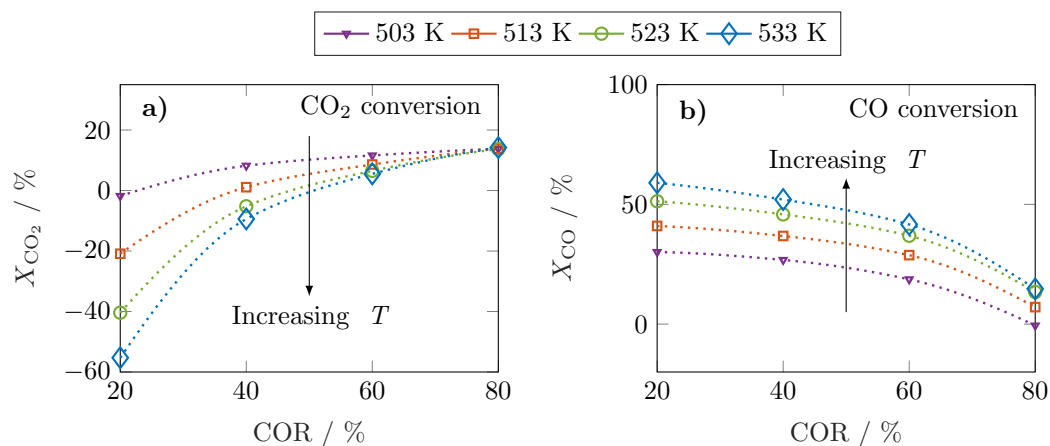


Figure 2.10: CO₂ and CO conversion for all evaluated CORs and temperatures. $\mu = 2$.

2.5 Summary and conclusions

The reaction kinetics of the direct DME synthesis over Cu/ZnO/Al₂O₃ (CZA) and γ -Al₂O₃ were investigated at high pressure (5 MPa) in a temperature range between 503 and 533 K, CZA-to- γ -Al₂O₃ weight ratios from 1 to 5, space times from 240 to 400 kg_{cat} s/m³_{gas}, and carbon oxide ratios (CO₂/CO_x) from 20 to 80 %. The successful fitting to these data resulted in the main contribution of this paper: a mechanistically sound re-

action kinetic model with a particularly large range of validity. Due to its wide validity range, the reaction kinetic model provided in this contribution is suitable aiming towards optimal reactor and/or process design, and optimization of novel technologies for the direct DME synthesis.

The influence of key process variables on reaction rates was examined in light of the derived model, and representative results were presented with the goal of determining causality and providing a comprehensive understanding of the observed phenomena. An increased CZA-to- γ -Al₂O₃ ratio was found to be favorable in terms of DME yield, although this reduced the amount of dehydrogenation catalyst. This is attributed to the synergistic effects of direct DME synthesis, i.e., an increased methanol production rate also accelerates the dehydration of methanol to DME. With regard to the composition of the feed, a high CO content leads to an increased DME yield, since the water gas shift reaction and thus the water consumption in the system are accelerated. Conversely, a high CO₂ content leads to a significantly increased water concentration. This is due to a strong effect of reverse water gas shift at the reactor inlet, which increases with CO₂ content. Moreover, it was shown that increasing temperatures lead to higher DME yield and selectivity regardless of the feed composition. However, at high CO₂ content in the feed, the attainable enhancement by optimization of the reaction conditions might not lead to sufficiently high DME yields for the process to be economically feasible. Therefore, additional technical improvements are necessary to achieve a significant increase in overall performance. Possible technical improvements include water removal, novel reactor concepts such as membrane reactors or reactive distillation, as well as a customized product separation.

3. DATA-BASED MODEL

In this chapter, Artificial Neural Networks (ANNs) are designed and implemented to model the direct DME synthesis from syngas over a commercial catalyst system. The predictive power of the ANNs is assessed by comparison with the predictions of a lumped model parameterized to fit the same data used for ANN training. The ANN training converges much faster than the parameter estimation of the lumped model, and the predictions show a higher degree of accuracy under all conditions. Furthermore, the simulations show that the ANN predictions are also accurate even at some conditions beyond the validity range.

3.1 Introduction

Using artificial neural networks (ANNs) is the most widespread machine learning approach for modeling complex phenomena due to their simple formulation, flexibility and robustness [50, 51, 107]. ANNs have proven to be suitable for creating predictive models for chemical engineering processes. Hence, several applications have been subject of research in the last decades, such as the evaluation and modeling of complex kinetic data [48, 108, 109], catalyst design [110, 111], soft sensing [50, 112], advanced process control [113], and others [47]. Studies regarding the application of ANNs for the DME synthesis have been reported e.g., for the screening of additives [110, 111], the optimization of temperature profiles in a temperature gradient reactor [114], and the modeling of the single process steps [115, 116]. Furthermore, ANNs have been used for predicting the performance of the liquid phase direct synthesis of DME over CuO/ZnO/Al₂O₃ and H-ZSM-5 catalysts [112]. In this chapter, ANNs are used to model the direct synthesis of DME from CO₂ rich synthesis gas over a mixed catalyst bed of commercial CuO/ZnO/Al₂O₃ (CZA) and γ -Al₂O₃ catalysts at high pressure. The ANNs applied are fully connected multi-layer feedforward networks trained by supervised learning to map the input-output relationships in intrinsic kinetic data. For the ANN design, several back-propagation training algorithms as well as different activation functions and network architectures have been tested. Additionally, a data partitioning scheme is presented, which enables the data division for training and testing in an automated fashion. Simulations within and beyond the model's validity range are conducted to shed light on the ANN's predictive ability in both operational windows, and to report on the ability of simple ANNs in modeling this system in comparison to that of a lumped kinetic model fitted to the same data.

3.2 Artificial Neural Networks - Key Design Parameters and Modeling

In this section, fundamentals for the ANN design are introduced. The theoretical framework is intended to describe the general functionality of ANNs and the features that are relevant here for modeling the direct DME synthesis.

3.2.1 Features and Functional Principles

ANNs are a mathematical portrayal of the human neural system. Similar to the biological system, ANNs consist of interconnected neurons that are responsible for the processing and forwarding of data. There is an extensive number of general ANN types that can be classified based on their application, topology, connection pattern and the applied learning method as depicted in Figure 3.1. The ANNs relevant for this contribution are multilayer, feedforward networks used for function evaluation (i.e., nonlinear regression) and trained by supervised learning method. These features are briefly discussed in the following.

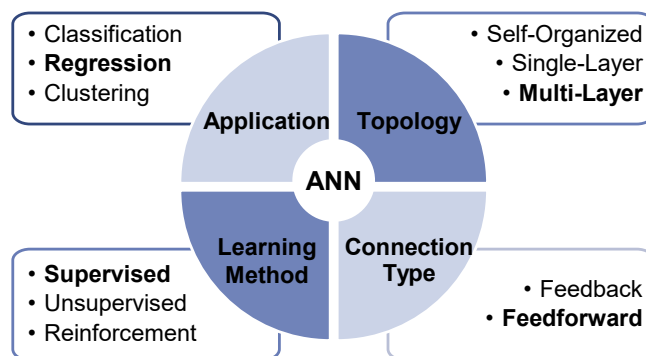


Figure 3.1: Classification of ANNs (created from Sohrab Zendehboudi et al. [54]).

In multilayer feedforward networks, the elementary units (neurons) are organized into layers, as depicted in Figure 3.2a. There is one input layer containing the input signals and one output layer containing all output signals of the network. Additionally, they may also have one or more hidden layers located between input and output. These networks are known as “shallow” or “deep” ANNs respectively. Moreover, the “feedforward” connection type between neurons indicates that information is transferred unidirectionally from the input to the output layer.

The functional principle of an artificial neuron is shown in Figure 3.2b. The input signals x_i are multiplied with connections weights w_i that define the influence of the re-

spective input data on the neuron’s output signal. The net input n of the neuron is the sum of all weighted input signals and the bias b , which represents the neuron’s threshold. If this threshold is exceeded, the neuron will be activated, i.e., an output signal y will be produced. The neural output signal is calculated using the activation function $f(n)$ that transforms the input of the neuron e.g., introducing nonlinearities. This output signal is then transferred to the next artificial neuron.[52, 54]

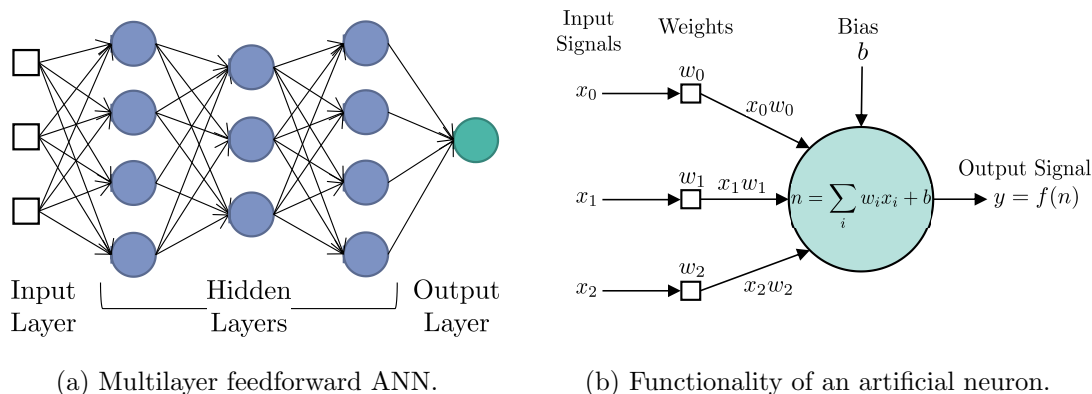


Figure 3.2: ANN structure and functionality of an artificial neuron.

The number of neurons in the input and output layers is constraint by the scenario under consideration, while the number of hidden layers and hidden neurons must be determined by the designer based on trial-and-error or using rules-of-thumb [50, 52]. Clearly, an increasing number of hidden layers would lead to an increasing number of parameters. In some cases, a large network can be favorable for the model prediction accuracy. However, too many hidden layers can also lead to an excessive information processing capacity, and thus to the memorization of the training samples (overfitting). On the other hand, an insufficient number of parameters can result in poor forecasting abilities of the network. One approach for choosing the network structure is provided by the universal approximation theorem[117, 118]. This theorem states that a network with at least one hidden layer and nonlinear hidden neurons would be capable of approximating any continuous function in a closed and bounded domain. Therefore, this type of network can be applied universally for function approximation when theoretical models are not available [52, 119].

Furthermore, “supervised learning” refers to the learning method in which the available dataset contains information about the inputs (i.e., the composition of the participating chemical species and the operating conditions) and the desired output data or targets (i.e., the measured composition of the gaseous products). The network “learns”

by systematically changing the network parameters in order to minimize the error between predictions and targets. The “training” of a multilayer network, i.e., the estimation of the parameters (weights and biases) that adapt the predictions to the available data, is conducted using numerical optimization algorithms. These may use the gradient of the error function with respect to the network parameters or the Jacobian matrix of the errors [120]. Both the gradients and the Jacobian matrix can be calculated using the backpropagation algorithm as follows: First, the output signals of the network are calculated using the input data and the initial values of the network’s parameters. Afterwards, an error function is calculated (e.g., sum of squared errors) using the training data. The computed error is subsequently (back) propagated through the network using the chain rule of calculus to determine the error caused by each parameter. The weights and biases are adjusted accordingly and the previous steps are repeated iteratively in order to minimize the value of the calculated error function.

3.2.2 Generalization

One of the most relevant features of ANNs is their ability to generalize. A good generalization implies that the model did not merely memorized the training examples, but that it can make reliable predictions on unseen data as well. Three of the numerous approaches to improve generalization are: growing, regularization and early stopping. When growing is applied, the size of the network is systematically increased until adequate performance is achieved. This technique aims to find the simplest (smallest) network architecture that will provide just enough complexity to fit the data while avoiding overfitting. In contrast, regularization suppresses the model complexity by restricting, not the number, but the magnitude of the network parameters. Typically, the error function is given by the mean squared error (MSE),

$$MSE = \frac{1}{N} \sum_{i=1}^N (\hat{y}_i - y_i)^2, \quad (3.1)$$

where y_i represents the targets, \hat{y}_i the network predictions and N the total number of training samples. In regularization, this function is modified by adding the sum of square weights and biases given by

$$MSW = \frac{1}{n} \sum_{j=1}^n w_j^2. \quad (3.2)$$

The modified error function then takes the following form:

$$E = (1 - \gamma)MSE + \gamma MSW, \quad (3.3)$$

where γ is the performance ratio. Using this expression as the regularization objective function, both the prediction errors and the network parameters are minimized simultane-

ously during training, thus, attaining a smooth network response and good generalization.

Early stopping involves the monitoring of the training progress to determine when the training must be terminated. For this, the available data must be divided into at least two subsets: training and validation data. The training data are used to compute the gradients or the Jacobian matrix necessary to update the values of the network parameters. On the other hand, the validation data are used to monitor the generalization ability of the network at each training step as illustrated in Figure 3.3. Throughout the course of training, the training error will decrease since the parameters are being updated to fit these data. Similarly, the validation error decreases with each step until the network begins to memorize the training data resulting in poor performance on the validation subset. The training is terminated when the validation error starts to rise, and the parameter vector at the point with the lowest validation error is selected as the optimal parameter set. [52, 121] A common praxis is to use an additional testing data set to assess the model’s generalization ability and for model selection. This data set should only be used after the training procedure has been completed to ensure an unbiased assessment.

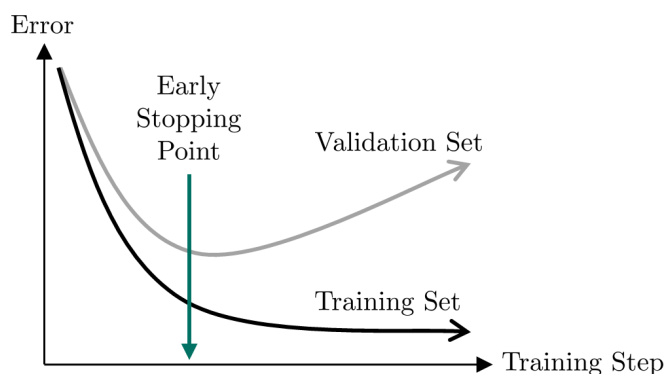


Figure 3.3: Schematic representation of early stopping.

3.3 Data and Methodology for the ANN’s Design

Shallow feedforward ANNs (ANNs with one hidden layer) were designed and implemented in MATLAB software R2018a v9.4.0. The experimental kinetic data used for training and testing were acquired and published in a previous work [1]. The used data set consists of 180 experiments carried out in a fixed bed reactor at 5 MPa using a 1:1 mechanical mixture of a commercial CZA catalyst and $\gamma\text{-Al}_2\text{O}_3$. The syngas composition, the temperature (T) and the total gas flow (\dot{V}_{in}) were varied during the experiments as summarized in Table 3.1, while the hydrogen amount in the feed gas was determined

for each experiment according to Equation 3.4. The remaining fraction of the feed gas consisted of a mixture of the inert gases argon and nitrogen.

$$y_{\text{H}_2,\text{in}} = 2.3 (y_{\text{CO},\text{in}} + y_{\text{CO}_2,\text{in}}) + y_{\text{CO}_2,\text{in}}. \quad (3.4)$$

Table 3.1: Conditions of kinetic data, taken from Delgado Otalvaro et al. [1]

Param.	Value	Unit
T	493, 503, 513, 523, 533	K
\dot{V}_{in}	0.2, 0.3, 0.4, 0.5, 0.6, 0.7	SLPM*
$y_{\text{CO}_2,\text{in}}$	0, 1, 3	%
$y_{\text{CO},\text{in}}$	4, 8, 15	%

* Standard liters per minute, $T = 0$ °C and $p = 1.01325$ bar.

The ANNs were trained to predict the mole fraction of the main species (CO, CO₂, H₂ and DME) in the product gas based on the composition of the syngas ($y_{\text{CO},\text{in}}$, $y_{\text{CO}_2,\text{in}}$, $y_{\text{H}_2,\text{in}}$) and the varied operating conditions. Hence, the input (x) and target vector (y) are summarized as follows:

$$x^T = [y_{\text{CO},\text{in}}, y_{\text{CO}_2,\text{in}}, y_{\text{H}_2,\text{in}}, T, \dot{V}_{\text{in}}] \quad (3.5)$$

and

$$y^T = [y_{\text{CO},\text{out}}, y_{\text{CO}_2,\text{out}}, y_{\text{H}_2,\text{out}}, y_{\text{DME},\text{out}}]. \quad (3.6)$$

For the design of ANNs the network architecture i.e., the number of neurons in the hidden layer as well as a suitable activation function of these neurons and a training algorithm must be determined. Since there is no generally accepted theoretical basis to address these questions, answers are obtained empirically. For this purpose, various network architectures and multiple functions were screened and analyzed. The assessment was carried out in regard to the mean squared error (MSE) and the convergence time. For this initial screening, the experimental input data were divided randomly into three data subsets: training, validation and test data containing 70 %, 15 % and 15 % of the experimental data, respectively. The validation subset was used for training to improve generalization through early stopping, except in the case of Bayesian regularization where generalization is achieved by regularization and no validation subset is required [121, 122]. The randomized data classification was constant for all trials conducted in this initial screening to ensure that the same samples were used in all cases, thus, excluding any influence of the data division from the preliminary results.

3.3.1 Activation Function

The nonlinear activation functions listed in Table 3.2 were used in the hidden neurons to include the known nonlinearities of the kinetic data in the model and to increase computational flexibility, while linear neurons were used in the output layer. While testing the listed activation functions, the remaining design parameters were kept constant at the default values in MATLAB, namely the Levenberg-Marquardt training algorithm and 10 neurons in the hidden layer.

Table 3.2: Tested activation functions [120, 123]

Abbr.	Name of Function	Equation
elliotsig	Elliot Symmetric Sigmoid	$f(n) = \frac{n}{1 + n }$
logsig	Logarithmic Sigmoid	$f(n) = \frac{n}{1 + e^{-n}}$
poslin	Positive Linear (ReLU)	$f(n) = \begin{cases} 0, & n \leq 0 \\ n, & n \geq 0 \end{cases}$
radbasn	Normalized Radial Basis	$f(n) = \frac{e^{-n^2}}{\sum e^{-n^2}}$
satlin	Saturating Linear	$f(n) = \begin{cases} 0, & n \leq 0 \\ n, & 0 < n < 1 \\ 1, & n \geq 1 \end{cases}$
softmax	Softmax	$f(n) = \frac{e^n}{\sum e^n}$
satlins	Symmetric Saturating Linear	$f(n) = \begin{cases} -1, & n \leq -1 \\ n, & -1 < n < 1 \\ 1, & n \geq 1 \end{cases}$
tansig	Hyperbolic Tangent Sigmoid	$f(n) = \frac{2}{1 + e^{-2n}} - 1$
tribas	Triangular Basis	$f(n) = \begin{cases} 0, & n \leq 0 \\ 1 - n , & 0 < n < 1 \\ 0, & n \geq 1 \end{cases}$

3.3.2 Training Algorithm

There are several algorithms for training ANNs with backpropagation. They all have different computational properties, mathematical backgrounds, memory requirements, etc., so no algorithm is optimally suited for all instances. Here, the functions listed in Table 3 were applied using the abovementioned network architecture and the logarithmic sigmoid activation function (logsig). As a detailed description of the individual training

algorithms would go beyond the scope of this paper, relevant bibliographic information is provided in Table 3.3.

Table 3.3: Tested training algorithms [124]

Abbr.	Algorithm	References
bfq	BFGS Quasi-Newton	[125, 126]
br	Bayesian Regularization	[121, 122, 127]
cgb	Conjugate Gradient with Powell/Beale Restarts	[128, 129]
cgf	Fletcher-Powell Conjugate Gradient	[120, 130]
cgp	Polak-Ribiere Conjugate Gradient	[120, 130]
gd	Gradient Descent	[120]
gdm	Gradient Descent with Momentum	[120]
gdx	Variable Learning Rate Gradient Descent	[120]
lm	Levenberg-Marquardt	[120, 131, 132]
oss	One Step Secant	[133]
rp	Resilient Backpropagation	[134]
scg	Scaled Conjugate Gradient	[135]

3.3.3 Data Division Scheme and Training Strategy

The proposed data division and training procedure is illustrated in Figure 3.4. In the first stage of data division, the samples were randomly assigned to two subsets: the "Design Data" and the "Test Data A". In the second stage, the "Design Data" subset containing 90 % of the samples was divided into "Train Data", which is used to calculate weights and biases and "Test Data B" used to compare different models within the framework of Bayesian regularization (without a validation subset). Afterwards, the multi-start strategy was applied by restarting the training procedure from different initial parameter values 100 times. This procedure, labeled as (1) in Figure 3.4, screens the parameter space in order to generate different solutions of the optimization problem, and thus, to overcome possible local optimality. After completion, the second stage of data partitioning is repeated to train the networks based on a different data division (label (2) in Figure 3.4). All trained networks and training records were stored in a 100 by 100 array for the subsequent network selection. Finally, the "Test Data A" subset, which contains 10 % of the original samples, was used to provide an unbiased assessment of the network performance on separate data, and thus, of its generalization ability. Thereby, the ANN with the lowest error on these data exhibits the best generalization to the independent data set and was chosen as the most suitable network. A pseudo-random division is advantageous for the problem at hand considering the multidimensionality of the input space. The presented scheme allows data partitioning in an automated fashion and increases the adaptability of the proposed modeling routine to new data sets of different

structures.

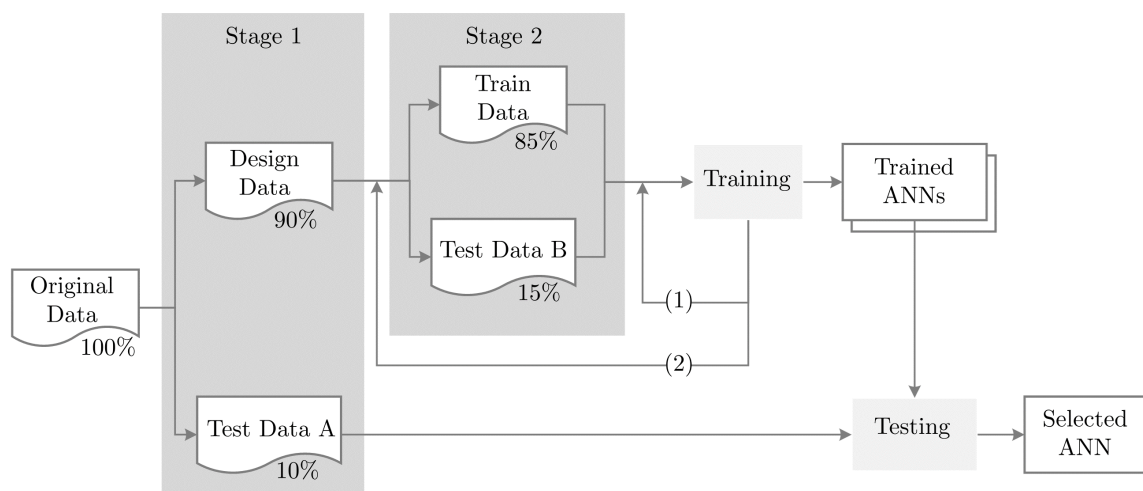


Figure 3.4: Data division scheme and training strategy.

3.3.4 Network's Architecture

Based on the universal approximation theorem, shallow ANNs (1 hidden layer) were implemented. The number of hidden neurons was varied from one to 15 in order to evaluate the influence of the layer size on the obtained accuracy, and hence, to select a network architecture that provides sufficient model complexity. For this purpose, the best activation function, training algorithm and described data partitioning scheme were utilized.

3.3.5 Evaluation of the Selected ANN

Posterior to the training and network selection, simulations were performed with the selected network. The responses of the ANN were evaluated in comparison to that of the lumped kinetic model of a previous work [1], which was parametrized to the same experimental data used for the ANN training. The parameters of the lumped model were fitted to kinetic data measured in the absence of transport limitations. The assumptions of steady state, isothermal and isobaric operation, negligible gradients in radial direction and negligible back-mixing effects apply. Therefore, only the effects of chemical reaction and thermodynamic equilibria are included in this model. However, since the lumped kinetic model is based on balance equations and partially on knowledge of the reaction mechanism, it is expected to deliver better predictions than the ANN when extrapolated.

The adjusted coefficient of determination $R_{adj.}^2$ was computed as a measure of the goodness of fit (Equation 3.7). Different from the coefficient of determination R^2 (Equation 3.8), $R_{adj.}^2$ takes the number of degrees of freedom of each model into consideration, hence, providing an unbiased basis for the comparison of two different model structures.

$$R_{adj.}^2 = 1 - \frac{(1 - R^2)(N - 1)}{(N - p)} \quad (3.7)$$

$$R^2 = 1 - \frac{\sum_{n=1}^N (y_{n,out} - \hat{y}_{n,out})^2}{\sum_{n=1}^N (y_{n,out} - \bar{y}_{n,out})^2} \quad (3.8)$$

In Equations 3.7 and 3.8 N is the total number of experiments, and p is the number of model parameters. $\hat{y}_{n,out}$ and $y_{n,out}$ are the predicted and measured mole fraction of an arbitrary component in the product gas for experiment n , and $\bar{y}_{n,out}$ is the mean value of the measured mole fraction over all experiments.

3.4 Results and Discussion

3.4.1 Network Design and Training

Figure 3.5a displays the mean squared error values of all activation functions tested. The piecewise linear functions (poslin, satlin, tribas and satlins) perform poorly in comparison to the nonlinear functions (radbasn, elliotstg, tansig, softmax and logsig). The best performance was obtained with the widely used logarithmic sigmoid function. This function has well applicable mathematical properties: it is defined for all real input values, it is bounded, monotonically increasing and continuously differentiable. Therefore, it is suitable for backpropagation and meets the requirements of the universal approximation theorem [119, 136, 137].

The minimized MSE obtained with the tested training algorithms is outlined in Figure 3.5b. Since the training with the algorithms Gradient Descent (gd) and Gradient Descent with Momentum (gdm) did not converge in any of the run trials, these were excluded from this diagram. It is obvious that the Jacobian backpropagation methods Levenberg-Marquardt (lm) and Bayesian regularization (br) provide more accurate predictions than the gradient descent algorithms (cgp, scg, rp, bfg and cgf). Between lm and br, the lowest MSE and fastest convergence was achieved with Bayesian Regularization. This MATLAB® training function is based on the Bayesian interpolation frame proposed by MacKay [138]. With this algorithm, the regularization parameters i.e., the performance ratio, are computed automatically during training, being advantageous for problems where the data set is limited, since no validation subset is required [121]. Furthermore, Bayesian regularization calculates and trains only the number of parameters

necessary to minimize the target function (effective number of parameters) [127, 139]. As a result, fewer parameters are used than are available reducing the model sensitivity to the network architecture, as long as the minimum number of neurons is provided. Based on these advantages and the empirically obtained results, Bayesian regularization was selected for the network design.

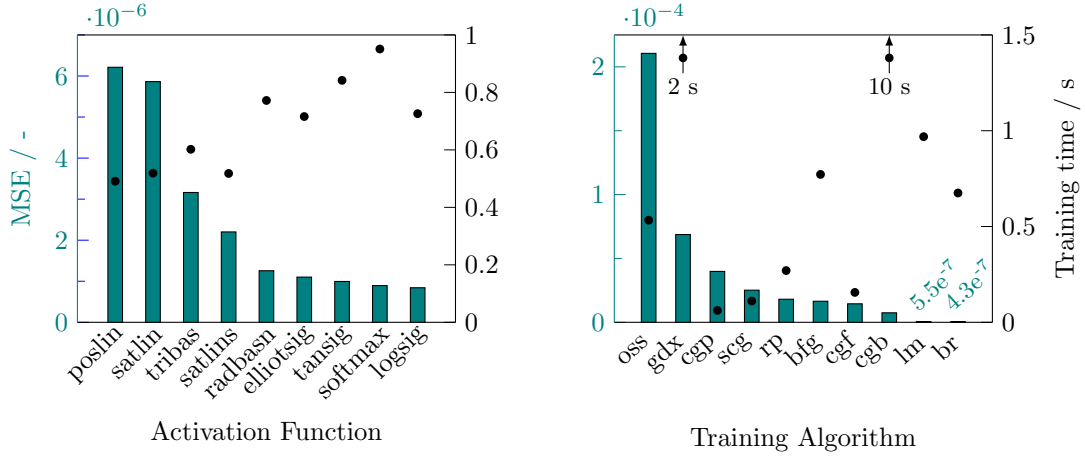


Figure 3.5: Performance of activation functions and training algorithms regarding the mean squared error (MSE) and training time for a single network.

The training strategy was conducted for networks with up to 15 neurons in the hidden layer. This screening showed that five hidden neurons provide enough complexity for the network to adapt sufficiently to the available data set. Therefore, the network with a 5-5-4 architecture (5 input, 5 hidden and 4 output neurons) was selected. This structure ensures a sufficient number of parameters to avoid underfitting, while the problem of overfitting is prevented by training the network with Bayesian regularization. The resulting ANN is shown schematically in Appendix B, Figure B.1, along with the ANN parameters. The proposed approach is applicable when modeling with ANNs due to their remarkably fast convergence. For the chosen architecture, the time elapsed after the training of 10000 networks was 7.9 minutes (Figure 3.6b). In contrast, the parametrization of the lumped kinetic model to the same data takes approximately 3.5 hours using the same CPU (on windows 10 Pro (64-bit) operating system with i5 processor and 8 GB RAM). The resulting ANN is shown schematically in Figure B.1, the connection weights between input and hidden layer, and between hidden and output layer are contained in the matrices $w^{0,1}$ and $w^{1,2}$, while the biases of the hidden and output neurons are contained in the vectors b^1 and b^2 .

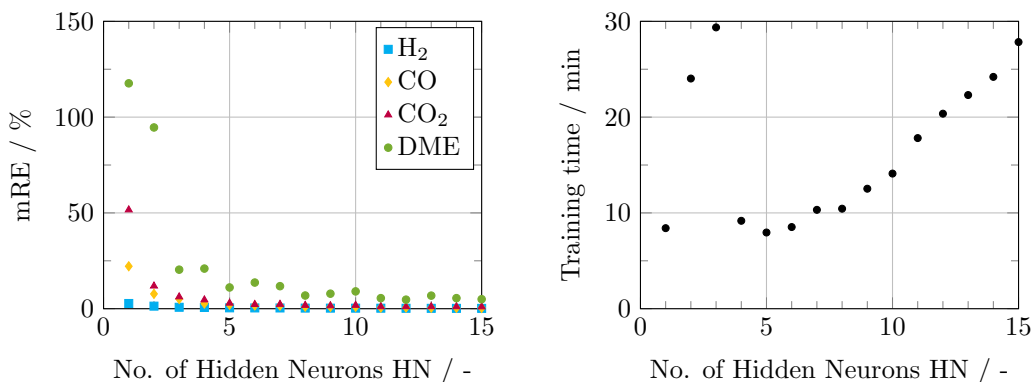


Figure 3.6: Effect of the hidden layer size on the species mean relative error of prediction, and on the training time of multiple networks.

3.4.2 Best Network's Evaluation

Simulations were performed to evaluate the predictive ability of the selected network. Figure 3.7 shows parity plots itemized for the main components in the system displaying the agreement between the measured and predicted concentrations in the product gas for all experiments. Clearly, the model is capable of simulating the observed trends accurately. For all components, the simulated points are evenly distributed around the bisectrix, indicating that there are no pronounced systematic deviations between model predictions and experimental data.

The observed goodness of fit can be attributed to the fact that appropriate activation and training functions were chosen as well as a network architecture that provides sufficient model complexity and flexibility for modeling. Additionally, the proposed data partitioning scheme proved to be effective in enabling the model to gain insight into the underlying phenomena with the available data.

The mean relative error (RE) over all inlet compositions is shown in Figure 3.8 against the temperature and the inlet volume flow. Clearly, the ANN shows a higher predictive accuracy than the lumped kinetic model for all species in the entire experimentally covered operating window. This is caused by the flexibility and higher dimensionality of the ANN and its superior capacity to adapt to the data. The RE of CO, CO₂ and H₂ over all data lie below 3 % (2 %, 2.9 % and 0.4 % respectively), while the RE of DME amounts to 11 %. Both response surfaces for DME follow the same trend, with the prediction error decreasing with increasing temperature. At low temperatures, the low reaction rates lead to overall low conversion and yield. Hence, resulting in small DME amounts in the product gas and thus in a reduced measuring accuracy [1]. Therefore, the deviations of both

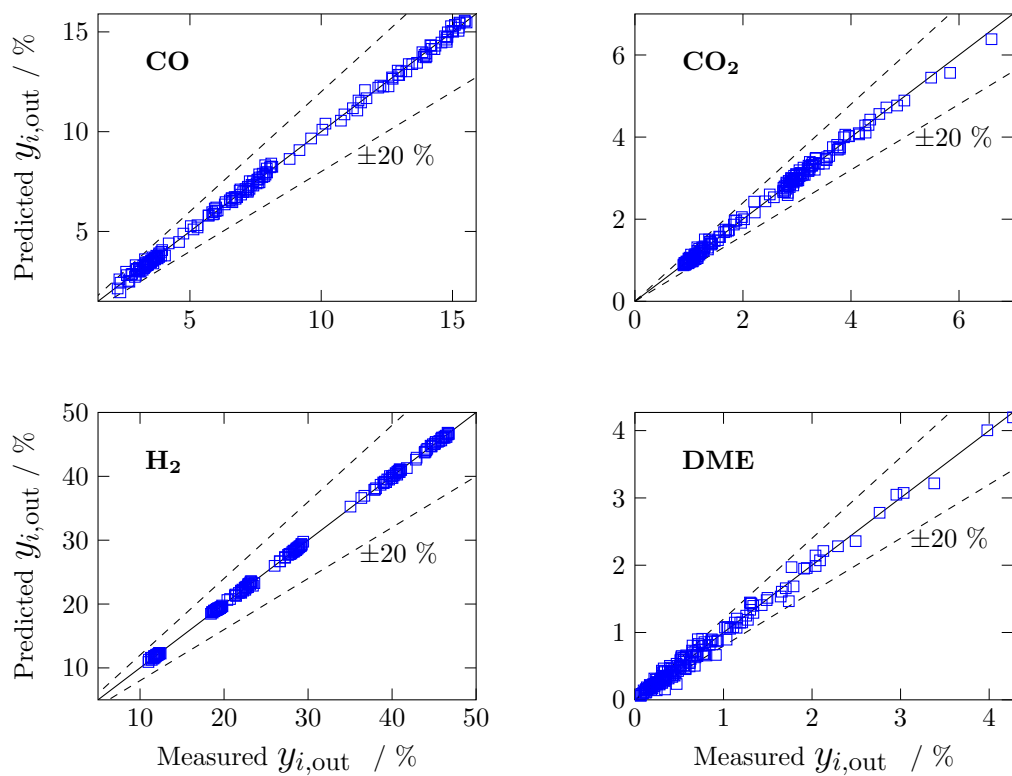


Figure 3.7: Parity plots for mole percent of CO, CO₂, H₂ and DME in the product gas for all data and simulations conducted with the selected ANN.

models can be mainly attributed to experimental measurement uncertainties. Additionally, the fact that the ANN did not adapt to the measured values, although the network has sufficient flexibility, is an indication that overfitting was successfully avoided and the data were not simply stored by the network, but the input-output relationships were effectively identified. The adjusted coefficients of determination reported in Table 3.4 highlight the suitability of both models and confirm the better adjustment of the ANN to the experimental data especially for the fractions of DME and CO_2 .

Table 3.4: Adjusted coefficients of determination R_{adj}^2 for for lumped model and ANN.

R_{adj}^2	$y_{\text{H}_2,\text{out}}$	$y_{\text{CO},\text{out}}$	$y_{\text{CO}_2,\text{out}}$	$y_{\text{DME},\text{out}}$
ANN Model	0.999	0.998	0.994	0.984
Lumped Model	0.998	0.992	0.984	0.943

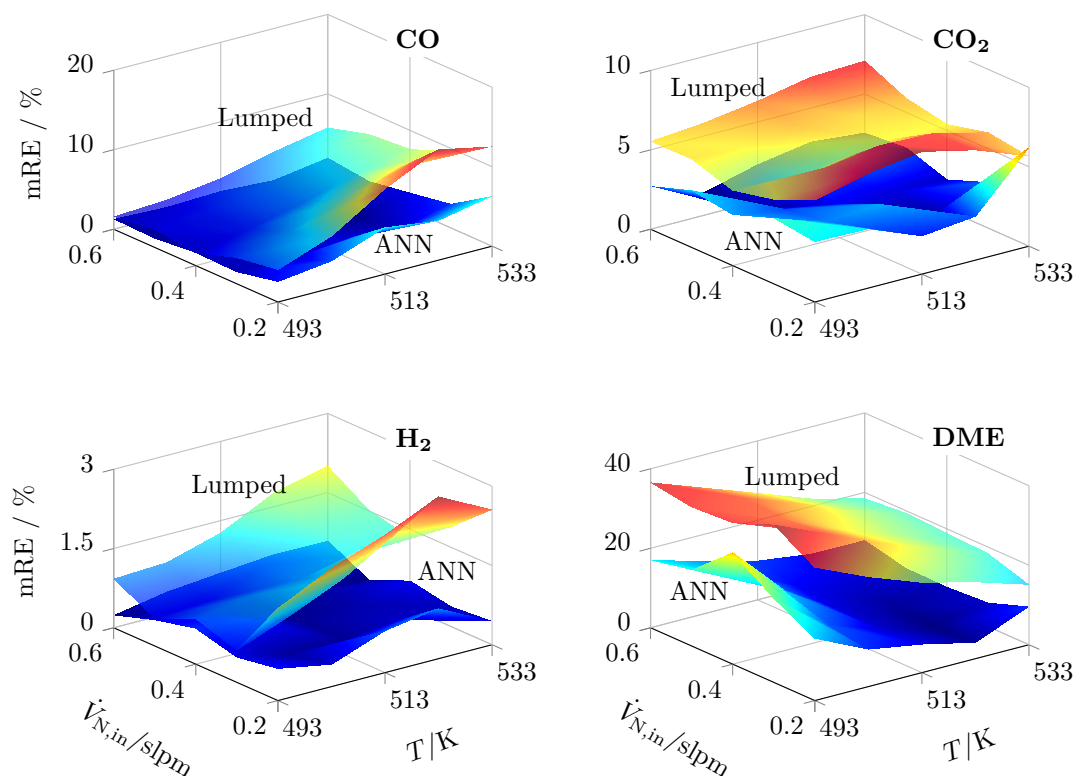


Figure 3.8: Mean relative error (RE) of prediction for the lumped model and ANN over all data within the experimentally studied ranges of temperature and total gas flow show the higher predictive accuracy of the ANN for all species.

In order to determine if the trained ANN is suitable as a non-linear regression tool, the ANN's generalization ability and its suitability to make predictions on unseen data

have to be tested. For this purpose, additional simulations were performed for unobserved data within and beyond the model's validity range. A lumped model [1] is employed for a comparative analysis of the ANN's predictions. Since both models were fitted to the same experimental data, these are valid in the same range of conditions, thus, providing a sufficient basis for comparison. In the following, representative results are presented that illustrate and compare the responses of both models. Additional simulation results are given in the Appendix B.

In Figure 3.9, the experimental values are sorted arbitrarily in ascending order and depicted along with the superimposed confidence intervals of both fits at a significance level of 95 %. It can be observed that the confidence intervals of the ANN predictions are narrower than the confidence interval of the lumped model. It is obvious, in particular for the fractions of DME and CO₂, that the respective confidence intervals of both models are wider in the low concentration range. This is in accordance with the presumption made before in this section that low concentrations of DME are subject to an increased measurement uncertainty, which also explains why this effect is not observable for the fractions of CO or H₂ where the confidence intervals appear to be of the same order of magnitude in the entire operating window.

Figure 3.10 displays simulation and experimental results in the temperature range between 453 K and 573 K. The range where both models are formally valid (between 493 K and 533 K) is marked in gray for better visualization. The predictions of the ANN within the model's validity range are slightly closer to the experimental values than the predictions obtained with the lumped kinetic model, consistent with the previous discussion. Since the phenomena in this range are dominated by reaction kinetics, the effects observed under these conditions can be explained by the temperature dependence of the reaction rate, described by the Arrhenius equation. With increasing temperature, the fraction of DME and CO₂ in the effluent increases, while the fraction of CO and H₂ decreases. The fact that CO₂ behaves as a product can be attributed to the water gas shift reaction which is promoted by the CZA catalyst and, in the evaluated range, is faster than the CO₂ hydrogenation. With regards to the total gas flow, it is observed that at decreasing values, the fraction of CO and H₂ at the reactor outlet decreases as well, while the fraction of DME and CO₂ increases. These results can be explained by the inverse relationship between the total gas flow with residence time and gas load, that lead to higher conversion and product yield. Furthermore, the consistency of this effect throughout the entire investigated gas flow range can be attributed to a constant selectivity towards DME. A detailed description of the observed phenomena will be omitted here, since the focus of this chapter is to evaluate the effects of the structural differences

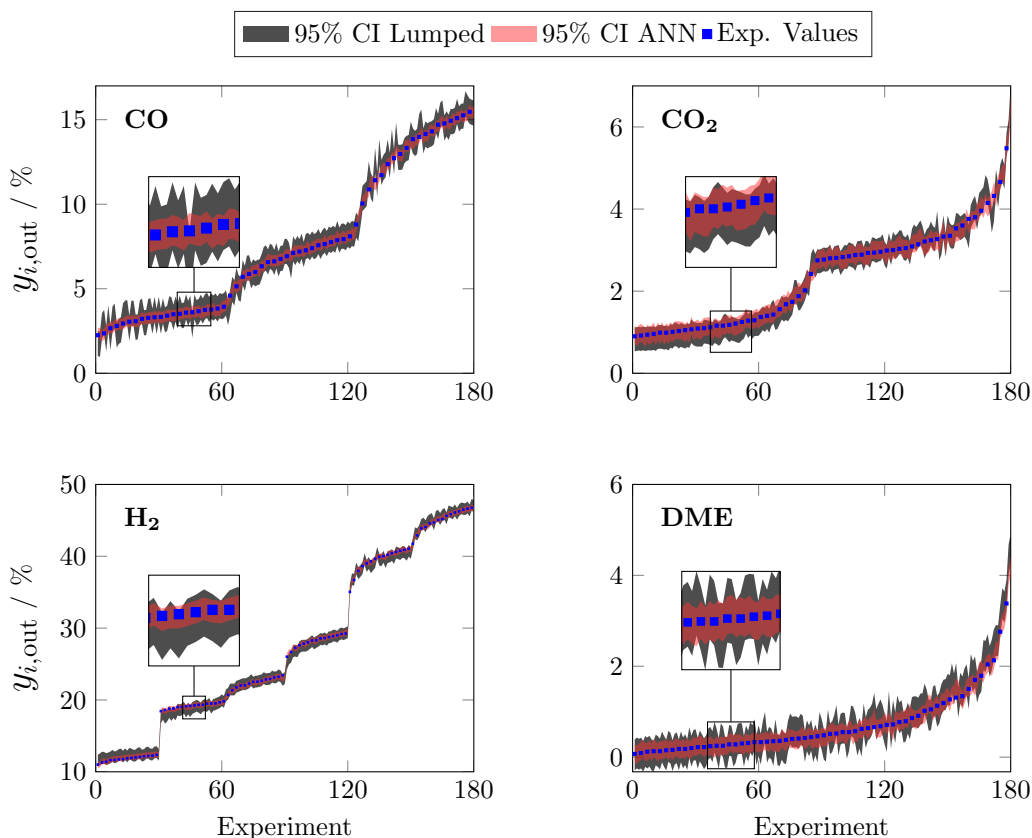


Figure 3.9: Measured concentrations in the product gas and 95% confidence intervals (CI) of the Data-based (ANN) and lumped model. For clarity, only every third experimental data point is shown.

between a lumped model and ANNs, more details can be found in the publication of the lumped model [1]. Model predictions in this operational range demonstrate the high level of agreement between the simulated and measured values, also showing a smooth mapping and the ANN’s ability to generalize and make predictions for unseen data within the model’s validity range.

Unexpectedly, the predictions of the lumped model and the ANN at temperatures below 493 K are similar although the ANN was not trained in this temperature range. Both models indicate that at low temperatures the reaction rates are too low to achieve high conversion. Hence, the concentrations of all components are close to the respective values in the feed gas. There are no additional constraints in the ANN’s structure that prevent negative concentrations to be computed (in the lumped kinetic model, this effect is prevented inherently by the balance equations). Thus, at low temperatures some negative values are predicted. However, for DME and CO_2 , progressions do not decrease steeply into the negative quadrant with decreasing temperatures. Instead, all values in this tem-

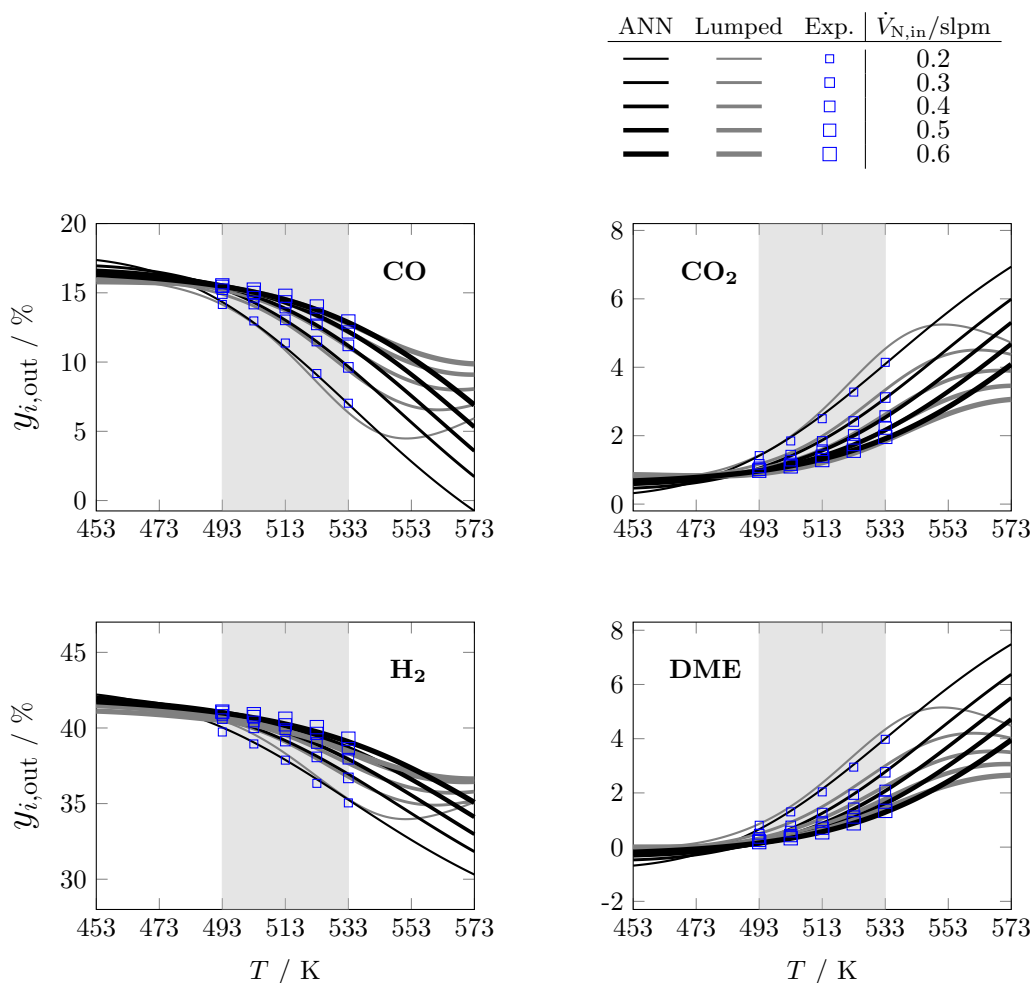


Figure 3.10: Components mole fraction in the product gas within and beyond the model’s validity range regarding the temperature. Gray area marks the range covered experimentally. Syngas composition: 16 % CO, 0.8 % CO₂, 42.3 % H₂, 40.8 % inert gas (Ar and N₂). $p = 5$ MPa.

perature range are close to zero. Similarly good prediction accuracy despite extrapolation was observed for most but not all feed compositions and components (Figures B.2 to B.6, Appendix B). Therefore, although the underlying model is able to extrapolate accurately for most conditions in this range, the quality of the predictions cannot be guaranteed in all cases. The predictions for temperatures above 533 K provide valuable insights into the phenomena comprised by the models. As the main chemical reactions involved in the DME synthesis are exothermic, high temperatures are kinetically favorable, but thermodynamically unfavorable. This trade-off of exothermic reactions is reflected by a change in the slope of the concentration profile and is taken into account in the lumped kinetic model by the equilibrium constants in the rate expressions. However, since the kinetic data were measured at conditions at which the influence of the equilibrium is minor (ki-

netic regime), the ANN has no information about the characteristics of this phenomenon, causing the predictions of both models to diverge at high temperatures. With increasing temperature, the concentration profiles predicted with ANN follow the observed trend in the experimentally covered range, i.e., increasing for DME and CO₂, and decreasing for H₂ and CO, while the concentration profiles computed with the lumped kinetic model exhibit the expected points of inflection. Similarly, predictions for low flow rates, at which mass transport limitation occurs, can be expected to be inaccurate because the model was parameterized to fit intrinsic kinetic data, i.e., in an operating range with negligible influence of mass and heat transport.

3.5 Summary and Conclusions

In this chapter ANNs were designed and used to model the direct synthesis of DME. The exact mechanism of this process is not yet fully understood, and modeling has so far only been possible in limited operating windows. The networks used are shallow, feed-forward and fully connected. It was demonstrated that the logarithmic sigmoid function is most applicable for the problem at hand, and that a higher accuracy is obtained when applying training algorithms that use Jacobian backpropagation, particularly Bayesian regularization. A pseudo-random data division scheme allowing data partitioning in an automated fashion was presented. The training was conducted for ANNs of different structures and five hidden neurons proved to provide sufficient model complexity to map the available data. The network with the best performance on unseen data was selected and its predictive ability was assessed by comparison with experimental data and with predictions of a lumped kinetic model parametrized to fit the same database. In summary, it was observed that the ANNs are remarkably fast, very flexible and exhibit a superior adaptability to the experimental data than the lumped kinetic model while still providing a comparable interpolation ability.

Moreover, accuracy of the model predictions outside the experimentally covered parameter range was also evaluated. When the model was extrapolated towards lower reaction rates, i.e., lower temperatures and higher flow rates, the ANN was able to deliver accurate predictions and to describe the single-stage DME synthesis systemically for most components and inlet feeds. This indicates that extrapolations of the model may be admissible for operating conditions at which the phenomena covered by the underlying model takes place. However, it is not possible to predict deviations prior to training. Extrapolations of the ANN towards higher reaction rates, on the other hand, lead as expected to divergent predictions, as overlapping effects occur (e.g., thermodynamic limitation of exothermic reactions at high temperatures) which, at the current

stage of development, cannot be reflected by the ANN that was trained to fit data taken in the operational window dominated only by reaction kinetics.

These findings underline the suitability of the ANN to act as a predictive tool for Brownfield applications such as soft sensing, real-time optimization, on-line control, predictive maintenance and others, where models with high flexibility and adaptability, the capacity to map complex nonlinear relationships as well as fast convergence and low computational cost are required. Furthermore, it can be concluded that ANNs have the potential to be used for modeling the direct DME synthesis in an even wider range of operation where the relationship between input and output variables is ambiguous and modeling under mechanistic assumptions was not yet possible. The presented data partitioning and training methodology can be applied for this purpose with simple requirements: the input-output relationships to be modelled must be measurable and enough data must be available for parameter discrimination, i.e., for the training of the network. One possible application is the modeling of catalyst deactivation as a function of the time on stream and/or the conditions to which the catalyst system is exposed to. Regardless of the catalyst system, most kinetic studies of the direct DME synthesis are carried out under steady state conditions, due to the highly dynamic behavior of the catalysts which makes the mechanistic modeling in a wide range of conditions very challenging. However, if the required data are available, the modeling with the proposed methodology can be easily adapted to new state variables that need to be considered.

4. HYBRID MODEL

Hybrid kinetic models represent a promising alternative to describe and evaluate the effect of multiple variables in the performance of complex chemical processes, since they combine system knowledge and extrapolability of the (semi-) mechanistic models in a wide range of reaction conditions with the adaptability and fast convergence of data-based approaches (e.g. artificial neural networks - ANNs). For the first time, a hybrid kinetic model for the direct DME synthesis was developed consisting of a reactor model i.e., balance equations, and an ANN for the reaction kinetics. The accuracy, computational time, interpolation and extrapolation ability of the new hybrid model were compared to those of a lumped and a data-based models with the same validity range using both simulations and experiments. The convergence of parameter estimation and simulations with the hybrid model is much faster than with the lumped model, and the predictions show a higher degree of accuracy within the models' validity range. A satisfactory dimension and range extrapolation was reached when the extrapolated variable was included in the knowledge module of the model. This feature is particularly dependent on the network architecture and phenomena covered by the underlying model, and less on the experimental conditions evaluated during model development.

4.1 Introduction

The detailed reaction mechanism of the direct DME synthesis has not yet been fully understood [31] and its modeling is challenging. Reasons for this are for example variable structural changes of the metallic catalyst depending on the reaction conditions [42], the variation of the dominant pathway of the methanol synthesis [43], as well as the deactivation of the dehydration catalyst e.g., by acidity loss due to H^+/Cu^{2+} ion exchange especially in the case of zeolite-based systems, and the sintering of the metallic catalyst in the presence of high water concentrations [23, 44, 140].

Several semi-mechanistic or lumped models that enable the modeling of the system in a specific operational range have been developed [1, 2, 32–41]. However, due to the mentioned difficulties, semi-mechanistic models for the direct DME synthesis are difficult to fit in a wide range of conditions. This is where the potential of machine learning approaches to extract and predict input-output relationships in large data sets comes into play. These methods, especially artificial neural networks (ANNs), have been used successfully in various areas of the chemical industry, mostly as predictive tools [46–49]. One of the general drawbacks of ANNs is that their predictions are only reliable in the range in

which the training data were measured and extrapolation is only possible in a slightly extended range. [52] However, unlike semi-mechanistic models, ANNs can be easily adapted to large amounts of multidimensional data in broad operational windows [48, 52].

Models that combine the features of both (semi-)mechanistic and data-based approaches represent a promising alternative for modeling the behavior of chemical reactors [54]. However, recent studies have highlighted that the adoption of machine learning approaches is still limited for chemical processes [49, 59, 60]. An extensive literature search on models for direct DME synthesis revealed that most models are semi-mechanistic, while only a few are data-based, and none of the models are hybrid in nature (Section 4.2). Therefore, in addition to providing a timely overview of the available models for direct DME synthesis, a main objective of this chapter is to establish an initial hybrid model for this system and to comprehensively compare the different types of models (Section 4.3). Simulation results obtained with the hybrid model are compared to those obtained with a semi-mechanistic and a data-based model that have the same range of validity, which enables an evaluation of the structural differences between the model types. Based on similar works [28, 53, 55], it is expected that the hybrid model provides a higher accuracy than the lumped model, while exhibiting an increased extrapolation capability than the data-based one. These hypotheses are evaluated in a quantitative manner in Section 4.4. In this section, critical model features such as accuracy, computational burden, interpolation and extrapolation ability are put to test, using both simulations and experiments.

4.2 Available models for the direct synthesis of DME - an overview

In this section, an overview of kinetic models for the direct synthesis of DME over the commercial catalyst system CZA/ γ -Al₂O₃ is presented.

4.2.1 Semi-mechanistic (lumped) models

In the semi-mechanistic modeling approach, assumptions about the reaction mechanism are made and experimental data is used to determine the reaction kinetic parameters. Therefore, the influence of relevant operating conditions on the DME direct synthesis is the focus of numerous current research projects. Overviews are given for example by Z. Azizi et al., [21] and U. Mondal and G. D. Yadav [6].

The ranges evaluated in available modeling studies [1, 2, 32–41] are presented in Figure 4.1 for process variables that are particularly relevant for reaction kinetics. I.e.,

the temperature, pressure, the CZA-to- γ -Al₂O₃ weight ratio (μ , Equation 4.1), the carbon oxide ratio (COR, Equation 4.2), and the stoichiometric number (SN, Equation 4.3).

$$\mu = \frac{m_{\text{CZA}}}{m_{\gamma\text{-Al}_2\text{O}_3}} \quad (4.1)$$

$$\text{COR} = 100 \% \frac{y_{\text{CO}_2,\text{in}}}{y_{\text{CO}_2,\text{in}} + y_{\text{CO},\text{in}}} \quad (4.2)$$

$$\text{SN} = \frac{y_{\text{H}_2,\text{in}} - y_{\text{CO}_2,\text{in}}}{y_{\text{CO},\text{in}} + y_{\text{CO}_2,\text{in}}} \quad (4.3)$$

The overlapping of the ranges is obvious and explained by the constraints inherent to the system under consideration. For example, the maximal temperature is defined based on the thermal stability of the catalysts, such as to avoid sintering of CZA except of course for studies where deactivation phenomena is investigated [33, 35]. The lowest temperature on the other hand is typically chosen under consideration of the other process variables as to have measurements in a range where the catalyst is active, and the signal to noise ratio is high. In the summarized studies, temperatures from 473 to 623 K have been evaluated (Figure 4.1a).

Since the process exhibits volume contraction, an increase in pressure has a positive effect on the process performance according to LeChatelier’s law. However, the maximal pressure is limited due to high investment costs and necessary safety measures. At lab scale, the pressure range is often constrained by the experimental rig. As shown in Figure 4.1b, some studies [1, 2, 36, 41] are conducted at 5 MPa, which is the typical industrial operational pressure for methanol synthesis, while others evaluate a pressure range instead of a constant pressure level [33–35, 37, 39, 40]. Overall, the summarized publications cover a pressure range from 0.9 to 7.2 MPa.

As depicted in Figure 4.1c, the CZA-to- γ -Al₂O₃ weight ratio (μ) was chosen to be equal or higher than one in most studies, because it has been demonstrated that an increased fraction of methanol catalyst is beneficial for the overall process [1, 32, 98]. The optimal catalyst bed composition has been shown to be a function of the operating conditions [1, 32] and the composition of syngas, especially regarding the CO₂ amount in the feed [2].

In terms of the feed gas composition, instead of a simple listing of this heterogeneous information reported by different authors, an unambiguous characterisation was conducted using the COR and SN in order to enable the comparison of the models.

The relevance of the COR lies in the high influence of the CO₂ content in the syngas on the process performance: High CO₂ levels in the feed have shown to promote wa-

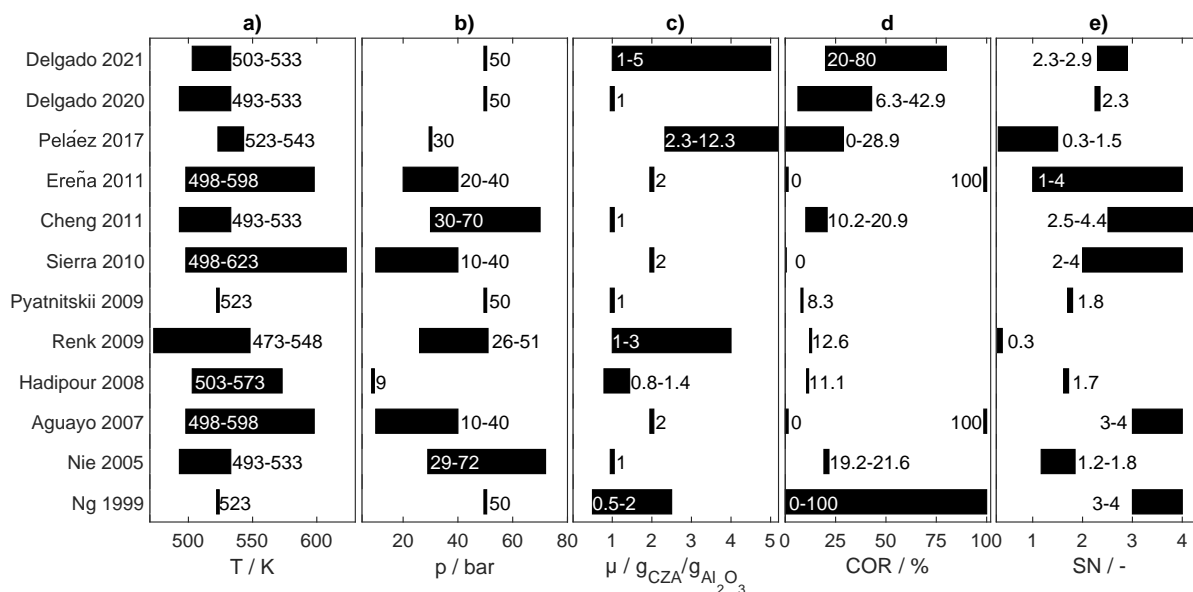


Figure 4.1: Overview of lumped models' validity ranges regarding **a)** temperature **b)** pressure **c)** CZA-to- γ - Al_2O_3 weight ratio μ **d)** carbon oxide ratio COR and **e)** stoichiometric number SN. Models ([1, 2, 32–41]) named after first author and year of publication.

ter formation and to reduce the attainable product yield [23, 69, 72]. However, kinetic models valid in a wide COR range are useful for process design and optimization, as interest in CO_2 utilization grows in the industry [15]. The wide pattern in Figure 4.1d illustrates that the influence of CO_2 has become increasingly important in recent years and is essential in current kinetic studies.

The SN is relevant in terms of the different hydrogen requirements for methanol production *via* CO or CO_2 hydrogenation. Since due to the different syngas production technologies, the H_2 content in the syngas is known to vary over a wide range [141], and adjustment of the H_2 content in the feed gas is not always economically feasible due to the lack of sustainable H_2 sources [18, 142]. As shown in Figure 4.1e, a large range of SN is covered by the presented kinetic studies. However, a closer look in each publication reveals that in most cases, the effect of this variable was not evaluated systematically. Clearly, operating conditions for kinetic studies are chosen with consideration of the concurrent effects on the other process variables. For example, if the system is operated at low pressure, higher temperatures and low dilutions are required to achieve product concentrations that can be measured accurately. As a consequence, optimal conditions found in these studies are often local optima within the validity range of each model or experimental range. For example, Pelaez et al. [32] observed an increasing yield of DME

with an increasing CZA fraction up to 92.5 wt.%, at a pressure of 3 MPa and no CO₂ in the feed. In contrast, in previous investigations 2 [2] conducted at 5 MPa and high CO₂ contents in the feed, an optimal catalyst bed composition was observed at approx. 66 wt.%. Hence, aiming towards the global optimization of the direct DME synthesis, a further systematic evaluation of process variables and their simultaneous effects is still necessary. However, in addition to the aforementioned process variables, many other factors play a significant role, such as the dynamic behavior of the catalysts, the reactor and its configuration, the composition of the CZA catalyst, the heat removal concept, etc. Therefore, in terms of time and resources, a comprehensive exploration of the state space is probably only feasible using models that have enough flexibility to evaluate larger operational ranges and number of process variables.

4.2.2 Data-based models

Artificial neural networks (ANNs) are one of the most powerful machine learning approaches for modeling [47, 50, 143], and as universal approximators, these can approximate nearly any continuous function in a bounded domain [117, 118]. An essential step of this modeling approach is answering the design questions for ANNs, e.g., which activation functions are appropriate for the problem at hand, and how many layers and neurons are required to achieve sufficient model complexity [52]. The performance of the networks is typically evaluated based on the prediction accuracy and the convergence time, which have been shown to be remarkable, and superior in comparison to that of traditional (semi-) mechanistic models [3, 54, 112, 116]. Further advantages of this modeling approach, is that no prior knowledge of the chemistry and physics of the system to be described is required and the high adaptability of ANNs to different structures and sizes of data sets [50, 54, 144]. Unlike semi-mechanistic models, ANNs (and in general machine learning approaches) have not been widely used for the modeling of the direct DME synthesis. Studies conducted for this process, or for the single steps are summarized in the following.

In a previous work [3] ANNs have been applied for the modeling of the direct synthesis of DME over the commercial catalyst system CZA/ γ -Al₂O₃ using data that was previously used for the parametrization of a lumped model. ANNs could be trained successfully even with the limited amount of data. The trained ANN exhibited a fast convergence, and a high adaptability to the experimental data. Moradi et al. [112] analyzed the use of ANNs for modeling the single-step DME synthesis over a bifunctional CZA-H-ZSM-5 catalyst. The authors successfully trained an ANN to predict the CO conversion as well as the DME selectivity and yield. Between 2003 and 2009, Omata et al. also conducted simulations of single-step DME synthesis using ANNs. Unlike Delgado Otalvaro et al.

and Moradi et al., they used ANNs aiming at the maximization of the CO conversion by optimizing the temperature profile in the reactor,[114, 145] and by identifying effective additives for the CZA/ γ -Al₂O₃ catalyst based on the physicochemical properties of the elements [110].

Additionally, studies using ANNs have been conducted for the single steps of the direct synthesis [115, 116, 146–148]. For example, Svitnic et al. [146] used ANNs for the prediction of by-product formation in the methanol synthesis from syngas, based on data from a pilot plant. Also, since the methanol dehydration to DME proceeds without any relevant side reactions, its rate is directly proportional to the rate of depletion and/or formation and it can be measured directly. This advantage of the methanol dehydration to DME was used by Valeh-E-Sheyda et al. [115] and Alamolhada et al. [116] who used kinetic data and ANNs for the data-based modeling of the kinetics of this reaction.

4.2.3 Hybrid models

No hybrid model could be found in the open literature for the direct synthesis of DME. However, some hybrid models have been derived for the individual steps of this process. Zahedi et al. [56], used a hybrid model for the modeling of the CO₂ hydrogenation to methanol. In their work, the authors applied a mechanistic, a data-based and a hybrid modeling approach and demonstrated the superior performance of the hybrid model regarding accuracy and computational effort. Potočník et al.,[57] used a kinetic model from the literature to predict the methanol production rate as a function of the pressure, temperature and the partial pressure of the main species in the system. ANNs were used in combination to this model as an error-corrector, enhancing the prediction accuracy in the range where experimental data was available. Alavi et al. [58] derived a mechanistic and a hybrid model for the methanol dehydration to DME. Here, an ANN was trained using data from a white-box model to predict the global reaction rate and it was integrated in the balance equations. The hybrid model was simpler and 20 times faster than the mechanistic model.

These studies show the potential of hybrid modeling for related systems. The second part of this chapter is devoted to the derivation of the first hybrid model for the direct DME synthesis.

4.3 Models' structures, modeling and experimental methodology

For the comparative study aimed in this chapter, the observed discrepancies between model predictions must be only attributable to the models' structural differences. Hence,

these must be valid in the same range of conditions. In this section, the models' structures are presented in order to identify crucial differences. The lumped and the data-based models are described first in sections 4.3.1 and 4.3.2, since elements from these types are necessary for the development of the hybrid model. The mathematical structure of the latter is subsequently introduced in Section 4.3.3. The results obtained with the hybrid model and the comparative analysis between the different model types is given in Section 4.4.

The structure of the models relevant in this chapter, i.e., the lumped, hybrid, and data-based models, is shown schematically in Figure 4.2. The lumped and the hybrid model both consist of a reaction kinetic model for the calculation of the reaction rates and a reactor model based on the balance equations for the laboratory reactor. The mole fraction profiles $y_i(z)$ of the different species in the system are calculated by integration of the differential equations. With the data-based model on the other hand, the mole fractions are predicted directly using ANNs.

The color spectrum in Figure 4.2 represents the level of information required for the different types of modeling; the darker the color, the less system knowledge is necessary. The ANNs, for example, are predictors based on training data i.e., black box models. The reactor model for the tube reactor is characterized as white box since it is derived based on the species and the total mass balance. In contrast, the lumped and the hybrid model are both characterized as gray box. The lumped model is the model with the highest knowledge content among the three, because the balance equations are generally valid and the rate expressions are based on mechanistic assumptions and thermodynamic considerations. It is considered a gray box model since the parameters of the Arrhenius and Van't Hoff equations are estimated to fit experimental data. Comparably, the hybrid model is also considered a gray box model, since it involves knowledge and data-based elements in its structure.

In this chapter, a hybrid model for the direct DME synthesis is derived and presented. Since this is the first model of this type for the DME synthesis, its assessment has been made based on validation experiments and comparison with a semi-mechanistic model [1] and a data-based model [3].

4.3.1 Lumped model

The lumped model was developed and validated in detail in a previous work [1]. It consists of balance equations, and of a lumped reaction kinetic model parametrized to fit intrinsic kinetic data. Equation 4.4 describes the change of the molar fraction of species i (y_i) along the axial coordinate (z). Equation 4.5 accounts for the drop of the gas velocity

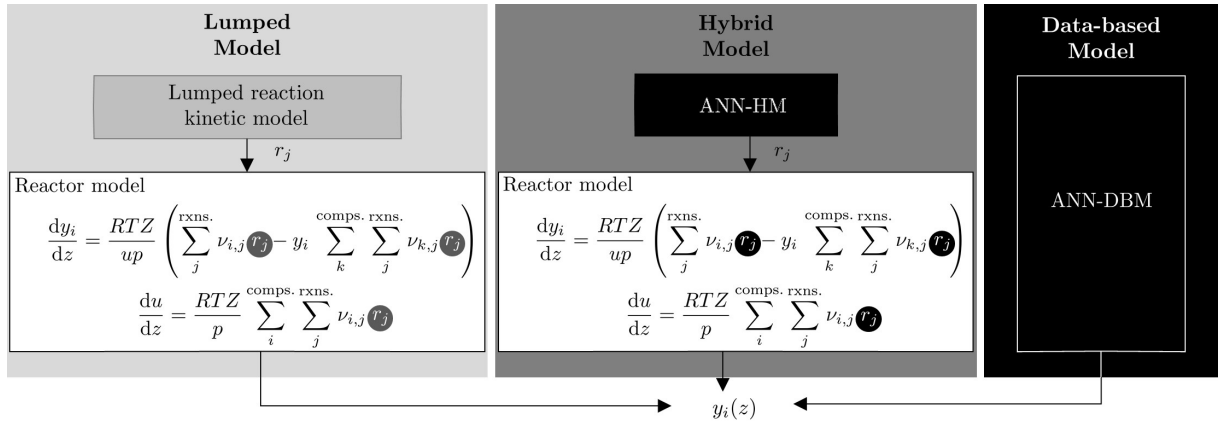


Figure 4.2: Schematic representation of the lumped, hybrid and data-based models evaluated in this chapter.

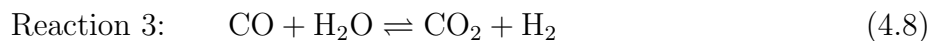
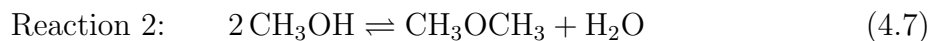
u due to the reaction-induced volume contraction.

$$\frac{dy_i}{dz} = \frac{RTZ}{up} \left(\sum_j^{\text{Nr}} \nu_{i,j} r_j - y_i \sum_k^{\text{Nc}} \sum_j^{\text{Nr}} \nu_{k,j} r_j^v \right) \quad (4.4)$$

$$\frac{du}{dz} = \frac{RTZ}{p} \sum_i^{\text{Nc}} \sum_j^{\text{Nr}} \nu_{i,j} r_j^v \quad (4.5)$$

In Equations 4.4 and 4.5, y_i is the molar fraction of component i , R is the universal gas constant in $\text{J mol}^{-1} \text{K}^{-1}$, T is the temperature in K, Z is the mixture's compressibility factor calculated with the Peng-Robinson equation of state (PR-EoS),^[84] u is the gas velocity in m s^{-1} , p is the pressure in Pa, $\nu_{i,j}$ is the stoichiometric coefficient of species i in reaction j . The abbreviations "Nr" and "Nc" refer to the number of reactions and components, respectively. Finally, r_j^v is the volume specific rate of reaction j in $\text{mol m}^{-3} \text{s}^{-1}$ which is defined by the reaction kinetic model described in the following.

The reaction kinetic model is based on the mechanistic study of Lu et al. ^[80] considering the CO_2 hydrogenation to methanol, the methanol dehydration to DME, and the water gas shift reaction (WGSR) (Equations 4.6 to 4.8). Other possible reactions such as CO_2 methanation were not included because no other products were detected at significant concentrations during the kinetic experiments.



The respective reaction rates in mol kg⁻¹ s⁻¹ are calculated with Equations 4.9 to 4.11.

$$r_1 = k_1 \frac{\left(f_{\text{CO}_2} f_{\text{H}_2}^3 - \frac{f_{\text{H}_2\text{O}} f_{\text{CH}_3\text{OH}}}{K_{f,1}} \right)}{\left(1 + K_{\text{CO}_2} f_{\text{CO}_2} + K_{\text{CO}} f_{\text{CO}} + \sqrt{K_{\text{H}_2} f_{\text{H}_2}} \right)^3} \quad (4.9)$$

$$r_2 = k_2 \left(f_{\text{CH}_3\text{OH}}^2 - \frac{f_{\text{DME}} f_{\text{H}_2\text{O}}}{K_{f,2}} \right) \quad (4.10)$$

$$r_3 = k_3 \frac{\left(f_{\text{H}_2\text{O}} - \frac{f_{\text{CO}_2} f_{\text{H}_2}}{K_{f,3} f_{\text{CO}}} \right)}{1 + K_{\text{CO}_2} f_{\text{CO}_2} + K_{\text{CO}} f_{\text{CO}} + \sqrt{K_{\text{H}_2} f_{\text{H}_2}}} \quad (4.11)$$

Finally, r_j^v is given by,

$$r_j^v = \begin{cases} r_j [(1 - \epsilon) \rho_{\text{CZA}} \xi_{\text{CZA}}], & j = 1 \vee j = 3 \\ r_j [(1 - \epsilon) \rho_{\gamma\text{-Al}_2\text{O}_3} \xi_{\gamma\text{-Al}_2\text{O}_3}], & j = 2. \end{cases} \quad (4.12)$$

In Equations 4.9 to 4.12, f_i is the fugacity of component i in bar, calculated using the fugacity coefficients obtained from the PR-EoS, ϵ is the catalyst bed void fraction, ρ_{CZA} and $\rho_{\gamma\text{-Al}_2\text{O}_3}$ are the CZA and $\gamma\text{-Al}_2\text{O}_3$ densities, and ξ_{CZA} and $\xi_{\gamma\text{-Al}_2\text{O}_3}$ are the respective volume fractions in the catalyst bed. The equilibrium constants ($K_{f,j}$) are calculated with Equation 4.13, whereas the reaction rate and adsorption constants (k_j and K_i) are defined by the re-parametrized Arrhenius and Van't Hoff equations (Equations 4.14 and 4.15) for a reference temperature T_R of 503 K.

$$K_{f,j} = 10^{\left(\frac{A_j}{T} - B_j\right)} \quad (4.13)$$

$$k_j = k_{j,T_R} \exp \left[-E_{A,j,n} \left(\frac{T_R}{T} - 1 \right) \right], \quad \text{with } E_{A,j,n} = \frac{E_{A,j}}{T_R R} \quad (4.14)$$

$$K_i = K_{i,T_R} \exp \left[-\Delta H_{i,n} \left(\frac{T_R}{T} - 1 \right) \right], \quad \text{with } \Delta H_{i,n} = \frac{\Delta H_i}{T_R R}. \quad (4.15)$$

The model specific parameters for Equations 4.13 to 4.15 (A_j , B_j , k_{j,T_R} , $E_{A,j,n}$, K_{i,T_R} , and $\Delta H_{i,n}$) are provided in Table 4.1.

Table 4.1: Model specific parameters for the lumped model used for the comparative evaluation of the hybrid model [1].

Reaction	Equation 4.13		Equation 4.14		Adsorbate	Equation 4.15	
	A	B	$\ln(k_{T_R})$	$E_{A,n}$		$\ln(K_{T_R})$	$\Delta H_{ads,n}$
1	3014.4029	10.3857	-6.94	21.81	CO	-15.32	-14.03
2	1143.9494	0.9925	-2.07	42.77	CO ₂	-0.57	0
3	2076.2131	2.0101	-2.75	10.82	H ₂	-19.51	-14.68

These parameters were determined based on intrinsic kinetic data acquired in a fixed bed reactor at a pressure of 5 MPa under variation of the temperature, the feed composition ($y_{\text{CO,in}}$, $y_{\text{CO}_2,\text{in}}$, $y_{\text{H}_2,\text{in}}$), and the total gas flow as summarized in Table 3.1. The

catalyst bed consisted of mechanically mixed CZA and $\gamma\text{-Al}_2\text{O}_3$ catalysts in a 1:1 mass ratio for a total catalyst mass of 2 g.

4.3.2 Data-based model and ANN training strategy

The data-based model derived and evaluated in Chapter 3 [3] consists of an ANN trained to predict the concentration of CO, CO₂, H₂, and DME in the product gas based on the composition of the feed gas ($y_{\text{CO},\text{in}}$, $y_{\text{CO}_2,\text{in}}$ and $y_{\text{H}_2,\text{in}}$), the total gas flow \dot{V}_{in} and the temperature (Figure 4.3). In this configuration, the ANN replaces both the reactor, and the reaction kinetic model. The model was trained using the same data used for the parameter estimation of the lumped kinetic model (Table 3.1) and hence, it has the same validity range.

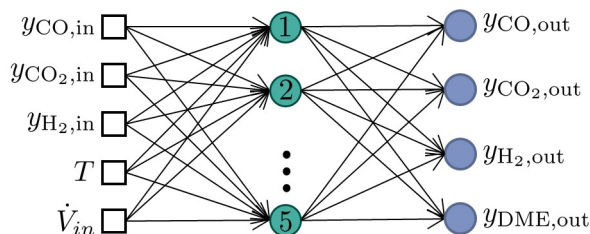


Figure 4.3: Representation of the data-based model used for the comparative evaluation of the hybrid model. Adapted from N. Delgado Otalvaro et al. [3]

Also relevant for this chapter is the data division and training strategy used for the data-based model, in Chapter 3 [3]. The ANN of the data-based model (ANN-DBM) and the one of the hybrid model (ANN-HM) are predictors for different quantities and trained using different data structures (Section 4.3.3). However, the data division and training methodology presented in Chapter 3 is automatic and adaptable to multidimensional data sets of different sizes and structures, and thus used in this chapter for the design of the ANN-HM. As depicted in Figure 3.4, the data division is conducted in two stages. In Stage 1, the data samples are divided into two subsets, one for the design/training of the networks (Design Data), and one for the posterior network selection based on separate data (Test Data A). In Stage 2 the design data is again divided into two subsets, the Train Data subset used in the backpropagation framework [149] to determine the network's parameters (weights and biases), and the Test Data B subset used in the framework of Bayesian regularization [138] to test the trained networks without a validation subset. The training is conducted iteratively under variation of the start parameter values (label (1)) to avoid local optimality, and of the data division of the design data (label (2)). The Test Data B is not used directly to determine the network's parameters, however, since the data in this subset is used for model selection, it introduces a certain bias in

the model. To guarantee that the network with the best generalization i.e., with the best performance on independent data samples is chosen, Test Data A is used for the final network selection.

4.3.3 Hybrid model

As depicted in Figure 4.2, the hybrid model consists of two parts: a reactor model, and an ANN. The reactor model is the same that is used in the lumped model (Equations 4.4 and 4.5). These are generally valid and constitute the "knowledge module" of the hybrid model. The ANN embedded within the framework of the ordinary differential equations, is used for the calculation of the reaction rates (r_j), and replaces the reaction kinetic model. Clearly, the ANN of the data-based model is not suitable for the calculation of the rates, since this ANN is trained to predict the product gas composition. In the following sections, the design of the ANN as a predictor of the rates for the hybrid model (ANN-HM) is described.

4.3.3.1 Architecture

Comparable to the architecture of the ANN-DBM, the ANN-HM is also shallow (one single hidden layer with a finite number of hidden neurons) and feedforward (unidirectional information flow from input to output), as depicted in Figure 4.4. The new ANN-HM is trained to replace the reaction kinetic model i.e., to predict the reaction rates along the axial coordinate z . Hence, the target vector y contains three elements, one representing the rate of each reaction (Equations 4.6 to 4.8) as follows,

$$y = [r_1, r_2, r_3] |_z. \quad (4.16)$$

The rates are calculated as a function of the temperature and the mole fractions of each species in the system. The input vector is thus defined by,

$$x = [y_{\text{CO}}, y_{\text{CO}_2}, y_{\text{H}_2}, y_{\text{H}_2\text{O}}, y_{\text{MeOH}}, y_{\text{DME}}, y_{\text{Ar}}, y_{\text{N}_2}, T] |_z. \quad (4.17)$$

The elements in Equations 4.16 and 4.17 correspond to the values at different positions of the axial coordinate z . Since all experiments were conducted under isothermal conditions, the temperature is constant along the reactor length L_{bed} and Equation 4.18 applies.

$$T|_z = T, \forall z \in [0, L_{\text{bed}}]. \quad (4.18)$$

Other process variables that are considered to be constant in the axial domain and over all data points, such as the catalyst distribution and pressure, are not included explicitly in the model. Furthermore, the proposed structure is one of innumerable possibilities

for the design of the ANN-HM, and additional input variables can be included in the network to consider further phenomena if the respective data is available. For example, including the time on stream (ToS) in the input vector and data samples measured at different ToS during the ANN training would enable to consider the effect of activity loss on the reactions rates.

While the number of input and output neurons is constrained by the input and output variables (Equations 4.16 and 4.17), the number of neurons in the hidden layer has to be determined empirically. For the selection of an appropriate number of hidden neurons (HN), architectures with up to 30 HN were tested. The best ANN was selected based on the prediction accuracy on "unseen" data, using a mean relative error of 5 % over all samples in Test Data A (Figure 3.4).

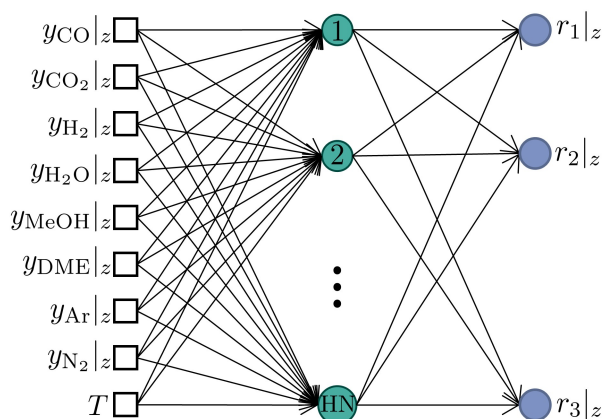


Figure 4.4: Schematic representation of ANN's architecture for the hybrid model (ANN-HM).

The remaining network's characteristics are chosen to be the same as in the data-based model in order to ensure comparability of the models. Hence, the logarithmic sigmoid and the positive linear functions were used as the activation function in the hidden and output neurons, respectively. The sigmoid function serves to map the known non-linearities in the system. Bayesian Regularization was chosen as training algorithm. This method proposed by McKay [138] aims to avoid overfitting by training only the number of parameters necessary to minimize the objective function, instead of all parameters available. Thus, the model sensibility to the network architecture is reduced and overfitting can be avoided.

4.3.3.2 Training data

For a comparative study of the models, possible biases must be excluded to ensure that the prediction discrepancies are caused only by the structural differences between the model types. For the comparison of the lumped and the data-based model, this was

achieved by training/parametrizing both models with the same experimental data. In the case of the hybrid model, the ANNs act as a predictor for the reaction rates, which are not metrologically accessible from integral experiments where the measurable variable is the composition of the product gas ($y_{i,\text{out}}$). Therefore, to generate training data for the ANN-HM, simulations are performed with the lumped model under the conditions of the experiments to which the lumped and data-based models were fitted (Table 3.1). The axial domain is discretized as shown in Figure 4.5 using different mesh refinements with 5, 10, 15, 50, and 100 uniformly distributed elements, and the reaction rates at the nodal points are used for training.

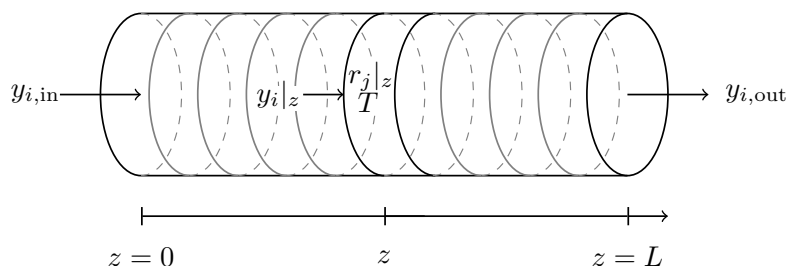


Figure 4.5: Schematic representation of the axial domain discretization, exemplary for 10 uniformly distributed elements.

4.3.4 Experimental equipment and procedures

New experiments were conducted with the same laboratory setup used for the measurement of the kinetic data for model development. These experiments were performed to validate the simulation results obtained during extrapolation analysis in Section 4.4.3. The reactor used for the experiments is a plug flow tube reactor made of stainless steel. It has a length of 460 mm and an internal diameter of 12 mm. For heating purposes the reactor outer wall is enclosed by four brass jaws with heating cartridges (Horst GmbH). The pressure of the reactor is regulated manually with a mechanical pressure regulator (Emerson Electric Co.) and mass flow controller (Bronkhorst High-Tech B.V.) are used to regulate the gas flow into the reactor. A fourier transformation infrared spectrometer (FTIR, Gaset Technologies) and a gas chromatograph (GC, Agilent Technologies) were used to quantitatively analyze the feed and product gases.

The syngas used for the experiments consisted of the feed gases hydrogen (H_2 , 99.9999 %), carbon monoxide (CO , 99.97 %), a mixture of carbon dioxide and nitrogen (CO_2/N_2 , 20:80 \pm 1.0 %) as well as of nitrogen (N_2 , 99.9999 %). The gases were purchased by Air Liquide Germany GmbH. A 1:1 mechanical mixture of the commercial catalysts $\text{CuO}/\text{ZnO}/\text{Al}_2\text{O}_3$ (CZA) and $\gamma\text{-Al}_2\text{O}_3$ (Alfa Aesar) was used. The size distribution of the catalyst parti-

cles lay within 250 μm and 500 μm . Silicon carbide (SiC, Hausen Mineraliengroßhandel GmbH) with the same particle size distribution was mechanically mixed with the commercial catalysts in order to avoid the formation of hot spots in the catalytic bed.

Before starting the experimental measurements, the catalyst was reduced using 5 % H_2 in N_2 at atmospheric pressure and temperatures between 363 K and 513 K. After that, the catalysts were conditioned and the measured species concentrations were monitored based on a reference experimental point to check for any loss of activity. After a stable catalytic activity was achieved, any deactivation of the catalysts could be ruled out. Additional information on the catalyst conditioning and deactivation can be found in Appendix C.

4.4 Hybrid model results

In this section, the results of the ANN-HM training are presented first, followed by the evaluation of the models performance and interpolation ability. Subsequently, a comparative analysis of the predictions of the three different model types is conducted and complemented with the experimental validation of simulation results.

4.4.1 ANN-HM training results

In the absence of an established systematic approach, determining the appropriate number of hidden neurons (HNs) is one of the major challenges in modeling with ANNs. If the number of HN is too low, the forecasting ability of the model is limited, and the input-output relationships in the data might not be represented accurately. If the number of HN is too high, overfitting might occur. In this case, the model can learn the data noise or “memorize” the training data, and the error on the test data, which is not used during training, typically begins to rise. [50, 52] In Figure 4.6 two error measures, namely the mean squared error (Figure 4.6a) and the mean relative error (Figure 4.6b) are shown as a function of the number of HNs. It is observed that as the number of HNs increases, the prediction accuracy also increases, which can be attributed to the increasing number of parameters and model complexity. Additionally, in the evaluated range with up to 30 HNs, the error on the test data set also decreased with increasing complexity (Figure 4.6b), which indicates that overfitting was suppressed effectively. Another observation from this figure is that the error on the training and test data sets is of the same order of magnitude, which is also an indication for the successful avoidance of overfitting. This is attributed to the training algorithm based on Bayesian regularization, which has proven to be effective for this purpose [3, 127, 138, 139].

Some approaches for network selection include empirical correlations [150–152] or graphical methods. One approach is the elbow method, where a loss function e.g., the mean squared error (MSE) between targets and model outputs is plotted against the number of hidden neurons, and the optimal network is determined based on the inflection point (elbow) of the curve [108]. According to this theory, the optimal number of HN is approx. 4 or 5 (see Figure 4.6a). On the other hand, the mean relative error of prediction (depicted in Figure 4.6b) shows that 5 HNs do not provide enough model complexity to achieve the targeted prediction accuracy. A mRE $\leq 5\%$ is achieved with networks with more than 25 HNs. Based on this and most importantly on the model performance regarding extrapolation (further discussion in Section 4.4.3) the ANN with 26 HN was chosen for the further analysis. A schematic representation of the resulting network as well as the model specific parameters are provided in Appendix C.

The time required to train 10000 ANNs (with 100 schemes for the division of design data and 100 set of start parameter values as described in Section 4.3.2) is also plotted in Figure 4.6a. Overall, the training time increases with the number of parameters. However, even at the highest number of parameters tested (with HN=30), the training time remained below 7 minutes. Considering that the training of the data-based model and the parameter estimation for the lumped kinetic model required approx. 7.9 min and 3.5 h, respectively [3], the computational burden can be assessed as remarkably low, as expected from related studies [54, 56, 58].

4.4.2 Hybrid model’s performance and interpolation ability

After integration of the selected ANN-HM into the differential equation framework, the predictions of the hybrid model can be evaluated in comparison with the experimental values and the predictions of the other models. First, the successful implementation of the hybrid model is validated by comparison with experimental data. The mean relative error between the experiments and the predictions of the lumped and the hybrid model are shown in Table 4.2. The high similarity between the deviations of both models from experimental data is explained by the fact the ANN-HM was trained with reaction rates calculated with the lumped model, and shows the high level of accuracy obtained with the hybrid approach. Similarly to the computational burden, the accuracy of hybrid models has been previously investigated in related studies [56, 58, 153] which show, agreement with the results here, the remarkable performance of this model type.

The interpolation ability of the hybrid model was also evaluated, and no difficulties were observed. This is shown for an exemplary feed gas composition in Figure 4.7 (Further examples are given in the supplementary material). In this figure, the mole fractions

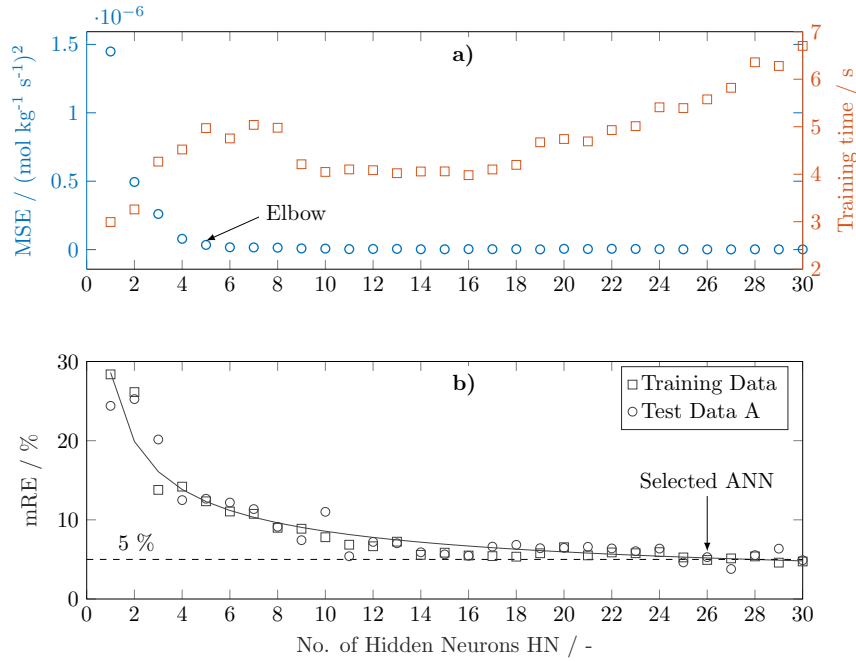


Figure 4.6: Training results for different architectures of the hybrid model's artificial neural network (ANN-HM). **a)** Mean squared error (MSE) and training time **b)** mean relative error (mRE) on training and testing data sets.

Table 4.2: Mean relative errors (mRE) between the experiments and the predictions of the lumped and hybrid model.

Model	mRE $y_{\text{H}_2,\text{out}}$	mRE $y_{\text{CO},\text{out}}$	mRE $y_{\text{CO}_2,\text{out}}$	mRE $y_{\text{DME},\text{out}}$
Lumped	1.49 %	5.49 %	6.02 %	28.89 %
Hybrid	1.49 %	5.45 %	6.08 %	28.36 %

of H₂, CO, CO₂ and DME predicted with the hybrid model within the temperature and total gas flow ranges are shown. At increasing temperatures the reaction rates also increase, leading to higher product concentration (DME and CO₂), and lower concentration of the educts CO and H₂ at the reactor outlet. Similarly, a decreasing total gas flow leads to longer residence times, which affects the outlet concentrations in the same way as increasing temperatures. These expected trends and also smooth gradients are observed over the response surfaces for all species. A further illustration of the interpolation ability of the hybrid model can be observed in Figures 4.10 and 4.11 between the dashed lines that represent the models' range of validity. In this range, the predictions of the hybrid and the lumped models are almost identical and the predictions of the data-based model are comparable to those of the other two models, but show a slightly better agreement with the experiments.

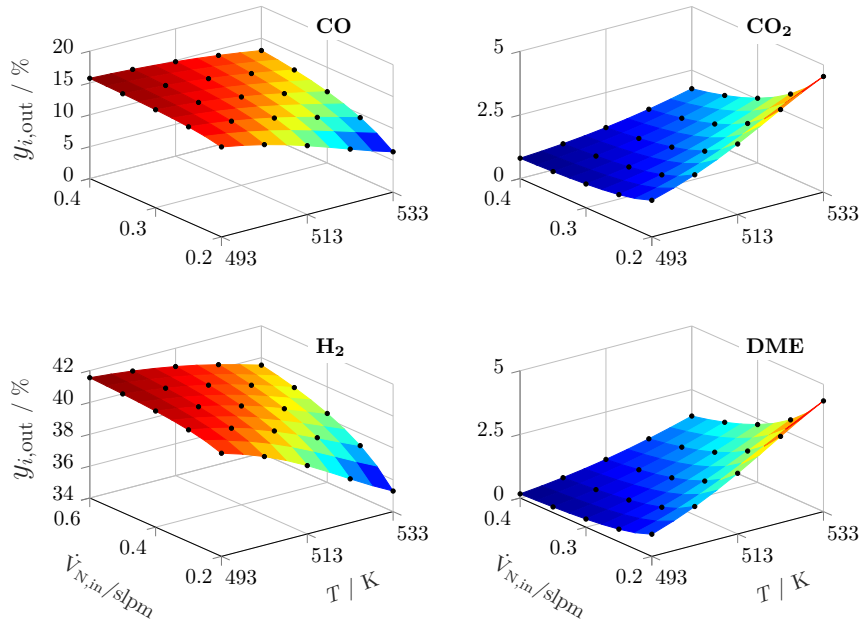


Figure 4.7: Surface response for the hybrid model predictions of the mole fractions of H_2 , CO , CO_2 and DME within the validity range of the temperature and total gas flow. The black points represent the conditions at which the data for model development was measured. Feed composition: 42.33 % H_2 , 16.14 % CO , 0.82 % CO_2 . Pressure 5 MPa. CZA-to- γ - Al_2O_3 -ratio $\mu = 1$. ANN-HM with 26 HNs.

Another relevant feature between the different model types is the convergence time. To provide a quantitative comparison, simulations were conducted with the three models for all the operating points in the data base (on windows 10 Pro (64-bit) operating system with i5 processor and 8GB RAM). The time required by each model to simulate the 180 operating points was:

- Data-Based: 0.0798 s
- Hybrid: 4.2432 s
- Lumped: 16.4095 s

The superiority of the data-based model regarding the convergence time is obvious, and although the hybrid model is slower than the data-based one, the former is still approx. four times faster than the lumped model.

The convergence time is of special interest when the models are used for optimization purposes and large number of simulations have to be conducted to screen the state space. A further characteristic relevant for optimization is the extrapolation ability of the models, which is evaluated in the following section.

4.4.3 Models' extrapolation ability

The following sections are dedicated to the evaluation of the models' predictive ability outside the range of validity i.e., the extrapolation ability. For this purpose, two types of extrapolation are evaluated; dimension and range extrapolation. Dimension extrapolation refers to the extrapolation of a variable that was held constant during the experiments for model development. Range extrapolation, on the other hand, refers to the evaluation of a variable outside the range screened during these experiments [154]. The pressure and the catalyst bed composition are used here as exemplary variables to evaluate the dimension extrapolation (Section 4.4.3.1). Range extrapolation is analysed based on the temperature in Section 4.4.3.2. Experimental values used for validation of the simulations at extrapolated conditions are reported in the supplementary material.

4.4.3.1 Dimension extrapolation

Since all the experimental data used for the parametrization of the hybrid model were acquired at constant pressure and catalyst bed composition ($p=5$ MPa and CZA-to γ -Al₂O₃ mass ratio $\mu=1$), these variables are suitable for the evaluation of the hybrid model regarding dimension extrapolation.

The pressure was evaluated in a range between 4 and 6 MPa by the means of experiments and simulations. The data-based model was not used for this analysis since the structure of the ANN-DBM, that only takes the concentration of the syngas, the temperature and the total gas flow into account, does not allow simulations at other pressure levels (refer to ANN structure, Figure 4.3).

At 5 MPa, the deviation between the experiments for model development and for validation show a very good agreement, with a maximal deviation of 4.5 %. Furthermore, the validation experiments show the expected behavior i.e., with increasing pressure the product gas concentration of the educts decreases, and that of the products increases (Figure 4.8). Due to the volume contraction of the methanol synthesis from CO₂ (Equation 4.6), the rate of this reaction is favored by high pressures. Hence, from the thermodynamic perspective, the pressure has always a positive effect on the overall process performance. This effect is reflected by the lumped model for all species in the entirety of the evaluated pressure range. The average deviations between the experiments and the predictions of the lumped model lie by 2.1 % for H₂, 1.5 % for CO, 6.9 % for CO₂ and 12.6 % for DME within the prediction accuracy of the model, confirming the high fidelity of the semi-mechanistic model approach. The concentration profiles obtained with the hybrid model, on the other hand, are nearly constant over all evaluated pressures at the

value predicted for 5 MPa. Similar to the ANN-DBM, the structure of the ANN-HM does not allow the variation of the pressure (Figure 4.4) since all the training data was measured at only one pressure level. Thus, the pressure dependency of the reaction rates is not considered by the hybrid model and dimension extrapolation regarding this variable is not possible.

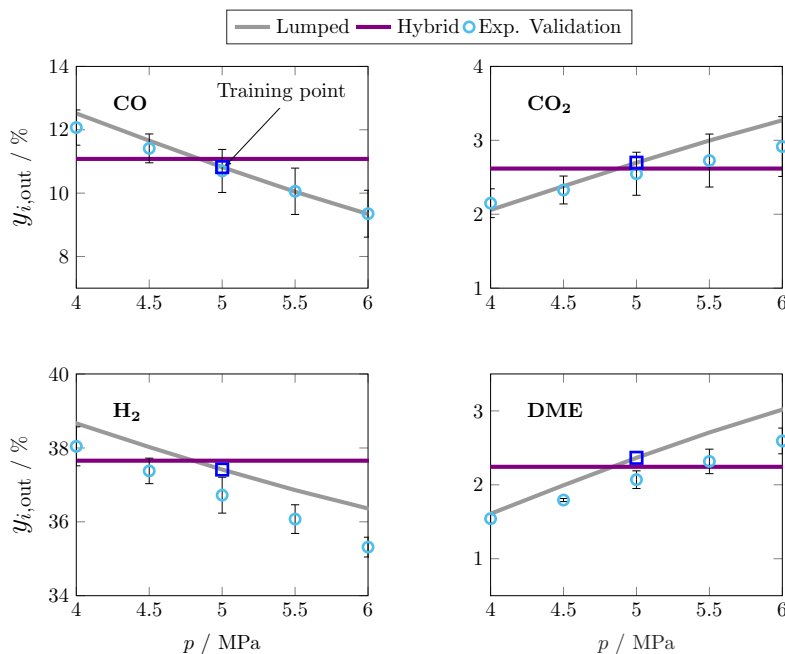


Figure 4.8: Experimental validation of dimensional extrapolation of the pressure. Feed composition: 42.3 % H₂, 16.1 % CO, 0.82 % CO₂. Total gas flow 0.4 slpm. Temperature 533 K. CZA-to- γ -Al₂O₃-ratio $\mu = 1$. ANN-HM with 26 HNs.

The catalyst bed composition μ is also suitable for testing the dimension extrapolation of the hybrid model, since all the experiments for model development were measured with $\mu=1$. Unlike the pressure, μ does not have a direct influence on the reaction rates, and hence extrapolating this variable does not imply the extrapolation of the ANN-HM. Therefore, better extrapolation results are expected. For this analysis, μ was varied from 0 to 5 and simulations with the lumped and hybrid model were conducted. Representative results are shown in Figure 4.9.

With the lumped model an increasing conversion of CO_x and yield of DME with increasing μ is predicted, and the values at the highest μ display a high proximity to the values at equilibrium. This behavior is attributed to the synergy of the direct synthesis, where the equilibrium of the methanol synthesis is shifted towards the products by methanol consumption through the dehydration to DME. With an increasing μ methanol is produced faster, which boosts the methanol dehydration reaction and overcompensates

the decreased amount of dehydration catalyst [1].

The conversion and yield predicted by the selected hybrid model (ANN-HM with 26 HN) show a remarkably good agreement with the predictions of the lumped kinetic model over the entirety of the extrapolated range. The predictions of the lumped and the hybrid model overlap from μ up to 1, and proceed with a very similar trend. Although the deviation between the models' predictions increases as the distance from the training point $\mu=1$ becomes larger, the predictions are thermodynamic consistent, and very similar over the whole evaluated range (e.g., at $\mu=5$, $X_{\text{CO}_x}= 58.7$ and 55 % with the lumped and the hybrid model, respectively).

The predictions of hybrid models with ANN-HM with 5 and 28 HNs are shown in Figure 4.9a and c to illustrate the importance of considering model's extrapolation ability during the network selection. Both models displayed a relatively good performance on the training data in Section 4.4.1. This is also evident in Figure 4.9a and c, where the conversion and yield profiles predicted by all hybrid models overlap near the training point. However, the hybrid models with 5 and 28 HN clearly lack of the ability extrapolate. The predictions of these models do not follow the expected trend, nor do they respect the laws of thermodynamics. This illustrates one of the major drawbacks of data-based and/or hybrid approaches. Both models delivered a good performance on the training data and exhibited a good interpolation ability. However, it is not possible to predict the quality of the forecasts beyond the range where these models were trained, since the predictions at extrapolated conditions (especially regarding dimension extrapolation) are only dependent on the mathematical structure of the network, without an explainable phenomenological reason.

As mentioned in Section 4.3.3.2, different mesh refinements of the axial domain were tested during the generation of training data. Figure 4.9b and d show the CO_x conversion and DME yield at mesh refinements with 5, 10, and 15 axially distributed elements. Evidently, the mesh refinement with 5 elements does not provide enough data for training, leading to poor extrapolation capability of the hybrid model. With 15 elements, on the other hand, no relevant improvement of the network generalization is achieved and the predictions almost entirely overlap with those obtained with 10 axial elements. Similarly, no improvement was achieved with mesh refinements with 50 and 100 elements, however, the training time increased noticeably with the large number of data samples.

In this section, it was shown that the data-based models (ANN-DBM and ANN-HM) lack on extrapolation ability, while the hybrid model could be extrapolated successfully in a large range when the extrapolation variable was not in the data-based module of

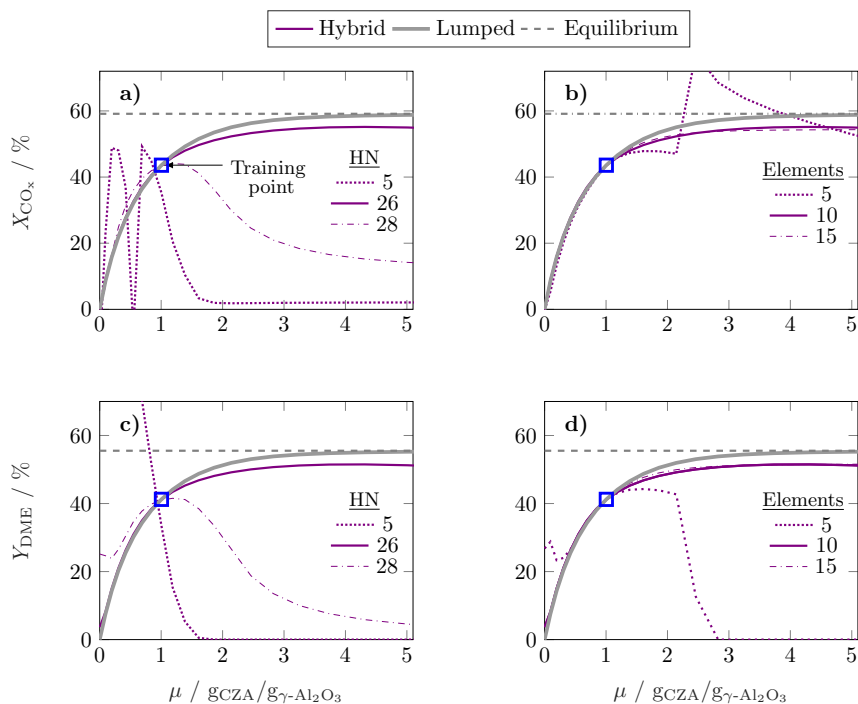


Figure 4.9: Dimension extrapolation of the catalyst bed composition. The plots show **a)** the COx conversion calculated with the lumped model and with the hybrid models consisting of various HN, **b)** the COx conversion at various mesh refinements, **c)** the DME yield calculated with the lumped model and hybrid models consisting of various HN as well as **d)** the DME yield at different mesh refinements. The results are plotted against μ ranging from 0 to 5. Feed composition: 48.42 % H₂, 16.07 % CO, 2.81 % CO₂. Total gas flow 0.2 slpm. Temperature 533 K. Pressure 5 MPa.

the hybrid structure and the extrapolation ability was taken into account during model development. This requires knowledge of the system and/or of the expected trends, and is only relevant if extrapolation is relevant for the aimed application of the hybrid model.

4.4.3.2 Range extrapolation

Range extrapolation refers to the evaluation of a variable that was varied during model development, outside the range in which that variation occurred [154]. For the evaluation of this extrapolation case, experiments and simulations with the three models were conducted at temperatures between 453 and 573 K at two different total gas flow rates. Initially, the results at a total gas flow of 0.2 slpm are shown and discussed, followed by results at 0.6 slpm. The hybrid model with ANN-HM with 26 HNs was used here, as it was the only model that delivered good extrapolation ability for the catalyst bed composition. Equivalent results with other architectures of the ANN-HM are given

in the supplementary material.

Figure 4.10 shows the predictions of the three models as well as the experiments used for model development (conducted in a previous work [1]) and validation for a total gas flow of 0.2 slpm. Additionally, the molar fractions at equilibrium calculated with the RG-bibbs reactor in Aspen Plus are displayed, along with the models' validity range which is marked gray.

The experiments for experimental validation were conducted in the same reactor in which the kinetic measurements for model development were performed. Additionally, the same catalyst reduction and conditioning procedure were followed. As a result, the experiments from the previous work [1] could be verified, and the experiments in the temperature range between 493 and 533 K overlap with a low relative deviation of maximal 6.6 % (max. mRE between experiments for model development and experiments for validation).

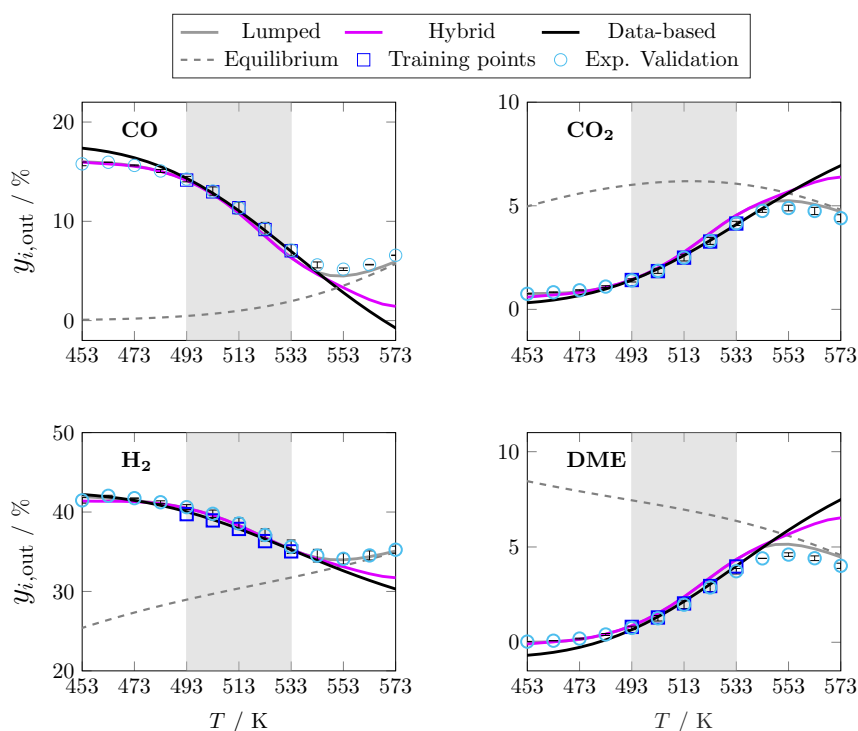


Figure 4.10: Evaluation of range extrapolation by comparison of models' predictions and experimental results beyond the models' validity range for temperature. Feed composition: 42.3 % H₂, 16.1 % CO, 0.82 % CO₂. Total gas flow 0.2 slpm. Pressure 5 MPa. CZA-to- γ -Al₂O₃-ratio $\mu = 1$. ANN-HM with 26 HNs.

Bellow 493 K, the predictions of the hybrid and the lumped models are virtually identical. The predictions of the data-based model slightly differ, however, the correct and expected tendency is observable. At low temperatures, the rate of the reactions is low and almost no conversion takes place. Hence, the concentration of each species should be equal to the concentration in the feed gas, i.e., 42.3 % H₂, 16.1 % CO, 0.82 % CO₂, and 0 % DME. The hybrid model predicts this behavior correctly and the predictions do not deviate from those of the lumped model, although, the model was not explicitly trained in this range. This can be explained by the fact that the phenomena that play a significant role in this temperature range are the same as in the range where the model was trained. The influence of the thermodynamic equilibrium is low compared to that of the reaction kinetics as it can be inferred from the distance to the values in equilibrium. Similarly, *a priori* criteria confirmed that no mass or heat transport limitations take place (refer to Appendix C). Hence, it can be concluded that, although, the rate of reactions is low, the reaction kinetics control the process performance also in this temperature range and the performance can be described correctly by the hybrid model which was trained to predict this phenomena. In addition, the hybrid model yields physically reasonable results and the predicted concentrations remain above 0 for all conditions, unlike the predictions of the data-based model, which also assume negative values.

Above 533 K, the predictions of the three models diverge. At increasing temperature levels the influence of the thermodynamic equilibrium also increases, as the concentrations get closer to those at equilibrium. The rates of reversible exothermic reactions increase initially due to the positive influence of the temperature, but decrease at the proximity of the thermodynamic equilibrium when the back-reaction is favored. At the temperature at which thermodynamics prevails over reaction kinetics, an inflection point occurs, as can be clearly observed in the predictions of the lumped model (gray lines). The concentration of the educts, in this case CO and H₂, then rises and that of the products DME and CO₂ decreases as the reaction rates decrease. This can be predicted by the lumped model successfully due to the Hougen–Watson formulation of the rate expressions, that accounts for the effect of the proximity to the thermodynamic equilibrium on the rates by the means of the equilibrium constants ($K_{f,j}$). The predictions of the data-based model do not show any inflection point and the concentration profiles follow the same trend as in the range of validity. Indicating that the data-based model only reflects the effect of the temperature on the reaction rate, but not the effect of the proximity to the thermodynamic equilibrium. In this temperature range, the hybrid model predictions lie between the predictions of the data-based and the lumped model in all cases. The molar fraction profiles flatten with increasing temperature, but a clear inflection point is not evident in the evaluated range. Unlike the lumped model, the hybrid approach attains

knowledge about phenomena affecting the reaction rates only from data. Hence, since most operational points in the training data set were measured at conditions at which reaction kinetics prevail and thermodynamic equilibrium has a negligible effect, the hybrid model does not have enough information about the effects the equilibrium can have on the rates and on the process performance. The measured values at temperatures above 533 K showed that the lumped model exhibits the highest accuracy, especially in terms of the shape of the curve with a clearly visible inflection point.

Equivalent results measured/simulated are shown in Figure 4.11 for a total gas flow of 0.6 slpm. The residence time for this gas low rate is shorter than at 0.2 slpm, and lower conversions are attained. Therefore, the distance to thermodynamic equilibrium is larger which, according to the discussion above, leads to the observed higher prediction accuracy.

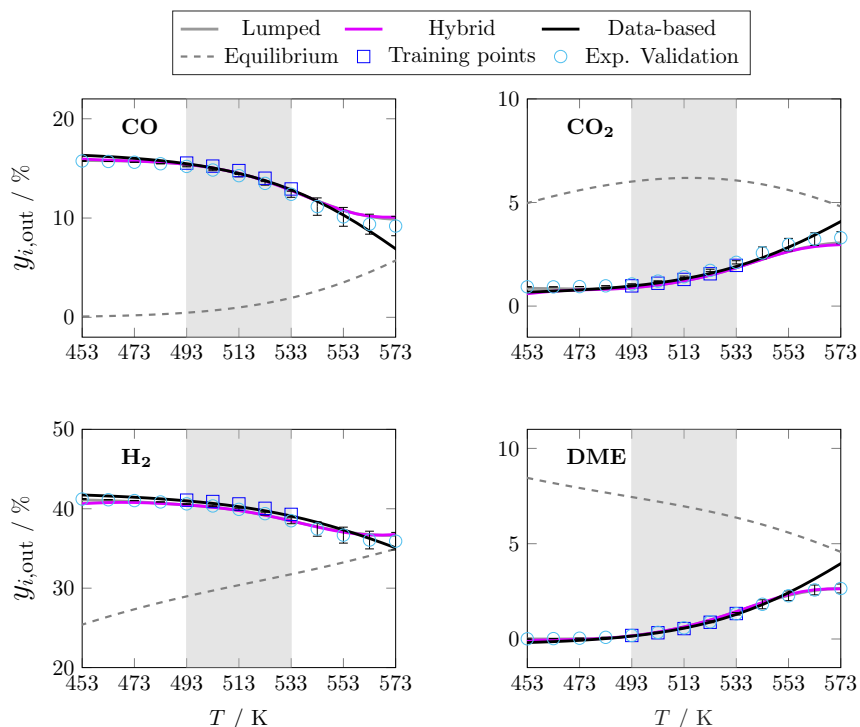


Figure 4.11: Evaluation of range extrapolation by comparison of models' predictions and experimental results beyond the models' validity range for temperature. Feed composition: 42.3 % H₂, 16.1 % CO, 0.82 % CO₂. Total gas flow 0.6 slpm. Pressure 5 MPa. CZA-to- γ -Al₂O₃-ratio $\mu = 1$. ANN-HM with 26 HNs. Predictions of the lumped and hybrid model overlap over the entire temperature range.

At this gas flow rate the simulations of the three models are very similar in the whole temperature range. A slight difference is noticed at temperatures above 553 K, where

the predictions of the data-based model diverge. However, the predictions of the lumped and the hybrid model remain superimposed with a maximal relative deviation of 3 % (computed for CO₂ at 573 K).

This confirms that the reason for the model discrepancy is the influence of the thermodynamic equilibrium which becomes more relevant at higher temperatures, and indicates that the extrapolation limits of data-based and hybrid models do not strictly depend on the evaluated range of conditions, but more on the effects considered by the underlying models.

4.5 Summary and conclusions

The first part of this chapter provides a timely overview of the models available for the direct DME synthesis. It has been shown that most of the available models for the direct DME synthesis are semi-mechanistic i.e., based on mechanistic assumptions. Since these models are only valid in a limited operational range, special attention was paid to the validity of each of the semi-mechanistic models, which were compared graphically to enable a fast overview of the investigated ranges in each work. Additionally, works where data-based models were used for the direct DME synthesis have been summarized. No hybrid model could be found in the open literature for this system.

The second part of this chapter deals with the implementation and evaluation of a hybrid model for the direct DME synthesis, aiming to identify and evaluate specific advantages and disadvantages of hybrid modeling approaches for this system. The developed hybrid model displayed a high level of accuracy and good interpolation ability over the entirety of the validity range. Additionally, it exhibited a low computational burden. E.g., the training of this model was approx. 30 times faster than the parametrization of a lumped model, and simulations compiled almost 4 times faster on the same CPU. These results are broadly consistent with studies in the open literature and confirmed expected outcomes regarding accuracy and computational effort.

As one of the main concerns about hybrid models, the extrapolation ability has been put to test and the predictions of a semi-mechanistic and a data-based model, as well as experiments have been used for the evaluation of the hybrid model performance. Based on exemplary variables (pressure, catalyst bed composition, and temperature), it has been shown that dimension extrapolation i.e., extrapolation of a variable that was kept constant during model development, was not possible when this variable directly affects the data-based module of the hybrid model. E.g., simulations and experiments show that the effect of the pressure on the reaction rates could not be considered by the ANN, which

was trained at one pressure level only. In contrast, a good extrapolation ability in a broad range was achieved when the extrapolated variable was in the knowledge-module of the hybrid model. As an example, it is shown that the extrapolation of the CZA-to- γ -Al₂O₃ weight ratio was possible and delivered qualitatively accurate results in the broad range between ratios of zero to five, although all experiments used for model development were conducted with a ratio of one. A suitable ANN architecture proved to be essential for the accuracy of predictions at extrapolated conditions. Range extrapolation i.e., the evaluation of a variable outside the range where it was screened during model development, was possible though in a limited range. It could be concluded that the limit for extrapolation is defined by the phenomena the underlying models can map which depends strongly on the network architecture, instead of the range defined by conditions evaluated experimentally during model development.

Since there is currently no theoretical framework for network selection, and broadly used rules of thumbs failed to deliver a suitable network in this study, the best network was chosen manually based on simulations results. Clearly, this represents a major drawback when a large number of network architectures must be tested which limits the transferability of the presented results. Based on the gained insights, it can be concluded that the hybrid modeling approach could be best applied when large data sets in wide operational windows are available, and the input-output relationships between the data are not yet fully understood. This way, the advantages of the hybrid model (i.e., high accuracy and low computation effort) could be exploited to fill knowledge gaps, while avoiding extrapolation. Specifically for direct DME synthesis, one application with high potential for immediate use is to expand the model scope using the numerous lumped kinetic models available in the literature. These are valid in different operating windows and can be used to generate reaction kinetics data, analogous to the procedure followed in this work. After the training of ANNs with these data and integration of these ANNs in the hybrid model structure, the expected outcome is a model that enables cross-evaluation of multiple process variables such as different catalysts, reactor types, and reaction conditions throughout nearly the entire relevant operating window.

5. SUMMARY

In this work, three models for the direct DME synthesis from CO₂-enriched synthesis gas have been developed, presented and evaluated. A highlight of this work is that for the considered system, each model extends the reach of available models in their categories, thus providing valuable tools for the further design and optimization of this promising process. The lumped model presented in Chapter 2 covers a wide range of CO₂-rich feed compositions, and CZA-to- γ -Al₂O₃ weight ratios. The data-based and hybrid models presented in Chapters 3 and 4 are the first of each type for the direct DME synthesis with the commercial catalyst system at an industrially relevant pressure level. All models types offer different advantages and have unsolved challenges, which are briefly discussed in the following, along with the methodology followed in each chapter and the main results.

- **Chapter 2: Semi-mechanistic Model.** In this chapter, a semi-mechanistic (lumped) model was derived and evaluated.

The experiments for the model discrimination were performed in an operating window wider than those modeled in the literature to date, namely at an industrially relevant pressure of 5 MPa under variation of the carbon oxide ratio in the feed (CO₂ in CO_x from 20 to 80 %), temperature (503 – 533 K), space-time (240 – 400 kg_{cat} s/m³_{gas}), and the CZA-to- γ -Al₂O₃ weight ratio (from 1 to 5).

To answer the questions stated in Section 1.2, “what is the most appropriate model structure i.e., which mechanistic approach is most suitable for the system description within the evaluated operating window” and “which model-specific parameters enable accurate predictions in the evaluated range”, a systematic approach consisting of model discrimination and parametrization was followed.

For the initial model discrimination, the available experimental data were simulated using eight different kinetic models from the open literature. Subsequently, the five models with the lower residual squared sum were parametrized to fit the data.

The mechanistic assumptions and structure of the model with the highest accuracy were chosen for fine-tuning of the model-specific parameters aiming towards a high statistical significance. The mechanistic approach that enabled the most accurate system description in the evaluated operating window considered three main reactions, namely the CO₂ hydrogenation to methanol, the methanol dehydration to DME, and the water gas shift reaction (WGSR). Additional assumptions

include that the dehydration reaction is promoted by the γ -Al₂O₃ only, and that the methanol synthesis and the WGSR are promoted by the CZA catalyst. The rate expressions were postulated based on the general Hougen-Watson formulation assuming elementary reactions, a relevant influence of the adsorption of CO₂, CO and dissociated H₂ on the CZA catalyst, and no adsorption on the surface of the γ -Al₂O₃ catalyst.

The model-specific parameters were determined based on experiments, balance equations, and the described assumptions about the reaction mechanism. Confidence intervals, correlation coefficients, and the analysis of the parameters underline the high statistical significance and physical and chemical consistency of the estimated kinetic parameters. Compared to the adsorption of other species, CO₂ adsorption on the CZA catalyst has a strong influence on the reaction rates under the conditions studied and in the presence of CO₂-rich syngas. The successful fitting to the experimental data resulted in the highlight of this chapter: a mechanistically sound reaction kinetic model with a particularly large range of validity especially regarding the composition of the mixed catalyst bed and the CO₂ concentration in the syngas. This model enables model-based optimization and/or reactor and process design for the direct DME synthesis under consideration of these variables. It can be stated that semi-mechanistic models provide a rather limited flexibility due to the complex model structure consisting of coupled balance and constitutive equations (e.g. equations of state, kinetic approaches and thermodynamic considerations). This prevents the model from adapting to the available data and leads to deviations in the model predictions. The deviations of the model presented in this work could be attributed to measurement uncertainties, especially at low concentrations of DME. Hence, the fact that the model does not have enough flexibility to adapt to measurements with a low signal-to-noise ratio proves the reliability of its predictions and is a major advantage, if not a prerequisite, for exploratory purposes and applications such as rigorous optimization and optimal reactor design.

- **Chapter 3: Data-based Model.** In this chapter, an artificial neural network (ANN) was designed, trained, evaluated and put to test in comparison to a semi-mechanistic model parametrized to the same data.

Since each ANN is strictly specific and due to the lack of a theoretical framework, the design questions for ANNs postulated in Section 1.2 “what is a suitable activation function, backpropagation algorithm, network architecture, data division, and training strategy?” must be answered empirically.

It was shown that, for the system under consideration, non linear activation functions performed better than the (piece-wise) linear functions, and that algorithms

based on Jacobian backpropagation are superior to gradient descent methods in terms of accuracy, whereas no relevant effect of the activation function or training algorithm on the convergence time could be identified.

Moreover, an automated scheme for data partitioning, network training, and network selection was proposed. A total of 10000 ANNs per architecture were trained using this strategy. Different starting parameter values were used to avoid local optimality, and different schemes of data partitioning between training and testing were evaluated. Subsequently, the best network was selected based on its performance on a separate data set to guarantee that the chosen ANN is the one with the best generalization i.e., with the best results on new data.

The training of 10000 ANNs was completed in 7.9 minutes, while the parameter estimation of the lumped model parametrized to the same number of data points took approximately 3.5 hours. It is worth mentioning that the total time required to parameterize the lumped model is much longer when other steps of the process that are more difficult to quantify are taken into account, such as the implementation of different models structures in the framework of model discrimination, the determination of adequate start parameter values, etc.

The ANNs also outperform the lumped model in regards to the accuracy of predictions. To name an example, the relative error of predictions for the DME molar fraction over all data could be reduced by approx. 54 % (from 24 % to 11 %). The remaining predictive deviation is attributed to the mentioned measurement uncertainties, and to the fact that the ANN could be trained successfully to identify the input-output relationships in the data, rather than simply storing and replaying the provided samples.

These findings underline the suitability of the ANN to act as a predictive tool for Brownfield applications such as soft sensing, real-time optimization, on-line control, predictive maintenance, and others, where models with high flexibility and adaptability, the capacity to map complex nonlinear relationships as well as fast convergence and low computational cost are required.

Furthermore, the interpolation capability of the network was tested. It was confirmed that the chosen ANN is a reliable predictor in this operating window, although the data set was relatively small (180 experimental points). This answers the question “whether or not relatively small data sets are sufficient to meet the data requirements of a simple ANN” and demonstrates the remarkable power of data based models in contrast to semi-mechanistic approaches in regards to computational burden and accuracy within the evaluated operational window.

To assess the model’s extrapolation ability and answer the stated question “to what extent, if at all, the data-based model can be extrapolated”, simulations beyond the

validity range were performed. The ANN delivered unexpected predictions at these conditions. While it is widely accepted that data-based models are not reliable when extrapolated, the analysis conducted in this work showed that extrapolation of the ANN is indeed possible in the range where the phenomena covered by the underlying model prevail, even if these conditions are outside the model's validity range. Nevertheless, at conditions where other phenomena unknown for the ANN take place, the expected deviations were observed. This points out the necessity for a new definition of "validity range" when dealing with data-based approaches. Furthermore, only the parameters varied during the experimental investigations can be included in the model structure of the ANN, which limits the suitability of the model for exploratory purposes in operating windows not yet experimentally investigated.

- **Chapter 4: Hybrid Model.** The first part of this provides a timely overview of the models available for the direct DME synthesis. It has been shown that most of the available models for the direct DME synthesis are semi-mechanistic, while only a few works apply data-based models. No hybrid model could be found in the open literature for this system. The second part of this chapter deals with the implementation of a model of this type for the direct DME synthesis, and provides a comprehensive comparison of the three model types handled in this work. Since there are innumerable possible hybrid model structures, the first step was to determine "what is a suitable structure to integrate available system knowledge with data-based approaches to fill knowledge gaps?". The postulated model consists of balance equations of the tube reactor where the experiments used for model design were measured. These equations are based on thermodynamic laws and hence introduce known effects in the model. On the other hand, the unknown factor when modeling the DME synthesis, i.e., the reaction kinetics are described by an ANN trained to predict the rate of reactions with no mechanistic assumptions. To answer "what are the advantages of a hybrid model over conventional semi-mechanistic and/or data-based models in terms of computational burden, extrapolation capability, and other critical properties of predictive models?" the characteristics of the hybrid model were assessed using experiments and simulations with a semi-mechanistic and a data-based model. For this purpose, all models must have the same range of validity, which enables an evaluation of the structural differences between the models especially regarding extrapolation. Additionally, the characteristics of the data-based and the ANN of the hybrid model were also chosen to be the same in order to ensure comparability of these models.

The developed hybrid model could be trained very fast and it displayed a high level of accuracy as well as short simulation time, especially when compared to the semi-mechanistic model (e.g., 30 times faster parameter estimation and 4 times faster simulations).

The interpolation ability was also tested, and the expected accurate and smooth model predictions were observed. These results are broadly consistent with studies in the open literature where hybrid model modeling was applied to similar systems. Special attention was paid to the extrapolation ability of the hybrid model as one of the critical features of data-based and hybrid modeling approaches. Based on exemplary variables, it has been shown that dimension extrapolation i.e., extrapolation of a variable that was kept constant during model development, was not possible when this variable directly affects the data-based module (ANN) of the hybrid model. In contrast, a good extrapolation ability in a broad range was achieved when the extrapolated variable was in the balance equations i.e., in the knowledge-module of the hybrid model, and a suitable network architecture was chosen. Range extrapolation i.e., the evaluation of a variable outside the range where it was screened during model development was possible, though in a limited range.

It could be concluded that the phenomena the underlying models can map is the crucial factor regarding the limit for extrapolation, rather than only the range evaluated experimentally during model development. Furthermore, these phenomena depend strongly on whether or not the data used for training reflect the corresponding effects, and on the network mathematical structure (architecture and parameters).

As it was shown in the literature overview, the direct DME synthesis has been widely studied in the literature over the last decades leading to numerous lumped kinetic models, each of them only valid in a limited range of conditions.

Future studies could explore the possibility of using these models in a manner analogous to that used in this chapter to expand the scope of the hybrid model. Through synthetic data generation, reaction kinetic data can thus be generated in the operating window in which the respective models were validated and subsequently used to train the ANN of the hybrid model postulated here. Due to its high flexibility, the hybrid model has the ability to integrate the knowledge captured by these models and it would be valid in all the ranges combined. Although the actual reaction mechanism would remain unclear with this approach, from the insights obtained in this work it can be expected that such a model enables cross-evaluation of the multiple process variables investigated in the single studies such as different catalysts, reactor types and geometries, and reaction conditions throughout nearly the entire relevant operating window. Thus, the exploration

and design of novel reactor or process concepts for this system could be conducted under consideration of a broad scope of process parameters and ranges. A challenge of this task is the highly heterogeneous information given in the different studies. E.g., for the carbon containing compounds some authors report the content of CO, CO₂, CO_x (CO + CO₂), and/or the CO₂-to-CO_x ratio. Similarly, the H₂ fraction, and/or the H₂-to-CO, or the H₂-to-CO₂ ratio are reported to indicate the hydrogen content in the feed. Additionally, published data is in many instances incomplete, which hinders model implementation and validation.

At the current stage of development, the main advantages of the data-based and hybrid models presented in this work are related to low computational burden and remarkable accuracy and flexibility to adapt to heterogeneous and multidimensional data. A major drawback is the lack of a theoretical framework for network selection when additional criteria such as extrapolation ability must be considered. These features highlight the potential of these approaches for brownfield applications, where an existing process is to be optimized, controlled, or monitored, while their usage for greenfield approaches or exploratory applications is rather limited. In the latter case, reliable predictions at extrapolated conditions are necessary which cannot be guaranteed with data-based or hybrid models. Here, (semi-) mechanistic approaches represent the better option.

ZUSAMMENFASSUNG

In dieser Arbeit wurden drei Modelle für die direkte DME-Synthese aus CO₂-reichem Synthesegas entwickelt, beschrieben und bewertet. Ein Highlight dieser Arbeit ist, dass jedes Modell für das betrachtete System den Gültigkeitsbereich der verfügbaren Modelle in ihren Kategorien erweitert und somit wertvolle Werkzeuge für die weitere Entwicklung und Optimierung dieses vielversprechenden Prozesses bereitstellt. Das in Kapitel 2 vorgestellte formalkinetische Modell deckt einen breiten Bereich von CO₂-reichen Feedzusammensetzungen und Gewichtsverhältnissen von CZA zu γ -Al₂O₃ ab. Die in den Kapiteln 3 und 4 vorgestellten datenbasierten und hybriden Modelle sind die ersten ihrer Art für die direkte DME-Synthese mit einem kommerziellen Katalysatorsystem und industriell relevantem Druckniveau. Die jeweiligen Modelltypen bieten verschiedene Vorteile und stellen unterschiedliche Herausforderungen dar, die im Folgenden kurz erörtert werden, wie auch die in den einzelnen Kapiteln angewandte Methodik und die wichtigsten Ergebnisse.

- **Kapitel 2:** Semi-mechanistisches Modell. In diesem Kapitel wurde ein semi-mechanistisches (formalkinetisches) Modell entwickelt und bewertet.

Die Experimente zur Modelldiskriminierung wurden in einem im Vergleich zur bestehenden Literatur breiteren Betriebsfenster durchgeführt, bei einem industriell relevanten Druck von 5 MPa unter Variation des Kohlendioxidanteils im Feed (CO₂ in CO_x: 20 - 80 %), der Temperatur (503 - 533 K), der Raum-Zeit (240 – 400 kg_{Kat} s/m³_{Gas}) und des Gewichtsverhältnisses CZA zu γ -Al₂O₃ (1 bis 5).

Zur Beantwortung der in Abschnitt 1.2 gestellten Fragen, “welche Modellstruktur am besten geeignet ist, d. h. welcher mechanistische Ansatz am besten für die Systembeschreibung innerhalb des untersuchten Betriebsfensters geeignet ist” und “welche modellspezifischen Parameter präzise Vorhersagen im untersuchten Bereich ermöglichen”, wurde ein systematischer Ansatz verfolgt, der aus Modellunterscheidung und Parametrisierung besteht.

Zunächst wurden die experimentellen Daten mit acht verschiedenen kinetischen Modellen aus der Literatur simuliert, um die Modelle zu diskriminieren. Anschließend wurden die fünf Modelle mit der niedrigsten Residuenquadratsumme an die Daten angepasst und parametrisiert.

Die mechanistischen Annahmen und die Struktur des Modells mit der höchsten Genauigkeit wurden für die Feinjustierung der modellspezifischen Parameter aus-

gewählt, um eine hohe statistische Signifikanz zu erreichen. Der mechanistische Ansatz, der die genaueste Beschreibung des Systems im bewerteten Betriebsfenster ermöglichte, umfasste drei Hauptreaktionen, die CO₂-Hydrierung zu Methanol, die Dehydratisierung von Methanol zu DME und die Wasser-Gas-Shift-Reaktion (WGSR). Weitere Annahmen sind, dass die Dehydratisierungsreaktion nur durch das γ -Al₂O₃ katalysiert wird und die Methanolsynthese und die WGSR durch den CZA-Katalysator begünstigt werden. Die Ausdrücke für die Reaktionsraten wurden auf der Grundlage der allgemeinen Formulierung von Hougen-Watson unter der Annahme von Elementarreaktionen, eines relevanten Einflusses der Adsorption von CO₂, CO und dissoziiertem H₂ am CZA-Katalysator und keiner Adsorption an der Oberfläche des γ -Al₂O₃ -Katalysators postuliert.

Die modellspezifischen Parameter wurden auf der Grundlage von Experimenten, Bilanzgleichungen und den beschriebenen Annahmen über den Reaktionsmechanismus bestimmt. Konfidenzintervalle, Korrelationskoeffizienten und die Analyse der Parameter unterstreichen die hohe statistische Signifikanz und die physikalische und chemische Konsistenz der ermittelten kinetischen Parameter. Im Vergleich zur Adsorption anderer Spezies hat die CO₂-Adsorption am CZA-Katalysator unter den untersuchten Bedingungen und bei CO₂-reichem Synthesegas einen starken Einfluss auf die Reaktionsgeschwindigkeit. Die erfolgreiche Anpassung an die experimentellen Daten führte zum Highlight dieses Kapitels: ein mechanistisch fundiertes reaktionskinetisches Modell mit einem besonders umfangreichen Gültigkeitsbereich, insbesondere in Bezug auf die Zusammensetzung des Katalysatormischbetts und die CO₂-Konzentration im Synthesegas. Dieses Modell ermöglicht die modellgestützte Optimierung und/oder das Reaktordesign für die direkte DME Synthese unter Berücksichtigung dieser Variablen.

Es lässt sich feststellen, dass semimechanistische Modelle aufgrund der komplexen Modellstruktur, die aus gekoppelten Gleichgewichts- und Konstitutivgleichungen (z. B. Zustandsgleichungen, kinetischen Ansätzen und thermodynamischen Zusammenhängen) besteht, eine eher begrenzte Flexibilität besitzen. Dies erschwert die Anpassung des Modells an die verfügbaren Daten und führt zu Abweichungen bei den Modellvorhersagen. Die Abweichungen des in dieser Arbeit vorgestellten Modells könnten auf Messunsicherheiten zurückgeführt werden, insbesondere bei niedrigen DME-Konzentrationen. Die fehlende Flexibilität des Modells bei der Anpassung an Messungen mit geringem Signal-Rausch-Verhältnis unterstreicht die Zuverlässigkeit der Vorhersagen und ist ein großer Vorteil, wenn nicht sogar eine Voraussetzung, für Untersuchungszwecke und Anwendungen wie eine rigorose Optimierung und ein optimales Reaktordesign.

- **Kapitel 3: Datenbasiertes Modell.** In diesem Kapitel wurde ein künstliches neuronales Netz (KNN) entwickelt, trainiert, bewertet und im Vergleich zu einem semi-mechanistischen Modell, das auf die gleichen Daten parametrisiert wurde, getestet.

Da jedes KNN streng spezifisch ist und ein theoretischer Rahmen fehlt, müssen die in Abschnitt 1.2 postulierten KNN-Designfragen “Was ist eine geeignete Aktivierungsfunktion, ein geeigneter Backpropagation-Algorithmus, eine geeignete Netzwerkarchitektur, eine geeignete Datenaufteilung und eine geeignete Trainingsstrategie?” empirisch beantwortet werden.

Für das betrachtete System konnte gezeigt werden, dass nichtlineare Aktivierungsfunktionen besser performen als (stückweise) lineare Funktionen und dass Algorithmen, die auf Jacobischer Backpropagation basieren, den Gradienten-Verfahren in Bezug auf die Genauigkeit überlegen sind, während kein relevanter Einfluss der Aktivierungsfunktion oder des Trainingsalgorithmus auf die Konvergenzzeit festgestellt werden konnte.

Darüber hinaus wurde ein automatisiertes Schema für die Datenpartitionierung, das Netztraining und die Netzauswahl vorgestellt. Mit dieser Strategie wurden insgesamt 10000 ANNs pro Architektur trainiert. Es wurden verschiedene Startparameterwerte verwendet, um lokale Optimalität zu vermeiden. Weiter wurden verschiedene Schemata der Datenpartitionierung zwischen Training und Test bewertet. Anschließend wurde das beste Netz in Bezug auf seine Performance bei einem separaten Datensatz Daten ausgewählt, um zu gewährleisten, dass das gewählte KNN dasjenige mit der besten Generalisierung ist, d. h. mit den besten Ergebnissen bei der Auswertung neuer Daten.

Das Training von 10000 KNNs war in 7,9 Minuten abgeschlossen, während die Parameterschätzung des auf die gleiche Anzahl von Datenpunkten parametrisierten formalkinetischen Modells etwa 3,5 Stunden dauerte. Dabei sollte bedacht werden, dass die Gesamtzeit für die Parametrisierung des formalkinetischen Modells wesentlich länger ist, wenn weitere, schwieriger zu quantifizierende Schritte des Prozesses berücksichtigt werden, wie z.B. die Implementierung verschiedener Modellstrukturen im Rahmen der Modelldiskriminierung, die Bestimmung geeigneter Startparameterwerte usw.

Die KNNs sind auch hinsichtlich der Genauigkeit der Vorhersagen besser als das formalkinetische Modell. So konnte beispielsweise der relative Fehler der Vorhersagen für den molaren Anteil von DME über alle Daten hinweg um ca. 54 % (von 24 % auf 11 %) reduziert werden. Die verbleibende Vorhersageabweichung wird auf die erwähnten Messunsicherheiten zurückgeführt und auf die Tatsache, dass das KNN erfolgreich darauf trainiert werden konnte, die Input-Output-Beziehungen in

den Daten zu erkennen, anstatt lediglich die bereitgestellten Daten zu speichern und wiederzugeben.

Diese Ergebnisse verdeutlichen die Eignung von KNN als prädiktives Werkzeug für Brownfield-Anwendungen wie Soft-Sensoring, Echtzeit-Optimierung, Online-Kontrolle, vorausschauende Wartung und andere Anwendungen, bei denen Modelle mit hoher Flexibilität und Anpassungsfähigkeit, der Fähigkeit zur Abbildung komplexer nichtlinearer Beziehungen sowie schneller Konvergenz und geringen Rechenaufwand erforderlich sind.

Ferner wurde die Interpolationsfähigkeit des Netzes getestet. Es wurde bestätigt, dass das gewählte KNN ein zuverlässiger Prädiktor in diesem Betriebsfenster ist, trotz des relativ kleinen Datensatzes bestehend aus 180 Versuchspunkten. Dies beantwortet die Frage, ob relativ kleine Datensätze ausreichen, um die Datenanforderungen eines einfachen ANN zu erfüllen und zeigt die bemerkenswerte Leistungsfähigkeit datenbasierter Modelle im Gegensatz zu mechanistischen Ansätzen in Bezug auf Rechenaufwand und Genauigkeit innerhalb eines untersuchten Betriebsfensters.

Zur Beurteilung der Extrapolationsfähigkeit des Modells und zur Beantwortung der Frage, inwieweit das datenbasierte Modell überhaupt extrapoliert werden kann, wurden Simulationen über den Gültigkeitsbereich hinaus durchgeführt. Das KNN lieferte unter diesen Bedingungen unerwartete Vorhersagen. Allgemein ist anerkannt, dass datenbasierte Modelle bei Extrapolation nicht zuverlässig sind. Jedoch hat die in dieser Arbeit durchgeführte Analyse gezeigt, dass eine Extrapolation des KNN in dem Bereich, in dem die vom unterliegenden Modell erfassten Phänomene vorherrschen, wohl möglich ist, selbst wenn diese Bedingungen außerhalb des Gültigkeitsbereichs des Modells liegen. Dennoch wurden unter Bedingungen, bei denen andere, für das KNN unbekannte Phänomene auftreten, die erwarteten Abweichungen beobachtet. Dies weist auf die Notwendigkeit einer neuen Definition von "Gültigkeitsbereich" hin, wenn datengestützte Ansätze eingesetzt werden. Des Weiteren können nur die in den experimentellen Untersuchungen variierten Parameter in die Modellstruktur des KNN einbezogen werden, was die Eignung des Modells für explorative Zwecke in noch nicht experimentell untersuchten Betriebsfenstern ausschließt.

- **Kapitel 4: Hybrid Model.** Der erste Teil dieses Kapitels gibt einen Überblick über die für die direkte DME-Synthese verfügbaren Modelle. Die meisten der in der Literatur verfügbaren Modelle für die direkte DME-Synthese sind semi-mechanistisch, wohingegen nur einige wenige Arbeiten datenbasierte Modelle verwenden. Ein hybrides Modell für das betrachtete System konnte nicht gefunden

werden. Der zweite Teil dieses Kapitels befasst sich mit der Implementierung eines solchen Modells für die direkte DME-Synthese und enthält einen umfassenden Vergleich der drei in dieser Arbeit behandelten Modelltypen.

Da es unzählige mögliche hybride Modellstrukturen gibt, wurde in einem ersten Schritt definiert, welche Struktur dazu geeignet ist, vorhandenes Systemwissen mit datenbasierten Ansätzen zu integrieren, um bestehende Wissenslücken zu schließen. Das postulierte Modell besteht aus Bilanzgleichungen des Rohrreaktors, in dem die für die Modellentwicklung verwendeten experimentellen Daten ermittelt wurden. Diese Gleichungen beruhen auf thermodynamischen Gesetzen und führen daher bekannte Effekte in das Modell ein. Die unbekannte Größe bei der Modellierung der DME-Synthese, die Reaktionskinetik, wird hingegen durch ein ANN beschrieben, das darauf trainiert ist, die Reaktionsgeschwindigkeit ohne mechanistische Festlegungen vorherzusagen.

Zur Beantwortung der Frage "Welche Vorteile hat ein Hybridmodell gegenüber herkömmlichen semi-mechanistischen und/oder datenbasierten Modellen in Bezug auf den Rechenaufwand, die Extrapolationsfähigkeit und andere kritische Eigenschaften von prädiktiven Modellen?" wurden die Eigenschaften des hybriden Modells anhand von Experimenten und Simulationen mit einem semi-mechanistischen und einem datenbasierten Modell verglichen. Für alle Modelle wurde der gleiche Gültigkeitsbereich gewählt, was eine Bewertung der strukturellen Unterschiede zwischen den Modellen insbesondere hinsichtlich der Extrapolation ermöglicht. Um die Vergleichbarkeit dieser Modelle zu gewährleisten, entsprechen die Eigenschaften des KNN des Hybridmodells denen des datenbasierten Modells.

Das entwickelte hybride Modell konnte sehr schnell trainiert werden und wies eine hohe Genauigkeit sowie kurze Simulationszeiten auf, insbesondere im Vergleich zum semi-mechanistischen Modell (z. B. 30-mal schnellere Parameterschätzung und 4-mal schnellere Simulationen).

Ferner wurde die Interpolationsfähigkeit getestet und es wurden die erwarteten präzisen und stetigen Modellvorhersagen beobachtet. Diese Ergebnisse stimmen weitgehend mit Studien in der Literatur überein, in denen die hybride Modellierung bei vergleichbaren Systemen angewendet wurde.

Besonderes Interesse galt der Extrapolationsfähigkeit des hybriden Modells als einem der kritischen Merkmale von datenbasierten und hybriden Modellierungsansätzen. Anhand von Beispielvariablen wurde gezeigt, dass die Extrapolation in der Dimension, d. h. die Extrapolation einer Variablen, die während der Modellentwicklung konstant gehalten wurde, nicht möglich war, wenn diese Variable das datenbasierte Modul (KNN) des Hybridmodells direkt beeinflusst. Im Gegensatz dazu wurde in einem weiten Bereich eine gute Extrapolationsfähigkeit erreicht, wenn die ex-

trapolierte Variable in den Bilanzgleichungen, d. h. im Wissensmodul des Hybridmodells, enthalten war und eine geeignete Netzwerkarchitektur gewählt wurde. Die Extrapolation des Gültigkeitsbereichs, d. h. die Bewertung einer Variablen außerhalb des Bereichs, in dem sie während der Modellentwicklung untersucht wurde, war möglich, allerdings lediglich in einem begrenzten Bereich.

Es lässt sich daraus schließen, dass die Phänomene, die die zugrunde liegenden Modelle abbilden können, der entscheidende Faktor für die Grenze der Extrapolation sind und nicht allein der Bereich, der während der Modellentwicklung experimentell untersucht wurde. Darüber hinaus hängen diese Phänomene stark von der mathematischen Struktur des Netzes (Architektur und Parameter) ab sowie davon ob die zum Training verwendeten Daten die entsprechenden Effekte widerspiegeln.

Wie aus dem Literaturüberblick hervorgeht, wurde die direkte DME-Synthese in den letzten Jahrzehnten in der Literatur intensiv untersucht, was zu zahlreichen formalkinetischen Modellen führte, die jeweils nur für einen begrenzten Bereich von Bedingungen gültig sind. In nachfolgenden Studien könnte die Möglichkeit untersucht werden, diese Modelle analog zu dem in diesem Kapitel angewandten Vorgehen zu verwenden, um den Anwendungsbereich des Hybridmodells zu erweitern. Durch synthetische Datengenerierung können so reaktionskinetische Daten in dem Betriebsfenster erzeugt werden, in dem die jeweiligen Modelle validiert wurden, und anschließend zum Training der ANN des hier postulierten Hybridmodells verwendet werden. Aufgrund seiner hohen Flexibilität ist das hybride Modell in der Lage, das von diesen Modellen erfasste Wissen zu integrieren, wodurch es in einem übergreifenden Bereich Gültigkeit erlangt. Obwohl der eigentliche Reaktionsmechanismus bei diesem Ansatz unklar bliebe, kann aufgrund der Ergebnisse dieser Arbeit davon ausgegangen werden, dass ein solches Modell eine Bewertung der zahlreichen in den einzelnen Studien untersuchten Prozessvariablen (z. B. verschiedene Katalysatoren, Reaktortypen und -geometrien sowie Reaktionsbedingungen) ermöglichen würde. Die Untersuchung und Auslegung neuartiger Reaktor- oder Verfahrenskonzepte für dieses System könnte daher unter Berücksichtigung eines breiten Spektrums von Verfahrensparametern und -bereichen durchgeführt werden. Eine Herausforderung bei dieser Aufgabe ist die große Heterogenität der Informationen in den verschiedenen Studien. Beispielsweise geben einige Autoren für die kohlenstoffhaltigen Verbindungen den Gehalt an CO, CO₂, CO_x (CO + CO₂) und/oder das Verhältnis von CO₂ zu CO_x an. In ähnlicher Weise werden der H₂-Anteil und/oder das H₂/CO- bzw. das H₂/CO₂-Verhältnis angegeben, um den Wasserstoffgehalt im Feedgas zu beschreiben. Außerdem sind die veröffentlichten Daten in vielen Fällen unvollständig, was die Implementierung und Validierung von Modellen erschwert.

Im gegenwärtigen Entwicklungsstadium bestehen die Hauptvorteile der in dieser Arbeit vorgestellten datenbasierten und hybriden Modelle in der geringen Rechenleistung und der bemerkenswerten Genauigkeit und Flexibilität bei der Anpassung an heterogene und multidimensionale Daten. Ein entscheidender Nachteil ist im Gegenzug das Fehlen eines theoretischen Rahmens für die Netzauswahl, wenn zusätzliche Kriterien wie die Extrapolationsfähigkeit berücksichtigt werden müssen. Diese Eigenschaften unterstreichen das Potenzial dieser Ansätze für “Brownfield”-Anwendungen, bei denen ein bestehender Prozess optimiert, gesteuert oder überwacht werden soll. Die Verwendung für “Greenfield”-Ansätze oder explorative Anwendungen ist hingegen nur beschränkt möglich. Im zweiten Fall sind zuverlässige Vorhersagen unter extrapolierten Bedingungen erforderlich, die mit datenbasierten oder hybriden Modellen nicht gewährleistet werden können. Zu diesem Zweck sind (semi-)mechanistische Ansätze nach wie vor die geeignetere Wahl.

BIBLIOGRAPHY

- [1] Nirvana Delgado Otalvaro, Markus Kaiser, Karla Herrera Delgado, Stefan Wild, Jörg Sauer, and Hannsjörg Freund. Optimization of the direct synthesis of dimethyl ether from CO₂ rich synthesis gas: closing the loop between experimental investigations and model-based reactor design. *Reaction Chemistry & Engineering*, 5: 949–960, 2020. doi: 10.1039/D0RE00041H. URL <http://dx.doi.org/10.1039/D0RE00041H>.
- [2] Nirvana Delgado Otalvaro, Gerardo Sogne, Karla Herrera Delgado, Stefan Wild, Stephan Pitter, and Jörg Sauer. Kinetics of the direct DME synthesis from CO₂ rich syngas under variation of the CZA-to- γ -Al₂O₃ ratio of a mixed catalyst bed. *RSC Advances*, 11(40):24556–24569, 2021. ISSN 2046-2069. doi: 10.1039/D1RA03452A. URL <http://xlink.rsc.org/?DOI=D1RA03452A>.
- [3] Nirvana Delgado Otalvaro, Pembe Gül Bilir, Karla Herrera Delgado, Stephan Pitter, and Jörg Sauer. Modeling the direct synthesis of dimethyl ether using artificial neural networks. *Chemie Ingenieur Technik*, 93:754–761, 2021. URL <https://doi.org/10.1002/cite.202000226>.
- [4] Nirvana Delgado Otalvaro, Pembe Gül Bilir, Karla Herrera Delgado, Stephan Pitter, and Jörg Sauer. Kinetics of the direct dme synthesis: State of the art and comprehensive comparison of semi-mechanistic, data-based and hybrid modeling approaches. *Catalysts*, 12(3), 2022. ISSN 2073-4344. doi: 10.3390/catal12030347. URL <https://www.mdpi.com/2073-4344/12/3/347>.
- [5] Takashi Ogawa, Norio Inoue, Tutomu Shikada, and Yotaro Ohno. Direct dimethyl ether synthesis. *Journal of natural gas chemistry*, 12(4):219–227, 2003. URL <http://citeseerx.ist.psu.edu/viewdoc/download?doi=10.1.1.585.7743&rep=rep1&type=pdf>.
- [6] Ujjal Mondal and Ganapati D Yadav. Perspective of dimethyl ether as fuel: Part i. catalysis. *Journal of CO₂ Utilization*, 32:299–320, 2019. URL <https://doi.org/10.1016/j.jcou.2019.02.003>.
- [7] Japan DME Forum. *DME Handbook*, volume 1. Japan DME Forum, Tokyo, 2007. ISBN 978-4-9903839-0-9 C3050.
- [8] Virum Bodil Voss. Acetic acid reactive distillation process based on DME/methanol carbonylation, 2001. URL <https://patents.google.com/patent/US6175039B1/en>. US Patent 6,175,039.
- [9] Shurong Wang, Wenwen Guo, Lingjun Zhu, Haixia Wang, Kunzan Qiu, and Kefa Cen. Methyl Acetate Synthesis from Dimethyl Ether Carbonylation over Mordenite Modified by Cation Exchange. *The Journal of Physical Chemistry C*, 119(1):524–

- 533, jan 2015. ISSN 1932-7447. doi: 10.1021/jp511543x. URL <https://pubs.acs.org/doi/10.1021/jp511543x>.
- [10] Qingde Zhang, Yisheng Tan, Caihong Yang, Hongjuan Xie, and Yizhuo Han. Characterization and catalytic application of MnCl₂ modified HZSM-5 zeolites in synthesis of aromatics from syngas via dimethyl ether. *Journal of Industrial and Engineering Chemistry*, 19(3):975–980, may 2013. ISSN 1226086X. doi: 10.1016/j.jiec.2012.11.019. URL <https://linkinghub.elsevier.com/retrieve/pii/S1226086X12003875>.
- [11] Sahriah Basri and Siti Kartom Kamarudin. Chapter 8 - direct dimethyl ether fuel cells (ddmefcs). In Ramiz Gültekin Akay and Ayşe Bayrakçeken Yurtcan, editors, *Direct Liquid Fuel Cells*, pages 177–189. Academic Press, 2021. ISBN 978-0-12-818624-4. doi: <https://doi.org/10.1016/B978-0-12-818624-4.00008-X>. URL <https://www.sciencedirect.com/science/article/pii/B978012818624400008X>.
- [12] T.H. Fleisch, A. Basu, M.J. Gradassi, and J.G. Masin. Dimethyl ether: A fuel for the 21st century. *Studies in Surface Science and Catalysis*, 107:117–125, 1997. doi: 10.1016/S0167-2991(97)80323-0. URL <https://linkinghub.elsevier.com/retrieve/pii/S0167299197803230>.
- [13] Constantine Arcoumanis, Choongsik Bae, Roy Crookes, and Eiji Kinoshita. The potential of di-methyl ether (DME) as an alternative fuel for compression-ignition engines: A review. *Fuel*, 87(7):1014–1030, jun 2008. ISSN 00162361. doi: 10.1016/j.fuel.2007.06.007. URL <https://linkinghub.elsevier.com/retrieve/pii/S0016236107002955>.
- [14] Paul Nieuwenhuis and Peter Wells. 6 - powertrain and fuel. In Paul Nieuwenhuis and Peter Wells, editors, *The Automotive Industry and the Environment*, pages 73–86. Woodhead Publishing, 2003. ISBN 978-1-85573-713-6. doi: <https://doi.org/10.1016/B978-1-85573-713-6.50009-3>. URL <https://www.sciencedirect.com/science/article/pii/B9781855737136500093>.
- [15] Enrico Catizzone, Giuseppe Bonura, Massimo Migliori, Francesco Frusteri, and Girolamo Giordano. CO₂ Recycling to Dimethyl Ether: State-of-the-Art and Perspectives. *Molecules*, 23(1):31, dec 2017. ISSN 1420-3049. doi: 10.3390/molecules23010031. URL <http://www.mdpi.com/1420-3049/23/1/31>.
- [16] Martin Bertau, Heribert Offermanns, Ludolf Plass, Friedrich Schmidt, and Hans-Jürgen Wernicke. *Methanol: the basic chemical and energy feedstock of the future*. Springer, 2014.
- [17] Kaoru Takeishi. Dimethyl ether and catalyst development for production from syngas. *Biofuels*, 1(1):217–226, jan 2010. ISSN 1759-7269. doi: 10.4155/bfs.09.16. URL <https://www.tandfonline.com/doi/full/10.4155/bfs.09.16>.
- [18] Francesco Dalena, Alessandro Senatore, Alessia Marino, Amalia Gordano, Marco Basile, and Angelo Basile. Methanol Production and Applica-

- tions: An Overview. In *Methanol*, pages 3–28. Elsevier, 2018. doi: 10.1016/B978-0-444-63903-5.00001-7. URL <https://linkinghub.elsevier.com/retrieve/pii/B9780444639035000017>.
- [19] Cristina Peinado, Dalia Liuzzi, Rosa María Ladera-Gallardo, María Retuerto, Manuel Ojeda, Miguel A. Peña, and Sergio Rojas. Effects of support and reaction pressure for the synthesis of dimethyl ether over heteropolyacid catalysts. *Scientific Reports*, 10(1):8551, dec 2020. ISSN 2045-2322. doi: 10.1038/s41598-020-65296-3. URL <http://www.nature.com/articles/s41598-020-65296-3>.
- [20] Manfred Müller and Ute Hübsch. Dimethyl Ether. In *Ullmann’s Encyclopedia of Industrial Chemistry*, pages 305–308. Wiley-VCH Verlag GmbH & Co. KGaA, Weinheim, Germany, jun 2000. doi: 10.1002/14356007.a08_541. URL http://doi.wiley.com/10.1002/14356007.a08_541.
- [21] Zoha Azizi, Mohsen Rezaeimanesh, Tahere Tohidian, and Mohammad Reza Rahimpour. Dimethyl ether: A review of technologies and production challenges. *Chemical Engineering and Processing: Process Intensification*, 82:150–172, 2014. ISSN 02552701. doi: 10.1016/j.cep.2014.06.007. URL <http://dx.doi.org/10.1016/j.cep.2014.06.007>.
- [22] Miriam Stiefel, Ruaa Ahmad, Ulrich Arnold, and Manfred Döring. Direct synthesis of dimethyl ether from carbon-monoxide-rich synthesis gas: Influence of dehydration catalysts and operating conditions. *Fuel Processing Technology*, 92:1466–1474, aug 2011. ISSN 03783820. doi: 10.1016/j.fuproc.2011.03.007. URL <https://doi.org/10.1016/j.fuproc.2011.03.007>.
- [23] Wei-Hsin Chen, Chih-Liang Hsu, and Xiao-Dong Wang. Thermodynamic approach and comparison of two-step and single step DME (dimethyl ether) syntheses with carbon dioxide utilization. *Energy*, 109:326–340, aug 2016. ISSN 03605442. doi: 10.1016/j.energy.2016.04.097. URL <https://linkinghub.elsevier.com/retrieve/pii/S0360544216305102>.
- [24] N. Dahmen, U. Arnold, N. Djordjevic, T. Henrich, T. Kolb, H. Leibold, and J. Sauer. High pressure in synthetic fuels production. *Journal of Supercritical Fluids*, 96:124–132, jan 2015. ISSN 08968446. doi: 10.1016/j.supflu.2014.09.031. URL <http://dx.doi.org/10.1016/j.supflu.2014.09.03>.
- [25] Joint news release: BASF and lutianhua plan to pilot a new production process that significantly reduces CO₂ emissions. <https://www.basf.com/global/en/media/news-releases/2019/06/p-19-249.html>, 2019. Last visited on 01.04.2021.
- [26] Zhiqi Wang, Tao He, Jianqing Li, Jingli Wu, Jianguang Qin, Guangbo Liu, Dezhi Han, Zhongyue Zi, Zhuo Li, and Jinhua Wu. Design and operation of a pilot plant for biomass to liquid fuels by integrating gasification, DME synthesis and DME to gasoline. *Fuel*, 186:587–596, dec 2016. ISSN 00162361. doi: 10.1016/j.fuel.2016.08.108. URL <https://linkinghub.elsevier.com/retrieve/pii/S0016236116308560>.

- [27] Vincent Dieterich, Alexander Buttler, Andreas Hanel, Hartmut Spliethoff, and Sebastian Fendt. Power-to-liquid via synthesis of methanol, DME or Fischer–Tropsch-fuels: a review. *Energy & Environmental Science*, 13(10):3207–3252, 2020. ISSN 1754-5692. doi: 10.1039/D0EE01187H. URL <http://xlink.rsc.org/?DOI=DOEE01187H>.
- [28] Moritz von Stosch, Rui Oliveira, Joana Peres, and Sebastião Feyo de Azevedo. Hybrid semi-parametric modeling in process systems engineering: Past, present and future. *Computers & Chemical Engineering*, 60:86–101, jan 2014. ISSN 00981354. doi: 10.1016/j.compchemeng.2013.08.008. URL <https://linkinghub.elsevier.com/retrieve/pii/S0098135413002639>.
- [29] Chirag Mevawala, Yuan Jiang, and Debangsu Bhattacharyya. Techno-economic optimization of shale gas to dimethyl ether production processes via direct and indirect synthesis routes. *Applied Energy*, 238:119–134, mar 2019. ISSN 03062619. doi: 10.1016/j.apenergy.2019.01.044. URL <https://linkinghub.elsevier.com/retrieve/pii/S0306261919300455>.
- [30] Raquel Peláez, Pablo Marín, Fernando V. Díez, and Salvador Ordóñez. Direct synthesis of dimethyl ether in multi-tubular fixed-bed reactors: 2D multi-scale modelling and optimum design. *Fuel Processing Technology*, 174:149–157, 2018. ISSN 03783820. doi: 10.1016/j.fuproc.2018.02.025. URL <https://doi.org/10.1016/j.fuproc.2018.02.025>.
- [31] Jongmin Park, Hyo Seok Kim, Won Bo Lee, and Myung-June Park. Trends and Outlook of Computational Chemistry and Microkinetic Modeling for Catalytic Synthesis of Methanol and DME. *Catalysts*, 10(6):655, jun 2020. ISSN 2073-4344. doi: 10.3390/catal10060655. URL <https://www.mdpi.com/2073-4344/10/6/655>.
- [32] Raquel Peláez, Pablo Marín, and Salvador Ordóñez. Direct synthesis of dimethyl ether from syngas over mechanical mixtures of CuO/ZnO/Al₂O₃ and Γ -Al₂O₃ : Process optimization and kinetic modelling. *Fuel Processing Technology*, 168:40–49, 2017. ISSN 03783820. doi: 10.1016/j.fuproc.2017.09.004. URL <http://dx.doi.org/10.1016/j.fuproc.2017.09.004>.
- [33] Javier Ereña, Irene Sierra, Andrés T. Aguayo, Ainara Ateka, Martin Olazar, and Javier Bilbao. Kinetic modelling of dimethyl ether synthesis from (H₂ +CO₂) by considering catalyst deactivation. *Chemical Engineering Journal*, 174:660–667, 2011. doi: 10.1016/j.cej.2011.09.067. URL <https://doi.org/10.1016/j.cej.2011.09.067>.
- [34] Chengyuan Cheng, Haitao Zhang, Weiyong Ying, and Dingye Fang. Intrinsic kinetics of one-step dimethyl ether synthesis from hydrogen-rich synthesis gas over bi-functional catalyst. *Korean Journal of Chemical Engineering*, 28(7):1511–1517, 2011. ISSN 02561115. doi: 10.1007/s11814-011-0018-4. URL <https://doi.org/10.1007/s11814-011-0018-4>.

- [35] Irene Sierra, Javier Ereña, Andrés T. Aguayo, Martin Olazar, and Javier Bilbao. Deactivation kinetics for direct dimethyl ether synthesis on a CuO-ZnO-Al₂O₃ / γ -Al₂O₃ Catalyst. *Industrial and Engineering Chemistry Research*, 49(2):481–489, 2010. ISSN 08885885. doi: 10.1021/ie900978a. URL <https://doi.org/10.1021/ie900978a>.
- [36] Yu. I. Pyatnitskii, P. E. Strizhak, and N. K. Lunev. Kinetic modeling for the conversion of synthesis gas to dimethyl ether on a mixed Cu-ZnO-Al₂O₃ catalyst with γ -Al₂O₃. *Theoretical and Experimental Chemistry*, 45(5):325–330, sep 2009. ISSN 0040-5760. doi: 10.1007/s11237-009-9101-x.
- [37] Christian Peter Renk. *Die einstufige Dimethylether-Synthese aus Synthesegas*. PhD thesis, Forschungszentrum Karlsruhe GmbH, 2009. URL <https://books.google.de/books?id=xNTxSAAACAAJ>.
- [38] Ali Hadipour and Morteza Sohrabi. Synthesis of some bifunctional catalysts and determination of kinetic parameters for direct conversion of syngas to dimethyl ether. *Chemical Engineering Journal*, 137:294–301, 2008. ISSN 13858947. doi: 10.1016/j.cej.2007.04.039. URL <https://doi.org/10.1016/j.cej.2007.04.039>.
- [39] Andrés T. Aguayo, Javier Ereña, Diana Mier, José M. Arandes, Martin Olazar, and Javier Bilbao. Kinetic Modeling of Dimethyl Ether Synthesis in a Single Step on a CuO-ZnO-Al₂O₃ Al₂O₃ Catalyst. *Industrial & Engineering Chemistry Research*, 46:5522–5530, 2007. ISSN 0888-5885. doi: 10.1021/ie070269s. URL <https://pubs.acs.org/doi/10.1021/ie070269s>.
- [40] Zhaoguang Nie, Hongwei Liu, Dianhua Liu, Weiyong Ying, and Dingye Fang. Intrinsic Kinetics of Dimethyl Ether Synthesis from Syngas. *Journal of Natural Gas Chemistry*, 14(1):22–28, 2005. URL <http://citeseerx.ist.psu.edu/viewdoc/download?doi=10.1.1.524.7031&rep=rep1&type=pdf>.
- [41] K.L. Ng, D. Chadwick, and B.A. Toseland. Kinetics and modelling of dimethyl ether synthesis from synthesis gas. *Chemical Engineering Science*, 54(15-16):3587–3592, jul 1999. ISSN 00092509. doi: 10.1016/S0009-2509(98)00514-4. URL <https://linkinghub.elsevier.com/retrieve/pii/S0009250998005144>.
- [42] J. D. Grunwaldt, A. M. Molenbroek, N. Y. Topsøe, H. Topsøe, and B. S. Clausen. In situ investigations of structural changes in Cu/ZnO catalysts. *Journal of Catalysis*, 194(2):452–460, sep 2000. ISSN 00219517. doi: 10.1006/jcat.2000.2930. URL <https://doi.org/10.1006/jcat.2000.2930>.
- [43] Rohit Gaikwad, Helena Reymond, Nat Phongprueksathat, Philipp Rudolf von Rohr, and Atsushi Urakawa. From CO or CO₂?: space-resolved insights into high-pressure CO₂ hydrogenation to methanol over Cu/ZnO/Al₂O₃. *Catalysis Science & Technology*, 10(9):2763–2768, 2020. ISSN 2044-4753. doi: 10.1039/D0CY00050G. URL <http://xlink.rsc.org/?DOI=D0CY00050G>.

- [44] Oliver Martin, Cecilia Mondelli, Antonio Cervellino, Davide Ferri, Daniel Curulla-Ferré, and Javier Pérez-Ramírez. Operando Synchrotron X-ray Powder Diffraction and Modulated-Excitation Infrared Spectroscopy Elucidate the CO₂ Promotion on a Commercial Methanol Synthesis Catalyst. *Angewandte Chemie International Edition*, 55(37):11031–11036, sep 2016. ISSN 14337851. doi: 10.1002/anie.201603204. URL <http://doi.wiley.com/10.1002/anie.201603204>.
- [45] Kai F. Kalz, Ralph Kraehnert, Muslim Dvoyashkin, Roland Dittmeyer, Roger Gläser, Ulrike Krewer, Karsten Reuter, and Jan-Dierk Grunwaldt. Future Challenges in Heterogeneous Catalysis: Understanding Catalysts under Dynamic Reaction Conditions. *ChemCatChem*, 9(1):17–29, jan 2017. ISSN 18673880. doi: 10.1002/cctc.201600996. URL <http://doi.wiley.com/10.1002/cctc.201600996>.
- [46] Sunil Kr Jha, Jasmin Bilalovic, Anju Jha, Nilesh Patel, and Han Zhang. Renewable energy: Present research and future scope of Artificial Intelligence. *Renewable and Sustainable Energy Reviews*, 77:297–317, 2017. ISSN 18790690. doi: 10.1016/j.rser.2017.04.018. URL <http://dx.doi.org/10.1016/j.rser.2017.04.018>.
- [47] Hao Li, Zhien Zhang, and Zhijian Liu. Application of Artificial Neural Networks for Catalysis: A Review. *Catalysts*, 7(10):306, oct 2017. ISSN 2073-4344. doi: 10.3390/catal7100306. URL <http://www.mdpi.com/2073-4344/7/10/306>.
- [48] Vinicius Goncalves, Kathia Maria, and Alberico Borges Ferreira da Silv. Applications of Artificial Neural Networks in Chemical Problems. In Kenji Suzuki, editor, *Artificial Neural Networks - Architectures and Applications*, chapter 10, pages 203–223. InTech, jan 2013. ISBN 9781634859790. doi: 10.5772/51275. URL <https://www.intechopen.com/books/artificial-neural-networks-architectures-and-applications/applications-of-artificial-neural-networks-in-chemical-problems>.
- [49] Felix Strieth-Kalthoff, Frederik Sandfort, Marwin H. S. Segler, and Frank Glorius. Machine learning the ropes: principles, applications and directions in synthetic chemistry. *Chemical Society Reviews*, 49(17):6154–6168, 2020. ISSN 0306-0012. doi: 10.1039/C9CS00786E. URL <http://xlink.rsc.org/?DOI=C9CS00786E>.
- [50] Jarinah Mohd Ali, M. A. Hussain, Moses O. Tade, and Jie Zhang. Artificial Intelligence techniques applied as estimator in chemical process systems - A literature survey. *Expert Systems with Applications*, 42:5915–5931, 2015. ISSN 09574174. doi: 10.1016/j.eswa.2015.03.023. URL <http://dx.doi.org/10.1016/j.eswa.2015.03.023>.
- [51] Michael Negnevitsky. *Artificial intelligence: a guide to intelligent systems*. Pearson education, 2005.
- [52] I.A. Basheer and M. Hajmeer. Artificial neural networks: fundamentals, computing, design, and application. *Journal of microbiological methods*, 43(1):3–31, dec 2000. ISSN 0167-7012. doi: 10.1016/S0167-7012(00)00201-3. URL <https://www.sciencedirect.com/science/article/pii/S0167701200002013>.

- [53] Libei Chen, Yves Hontoir, Dexian Huang, Jie Zhang, and A. Julian Morris. Combining first principles with black-box techniques for reaction systems. *Control Engineering Practice*, 12(7):819–826, jul 2004. ISSN 09670661. doi: 10.1016/j.conengprac.2003.09.006. URL <https://linkinghub.elsevier.com/retrieve/pii/S0967066103002119>.
- [54] Sohrab Zendehboudi, Nima Rezaei, and Ali Lohi. Applications of hybrid models in chemical, petroleum, and energy systems: A systematic review. *Applied Energy*, 228:2539–2566, 2018. ISSN 03062619. doi: 10.1016/j.apenergy.2018.06.051. URL <https://doi.org/10.1016/j.apenergy.2018.06.051>.
- [55] Kevin McBride and Kai Sundmacher. Overview of Surrogate Modeling in Chemical Process Engineering. *Chemie Ingenieur Technik*, 91(3):228–239, mar 2019. ISSN 0009286X. doi: 10.1002/cite.201800091. URL <https://onlinelibrary.wiley.com/doi/10.1002/cite.201800091>.
- [56] G. Zahedi, A. Elkamel, A. Lohi, A. Jahanmiri, and M. R. Rahimpour. Hybrid artificial neural network - First principle model formulation for the unsteady state simulation and analysis of a packed bed reactor for CO₂ hydrogenation to methanol. *Chemical Engineering Journal*, 115:113–120, 2005. ISSN 13858947. doi: 10.1016/j.cej.2005.08.018. URL <https://doi.org/10.1016/j.cej.2005.08.018>.
- [57] Primož Potočnik, Igor Grabec, Marko Šetinc, and Janez Levec. Neural net based hybrid modeling of the methanol synthesis process. *Neural Processing Letters*, 11(3):219–228, 2000. ISSN 13704621. doi: 10.1023/A:1009615710515. URL <https://doi.org/10.1023/A:1009615710515>.
- [58] Marjan Alavi, Hooshang Jazayeri-Rad, and Reza Mosayebi Behbahani. Optimizing the Feed Conditions in a Dimethyl Ether Production Process To Maximize Methanol Conversion Using a Hybrid First Principle Neural Network Approach. *Chemical Engineering Communications*, 201(5):650–673, 2014. ISSN 00986445. doi: 10.1080/00986445.2013.782294. URL <https://doi.org/10.1080/00986445.2013.782294>.
- [59] Joel Sansana, Mark N. Joswiak, Ivan Castillo, Zhenyu Wang, Ricardo Rendall, Leo H. Chiang, and Marco S. Reis. Recent trends on hybrid modeling for Industry 4.0. *Computers & Chemical Engineering*, 151:107365, aug 2021. ISSN 00981354. doi: 10.1016/j.compchemeng.2021.107365. URL <https://linkinghub.elsevier.com/retrieve/pii/S0098135421001435>.
- [60] Jason E. Hein. Machine learning made easy for optimizing chemical reactions. *Nature*, 590(7844):40–41, feb 2021. ISSN 0028-0836. doi: 10.1038/d41586-021-00209-6. URL <http://www.nature.com/articles/d41586-021-00209-6>.
- [61] Nicolaus Dahmen, Johannes Abeln, Mark Eberhard, Thomas Kolb, Hans Leibold, Jörg Sauer, Dieter Stapf, and Bernd Zimmerlin. The bioliq process for producing synthetic transportation fuels. *Wiley Interdisciplinary Reviews: Energy and En-*

- vironment*, 6(3):e236, may 2017. ISSN 20418396. doi: 10.1002/wene.236. URL <http://doi.wiley.com/10.1002/wene.236>.
- [62] Benjamin Niethammer, Simon Wodarz, Matthias Betz, Philipp Haltenort, Dorian Oestreich, Kathrin Hackbarth, Ulrich Arnold, Thomas Otto, and Jörg Sauer. Alternative Liquid Fuels from Renewable Resources. *Chemie Ingenieur Technik*, 90(1-2):99–112, jan 2018. ISSN 0009286X. doi: 10.1002/cite.201700117. URL <http://doi.wiley.com/10.1002/cite.201700117>.
- [63] Troy A. Semelsberger, Rodney L. Borup, and Howard L. Greene. Dimethyl ether (DME) as an alternative fuel. *Journal of Power Sources*, 156:497–511, 2006. ISSN 03787753. doi: 10.1016/j.jpowsour.2005.05.082. URL <https://doi.org/10.1016/j.jpowsour.2005.05.082>.
- [64] Hyun Gu Roh and Chang Sik Lee. Fuel Properties and Emission Characteristics of Dimethyl Ether in a Diesel Engine. In *Locomotives and Rail Road Transportation*, pages 113–128. Springer Singapore, Singapore, 2017. doi: 10.1007/978-981-10-3788-7_6. URL http://link.springer.com/10.1007/978-981-10-3788-7_6.
- [65] Koray Alper, Kubilay Tekin, Selhan Karagöz, and Arthur J. Ragauskas. Sustainable energy and fuels from biomass: a review focusing on hydrothermal biomass processing. *Sustainable Energy & Fuels*, 4(9):4390–4414, 2020. ISSN 2398-4902. doi: 10.1039/D0SE00784F. URL <http://xlink.rsc.org/?DOI=D0SE00784F>.
- [66] Liang Liu, Zenan Lin, Shanya Lin, Yeyun Chen, Lina Zhang, Shaopeng Chen, Xianhua Zhang, Jingdong Lin, Zhaoxia Zhang, Shaolong Wan, and Yong Wang. Conversion of syngas to methanol and DME on highly selective Pd/ZnAl₂O₄ catalyst. *Journal of Energy Chemistry*, 58:564–572, jul 2021. ISSN 20954956. doi: 10.1016/j.jechem.2020.10.003. URL <https://linkinghub.elsevier.com/retrieve/pii/S2095495620306938>.
- [67] Ruaa Ahmad, David Schrempp, Silke Behrens, Jörg Sauer, Manfred Döring, and Ulrich Arnold. Zeolite-based bifunctional catalysts for the single step synthesis of dimethyl ether from CO-rich synthesis gas. *Fuel Processing Technology*, 121: 38–46, may 2014. doi: 10.1016/j.fuproc.2014.01.006. URL <https://linkinghub.elsevier.com/retrieve/pii/S0378382014000095>.
- [68] Sabrina Polierer, David Guse, Stefan Wild, Karla Herrera Delgado, Thomas N Otto, Thomas A Zevaco, Matthias Kind, Jörg Sauer, Felix Studt, and Stephan Pitter. Enhanced Direct Dimethyl Ether Synthesis from CO₂-Rich Syngas with Cu/ZnO/ZrO₂ Catalysts Prepared by Continuous Co-Precipitation. *Catalysts*, 10(8):816, jul 2020. ISSN 2073-4344. doi: 10.3390/catal10080816. URL <https://www.mdpi.com/2073-4344/10/8/816>.
- [69] Ainara Ateka, Paula Pérez-Urriarte, Mónica Gamero, Javier Ereña, Andrés T. Aguayo, and Javier Bilbao. A comparative thermodynamic study on the CO₂ conversion in the synthesis of methanol and of DME. *Energy*, 120:796–804, 2017.

ISSN 03605442. doi: 10.1016/j.energy.2016.11.129. URL <https://doi.org/10.1016/j.energy.2016.11.129>.

- [70] Sajo P. Naik, Taegong Ryu, Vy Bui, Jan D. Miller, Nicholas B. Drinnan, and Wlodzimierz Zmierczak. Synthesis of DME from CO₂/H₂ gas mixture. *Chemical Engineering Journal*, 167(1):362–368, feb 2011. ISSN 13858947. doi: 10.1016/j.cej.2010.12.087. URL <https://linkinghub.elsevier.com/retrieve/pii/S1385894711000246>.
- [71] Stefan Wild, Sabrina Polierer, Thomas A. Zevaco, David Guse, Matthias Kind, Stephan Pitter, Karla Herrera Delgado, and Jörg Sauer. Direct DME synthesis on CZZ/H-FER from variable CO₂ /CO syngas feeds. *RSC Advances*, 11(5):2556–2564, 2021. ISSN 2046-2069. doi: 10.1039/D0RA09754C. URL <http://xlink.rsc.org/?DOI=DORA09754C>.
- [72] Minh Tri Luu, Dia Milani, Matthew Wake, and Ali Abbas. Analysis of di-methyl ether production routes: Process performance evaluations at various syngas compositions. *Chemical Engineering Science*, 149:143–155, jul 2016. ISSN 00092509. doi: 10.1016/j.ces.2016.04.019. URL <https://linkinghub.elsevier.com/retrieve/pii/S0009250916301828>.
- [73] I. A. Kurzina, S. I. Reshetnikov, N. I. Karakchieva, and L. N. Kurina. Direct synthesis of dimethyl ether from synthesis gas: Experimental study and mathematical modeling. *Chemical Engineering Journal*, 329:135–141, 2017. ISSN 13858947. doi: 10.1016/j.cej.2017.04.132. URL <http://dx.doi.org/10.1016/j.cej.2017.04.132>.
- [74] Katarzyna Bizon, Krzysztof Skrzypek-Markiewicz, and Gaetano Continillo. Enhancement of the Direct Synthesis of Dimethyl Ether (DME) from Synthesis Gas by Macro- and Microstructuring of the Catalytic Bed. *Catalysts*, 10(8):852, aug 2020. ISSN 2073-4344. doi: 10.3390/catal10080852. URL <https://www.mdpi.com/2073-4344/10/8/852>.
- [75] Cristina Peinado, Dalia Liuzzi, María Retuerto, Jurriaan Boon, Miguel A. Peña, and Sergio Rojas. Study of catalyst bed composition for the direct synthesis of dimethyl ether from CO₂-rich syngas. *Chemical Engineering Journal Advances*, 4: 100039, dec 2020. ISSN 26668211. doi: 10.1016/j.cej.2020.100039. URL <https://linkinghub.elsevier.com/retrieve/pii/S2666821120300399>.
- [76] Kevin McBride, Thomas Turek, and Robert Güttel. Direct dimethyl ether synthesis by spatial patterned catalyst arrangement: A modeling and simulation study. *AIChE Journal*, 58(11):3468–3473, nov 2012. ISSN 00011541. doi: 10.1002/aic.13730. URL <http://doi.wiley.com/10.1002/aic.13730>.
- [77] K.M.Vanden Bussche and G.F. Froment. A Steady-State Kinetic Model for Methanol Synthesis and the Water Gas Shift Reaction on a Commercial Cu/ZnO/Al₂O₃ Catalyst. *Journal of Catalysis*, 161(1):1–10, 1996. ISSN 00219517. doi: 10.1006/jcat.1996.0156. URL <https://doi.org/10.1006/jcat.1996.0156>.

- [78] G.H. Graaf, E.J. Stamhuis, and A.A.C.M. Beenackers. Kinetics of low-pressure methanol synthesis. *Chemical Engineering Science*, 43(12):3185–3195, 1988. ISSN 00092509. doi: 10.1016/0009-2509(88)85127-3. URL <https://linkinghub.elsevier.com/retrieve/pii/000925098851273>.
- [79] Gorazd Bercic and Janez Levec. Catalytic dehydration of methanol to dimethyl ether. Kinetic investigation and reactor simulation. *Industrial & Engineering Chemistry Research*, 32(11):2478–2484, nov 1993. ISSN 0888-5885. doi: 10.1021/ie00023a006. URL <https://pubs.acs.org/doi/abs/10.1021/ie00023a006>.
- [80] Wen-Zhi Lu, Li-Hua Teng, and Wen-De Xiao. Simulation and experiment study of dimethyl ether synthesis from syngas in a fluidized-bed reactor. *Chemical Engineering Science*, 59(22-23):5455–5464, 2004. doi: 10.1016/j.ces.2004.07.031.
- [81] Yong Tae Kim, Kwang-Deog Jung, and Eun Duck Park. A comparative study for gas-phase dehydration of glycerol over H-zeolites. *Applied Catalysis A: General*, 393(1-2):275–287, feb 2011. ISSN 0926860X. doi: 10.1016/j.apcata.2010.12.007. URL <https://linkinghub.elsevier.com/retrieve/pii/S0926860X10008185>.
- [82] Marcio Schwaab and José Carlos Pinto. Optimum reference temperature for reparameterization of the Arrhenius equation. Part 1: Problems involving one kinetic constant. *Chemical Engineering Science*, 62(10):2750–2764, may 2007. ISSN 00092509. doi: 10.1016/j.ces.2007.02.020. URL <https://linkinghub.elsevier.com/retrieve/pii/S0009250907001777>.
- [83] Kenneth Toch, Joris W. Thybaut, and Guy B. Marin. A systematic methodology for kinetic modeling of chemical reactions applied to n-hexane hydroisomerization. *AIChE Journal*, 61(3):880–892, mar 2015. ISSN 00011541. doi: 10.1002/aic.14680. URL <http://doi.wiley.com/10.1002/aic.14680>.
- [84] Ding-Yu Peng and Donald B Robinson. A new two-constant equation of state. *Industrial & Engineering Chemistry Fundamentals*, 15(1):59–64, 1976.
- [85] Kongmeng Ye, Hannsjörg Freund, and Kai Sundmacher. Modelling (vapour + liquid) and (vapour + liquid + liquid) equilibria of water (H₂O) + methanol (MeOH) + dimethyl ether (DME) + carbon dioxide (CO₂) quaternary system using the Peng-Robinson EoS with Wong-Sandler mixing rule. *Journal of Chemical Thermodynamics*, 43:2002–2014, 2011. doi: 10.1016/j.jct.2011.07.016. URL <http://dx.doi.org/10.1016/j.jct.2011.07.016>.
- [86] Antonio Tripodi, Matteo Compagnoni, Rocco Martinazzo, Gianguido Ramis, and Ilenia Rossetti. Process Simulation for the Design and Scale Up of Heterogeneous Catalytic Process: Kinetic Modelling Issues. *Catalysts*, 7(5):159, may 2017. ISSN 2073-4344. doi: 10.3390/catal7050159. URL <http://www.mdpi.com/2073-4344/7/5/159>.

- [87] P Ratamanalaya, S Limtrakul, T Vatanatham, and PA Ramachandran. Kinetics Study of Direct Dimethyl Ether Synthesis. In *TIChE International Conference 2011*, pages ee014.1–ee014.5, 2011.
- [88] Anil K. Agarwal and Michael L. Brisk. Sequential experimental design for precise parameter estimation. 1. Use of reparameterization. *Industrial & Engineering Chemistry Process Design and Development*, 24(1):203–207, jan 1985. ISSN 0196-4305. doi: 10.1021/i200028a034. URL <https://pubs.acs.org/doi/abs/10.1021/i200028a034>.
- [89] David M. Espie and Sandro Macchietto. Nonlinear transformations for parameter estimation. *Industrial & Engineering Chemistry Research*, 27(11):2175–2179, nov 1988. ISSN 0888-5885. doi: 10.1021/ie00083a037. URL <https://pubs.acs.org/doi/abs/10.1021/ie00083a037>.
- [90] F Vegliò, M Trifoni, F Pagnanelli, and L Toro. Shrinking core model with variable activation energy: a kinetic model of manganiferous ore leaching with sulphuric acid and lactose. *Hydrometallurgy*, 60(2):167–179, apr 2001. ISSN 0304386X. doi: 10.1016/S0304-386X(00)00197-3. URL <https://linkinghub.elsevier.com/retrieve/pii/S0304386X00001973>.
- [91] G H Graaf, P J J M Sijtsema, E J Stamhuis, and Et Al. Chemical equilibria in methanol synthesis. *Chemical Engineering Science*, 41(11):2883–2890, 1986. URL [https://doi.org/10.1016/0009-2509\(86\)80019-7](https://doi.org/10.1016/0009-2509(86)80019-7).
- [92] Ainara Ateka, Irene Sierra, Javier Ereña, Javier Bilbao, and Andrés T. Aguayo. Performance of CuO–ZnO–ZrO₂ and CuO–ZnO–MnO as metallic functions and SAPO-18 as acid function of the catalyst for the synthesis of DME co-feeding CO₂. *Fuel Processing Technology*, 152:34–45, nov 2016. ISSN 03783820. doi: 10.1016/j.fuproc.2016.05.041. URL <http://linkinghub.elsevier.com/retrieve/pii/S0378382016302387>.
- [93] K. Klier, V. Chatikavanij, R.G. Herman, and G.W. Simmons. Catalytic synthesis of methanol from CO/H₂ IV. The effects of carbon dioxide. *Journal of Catalysis*, 74(2):343–360, apr 1982. ISSN 00219517. doi: 10.1016/0021-9517(82)90040-9. URL <https://linkinghub.elsevier.com/retrieve/pii/0021951782900409>.
- [94] Jong Wook Bae, H. S. Potdar, Suk Hwan Kang, and Ki Won Jun. Coproduction of methanol and dimethyl ether from biomass-derived syngas on a Cu-ZnO-Al₂O₃ / γ -Al₂O₃ hybrid catalyst. *Energy and Fuels*, 22(1):223–230, 2008. ISSN 08870624. doi: 10.1021/ef700461j. URL <https://doi.org/10.1021/ef700461j>.
- [95] José Palomo, Miguel Ángel Rodríguez-Cano, José Rodríguez-Mirasol, and Tomás Cordero. ZSM-5-decorated CuO/ZnO/ZrO₂ fibers as efficient bifunctional catalysts for the direct synthesis of DME from syngas. *Applied Catalysis B: Environmental*, 270:118893, aug 2020. ISSN 09263373. doi: 10.1016/j.apcatb.2020.118893. URL <https://linkinghub.elsevier.com/retrieve/pii/S0926337320303088>.

- [96] Andrés García-Trenco and Agustín Martínez. Direct synthesis of DME from syngas on hybrid CuZnAl/ZSM-5 catalysts: New insights into the role of zeolite acidity. *Applied Catalysis A: General*, 411-412:170–179, jan 2012. ISSN 0926860X. doi: 10.1016/j.apcata.2011.10.036. URL <https://linkinghub.elsevier.com/retrieve/pii/S0926860X11006314>.
- [97] M.P. Rohde, G. Schaub, S. Khajavi, J.C. Jansen, and F. Kapteijn. Fischer–Tropsch synthesis with in situ H₂O removal – Directions of membrane development. *Microporous and Mesoporous Materials*, 115(1-2):123–136, oct 2008. ISSN 13871811. doi: 10.1016/j.micromeso.2007.10.052. URL <https://linkinghub.elsevier.com/retrieve/pii/S1387181108000772>.
- [98] Andrés T. Aguayo, Javier Ereña, Irene Sierra, Martin Olazar, and Javier Bilbao. Deactivation and regeneration of hybrid catalysts in the single-step synthesis of dimethyl ether from syngas and CO₂. *Catalysis Today*, 106:265–270, 2005. ISSN 09205861. doi: 10.1016/j.cattod.2005.07.144. URL <https://doi.org/10.1016/j.cattod.2005.07.144>.
- [99] Ujjal Mondal and Ganapati D Yadav. Perspective of dimethyl ether as fuel: Part ii-analysis of reactor systems and industrial processes. *Journal of CO₂ Utilization*, 32:321–338, 2019. URL <https://doi.org/10.1016/j.jcou.2019.02.006>.
- [100] Nazely Diban, Ane M. Urriaga, Inmaculada Ortiz, Javier Ereña, Javier Bilbao, and Andrés T. Aguayo. Improved Performance of a PBM Reactor for Simultaneous CO₂ Capture and DME Synthesis. *Industrial & Engineering Chemistry Research*, 53(50):19479–19487, dec 2014. ISSN 0888-5885. doi: 10.1021/ie503663h. URL <https://pubs.acs.org/doi/10.1021/ie503663h>.
- [101] I. Iliuta, F. Larachi, and P. Fongarland. Dimethyl Ether Synthesis with in situ H₂O Removal in Fixed-Bed Membrane Reactor: Model and Simulations †. *Industrial & Engineering Chemistry Research*, 49(15):6870–6877, aug 2010. ISSN 0888-5885. doi: 10.1021/ie901726u. URL <https://pubs.acs.org/doi/10.1021/ie901726u>.
- [102] Marcello De Falco, Mauro Capocelli, and Gabriele Centi. Dimethyl ether production from CO₂ rich feedstocks in a one-step process: Thermodynamic evaluation and reactor simulation. *Chemical Engineering Journal*, 294:400–409, jun 2016. ISSN 13858947. doi: 10.1016/j.cej.2016.03.009. URL <https://linkinghub.elsevier.com/retrieve/pii/S138589471630239X>.
- [103] S.K. Wilkinson, L.G.A. Van de Water, B. Miller, M.J.H. Simmons, E.H. Stitt, and M.J. Watson. Understanding the generation of methanol synthesis and water gas shift activity over copper-based catalysts - A spatially resolved experimental kinetic study using steady and non-steady state operation under CO/CO₂ /H₂ feeds. *Journal of Catalysis*, 337:208–220, 2016. ISSN 10902694. doi: 10.1016/j.jcat.2016.01.025. URL <http://dx.doi.org/10.1016/j.jcat.2016.01.025>.
- [104] Majid Mollavali, Fereydoon Yaripour, Hossein Atashi, and Saeed Sahebdehfar. Intrinsic Kinetics Study of Dimethyl Ether Synthesis from Methanol on γ -Al₂O₃ Cat-

- alysts. *Industrial & Engineering Chemistry Research*, 47(9):3265–3273, may 2008. ISSN 0888-5885. doi: 10.1021/ie800051h. URL <https://pubs.acs.org/doi/10.1021/ie800051h>.
- [105] Vicente Sanchez Escribano, Gabriella Garbarino, Elisabetta Finocchio, and Guido Busca. γ -Alumina and Amorphous Silica–Alumina: Structural Features, Acid Sites and the Role of Adsorbed Water. *Topics in Catalysis*, 60(19-20):1554–1564, dec 2017. ISSN 1022-5528. doi: 10.1007/s11244-017-0838-5. URL <http://link.springer.com/10.1007/s11244-017-0838-5>.
- [106] Jehad Abu-Dahrieh, David Rooney, Alexandre Goguet, and Youssef Saih. Activity and deactivation studies for direct dimethyl ether synthesis using CuO–ZnO–Al₂O₃ with NH₄ZSM-5, HZSM-5 or γ -Al₂O₃. *Chemical Engineering Journal*, 203:201–211, sep 2012. ISSN 13858947. doi: 10.1016/j.cej.2012.07.011. URL <https://linkinghub.elsevier.com/retrieve/pii/S1385894712009023>.
- [107] Gerard O’Regan. *A brief history of computing*. Springer Science & Business Media, 2008. URL http://link.springer.com/10.1007/978-1-4471-2359-0_15.
- [108] Filippo Amato, José Luis González-Hernández, and Josef Havel. Artificial neural networks combined with experimental design: A ”soft” approach for chemical kinetics. *Talanta*, 93:72–78, 2012. ISSN 00399140. doi: 10.1016/j.talanta.2012.01.044. URL <http://dx.doi.org/10.1016/j.talanta.2012.01.044>.
- [109] Mehdi Shiva, Hossein Atashi, Farshad Farshchi Tabrizi, Ali Akbar Mirzaei, and Akbar Zare. The application of hybrid DOE/ANN methodology in lumped kinetic modeling of Fischer-Tropsch reaction. *Fuel Processing Technology*, 106:631–640, 2013. ISSN 03783820. doi: 10.1016/j.fuproc.2012.09.056. URL <http://dx.doi.org/10.1016/j.fuproc.2012.09.056>.
- [110] Kohji Omata, Sutarto, Masahiko Hashimoto, Gunji Ishiguro, Yuhsuke Watanabe, Tetsuo Umegaki, and Muneyoshi Yamada. Design and development of cu-zn oxide catalyst for direct dimethyl ether synthesis using an artificial neural network and physicochemical properties of elements. *Industrial & Engineering Chemistry Research*, 45(14):4905–4910, jul 2006. ISSN 0888-5885. doi: 10.1021/ie050640g. URL <https://pubs.acs.org/doi/10.1021/ie050640g>.
- [111] Kohji Omata, Sutarto, Masahiko Hashimoto, Gunji Ishiguro, Yuhsuke Watanabe, Tetsuo Umegaki, and Muneyoshi Yamada. Artificial Neural Network-Aided Catalyst Research for Low-Pressure DME Synthesis from Syngas. In *Ultra-clean Transportation Fuels*, pages 211–224. ACS Publications, apr 2007. doi: 10.1021/bk-2007-0959.ch016. URL <https://pubs.acs.org/doi/abs/10.1021/bk-2007-0959.ch016>.
- [112] G. R. Moradi and F. Parvizian. An expert model for estimation of the performance of direct dimethyl ether synthesis from synthesis gas. *The Canadian Journal of Chemical Engineering*, 89(5):1266–1273, oct 2011. ISSN 0008-4034. doi: 10.1002/

- cjce.20558. URL <https://onlinelibrary.wiley.com/doi/abs/10.1002/cjce.20558>.
- [113] Joerg Appel, Corrado Colombo, Urs Dätwyler, Yun Chen, and Nimet Kerimoglu. Comprehensive Analysis Competence and Innovative Approaches for Sustainable Chemical Production. *CHIMIA International Journal for Chemistry*, 70(9):621–627, sep 2016. ISSN 00094293. doi: 10.2533/chimia.2016.621. URL <http://www.ingentaconnect.com/content/10.2533/chimia.2016.621>.
- [114] Kohji Omata, Toshihiko Ozaki, Tetsuo Umegaki, Yuhsuke Watanabe, Noritoshi Nukui, and Muneyoshi Yamada. Optimization of the Temperature Profile of a Temperature Gradient Reactor for DME Synthesis Using a Simple Genetic Algorithm Assisted by a Neural Network. *Energy & Fuels*, 17(4):836–841, jul 2003. ISSN 0887-0624. doi: 10.1021/ef0202438. URL <https://pubs.acs.org/doi/10.1021/ef0202438>.
- [115] Peyvand Valeh-E-Sheyda, Fereydoon Yaripour, Gholamreza Moradi, and Mohammad Saber. Application of artificial neural networks for estimation of the reaction rate in methanol dehydration. *Industrial and Engineering Chemistry Research*, 49(10):4620–4626, 2010. ISSN 08885885. doi: 10.1021/ie9020705. URL <https://doi.org/10.1021/ie9020705>.
- [116] S. Alamolhoda, M. Kazemeini, A. Zaherian, and M.R. Zakerinasab. Reaction kinetics determination and neural networks modeling of methanol dehydration over nano γ -Al₂O₃ catalyst. *Journal of Industrial and Engineering Chemistry*, 18(6):2059–2068, nov 2012. ISSN 1226-086X. doi: 10.1016/J.JIEC.2012.05.027. URL <http://dx.doi.org/10.1016/j.jiec.2012.05.027>.
- [117] Kurt Hornik, Maxwell Stinchcombe, and Halbert White. Multilayer feedforward networks are universal approximators. *Neural networks*, 2(5):359–366, 1989. URL [https://doi.org/10.1016/0893-6080\(89\)90020-8](https://doi.org/10.1016/0893-6080(89)90020-8).
- [118] G Cybenko. Mathematics of Control, Signals, and Systems Approximation by Superpositions of a Sigmoidal Function*. *Math. Control Signals Systems*, 2:303–314, 1989. URL <https://doi.org/10.1007/BF02551274>.
- [119] Kurt Hornik. Approximation Capabilities of Multilayer Neural Network. *Neural Networks*, 4(1989):251–257, 1991. ISSN 0893-6080. doi: 10.1016/0893-6080(91)90009-T. URL [https://doi.org/10.1016/0893-6080\(91\)90009-T](https://doi.org/10.1016/0893-6080(91)90009-T).
- [120] Mark Hudson Beale, Martin T Hagan, and Howard B Demuth. *Neural network toolbox*, volume 2. Citeseer, 2013.
- [121] Zeke S.H. Chan, H.W. Ngan, A.B. Rad, A.K. David, and N. Kasabov. Short-term ANN load forecasting from limited data using generalization learning strategies. *Neurocomputing*, 70:409–419, dec 2006. ISSN 0925-2312. doi: 10.1016/J.NEUCOM.2005.12.131. URL <https://www.sciencedirect.com/science/article/pii/S0925231206001950{#}bib26>.

- [122] David J C Mackay. Probable networks and plausible predictions — a review of practical Bayesian methods for supervised neural networks. *Network: Computation in Neural Systems*, 6(3):469–505, jan 1995. ISSN 0954-898X. doi: 10.1088/0954-898X.6.3.011. URL <https://www.tandfonline.com/doi/full/10.1088/0954-898X{ }6{ }3{ }011>.
- [123] H. Yonaba, F. Anctil, and V. Fortin. Comparing Sigmoid Transfer Functions for Neural Network Multistep Ahead Streamflow Forecasting. *Journal of Hydrologic Engineering*, 15(4):275–283, apr 2010. ISSN 1084-0699. doi: 10.1061/(ASCE)HE.1943-5584.0000188. URL <http://ascelibrary.org/doi/10.1061/{ }28ASCE{ }29HE.1943-5584.0000188>.
- [124] Choose a Multilayer Neural Network Training Function - MATLAB & Simulink - MathWorks United Kingdom. <https://uk.mathworks.com/help/deeplearning/ug/choose-a-multilayer-neural-network-training-function.html>, 2020. Last visited on 22.06.2022.
- [125] John E. Dennis and Robert B Schnabel. *Numerical Methods for Unconstrained Optimization and Nonlinear Equations*. Siam, 1996. URL <https://epubs.siam.org/doi/pdf/10.1137/1.9781611971200.fm>.
- [126] P.E. Gill, W. Murray, and M.H. Wright. *Practical Optimization*. Academic Press, 1981. ISBN 9780122839504.
- [127] Frank Burden and Dave Winkler. Bayesian Regularization of Neural Networks. *Methods in molecular biology (Clifton, N.J.)*, 458:23–42, 2009. doi: 10.1007/978-1-60327-101-1.3. URL <http://link.springer.com/10.1007/978-1-60327-101-1{ }3>.
- [128] M. J.D. Powell. Restart procedures for the conjugate gradient method. *Mathematical Programming*, 12(1):241–254, 1977. ISSN 00255610. doi: 10.1007/BF01593790. URL <https://doi.org/10.1007/BF01593790>.
- [129] E M L Beale. *Numerical methods for nonlinear optimization*. A Derivation of Conjugate Gradients. Academic Press Inc, 1972. ISBN 0124556507.
- [130] L E Scales. *Introduction to Non-Linear Optimization*. Computer Science Series. Macmillan Education UK, 1985. ISBN 9781349177417. URL <https://books.google.de/books?id=AEJdWAAQBAJ>.
- [131] Donald W Marquardt. An algorithm for least-squares estimation of nonlinear parameters. *Journal of the society for Industrial and Applied Mathematics*, 11(2): 431–441, 1963. URL <https://doi.org/10.1137/0111030>.
- [132] Martin T Hagan and Mohammad B Menhaj. Training feedforward networks with the marquardt algorithm. *IEEE transactions on Neural Networks*, 5(6):989–993, 1994. URL <https://ieeexplore.ieee.org/abstract/document/329697>.

- [133] Roberto Battiti. First-and second-order methods for learning: between steepest descent and Newton’s method. *Neural computation*, 4(2):141–166, 1992. URL <https://ieeexplore.ieee.org/document/6796060>.
- [134] Martin Riedmiller and Heinrich Braun. A direct adaptive method for faster backpropagation learning: The RPROP algorithm. In *IEEE international conference on neural networks*, volume 1, pages 586–591. IEEE, 1993. doi: 10.1109/ICNN.1993.298623. URL <https://ieeexplore.ieee.org/document/298623>.
- [135] Martin Fodslette Møller. A scaled conjugate gradient algorithm for fast supervised learning. *Neural Networks*, 6(4):525–533, 1993. ISSN 08936080. doi: 10.1016/S0893-6080(05)80056-5. URL [https://doi.org/10.1016/S0893-6080\(05\)80056-5](https://doi.org/10.1016/S0893-6080(05)80056-5).
- [136] Jun Han and Claudio Moraga. The influence of the sigmoid function parameters on the speed of backpropagation learning. In *International Workshop on Artificial Neural Networks*, pages 195–201. Springer, 1995. URL https://doi.org/10.1007/3-540-59497-3_175.
- [137] Kwara Nantomah. On some properties of the sigmoid function. *Asia Mathematica*, 3(1):79–90, 2019. URL <http://asiamath.org/issue1/vol3iss1/AM-1904-4107.pdf>.
- [138] David J. C. MacKay. Bayesian Interpolation. *Neural Computation*, 4(3):415–447, may 1992. ISSN 0899-7667. doi: 10.1162/neco.1992.4.3.415. URL <http://www.mitpressjournals.org/doi/10.1162/neco.1992.4.3.415>.
- [139] Hayrettin Okut. Bayesian Regularized Neural Networks for Small n Big p Data. In *Artificial Neural Networks - Models and Applications*, chapter 2. InTech, oct 2016. doi: 10.5772/63256. URL <http://www.intechopen.com/books/artificial-neural-networks-models-and-applications/bayesian-regularized-neural-networks-for-small-n-big-p-data>.
- [140] Ivana Miletto, Enrico Catizzone, Giuseppe Bonura, Chiara Ivaldi, Massimo Migliori, Enrica Gianotti, Leonardo Marchese, Francesco Frusteri, and Girolamo Giordano. In situ FT-IR characterization of CuZnZr/ferrierite hybrid catalysts for one-potCO₂-to-DME conversion. *Materials*, 11:2275–2289, 2018. ISSN 19961944. doi: 10.3390/ma11112275. URL <https://doi.org/10.3390/ma11112275>.
- [141] Florian Nestler, Matthias Krüger, Johannes Full, Max J. Hadrich, Robin J. White, and Achim Schaadt. Methanol Synthesis - Industrial Challenges within a Changing Raw Material Landscape. *Chemie Ingenieur Technik*, 90(10):1409–1418, oct 2018. ISSN 0009286X. doi: 10.1002/cite.201800026. URL <http://doi.wiley.com/10.1002/cite.201800026>.
- [142] Gabriele Centi and Siglinda Perathoner. Opportunities and prospects in the chemical recycling of carbon dioxide to fuels. *Catalysis Today*, 148(3-4):191–205,

- nov 2009. ISSN 09205861. doi: 10.1016/j.cattod.2009.07.075. URL <https://linkinghub.elsevier.com/retrieve/pii/S0920586109004416>.
- [143] Jacopo Panerati, Matthias A. Schnellmann, Christian Patience, Giovanni Beltrame, and Gregory S. Patience. Experimental methods in chemical engineering: Artificial neural networks—ANNs. *Canadian Journal of Chemical Engineering*, 97(9):2372–2382, 2019. ISSN 1939019X. doi: 10.1002/cjce.23507. URL <https://doi.org/10.1002/cjce.23507>.
- [144] Marcelo Blanco, Jordi Coello, Hortensia Iturriaga, Santiago MasPOCH, and Miguel Redón. Artificial Neural Networks for Multicomponent Kinetic Determinations. *Analytical Chemistry*, 67(24):4477–4483, 1995. ISSN 15206882. doi: 10.1021/ac00120a008. URL <https://doi.org/10.1021/ac00120a008>.
- [145] Kohji Omata, Masahiko Hashimoto, Sutarto, and Muneyoshi Yamada. Artificial neural network and grid search aided optimization of temperature profile of temperature gradient reactor for dimethyl ether synthesis from syngas. *Industrial and Engineering Chemistry Research*, 48(2):844–849, 2009. ISSN 08885885. doi: 10.1021/ie8008633. URL <https://doi.org/10.1021/ie8008633>.
- [146] Tibor Svitnic, Nga T. Q. Do, Timm Schuhmann, Thomas Renner, Stephane Haag, and Evrim Örs. Data-driven approach for predictive modeling of by-product formation in methanol synthesis. *Proceedings of the 30th European Symposium on Computer Aided Process Engineering*, pages 505–510, 2020. doi: 10.1016/B978-0-12-823377-1.50085-9. URL <https://doi.org/10.1016/B978-0-12-823377-1.50085-9>.
- [147] Jiansen Ye. Artificial neural network modeling of methanol production from syngas. *Petroleum Science and Technology*, 37(6):629–632, mar 2019. ISSN 1091-6466. doi: 10.1080/10916466.2018.1560321. URL <https://www.tandfonline.com/doi/full/10.1080/10916466.2018.1560321>.
- [148] Israf Ud Din, Maizatul S. Shaharun, Abdul Naeem, Mshari A. Alotaibi, Abdulrahman I. Alharthi, and Qazi Nasir. CO₂ Conversion to Methanol over Novel Carbon Nanofiber-Based Cu/ZrO₂ Catalysts—A Kinetics Study. *Catalysts*, 10(5):567, may 2020. ISSN 2073-4344. doi: 10.3390/catal10050567. URL <https://www.mdpi.com/2073-4344/10/5/567>.
- [149] Alaa Ali Hameed, Bekir Karlik, and Mohammad Shukri Salman. Back-propagation algorithm with variable adaptive momentum. *Knowledge-Based Systems*, 114(114):79–87, dec 2016. ISSN 0950-7051. doi: 10.1016/J.KNOSYS.2016.10.001. URL <https://www.sciencedirect.com/science/article/pii/S0950705116303811>.
- [150] Soteris A. Kalogirou and Milorad Bojic. Artificial neural networks for the prediction of the energy consumption of a passive solar building. *Energy*, 25(5):479–491, may 2000. ISSN 03605442. doi: 10.1016/S0360-5442(99)00086-9. URL <https://linkinghub.elsevier.com/retrieve/pii/S0360544299000869>.

- [151] Gerson Lachtermacher and J. David Fuller. Back propagation in time-series forecasting. *Journal of Forecasting*, 14(4):381–393, jul 1995. ISSN 02776693. doi: 10.1002/for.3980140405. URL <https://onlinelibrary.wiley.com/doi/10.1002/for.3980140405>.
- [152] Mansour Nasser Jadid and Daniel R. Fairbairn. Neural-network applications in predicting moment-curvature parameters from experimental data. *Engineering Applications of Artificial Intelligence*, 9(3):309–319, jun 1996. ISSN 09521976. doi: 10.1016/0952-1976(96)00021-8. URL <https://linkinghub.elsevier.com/retrieve/pii/0952197696000218>.
- [153] G. Zahedi, A. Lohi, and K.A. Mahdi. Hybrid modeling of ethylene to ethylene oxide heterogeneous reactor. *Fuel Processing Technology*, 92(9):1725–1732, sep 2011. ISSN 03783820. doi: 10.1016/j.fuproc.2011.04.022. URL <https://linkinghub.elsevier.com/retrieve/pii/S0378382011001433>.
- [154] Henricus J. L. Van Can, Hubert A. B. Te Braake, Sander Dubbelman, Chris Hellinga, Karel Ch. A. M. Luyben, and Joseph J. Heijnen. Understanding and applying the extrapolation properties of serial gray-box models. *AIChE Journal*, 44(5):1071–1089, may 1998. ISSN 00011541. doi: 10.1002/aic.690440507. URL <https://onlinelibrary.wiley.com/doi/10.1002/aic.690440507>.
- [155] D Mears. Diagnostic criteria for heat transport limitations in fixed bed reactors. *Journal of Catalysis*, 20(2):127–131, feb 1971. ISSN 00219517. doi: 10.1016/0021-9517(71)90073-X. URL <https://linkinghub.elsevier.com/retrieve/pii/002195177190073X>.
- [156] P.B. Weisz and C.D. Prater. Interpretation of Measurements in Experimental Catalysis. In W.G. Frankenburg, V.I. Komarewsky, and E.K. Rideal, editors, *Advances in Catalysis*, pages 143–196. Academic Press, 1954. doi: 10.1016/S0360-0564(08)60390-9. URL <https://linkinghub.elsevier.com/retrieve/pii/S0360056408603909>.
- [157] J.B. Anderson. A criterion for isothermal behaviour of a catalyst pellet. *Chemical Engineering Science*, 18(2):147–148, 1963.
- [158] Javier Pérez-Ramirez, Rob J Berger, Guido Mul, Freek Kapteijn, and Jacob A Moulijn. The six-flow reactor technology: A review on fast catalyst screening and kinetic studies. *Catalysis Today*, 60(1-2):93–109, 2000. URL [https://doi.org/10.1016/S0920-5861\(00\)00321-7](https://doi.org/10.1016/S0920-5861(00)00321-7).
- [159] Manfred Baerns, Arno Behr, Axel Brehm, Jürgen Gmehling, Hanns Hofmann, and Ulfert Onken. *Technische chemie*. Wiley-VCH, Weinheim, 2013. ISBN 978-3-527-33072-0.
- [160] Thomas Zeiser. *Simulation und Analyse von durchströmten Kugelschüttungen in engen Rohren unter Verwendung von Hochleistungsrechnern*. Doctoral dis-

sertation, Friedrich-Alexander-Universität Erlangen-Nürnberg, 2008. URL <http://en.scientificcommons.org/56131507>.

APPENDIX A. Additional Results on Semi-mechanistic Model

A.1 Reduction procedure and conditioning.

Before performing the kinetic measurements, the CZA share of the catalytic bed was activated at atmospheric pressure with a volume flow of 300 ml min⁻¹ containing 5 % of H₂ and 95 % of N₂. The system was heated from 373 to 473 K at a heating rate of 20 K h⁻¹. This temperature was hold for one hour, followed by further heating to 513 K at a heating rate of 12 K h⁻¹. Finally, the H₂ concentration in the gas flow was increased to 50 %, maintaining the same total flow rate for an additional hour. Posterior to the catalyst reduction, the operating conditions 300 ml min⁻¹, 503 K, 20 % COR and 50 bar, were set to allow the catalyst system to run in. This operating point was maintained and the concentration of the product gas was monitored until a steady state of the catalyst system could be assumed (between 12 and 20 h time on stream).

A.2 A priori Criteria.

Table A.1: Calculated criteria for the verification of assumptions.

Phenomena to be neglected	Criteria	Equation	Calculated Value*
Outer mass transfer	Mears [155]	$\eta Da_{II} = \frac{r_{j,eff} n }{\beta_i c_i} < 0.05$	0.0182
Inner mass transfer	Weisz-Prater [156]	$\psi = \frac{(r_{j,eff} l_c^2)}{D_{i,eff} c_{i,s}} \frac{n+1}{2} < 0.15$	9.30E-06
Outer heat transfer	Mears [155]	$\frac{ \Delta H_R r_{j,eff} R}{\lambda T} \frac{E_A}{R T} < 0.15$	0.0008
Inner heat transfer	Anderson [157]	$\frac{ \Delta H_R r_{j,eff} r_{kat}^2}{\lambda T_s} \frac{E_A}{R T} < 0.75$	0.0397
Radial Gradients	d/D -ratio [158]	$24 < \frac{d_{Tube}}{d_{Particle}} < 48$	24
Non-Isothermal operation	Rule of Thumb	$\Delta T = T_{max} - T_{min}$	2
Axial dispersion	Bodenstein No. [159]	$Bo = \frac{u_0 L}{D_{ax}} > 100$	481
Pressure drop	$\Delta p/L$ Zhavoronkov Correlation [160]	$\frac{\Delta p_{max}}{p} \approx 0$	5.0 E-08

*for the worst-case scenario

A.3 Model Discrimination.

For the initial model discrimination, the available experimental data were first simulated using eight different kinetic models from the open literature [1, 32, 33, 36, 37, 39, 40, 87]. The sum of the squared errors between the measured and predicted composition of the product gas was calculated for each model and depicted in Fig. A.1. In this figure, the models are named after the first author.

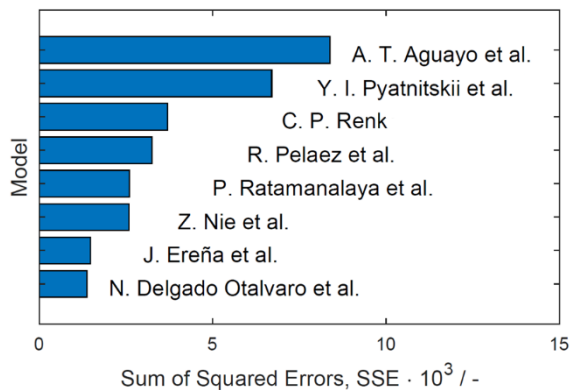


Figure A.1: Total sum of squared errors for the implemented models. Models name after first author.

After this initial screening, the five models with the lower residual squared sum were parametrized to fit the experimental data. The model by Delgado Otalvaro et al. [1] agreed best with the available experimental data. Hence, the model structure and respective mechanistic assumptions were chosen for fine-tuning. To enable a direct comparison of the tested models and parameters, these have been compiled in Table A.2. Additionally, the mean relative error between the predictions with the different models, and the experiments for each species i (RE_i) is also given. RE_i is calculated by:

$$RE_i = 100\% \frac{1}{No. Exps} \sum_{n=1}^{No. Exps} \frac{|y_{i,out,measured,n} - y_{i,out,predicted,n}|}{y_{i,out,measured,n}}$$

The indices of the reaction rates, and rate constants in Table S2 correspond to the following reactions:

1. $\text{CO}_2 + 3\text{H}_2 \rightleftharpoons \text{CH}_3\text{OH} + \text{H}_2\text{O}$
2. $2\text{CH}_3\text{OH} \rightleftharpoons \text{CH}_3\text{OCH}_3 + \text{H}_2\text{O}$
3. $\text{CO} + \text{H}_2\text{O} \rightleftharpoons \text{CO}_2 + \text{H}_2$
4. $\text{CO} + 2\text{H}_2 \rightleftharpoons \text{CH}_3\text{OH}$
5. $n\text{CO} + (2n+1)\text{H}_2 \rightleftharpoons \text{C}_n\text{H}_{2n+2} + n\text{H}_2\text{O}$

Table A.2: Compilation of tested reaction kinetic models during model discrimination with the respective specific parameters, and resulting relative error for each species.

Model	Rate expressions	Model specific parameter	RE / %
N. Delgado Otalvaro [1]	$r_1 = k_1 \frac{(f_{\text{CO}_2} f_{\text{H}_2}^3 - \frac{f_{\text{H}_2\text{O}} f_{\text{CH}_3\text{OH}}}{K_{f,1}})}{(1 + K_{\text{CO}_2} f_{\text{CO}_2} + K_{\text{CO}} f_{\text{CO}} + \sqrt{K_{\text{H}_2}} f_{\text{H}_2})^3} [(1 - \varepsilon_{\text{bed}}) \rho_{\text{CZA}} \xi_{\text{CZA}}]$	$k_1 = \exp(-6.94) \exp\left(-\frac{21.81}{R} \frac{T_R - 1}{T_R}\right)$	CO 9.7 CO ₂ 7.1 H ₂ 1.5 DME 54.5
	$r_2 = k_2 \left(f_{\text{CH}_3\text{OH}}^2 - \frac{f_{\text{DME}} f_{\text{H}_2\text{O}}}{K_{f,2}} \right) [(1 - \varepsilon_{\text{bed}}) \rho_{\text{CZA}} \xi_{\text{CZA}}]$	$k_2 = \exp(-2.07) \exp\left(-\frac{42.77}{R} \frac{T_R - 1}{T_R}\right)$	
	$r_3 = k_3 \frac{(f_{\text{H}_2\text{O}} - \frac{f_{\text{CO}_2} f_{\text{H}_2}}{K_{f,3}}) f_{\text{CO}}}{1 + K_{\text{CO}_2} f_{\text{CO}_2} + K_{\text{CO}} f_{\text{CO}} + \sqrt{K_{\text{H}_2}} f_{\text{H}_2}} [(1 - \varepsilon_{\text{bed}}) \rho_{\text{CZA}} \xi_{\text{CZA}}]$	$k_3 = \exp(-2.75) \exp\left[-\frac{10.82}{R} \frac{T_R - 1}{T_R}\right]$	
J. Ereña [33]	$r_1 = k_1 \frac{(f_{\text{CO}_2} f_{\text{H}_2}^3 - \frac{f_{\text{H}_2\text{O}} f_{\text{CH}_3\text{OH}}}{K_{f,1}})}{(1 + K_{\text{CO}_2} f_{\text{CO}_2} + K_{\text{CO}} f_{\text{CO}} + \sqrt{K_{\text{H}_2}} f_{\text{H}_2})^3} [(1 - \varepsilon_{\text{bed}}) \rho_{\text{ALOX}} \xi_{\text{ALOX}}]$	$K_{\text{CO}} = \exp(-15.32) \exp\left[\frac{14.03}{R} \frac{T_R}{T_R} \left(\frac{T_R}{T} - 1\right)\right]$	CO 11.3 CO ₂ 7.6 H ₂ 1.6 DME 62.8
	$r_2 = k_2 \left(f_{\text{CH}_3\text{OH}}^2 - \frac{f_{\text{DME}} f_{\text{H}_2\text{O}}}{K_2} \right)$	$K_{\text{CO}_2} = \exp(-0.57) \exp\left[-\frac{0}{R} \frac{T_R}{T_R} \left(\frac{T_R}{T} - 1\right)\right]$	
	$r_3 = k_3 \left(f_{\text{CO}} f_{\text{H}_2\text{O}} - \frac{f_{\text{CO}_2} f_{\text{H}_2}}{K_3} \right)$	$K_{\text{H}_2} = \exp(-19.51) \exp\left[\frac{14.68}{R} \frac{T_R}{T_R} \left(\frac{T_R}{T} - 1\right)\right]$	
	$r_4 = k_4 \frac{(f_{\text{H}_2}^2 f_{\text{CO}} - \frac{f_{\text{CH}_3\text{OH}}}{K_4}) \frac{r_{\text{CH}_3\text{OH}}}{(r_{\text{CH}_3\text{OH}})_0}}{(1 + K_{\text{H}_2\text{O}} f_{\text{H}_2\text{O}} + K_{\text{CO}_2} f_{\text{CO}_2})^2}$	$[r_j] = \text{mol m}^{-3} \text{s}^{-1}$	
	$r_5 = k_5 \frac{(f_{\text{CO}} f_{\text{H}_2}^3 - \frac{f_{\text{HC}} f_{\text{H}_2\text{O}}}{K_5})}{(1 + K_{\text{H}_2\text{O}} f_{\text{H}_2\text{O}} + K_{\text{CO}_2} f_{\text{CO}_2})}$	$k_2 = 3.41 \cdot 10^{-3} \exp\left(-\frac{63.5}{R} \left(\frac{1}{T} - \frac{1}{548}\right)\right)$ k_3 : not given $k_4 = 2.4 \cdot 10^{-5} \exp\left(-\frac{90.0}{R} \left(\frac{1}{T} - \frac{1}{548}\right)\right)$ $k_5 = 1.23 \cdot 10^{-7} \exp\left(-\frac{6.9}{R} \left(\frac{1}{T} - \frac{1}{548}\right)\right)$ $K_{\text{H}_2\text{O}} = 2.67 \cdot 10^{-3} \exp\left(\frac{384.8}{R} \left(\frac{1}{T} - \frac{1}{548}\right)\right)$ $K_{\text{CO}_2} = 1.13 \cdot 10^{-3} \exp\left(\frac{43.4}{R} \left(\frac{1}{T} - \frac{1}{548}\right)\right)$ $[k_2] = \text{molDME (molC)}^{-1} \text{g}_{\text{cat}}^{-1} \text{h}^{-1} \text{bar}^{-2}$ $[k_4] = \text{molCH}_3\text{OH (molC)}^{-1} \text{g}_{\text{cat}}^{-1} \text{h}^{-1} \text{bar}^{-3}$ $[k_5] = \text{molHC (molC)}^{-1} \text{g}_{\text{cat}}^{-1} \text{h}^{-1} \text{bar}^{-4}$ $[E_a] = \text{kJ mol}^{-1}$ $[\Delta H_{\text{ads}}] = \text{kJ mol}^{-1}$ $[K_i] = \text{bar}^{-1}$	
Z. Nie [40]	$r_1 = k_1 \frac{f_{\text{CO}_2} f_{\text{H}_2}^3 \left(1 - \frac{f_{\text{CH}_3\text{OH}} f_{\text{H}_2\text{O}}}{K_{f,1} f_{\text{CO}_2} f_{\text{H}_2}^3}\right)}{(1 + K_{\text{CO}} f_{\text{CO}} + K_{\text{CO}_2} f_{\text{CO}_2} + K_{\text{H}_2} f_{\text{H}_2})^4}$	$k_1 = 5.05910^3 \exp\left(-\frac{67515}{R} \frac{T}{T}\right)$	CO 36.5 CO ₂ 10.6 H ₂ 6.7 DME 100
	$r_2 = k_2 \frac{\left(1 - \frac{f_{\text{DME}} f_{\text{H}_2\text{O}}}{K_{f,2} f_{\text{CH}_3\text{OH}}^2}\right)^2}{(1 + \sqrt{K_{\text{CH}_3\text{OH}} f_{\text{CH}_3\text{OH}}})^2}$	$k_2 = 1.60210^3 \exp\left(-\frac{43473}{R} \frac{T}{T}\right)$	
	$r_4 = k_4 \frac{f_{\text{CO}} f_{\text{H}_2}^2 \left(1 - \frac{f_{\text{CH}_3\text{OH}}}{K_{f,4} f_{\text{CO}} f_{\text{H}_2}^2}\right)}{(1 + K_{\text{CO}} f_{\text{CO}} + K_{\text{CO}_2} f_{\text{CO}_2} + K_{\text{H}_2} f_{\text{H}_2})^3}$	$k_4 = 7.38010^3 \exp\left(-\frac{54307}{R} \frac{T}{T}\right)$	
	$r_5 = k_5 \frac{(f_{\text{CO}} f_{\text{H}_2}^3 - \frac{f_{\text{H}_2\text{O}} f_{\text{CH}_3\text{OH}}}{K_{f,5}})}{(1 + K_{\text{CO}_2} f_{\text{CO}_2} + K_{\text{CO}} f_{\text{CO}} + \sqrt{K_{\text{H}_2}} f_{\text{H}_2})^3}$	$K_{\text{CO}} = 3.93410^{-6} \exp\left(\frac{37373}{R} \frac{T}{T}\right)$ $K_{\text{CO}_2} = 1.85810^{-6} \exp\left(\frac{53795}{R} \frac{T}{T}\right)$ $K_{\text{H}_2} = 0.6716 \exp\left(-\frac{6476}{R} \frac{T}{T}\right)$ $K_{\text{CH}_3\text{OH}} = 3.48010^{-6} \exp\left(\frac{54689}{R} \frac{T}{T}\right)$	

Model	Rate expressions	Model specific parameter	RE / %
P. Ratamaya [87]	$r_2 = k_2 \frac{\left(p_{\text{CH}_3\text{OH}}^2 - \frac{p_{\text{DME}} p_{\text{H}_2\text{O}}}{K_{\text{eq2}}} \right)}{\left(1 + \sqrt{K_{\text{CH}_3\text{OH}} p_{\text{CH}_3\text{OH}} + K_{\text{H}_2\text{O}} p_{\text{H}_2\text{O}}} \right)^2}$	$k_2 = 1.69 \cdot 10^8 \exp\left(-\frac{69787}{R T}\right)$	CO 36.1
	$r_3 = k_3 \frac{\left(p_{\text{CO}} p_{\text{H}_2\text{O}} - \frac{p_{\text{CO}_2} p_{\text{H}_2}}{K_{\text{eq3}}} \right)}{\left(1 + K_{\text{CO}} p_{\text{CO}} + K_{\text{H}_2\text{O}} p_{\text{H}_2\text{O}} + K_{\text{CO}_2} p_{\text{CO}_2} + \sqrt{K_{\text{H}_2} p_{\text{H}_2}} \right)^2}$	$k_3 = 1202.8 \exp\left(-\frac{20437}{R T}\right)$	CO ₂ 10.7
	$r_4 = k_4 \frac{\left(p_{\text{CO}} p_{\text{H}_2}^2 - \frac{p_{\text{CH}_3\text{OH}}}{K_{\text{eq4}}} \right)}{\left(1 + K_{\text{CO}} p_{\text{CO}} + \sqrt{K_{\text{H}_2} p_{\text{H}_2}} + K_{\text{CH}_3\text{OH}} p_{\text{CH}_3\text{OH}} \right)^3}$	$k_4 = 40.498 \exp\left(-\frac{18203}{R T}\right)$	H ₂ 6.7
		$K_{\text{CH}_3\text{OH}} = 0.9535 \exp\left(\frac{16243}{R T}\right)$ $K_{\text{H}_2\text{O}} = 6.992 \exp\left(\frac{26452}{R T}\right)$ $K_{\text{CO}} = 4.49 \cdot 10^{-7} \exp\left(\frac{60528}{R T}\right)$ $K_{\text{CO}_2} = 1.092 \cdot 10^{-7} \exp\left(\frac{66924}{R T}\right)$ $K_{\text{H}_2} = 0.2487 \exp\left(\frac{30961}{R T}\right)$	DME 100
R. Pelaez [32]	$r_1 = \frac{k_1}{\left(1 + K_{\text{H}_2\text{O}} f_{\text{H}_2\text{O}} \right)^3} \left(f_{\text{CO}_2} f_{\text{H}_2} - \frac{f_{\text{CH}_3\text{OH}} f_{\text{H}_2\text{O}}}{K_{\text{eq1}} f_{\text{H}_2}^2} \right)$	Equation for temperature dependency of the rate or adsorption constants is not given. Parameter estimates: $k_{1,at 523 K} = 2.55 \cdot 10^{-3} \text{ mol kg}_{\text{cat}}^{-1} \text{ s}^{-1} \text{ bar}^{-2}$ $E_{a,1} = 3.8 \text{ kJ mol}^{-1}$	CO 25.8
	$r_2 = k_2 \left(f_{\text{CH}_3\text{OH}}^2 - \frac{f_{\text{DME}} f_{\text{H}_2\text{O}}}{K_{\text{eq2}}} \right)$	$k_{2,at 523 K} = 8.13 \text{ mol kg}_{\text{cat}}^{-1} \text{ s}^{-1} \text{ bar}^{-2}$	CO ₂ 13.2
	$r_3 = k_3 \left(f_{\text{CO}} f_{\text{H}_2\text{O}} - \frac{f_{\text{CO}_2} f_{\text{H}_2}}{K_{\text{eq3}}} \right)$	k_3 : not given (r_3 at equilibrium)	H ₂ 6.4
	$r_4 = \frac{k_4}{\left(1 + K_{\text{H}_2\text{O}} f_{\text{H}_2\text{O}} \right)^3} \left(f_{\text{CO}} f_{\text{H}_2} - \frac{f_{\text{CH}_3\text{OH}}}{K_{\text{eq4}} f_{\text{H}_2}} \right)$	$k_4, at 523 K = 6.43 \cdot 10^{-7} \text{ mol kg}_{\text{cat}}^{-1} \text{ s}^{-1} \text{ bar}^{-2}$ $E_{a,4} = 171.8 \text{ kJ mol}^{-1}$ $K_{\text{H}_2\text{O}} = 19 \text{ bar}^{-1}$	DME 99.5
C. P. Renk [37]	$r_2 = k_2 c_{\text{CH}_3\text{OH}}^{1,1} - k_{2'} c_{\text{DME}}^{1,2} c_{\text{H}_2\text{O}}$	$k_2 = 5.1 \cdot 10^1 \exp\left(-\frac{0}{R T}\right)$ $k_{2'} = 8.6 \cdot 10^6 \exp\left(-\frac{31}{R T}\right)$	CO 26.8
	$r_3 = k_3 c_{\text{CO}}^{0,2} c_{\text{H}_2\text{O}}^{1,3} - k_{3'} c_{\text{H}_2}^{0,4} c_{\text{CO}_2}^{0,2}$	$k_3 = 1.5 \cdot 10^4 \exp\left(-\frac{0.2}{R T}\right)$ $k_{3'} = 2.6 \cdot 10^9 \exp\left(-\frac{107}{R T}\right)$	CO ₂ 12.4
	$r_4 = k_4 c_{\text{H}_2}^{0,5} c_{\text{CO}}^{0,5} - k_{4'} c_{\text{CH}_3\text{OH}}^{2,4}$	$k_4 = 1.4 \cdot 10^{13} \exp\left(-\frac{138}{R T}\right)$ $k_{4'} = 1.1 \cdot 10^{11} \exp\left(-\frac{44}{R T}\right)$	H ₂ 7.6
		$[E_a] = \text{kJ mol}^{-1}$ $[k_{j'}] = [k_j] = \text{ml g}^{-1} \text{ s}^{-1} \text{ ml}^{n-1} \text{ mol}^{1-n}$	DME 100

Model	Rate expressions	Model specific parameter	RE / %
Y. I. Pyatnit- skii [36]	$r_1 = k_1 \frac{p_{\text{CO}_2} p_{\text{H}_2} \left(1 - \frac{p_{\text{H}_2\text{O}} p_{\text{CH}_3\text{OH}}}{K_1 p_{\text{H}_2} p_{\text{CO}_2}} \right)}{\left(1 + a_3 \frac{p_{\text{H}_2\text{O}}}{p_{\text{H}_2}} + a_1 \sqrt{p_{\text{H}_2}} + a_2 p_{\text{H}_2\text{O}} \right)^3}$	$k_1 = 0.00107 \exp\left(\frac{4414}{T}\right)$ $k_2 = 2.82 \cdot 10^6 \exp\left(-\frac{6938}{T}\right)$ $k_3 = 1.22 \cdot 10^7 \exp\left(-\frac{11398}{T}\right)$	CO 26.6
	$r_2 = k_2 \frac{p_{\text{CH}_3\text{OH}} \left(1 - \frac{p_{\text{DME}} p_{\text{H}_2\text{O}}}{K_2 p_{\text{CH}_3\text{OH}}} \right)}{1 + K_{\text{CH}_3\text{OH}} p_{\text{CH}_3\text{OH}} + \frac{p_{\text{H}_2\text{O}}}{K_{\text{H}_2\text{O}}}}$	$a_1 = 0.499 \exp\left(\frac{2068}{T}\right)$ $a_2 = 6.62 \cdot 10^{-11} \exp\left(\frac{14928}{T}\right)$ $a_3 = 3453.38$ $K_{\text{CH}_3\text{OH}} = 2.20 \cdot 10^{-5} \exp\left(\frac{7738}{T}\right)$ $K_{\text{H}_2\text{O}} = 0.051 \exp\left(\frac{626}{T}\right)$	CO ₂ 18.4
	$r_3 = k_3 \frac{p_{\text{CO}_2} \left(1 - K_3 \frac{p_{\text{H}_2\text{O}} p_{\text{CO}}}{p_{\text{H}_2} p_{\text{CO}_2}} \right)}{1 + a_3 \frac{p_{\text{H}_2\text{O}}}{p_{\text{H}_2}} + a_1 \sqrt{p_{\text{H}_2}} + a_2 p_{\text{H}_2\text{O}}}$	$[a_1] = \text{bar} - 0.5$, $[a_2] = \text{bar}^{-1}$, $[a_3] = -$ $[k_1] = \text{mol g}^{-1} \text{s}^{-1} \text{bar}^{-2}$ $[k_2] = \text{molDME g}^{-1} \text{h}^{-1} \text{bar}^{-1}$ $[k_3] = \text{mol g}^{-1} \text{s}^{-1} \text{bar}^{-1}$ $[K_{\text{CH}_3\text{OH}}] = \text{bar}^{-1}$, $[K_{\text{H}_2\text{O}}] = \text{bar}$	H ₂ 7.3 DME 98.5
A. T. Aguayo [39] (Model I)	$r_2 = k_2 \left(f_{\text{CH}_3\text{OH}}^2 - \frac{f_{\text{DME}} f_{\text{H}_2\text{O}}}{K_2} \right)$	$k_2 = 1.44 \exp\left(-\frac{80.64}{R} \left(\frac{1}{T} - \frac{1}{548} \right)\right)$	CO 35.7
	$r_3 = k_3 \left(f_{\text{CO}} f_{\text{H}_2\text{O}} - \frac{f_{\text{CO}_2} f_{\text{H}_2}}{K_3} \right)$	k_3 not given (r_3 in equilibrium) $k_4 = 1.91 \cdot 10^{-6} \exp\left(-\frac{11.3}{R} \left(\frac{1}{T} - \frac{1}{548} \right)\right)$ $k_5 = 2.04 \cdot 10^{-7} \exp\left(-\frac{15.92}{R} \left(\frac{1}{T} - \frac{1}{548} \right)\right)$	CO ₂ 9.9
	$r_4 = k_4 \left(f_{\text{CO}} f_{\text{H}_2}^2 - \frac{f_{\text{CH}_3\text{OH}}}{K_4} \right)$	$[E_a] = \text{kcal mol}^{-1}$	H ₂ 7.3
	$r_5 = k_5 \left(f_{\text{CO}} f_{\text{H}_2}^3 - \frac{f_{\text{HC}} f_{\text{H}_2\text{O}}}{K_5} \right)$	$[k_2] = \text{molDME (molH}_2\text{)}^{-1} \text{g}_{\text{cat}}^{-1} \text{h}^{-1} \text{bar}^{-2}$ $[k_4] = \text{molCH}_3\text{OH (molH}_2\text{)}^{-1} \text{g}_{\text{cat}}^{-1} \text{h}^{-1} \text{bar}^{-3}$ $[k_5] = \text{molHC (molH}_2\text{)}^{-1} \text{g}_{\text{cat}}^{-1} \text{h}^{-1} \text{bar}^{-4}$	DME 127.2

A.4 Selectivity

The selectivity towards DME is displayed here in Figs. A.2 and A.3 complementary to Figs. 1, 2 and 4 of the manuscript.

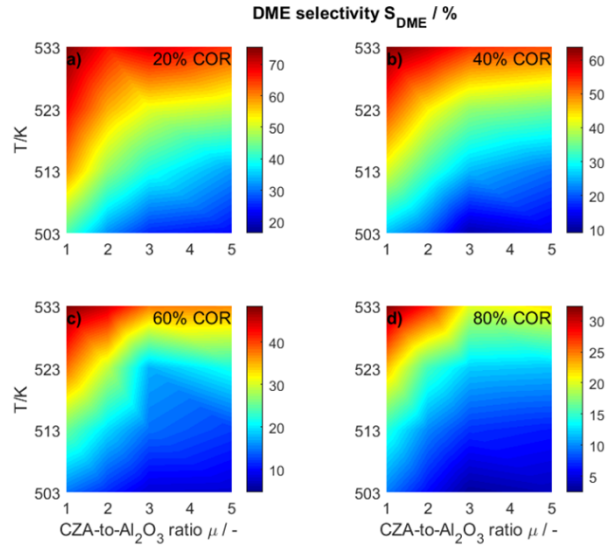


Figure A.2: DME selectivity determined experimentally and plotted as a function of the temperature (T) and the CZA-to- γ - Al_2O_3 ratio (μ) for CORs of **a)** 20 % **b)** 40 % **c)** 60 % **d)** 80 %.

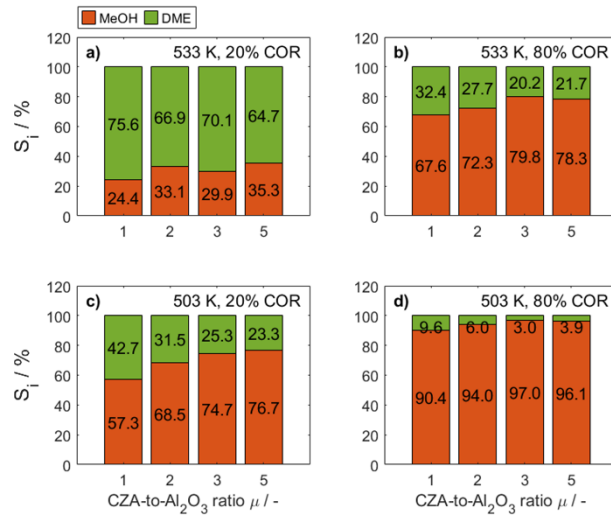


Figure A.3: Selectivity of methanol and DME at specific conditions: **a)** 533 K, 20 % COR, **b)** 533 K, 80 % COR, **c)** 492 K, 20 % COR **d)** 492 K, 80 % COR.

A.5 Mole percentage profiles including CO and CO₂

The concentration profiles of CO and CO₂ are shown here (Figures A.4 to A.7) for the sake of completeness.

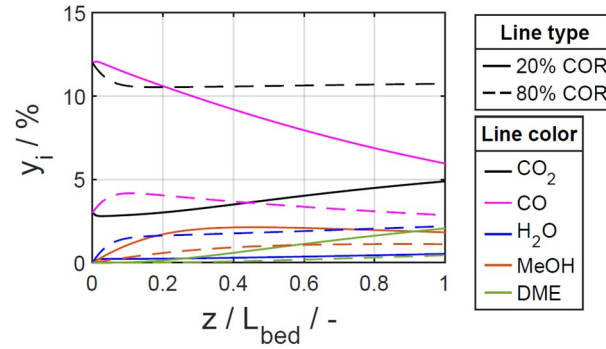


Figure A.4: Mole percentage profiles of CO, CO₂, water, methanol and DME at $T = 533$ K, $\mu = 2$. (—) Solid lines: 20% COR, (- - -) Dashed lines: 80% COR.

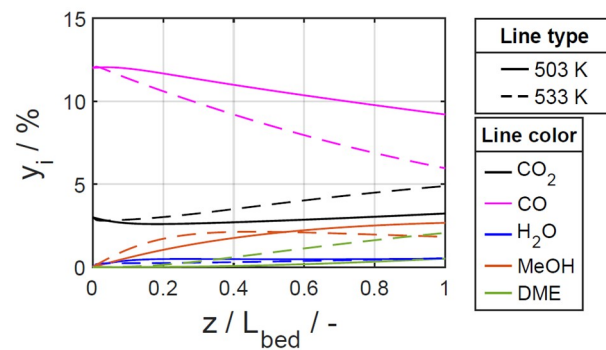


Figure A.5: Mole percentage profiles of CO, CO₂, water, methanol and DME at $\mu = 2$ and COR = 20%. (—) Solid lines: $T = 503$ K, (- - -) Dashed lines: $T = 533$ K

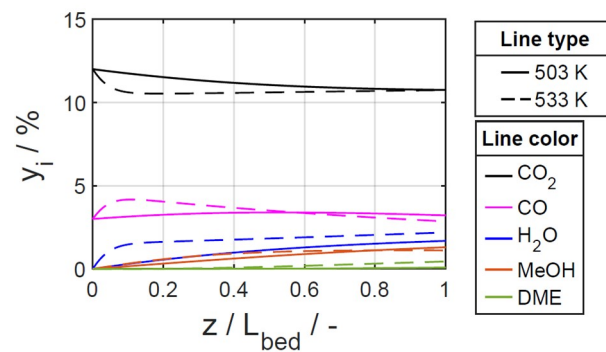


Figure A.6: Mole percentage profiles of CO, CO₂, water, methanol and DME at $\mu = 2$ and COR = 80%. (—) Solid lines: $T = 503$ K, (- - -) Dashed lines: $T = 533$ K

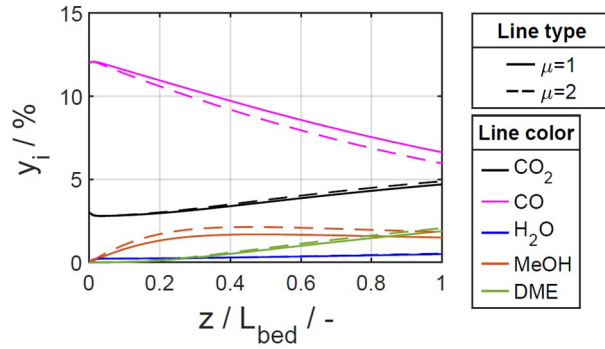


Figure A.7: Mole percentage profiles of CO, CO₂, water, methanol and DME at $T = 533$ K, COR = 20%. (—) Solid lines: $\mu = 1$, (- - -) Dashed lines: $\mu = 2$

A.6 Non re-parametrized model specific parameters

The non re-parametrized model specific parameters are listed in Table A.3 complementary to Table 2.4.

Table A.3: Estimated parameters in non re-parametrized form.

Reaction	$k_{0,j}$	$E_{A,j}$
CO ₂ hydrogenation	24.47 $\frac{\text{mol}}{\text{kg s bar}^4}$	32.6 J mol ⁻¹
MeOH dehydration	0.003 $\frac{\text{mol}}{\text{kg s bar}^2}$	105.7 J mol ⁻¹
WGSR	5.93 $\frac{\text{mol}}{\text{kg s bar}^2}$	175.3 J mol ⁻¹
Adsorbate	K_i	$\Delta H_{\text{ads},i}$
CO ₂	107.9 bar ⁻¹	-5.3 J mol ⁻¹
CO	1.52 bar ⁻¹	-343 J mol ⁻¹
H ₂	1238 bar ⁻¹	-21 J mol ⁻¹

A.7 Overview of selected studies conducted at different CZA-to- γ -Al₂O₃ ratios

Table A.4: Overview of selected studies conducted at different CZA-to- γ -Al₂O₃ ratios

Study named after - first author	Catalyst system and properties	Feed, conditions, reactor,* catalyst particle size	Optimal catalyst bed composition**
R. Pelaez et al. [32]	- CZA: CHEMPACK S _{BET} : m ² g ⁻¹ Pore volume: 0.257 cm ³ g ⁻¹ - γ -Al ₂ O ₃ : BASF S _{BET} : 239.9 m ² g ⁻¹ Pore volume: 0.545 cm ³ g ⁻¹	CO/CO ₂ /H ₂ 250-270 C, 30 bar, 0.067-0.244 kgh/Nm ³ 100-250 μ m CZA/ γ -Al ₂ O ₃ : 70/30, 85/15, 92.5/7.5 %	CZA/ γ -Al ₂ O ₃ :92.5/7.5 % regarding CO conversion and DME yield
N. Delgado Otalvaro et al. [1]	Commercial CZA/ γ -Al ₂ O ₃	CO/CO ₂ /H ₂ /Inert 220-260 C, 50 bar, 200-700 Nm ³ /min, 250-500 μ m (model-based optimization)	65.5 % CZA, 34.5 % γ -Al ₂ O ₃ (v.) without dilution. Regarding conversion of CO _x and DME yield
K. L. Ng et al. [41]	- CZA - γ -Al ₂ O ₃ : Norton Chemicals Co.	CO/CO ₂ /H ₂ /He, 250 C, 50 bar, 27500 h ⁻¹ , Gradientless, internal-recycle-type reactor, stacked catalysts, 250-500 μ m, CZA/ γ -Al ₂ O ₃ : 1/0, 1/0.5, 1/1, 1/2	CZA/ γ -Al ₂ O ₃ : 1/2 regarding DME yield***
C. Peinado et al. [75]	-CZA: Katalco 51-8 - γ -Al ₂ O ₃ : Alfa Aesar bimodal S _{BET} : 220-280 m ² g ⁻¹	CO/CO ₂ /H ₂ , 270-290 C, 25-50 bar, 5000-7500 h ⁻¹ , 250-300 μ m, CZA/ γ -Al ₂ O ₃ : 90/10, 50/50, 10/90	CZA/ γ -Al ₂ O ₃ : 50/50 regarding DME productivity
J. W. Bae et al. [94]	- CZA: prod. in-house CuO/ZnO/Al ₂ O ₃ =50/40/10 - γ -Al ₂ O ₃ : prod. in-house S _{BET} : 437.8 m ² g ⁻¹	CO/CO ₂ /H ₂ : 41/21/38 v. %, 250 C, 40 bar, 11000 h ⁻¹ Pellet form hybrid catalyst CZA/ γ -Al ₂ O ₃ : 1, 3, 5	CZA/ γ -Al ₂ O ₃ : 1 Regarding the DME selectivity CZA/ γ -Al ₂ O ₃ : 5 Regarding the CO conversion

Study named after - first author	Catalyst system and properties	Feed, conditions, reactor, catalyst particle size	Optimal catalyst bed composition**
J. Abu-Dahrieh et al. [106]	-CZA: prod. in-house CuO/ZnO/Al ₂ O ₃ =60/30/10 S _{BET} : 56.9 m ² g ⁻¹ pore size: 1.05 nm - NH ₄ ZSM-5, HZSM-5 and γ-Al ₂ O ₃ γ-Al ₂ O ₃ : prod. in-house, S _{BET} : 117 m ² g ⁻¹ , Pore size = 1.035 nm	CO/CO ₂ /H ₂ /Ar: 31/4/62/3 v. %, 200-260 C, 20 bar, 2400 ml g ⁻¹ h ⁻¹ , 250-425 μm, admixed catalyst, CZA/γ-Al ₂ O ₃ : 1, 2, 3	CZA/γ-Al ₂ O ₃ : 1 and CZA/HZSM-5: 3 regarding the DME yield
A. Ateka et al. [92]	Comparison of different commercial and in-hose made catalyst systems - CuO-ZnO-ZrO ₂ , CuO-ZnO-MnO, and CuO/ZnO/Al ₂ O ₃ CZA: S _{BET} : 24 m ² g ⁻¹ , Pore volume: 0.081 cm ³ g ⁻¹ Cu dispersion: 5.2 % - SAPO-18 and γ-Al ₂ O ₃ SAPO-18: S _{BET} : 480 m ² g ⁻¹ , Pore volume: 0.39 cm ³ g ⁻¹ Total acidity: 0.42 mmolNH ₃ /gcat	CO/CO ₂ /H ₂ , 275 C, 30 bar, 3.7 g h (molC) ⁻¹ , 125-500 μm, Bifunctional catalysts CZA/SAPO-18: 1, 2, 5, 10	CZA/SAPO-18: 2 regarding yield and selectivity of DME for CO ₂ free feeds (H ₂ /CO=3)

* The reactor type is a fixed bed tubular reactor, with mechanically mixed catalyst bed unless otherwise stated

** percentages and ratios in weight, unless otherwise stated

*** In this study the mass of CZA was held constant while the mass of γ-Al₂O₃ was increased to achieve a higher γ-Al₂O₃-to-CZA ratio. Hence, the γ-Al₂O₃-to-CZA ratio leading to the highest performance was the case at which the total catalyst mass was also the highest.

APPENDIX B. Additional Results on Data-based Model

B.1 Selected ANN and model specific parameters

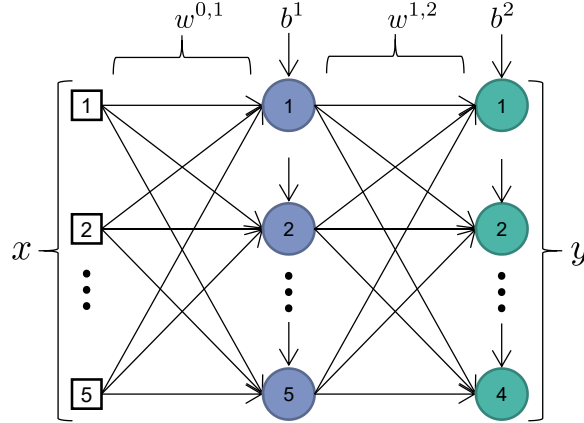


Figure B.1: Schematic representation of selected network architecture.

Table B.1: Model specific parameters of the chosen ANN. Connection weights of the input and hidden layer, biases of the hidden layer.

$\mathbf{W}_{i,h}$					\mathbf{b}_h
-0,5976	-3,3548	1,2525	0,6804	0,8233	2,8645
0,2729	17,1032	-14,0036	-0,2476	-0,0765	-1,3391
0,0559	0,4986	-2,8614	-0,0755	-0,0333	-0,2824
0,5491	5,5599	-0,9823	-1,0014	-1,3748	-3,5558
0,0695	10,9542	-8,9659	0,5755	-0,0215	-2,0255

B.2 Evaluation of the Selected ANN

Figure 3.10 in Chapter 3 displays simulation and experimental results in the temperature range between 180 and 300 °C. Complementary to this diagram, Figures B.2 to B.6 show the results for the remaining inlet feed compositions. The pressure is in all cases $p=5$ MPa.

Table B.2: Model specific parameters of the chosen ANN. Connection weights of the hidden and output layer, biases of the output layer.

$W_{h,o}$					b_o
1,0382	-0,9904	-1,9922	0,2485	1,8171	-0,2077
4,5827	-4,4135	-2,2968	1,2669	5,5258	-3,3151
-3,8560	5,2258	0,0799	-1,0704	-5,5635	2,7647
-6,7329	4,5728	0,1974	-1,8899	-5,7006	5,5805

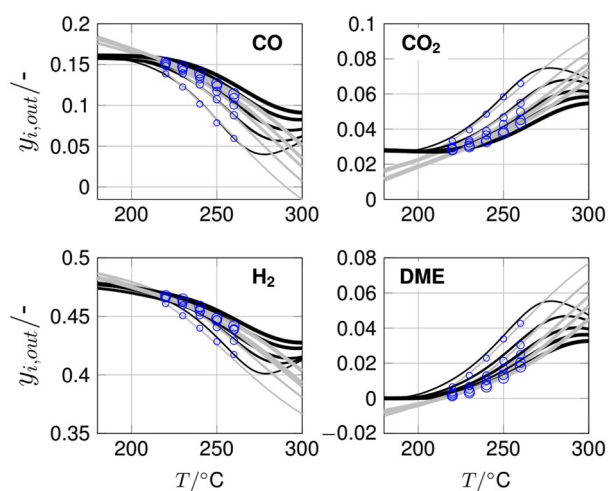


Figure B.2: Components mole fraction in the product gas. Feed: 16.1 % CO, 2.8 % CO₂, 48.8 % H₂, 32.3 % inert gas (Ar and N₂).

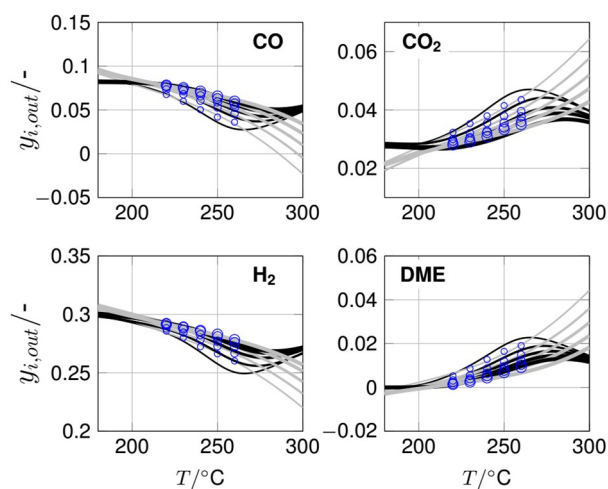


Figure B.3: Components mole fraction in the product gas. Feed: 8.4 % CO, 2.9 % CO₂, 30.3 % H₂, 58.4 % inert gas (Ar and N₂).

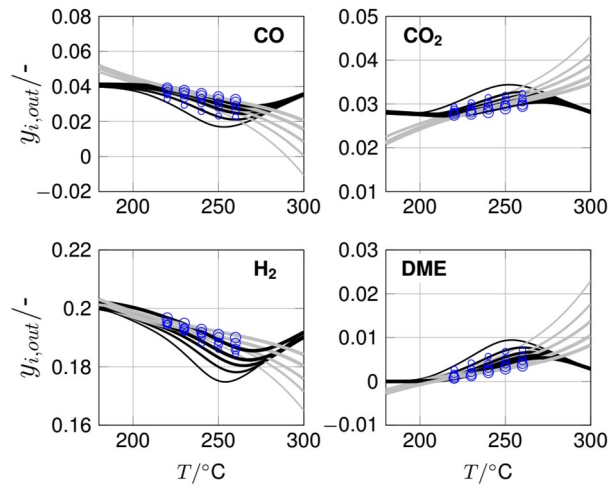


Figure B.4: Components mole fraction in the product gas. Feed: 4.1 % CO, 2.9 % CO₂, 20.3 % H₂, 72.7 % inert gas (Ar and N₂).

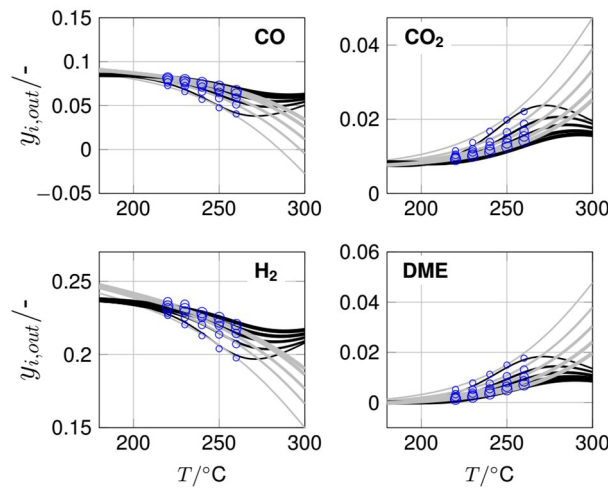


Figure B.5: Components mole fraction in the product gas. Feed: 8.6 % CO, 0.8 % CO₂, 24.0 % H₂, 66.6 % inert gas (Ar and N₂).

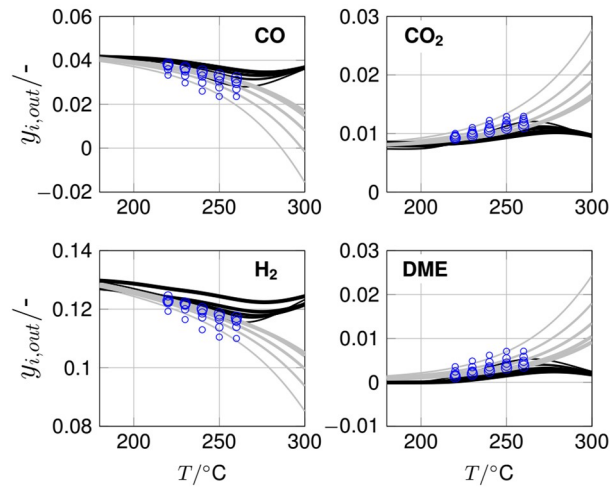


Figure B.6: Components mole fraction in the product gas. Feed: 4.3 % CO, 0.8 % CO₂, 13.1 % H₂, 81.8 % inert gas (Ar and N₂).

APPENDIX C. Additional Results on Hybrid Model

C.1 ANN of hybrid model

The model specific parameters of the ANN-HMs discussed in the manuscript (ANN-HM with 5, 26 and 28 HNs) are given in this section. Specifically, these are the connection weights between the input and the hidden layer ($W_{i,h}$) and between the hidden and the output layer ($W_{h,o}$), as well as the biases of the hidden and outputs neurons (b_h and b_o) as shown in Figure C.1.

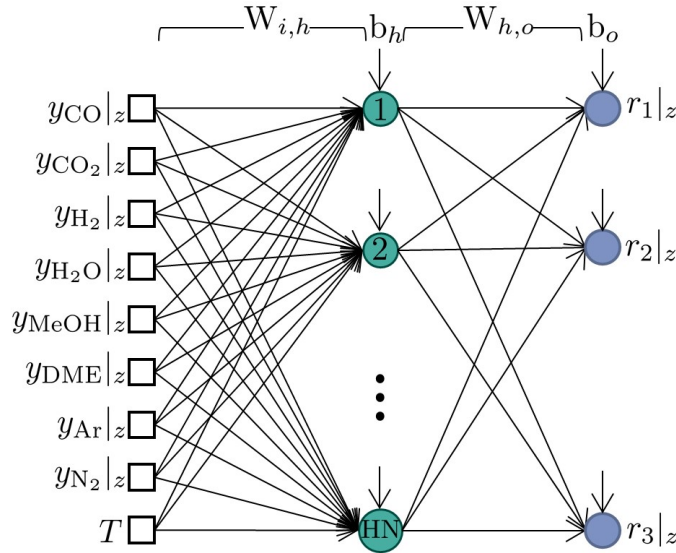


Figure C.1

Table C.1: Model specific parameters of the ANN-HM with 5 HNs. Connection weights of the input and hidden layer, biases of the hidden layer.

$W_{i,h}$									b_h
-0.60114	0.14025	-0.63213	0.80736	0.08968	-0.04125	-0.27108	0.00641	-0.43090	3.10519
-1.14673	0.65526	1.31330	1.05803	0.01463	-0.00635	-0.26234	0.05774	-0.44970	3.95600
-3.02931	-0.02462	-3.53521	0.79813	0.04093	19.72959	-3.39553	-0.23304	-1.22452	20.09301
3.98021	-5.89989	0.18136	-1.04395	-0.77207	-0.14084	0.37947	0.21915	0.88733	-7.69831
2.60925	0.85926	2.62343	0.47530	-1.60951	-18.55797	3.14491	0.16885	1.05177	-19.56385

C.2 Interpolation of hybrid model at complementary feed compositions

Table C.2: Model specific parameters of the ANN-HM with 5 HNs. Connection weights of the hidden and output layer, biases of the output layer.

$\mathbf{W}_{h,o}^{-1}$			\mathbf{b}_o
-14.986096	-16.498396	-14.484296	2.8317
4.86557018	5.96789325	4.68863279	10.1015
6.23236401	-0.5675959	-0.8749624	10.0811
-11.948762	-13.012473	-11.014278	
8.14194045	0.55032097	-1.1746633	

Table C.3: Model specific parameters of the chosen ANN-HM with 26 HNs. Connection weights of the input and hidden layer, biases of the hidden layer.

$\mathbf{W}_{i,h}$									\mathbf{b}_h
0.26106	0.12391	0.82471	0.33482	-0.72017	-0.16497	-0.19633	-0.32429	0.86960	-0.36237
0.19960	0.28507	-1.86320	0.22985	-0.67681	-1.02954	0.16398	0.11994	0.36954	-1.43625
-1.16703	-1.23930	1.94422	0.56587	0.49974	0.16683	1.36101	0.10762	0.45637	-1.66672
0.20960	0.84537	0.24244	0.16916	2.68825	-2.82029	0.66726	-0.00679	2.02909	-4.48702
0.09335	0.43959	-0.34136	0.30138	-0.16581	-0.58593	-0.26262	-0.07968	-1.58115	0.47128
0.00205	0.06033	-0.14307	-0.04459	0.11140	-0.40748	0.06257	-0.22526	0.28571	-0.02085
0.16260	0.45512	2.20344	-0.94117	-0.25011	-0.46153	0.34534	-0.03916	0.32684	-2.61076
-0.24824	-0.39428	0.83872	-0.18088	0.37006	-0.00575	0.06836	0.20577	-1.22799	1.04678
0.06642	0.20981	0.64012	0.33408	-0.77574	-1.37976	0.24136	-0.16015	0.97653	-1.36315
-0.22450	-0.46566	-0.82017	-0.21527	1.06934	0.04703	-0.35663	0.05209	-1.94161	3.53783
0.35660	0.70139	-0.16036	-0.35555	0.14775	0.37536	0.00984	0.08682	1.31660	-2.49721
-0.56388	-0.14535	0.24360	0.31073	-0.98601	-0.13431	0.77766	0.02603	0.25057	-1.83903
-0.79324	1.26824	1.96136	-1.87042	0.29754	0.27066	0.87333	0.10029	1.36528	-2.69636
0.85912	1.50609	-2.13724	-0.40449	-0.68632	-0.33117	-1.34989	-0.21578	-0.16249	2.31635
1.18093	0.13571	-2.43287	-0.26083	0.13894	-0.98120	-0.62123	-0.01411	0.16473	-0.56915
0.13604	0.99348	-0.45484	-0.78550	-0.55885	-1.27551	0.17066	0.31817	0.22216	-1.61553
0.21975	0.25746	-1.96152	0.22746	-0.90822	0.80587	-0.28249	-0.00652	-1.18703	0.06408
0.46520	0.10702	0.07642	0.22147	0.77300	0.61035	-0.50695	-0.01416	0.11848	0.16956
0.25148	0.94812	-0.01635	-0.31923	-0.37376	-0.26056	-0.16762	0.11647	-0.40989	-1.07456
0.65769	0.69521	-0.14171	-0.00214	0.16558	0.92229	-0.69206	-0.32748	-0.59464	-0.22123
0.47396	-0.10615	0.40137	0.06801	0.67045	0.12422	-0.72975	-0.20161	-1.00531	2.23222
0.27067	-0.45266	-1.49560	-0.23085	0.80500	-0.47034	0.42334	0.07572	0.62688	-2.28619
-0.30719	-0.34633	0.06663	1.04917	0.81328	0.10817	0.47108	-0.04857	1.04581	-1.57837
0.57060	0.64921	-1.08245	-0.15155	-0.39120	0.14038	-0.56275	-0.03471	-0.73006	0.16251
0.19670	-0.23625	-0.58807	0.57185	-0.11151	0.01358	-0.15972	0.04672	0.66813	0.32134
0.12129	-0.23764	-2.28032	1.35823	-0.28722	-0.20917	-0.11084	-0.00218	-0.25148	0.02584

Table C.4: Model specific parameters of the ANN-HM with 26 HNs. Connection weights of the hidden and output layer, biases of the output layer.

$\mathbf{W}_{h,o}^{-1}$			\mathbf{b}_o
0.6009	-0.1806	0.2787	-0.2325
-1.5689	0.0367	1.3037	-0.8352
0.5055	1.0450	1.8062	-0.4410
-0.2549	4.9671	0.2776	
-0.9679	0.4391	0.1689	
-0.5245	-0.2991	-0.3791	
1.4918	-0.1403	1.6442	
-0.5030	-1.7649	-0.2364	
-0.4736	-2.2558	-0.4178	
-1.6924	2.0570	0.3809	
2.9428	1.3525	0.0294	
0.7372	0.6209	-1.2581	
-2.6214	-1.4086	0.8564	
0.2751	1.0030	2.0603	
1.5861	2.0752	0.7404	
2.0191	0.6807	-0.0775	
0.3512	-1.8184	-0.0947	
-0.0987	0.2139	1.2012	
-2.3025	-1.8966	-1.4302	
0.4858	0.0648	-0.4688	
1.6234	0.2751	-0.5682	
-1.1198	-2.5540	-2.5515	
-1.5483	-1.0474	-1.0012	
-1.1105	-1.1005	-0.8157	
0.1349	-0.3539	-1.0865	
1.1528	-0.0161	-0.9238	

Table C.5: Model specific parameters of the ANN-HM with 28 HNs. Connection weights of the input and hidden layer, biases of the hidden layer.

$\mathbf{W}_{i,h}$									\mathbf{b}_h
0.46664	0.28557	0.43946	-0.00902	-0.16684	0.54786	-0.43955	0.21328	-0.19793	-0.16975
0.60392	0.25781	-0.59811	-1.10325	-0.45429	0.44810	-0.66461	-0.11598	0.98309	1.48690
0.07021	-0.02014	0.00078	0.01422	0.72290	-0.30191	-0.02811	0.14087	0.04316	-0.13027
-0.65256	-0.60885	-0.01501	-0.47318	0.50558	-0.77336	0.62161	0.16996	0.63660	0.93549
-0.19340	0.37544	-1.33623	0.05289	-0.24590	0.51843	-0.46170	-0.06380	-1.95280	2.33584
-0.12152	-0.18302	-1.03475	0.82643	0.44755	0.75689	0.47722	-0.03124	1.65909	-2.46539
0.04288	0.29545	0.68057	-0.10564	0.35736	-0.67963	-0.00200	-0.39468	0.95627	-0.38664
-0.56356	0.67832	2.15088	-0.97097	2.05435	-0.92779	0.52143	0.00043	1.51639	-0.88890
-0.57398	-0.33225	-0.48717	0.55994	-0.00700	1.28148	0.26237	-0.00604	-0.04937	0.32635
0.48020	-0.09632	1.15148	0.49759	-0.08547	1.44197	-0.99544	-0.29592	-0.29415	2.49784
-0.49102	-0.47841	0.52580	-0.25073	0.55789	-0.56585	0.53654	0.08371	0.09385	-0.09893
-0.18325	-0.13461	0.47380	-0.18808	0.43415	-0.08744	0.13086	0.05678	0.17174	0.11998
-0.06853	0.28728	0.73074	-0.53532	0.24692	-0.38353	-0.01040	-0.14186	-0.69265	0.32885
-0.24823	-0.48929	0.60280	-0.27136	1.18187	-1.33482	-0.17447	-0.01340	-1.50596	3.43600
-0.75584	-0.31503	1.63727	0.08533	1.34722	-0.20588	0.42242	-0.18111	0.90560	0.94341
-1.28804	-0.83502	-1.31090	-0.65176	-0.91017	-1.24448	1.05639	0.28885	-0.59850	1.50718
-0.44566	-0.36471	1.78173	-0.59253	0.53608	0.07252	0.27134	-0.01676	0.84184	0.93740
0.73352	-0.90533	-1.51640	2.18375	0.16292	-1.12499	-0.88997	-0.03892	-1.02122	2.41060
1.49650	1.85872	-2.08273	-2.02300	0.28420	-0.19405	-2.46870	-0.23513	-0.77545	6.15865
-0.44727	-0.36909	-0.31667	-0.18004	-0.21224	1.43467	0.19270	-0.01945	0.35410	0.54217
-0.17363	-0.40172	0.07947	0.27894	-0.19348	-0.23665	0.17962	0.07693	0.10611	0.02526
-0.07722	0.60267	-1.06913	-0.95967	0.15029	-0.05226	0.62780	0.02814	0.57058	-3.35825
-0.86457	0.74219	3.77944	-1.28672	0.87443	-0.04660	0.54564	0.00464	0.77024	-0.37002
-0.57021	-0.43266	-1.12872	0.23752	-0.51371	-0.83880	0.80082	0.27356	0.13021	-1.04363
-0.22845	0.49498	1.06860	-0.88429	0.87760	0.09871	0.36785	-0.10285	1.83416	-1.25260
0.09510	-0.11401	0.15330	0.24541	0.33723	-0.14926	-0.07379	0.13185	-0.16622	0.02456
0.49600	0.60806	-1.44494	-0.91344	-0.63084	-0.42098	-0.15879	0.11993	0.01247	-0.91623
0.25459	-0.19486	-0.00958	0.53563	0.49777	-0.08896	-0.23045	-0.21662	-0.94394	0.13169

Table C.6: Model specific parameters of the ANN-HM with 28 HNs. Connection weights of the hidden and output layer, biases of the output layer.

	$\mathbf{W}_{h,o}^{-1}$		\mathbf{b}_o
0.04726	-0.79667	0.43343	0.1063
-1.19233	-0.88727	0.03829	-0.6298
-0.69891	-0.61537	-0.24272	-0.4188
1.02313	1.75151	0.62214	
-1.01982	-1.59516	-0.84936	
-1.76369	-1.66547	-1.24119	
-0.25505	-1.44239	0.32571	
-1.59085	2.50186	0.09647	
-0.49080	0.93114	1.42095	
1.28131	0.54790	-0.37088	
0.28152	-1.14893	-0.84685	
0.13544	-0.88629	0.25524	
-1.00940	-0.10411	1.01269	
-3.10077	1.21421	0.07743	
1.35216	1.63563	-0.66500	
-1.00380	-1.34031	0.03127	
-0.13046	1.07453	1.51489	
2.51110	0.87342	-2.01953	
0.93582	1.24484	2.61213	
-0.03322	-1.04785	-1.38058	
0.18938	-0.40356	-0.61202	
0.13238	-1.13961	-2.50424	
0.15077	-3.01093	-0.01719	
-0.51431	-1.25468	-0.09573	
1.28006	-0.24813	-0.14723	
-0.35293	-0.46369	-0.09210	
2.32963	1.98265	-0.13629	
-0.50319	-0.76767	-0.46772	

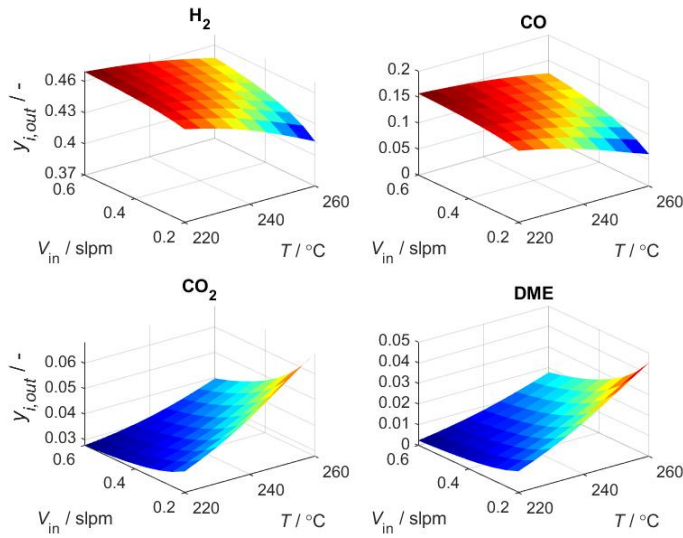


Figure C.2: Surface response for the hybrid model predictions of the mole fractions of H_2 , CO , CO_2 and DME within the validity range of the temperature and total gas flow. Feed composition: 48.0 % H_2 , 16.11 % CO , 2.88 % CO_2 . Pressure 50 bar. CZA-to- $\gamma\text{-Al}_2\text{O}_3$ -ratio $\mu = 1$. ANN-HM with 26 HNs.

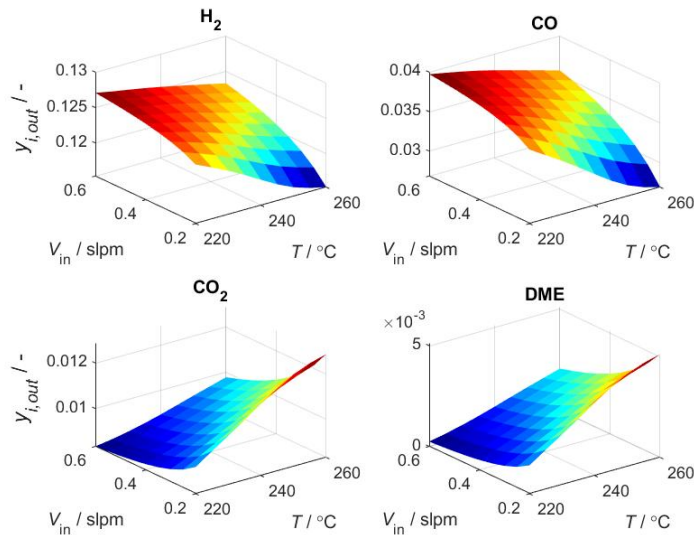


Figure C.3: Surface response for the hybrid model predictions of the mole fractions of H_2 , CO , CO_2 and DME within the validity range of the temperature and total gas flow. Feed composition: 13.05 % H_2 , 4.10 % CO , 0.86 % CO_2 . Pressure 50 bar. CZA-to- $\gamma\text{-Al}_2\text{O}_3$ -ratio $\mu = 1$. ANN-HM with 26 HNs.

C.3 Complementary Figures

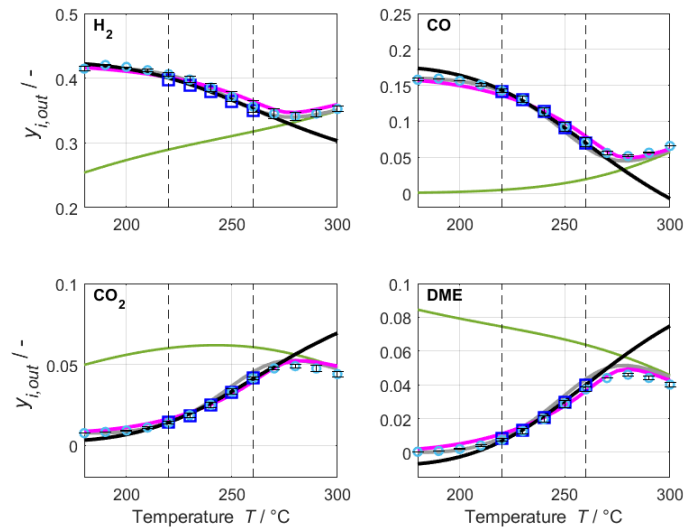


Figure C.4: Range extrapolation of the temperature. Nominal feed composition: 42.3 % H_2 , 16.1 % CO , 0.82 % CO_2 . Total gas flow 0.2 slpm. Pressure 50 bar. CZA-to- $\gamma\text{-Al}_2\text{O}_3$ -ratio $\mu = 1$. ANN-HM with 5 HNs.

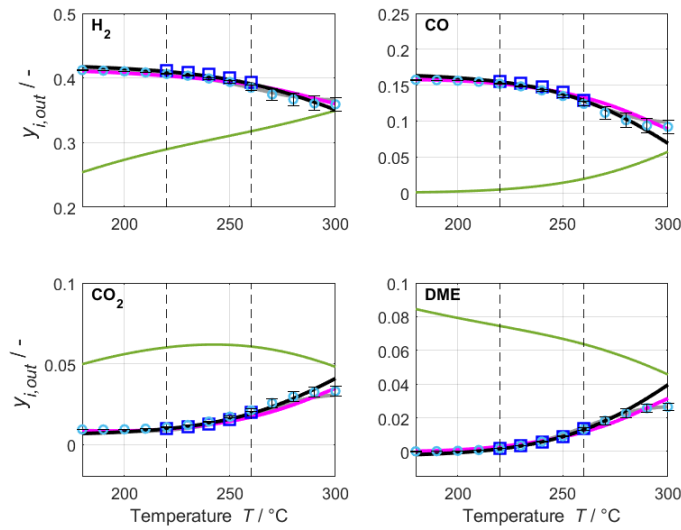


Figure C.5: Range extrapolation of the temperature. Nominal feed composition: 42.3 % H_2 , 16.1 % CO , 0.82 % CO_2 . Total gas flow 0.6 slpm. Pressure 50 bar. CZA-to- $\gamma\text{-Al}_2\text{O}_3$ -ratio $\mu = 1$. ANN-HM with 5 HNs.

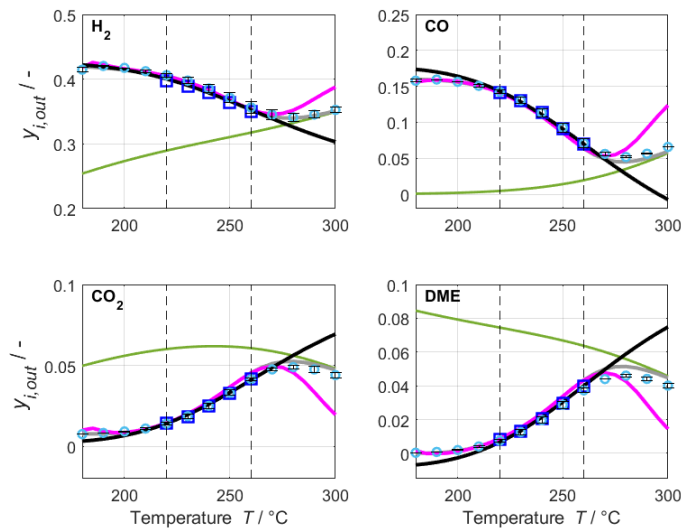


Figure C.6: Range extrapolation of the temperature. Nominal feed composition: 42.3 % H_2 , 16.1 % CO , 0.82 % CO_2 . Total gas flow 0.2 slpm. Pressure 50 bar. CZA-to- $\gamma\text{-Al}_2\text{O}_3$ -ratio $\mu = 1$. ANN-HM with 28 HNs.

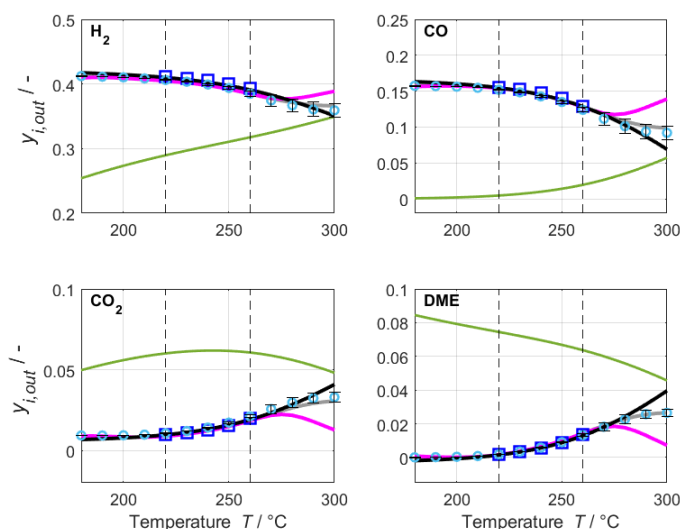


Figure C.7: Range extrapolation of the temperature. Nominal feed composition: 42.3 % H_2 , 16.1 % CO , 0.82 % CO_2 . Total gas flow 0.6 slpm. Pressure 50 bar. CZA-to- γ - Al_2O_3 -ratio $\mu = 1$. ANN-HM with 28 HNs.

C.4 A priori Criteria

A priori criteria were employed for ruling out mass and heat transport limitations. These criteria were calculated for temperatures between 180-300 °C and total gas flows between 0.15-0.8 slpm. The values calculated for the worst case scenarios are given in Table C.7 for each reaction, and show that mass and heat transport limitations do not play a significant role at the evaluated operating conditions.

C.5 Experimental values

The experimental values measured for validation of the simulation results at extrapolated conditions are given in Table C.8.

C.6 Catalyst conditioning and deactivation

Figure C.8 shows the CO_x -conversion (X_{CO_x}) as a function of the Time-On-Stream (ToS) for a reference operating point measured at 513 K, 50 bar and 0.4 slpm. Within the first 25 hours the reaction conditions were left constant at 513 K, 50 bar and 0.4 slpm. After that, the conditions were varied dynamically between 453-573 K, 40-60 bar and 0.15-0.8 slpm. After 129 hours the experiments for model validation at 453-573 K, 40-60 bar as well as 0.15-0.8 slpm were taken. Between the ToS of 129 and 160 hours,

Table C.7: Calculated a priori criteria for determination of transport limitations.

Phenomenon	Equation [158]	Max. Calculated Value
Outer mass transfer	$\frac{r_{j,eff} n }{a'k_f c_b} < 0.05$	For reaction 1: $3.29 \cdot 10^{-5}$ For reaction 2: $2.09 \cdot 10^{-5}$ For reaction 3: $5.74 \cdot 10^{-5}$
Outer heat transfer	$\frac{E_A}{RT_b} \left \frac{-\Delta H_R}{hT_b} \right \frac{r_{j,eff}}{a'} < 0.05$	For reaction 1: $4.75 \cdot 10^{-4}$ For reaction 2: $3.09 \cdot 10^{-4}$ For reaction 3: $4.97 \cdot 10^{-4}$
Inner mass transfer	$\frac{r_{j,eff}L^2(n+1)}{D_{eff}c_s} < 0.15$	For reaction 1: $4.62 \cdot 10^{-4}$ For reaction 2: $2.93 \cdot 10^{-4}$ For reaction 3: $8.06 \cdot 10^{-4}$
Inner heat transfer	$\frac{E_A}{RT_b} \left \frac{-\Delta H_R}{\lambda_{eff,p}T_b} \right r_{j,eff}L^2 < 0.1$	For reaction 1: $4.28 \cdot 10^{-5}$ For reaction 2: $2.78 \cdot 10^{-5}$ For reaction 3: $4.48 \cdot 10^{-5}$

where the experiments were conducted, the X_{CO_x} remains stable with a relative deviation of 10 % between the minimal and maximal measured X_{CO_x} .

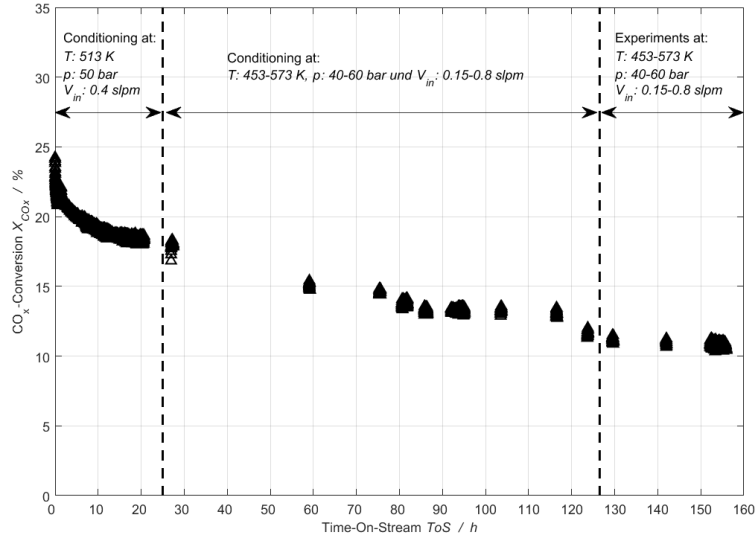


Figure C.8: The CO_x-conversion (X_{CO_x}) as a function of the Time-On-Stream (ToS) for a reference operating point measured at 513 K, 50 bar and 0.4 slpm.

Table C.8: Experimental values measured for validation of simulation results at extrapolated conditions. The catalyst bed consisted of 1.007g CZA, 0.9996 g γ -Al₂O₃, 9.98 g SiC, and it was 7.8 cm long.






$y_{i,in}$					Conditions					$y_{i,out}$					Standard Deviation $y_{i,out}$						
H ₂ %	CO %	CO ₂ %	N ₂ %	T °C	\dot{V}_{in} slpm	p bar	H ₂ %	CO %	H ₂ O %	CO ₂ %	MeOH %	DME %	N ₂ %	H ₂ %	CO %	H ₂ O %	CO ₂ %	MeOH %	DME %	N ₂ %	
37.7	15.2	0.8	46.2	180	0.20	50	41.47	15.79	0.09	0.75	0.16	0.04	41.71	0.35	0.19	0.01	0.01	0.01	0.01	0.00	0.53
37.7	15.2	0.8	46.2	190	0.20	50	42.04	15.95	0.10	0.83	0.23	0.08	40.77	0.07	0.00	0.01	0.02	0.03	0.03	0.01	0.14
37.7	15.2	0.8	46.2	200	0.20	50	41.75	15.63	0.10	0.92	0.32	0.20	41.09	0.02	0.05	0.01	0.03	0.06	0.06	0.02	0.05
37.7	15.2	0.8	46.2	210	0.20	50	41.23	15.07	0.11	1.10	0.38	0.41	41.70	0.18	0.15	0.01	0.04	0.08	0.08	0.05	0.14
37.7	15.2	0.8	46.2	220	0.20	50	40.62	14.25	0.12	1.40	0.43	0.75	42.43	0.31	0.27	0.02	0.08	0.09	0.09	0.09	0.31
37.7	15.2	0.8	46.2	230	0.20	50	39.78	13.05	0.17	1.86	0.47	1.26	43.42	0.47	0.42	0.03	0.12	0.08	0.14	0.14	0.51
37.7	15.2	0.8	46.2	240	0.20	50	38.56	11.35	0.23	2.50	0.52	1.97	44.86	0.69	0.59	0.04	0.16	0.06	0.21	0.21	0.81
37.7	15.2	0.8	46.2	250	0.20	50	37.11	9.26	0.28	3.30	0.57	2.88	46.61	0.76	0.63	0.01	0.17	0.03	0.22	0.22	0.97
37.7	15.2	0.8	46.2	260	0.20	50	35.63	7.09	0.28	4.15	0.59	3.73	48.53	0.85	0.58	0.01	0.10	0.01	0.14	0.14	1.16
37.7	15.2	0.8	46.2	270	0.20	50	34.51	5.61	0.27	4.75	0.58	4.40	49.89	0.79	0.30	0.00	0.07	0.00	0.00	0.00	1.16
37.7	15.2	0.8	46.2	280	0.20	50	34.11	5.17	0.26	4.89	0.56	4.60	50.40	0.66	0.13	0.01	0.14	0.00	0.09	0.09	1.01
37.7	15.2	0.8	46.2	290	0.20	50	34.53	5.63	0.27	4.75	0.54	4.41	49.86	0.57	0.03	0.02	0.17	0.00	0.12	0.12	0.89
37.7	15.2	0.8	46.2	300	0.20	50	35.26	6.58	0.29	4.40	0.51	4.01	48.96	0.45	0.02	0.00	0.17	0.00	0.14	0.14	0.72
37.5	14.9	1.0	46.7	180	0.60	50	41.22	15.74	0.07	0.93	0.09	0.01	41.93	0.07	0.04	0.03	0.00	0.07	0.03	0.03	0.02
37.5	14.9	1.0	46.7	190	0.60	50	41.13	15.70	0.09	0.93	0.13	0.02	42.00	0.02	0.01	0.01	0.00	0.01	0.00	0.00	0.04
37.5	14.9	1.0	46.7	200	0.60	50	41.03	15.62	0.11	0.94	0.18	0.04	42.08	0.02	0.01	0.00	0.00	0.01	0.00	0.00	0.03
37.5	14.9	1.0	46.7	210	0.60	50	40.86	15.47	0.11	0.98	0.23	0.09	42.26	0.01	0.00	0.00	0.00	0.02	0.00	0.00	0.00
37.5	14.9	1.0	46.7	220	0.60	50	40.62	15.20	0.12	1.07	0.26	0.19	42.55	0.07	0.04	0.00	0.01	0.02	0.00	0.00	0.08
37.5	14.9	1.0	46.7	230	0.60	50	40.35	14.84	0.13	1.20	0.28	0.35	42.85	0.09	0.07	0.00	0.02	0.03	0.01	0.01	0.09
37.5	14.9	1.0	46.7	240	0.60	50	39.93	14.27	0.13	1.42	0.27	0.58	43.40	0.14	0.12	0.00	0.03	0.01	0.03	0.03	0.18
37.5	14.9	1.0	46.7	250	0.60	50	39.38	13.49	0.16	1.72	0.28	0.91	44.06	0.18	0.18	0.01	0.06	0.01	0.05	0.05	0.25
37.5	14.9	1.0	46.7	260	0.60	50	38.49	12.39	0.22	2.11	0.31	1.32	45.15	0.37	0.30	0.03	0.08	0.02	0.07	0.07	0.52
37.5	14.9	1.0	46.7	270	0.60	50	37.45	11.15	0.27	2.57	0.34	1.82	46.40	0.91	0.88	0.03	0.29	0.04	0.24	0.24	1.19
37.5	14.9	1.0	46.7	280	0.60	50	36.68	10.12	0.36	2.97	0.38	2.27	47.23	1.01	0.95	0.03	0.30	0.04	0.25	0.25	1.33
37.5	14.9	1.0	46.7	290	0.60	50	36.06	9.38	0.38	3.23	0.40	2.57	47.97	1.11	1.01	0.01	0.31	0.04	0.26	0.26	1.51
37.5	14.9	1.0	46.7	300	0.60	50	35.92	9.20	0.39	3.30	0.40	2.65	48.14	1.10	0.98	0.01	0.29	0.04	0.23	0.23	1.51
38.2	15.2	1.0	45.7	260	0.40	40	38.04	12.07	0.23	2.15	0.25	1.54	44.33	0.53	0.56	0.03	0.20	0.05	0.06	0.06	1.79
38.2	15.2	1.0	45.7	260	0.40	45	37.38	11.41	0.24	2.33	0.31	1.79	45.00	0.35	0.46	0.02	0.19	0.06	0.02	0.02	1.64
38.2	15.2	1.0	45.7	260	0.40	50	36.72	10.70	0.29	2.55	0.39	2.07	45.65	0.49	0.68	0.01	0.29	0.09	0.12	0.12	1.81
38.2	15.2	1.0	45.7	260	0.40	55	36.07	10.06	0.31	2.73	0.47	2.32	46.25	0.39	0.73	0.03	0.36	0.14	0.17	0.17	1.71
38.2	15.2	1.0	45.7	260	0.40	60	35.31	9.35	0.29	2.92	0.55	2.59	46.78	0.27	0.74	0.01	0.40	0.15	0.17	0.17	1.82

APPENDIX D. Published Manuscripts

In the following, the published manuscripts corresponding to Chapters 2 to 4 are included along with the respective supplementary files.


 Cite this: *RSC Adv.*, 2021, 11, 24556

Kinetics of the direct DME synthesis from CO₂ rich syngas under variation of the CZA-to- γ -Al₂O₃ ratio of a mixed catalyst bed†

 Nirvana Delgado Otalvaro,  Gerardo Sogne, Karla Herrera Delgado, *
 Stefan Wild,  Stephan Pitter  and Jörg Sauer 

The one-step synthesis of dimethyl ether over mechanical mixtures of Cu/ZnO/Al₂O₃ (CZA) and γ -Al₂O₃ was studied in a wide range of process conditions. Experiments were performed at an industrially relevant pressure of 50 bar varying the carbon oxide ratio in the feed (CO₂ in CO_x from 20 to 80%), temperature (503–533 K), space-time (240–400 kg_{cat} s m_{gas}⁻³), and the CZA-to- γ -Al₂O₃ weight ratio (from 1 to 5). Factors favoring the DME production in the investigated range of conditions are an elevated temperature, a low CO₂ content in the feed, and a CZA-to- γ -Al₂O₃ weight ratio of 2. A lumped kinetic model was parameterized to fit the experimental data, resulting in one of the predictive models with the broadest range of validity in the open literature for the CZA/ γ -Al₂O₃ system.

 Received 3rd May 2021
 Accepted 3rd July 2021

DOI: 10.1039/d1ra03452a

rsc.li/rsc-advances

1. Introduction

Dimethyl ether (DME) has many uses in industries. Applications include its use as a coolant or a propellant, and as an important commodity for the production of lower olefins.¹ Other potential applications include its use as a diesel substitute or fuel additive.^{2,3} Compared with fossil diesel fuels, the combustion of DME produces less NO_x, CO, and particulate emissions, while still achieving a high performance with only minor modifications of the fuel storage and supply.^{4,5} DME is produced from synthesis gas, which originates from different sources such as coal, natural gas, and waste materials like biomass.^{4,6} Depending on the raw material and syngas production process, the composition of the syngas may change in a wide range, resulting in a variable feedstock for the DME synthesis.

The commercially established production route of DME involves two steps. The first step is methanol synthesis from syngas, followed by the methanol dehydration step in a second reactor. An alternative route is the direct or single-step synthesis, where DME is produced directly from syngas in a single reactor.⁴ Potential advantages of a single reactor are reduced complexity and investment costs. Also, the direct synthesis is thermodynamically advantageous compared to the conventional route.⁷ The *in situ* conversion of methanol by the dehydration reaction shifts the thermodynamic equilibrium of methanol synthesis towards the products. As a result, a higher conversion of the synthesis gas can be achieved under comparable conditions.⁷

Many dual catalyst systems have been proposed in the scientific literature for direct DME synthesis.^{8–10} These combine the properties of metallic catalysts for the methanol synthesis (typically copper-based),¹¹ and a solid acid catalyst for the selective methanol dehydration to DME (such as γ -Al₂O₃, zeolites, and silica-modified alumina).¹² In this contribution, we consider mechanical mixtures of the two commercial catalysts of each step *i.e.*, Cu/ZnO/Al₂O₃ (CZA) and γ -Al₂O₃.

Identifying and quantifying dependencies between process parameters and performance is essential for efficient, economically viable and safe process design and operation. Hence, numerous studies have been conducted investigating the influence of different variables on the performance of the direct DME synthesis from CO₂ rich synthesis gas.

CO₂ content in the synthesis gas

Ateka *et al.*¹³ investigated the effect of CO₂ content in the feed gas on the thermodynamics of the methanol and DME synthesis. Ng *et al.*¹⁴ studied the influence of CO₂-to-CO_x ratios and catalyst bed compositions on the kinetics of the DME synthesis at 250 °C and 5 MPa. Peláez *et al.*¹⁵ described the effects of different feed gas compositions on the process performance at a pressure of 30 bar. These and other works^{7,16–19} have shown that increasing CO₂ content in the feed decreases the process performance, and that water plays an important role, not only affecting the reaction kinetics, but also the catalyst structure by deactivation of the dehydration component γ -Al₂O₃.

Catalyst bed composition and configuration

With regard to the composition of the catalyst bed, previous investigations^{14,20–23} have shown on the basis of simulated and

Karlsruher Institute of Technology (KIT), Hermann-von-Helmholtz-Platz 1, D-76344 Eggenstein-Leopoldshafen, Germany. E-mail: karla.herrera@kit.edu; Tel: +49 721 608 28631

† Electronic supplementary information (ESI) available. See DOI: 10.1039/d1ra03452a

experimental data that optimization can lead to significant enhancement of the process performance. For instance, in the studies of Peláez *et al.*¹⁵ and Peinado *et al.*²⁴ the authors showed that for CO₂ rich synthesis gas a significant increase in the performance is achieved by increasing the CZA-to- γ -Al₂O₃ ratio. In a previous study,²¹ applying a dynamic optimization scheme and experimental validation we showed that these effects hold true also for high pressure (50 bar) and different compositions of CO₂ rich syngas, including a hydrogen-lean feed. Other studies^{20,21,25} on the loading and arrangement of physical catalyst mixtures have shown that homogeneously mixed catalyst beds achieve similarly good process performance compared to more complex configurations.

Quantification and prediction of system behavior

Reliable models able to predict the process performance in different operating windows are necessary to enable the optimal reactor and process design, especially if DME synthesis is to be conducted at dynamic conditions or changing feed compositions. Therefore, several kinetic models have been proposed in the open literature to quantitatively describe and predict the effects of process variables on process performance. A widely used modelling approach is the combination of available models for the methanol synthesis,^{26,27} and its dehydration.²⁸ Models derived for the direct DME synthesis under mechanistic assumptions include the works of Lu *et al.*,²⁹ Aguayo *et al.*,³⁰ Ereña *et al.*,³¹ and Peláez *et al.*¹⁵

Although so many studies have been carried out for the direct DME synthesis from CO₂ rich synthesis gas, the detail reaction mechanism is still controversial.³² Therefore, reliable kinetic models valid in a wide range of conditions at industrially relevant process conditions are still necessary. In this work, we develop a reaction kinetic model applicable for an extended range of catalyst bed compositions, and process parameters (CO₂ content in the synthesis gas, temperature and space time), extending the scope of available reaction kinetic models and providing a useful tool for model-based reactor and process design and optimization.

2. Experimental setup and procedures

In this chapter the equipment and methodology for the experimental kinetic investigations are described. First, the laboratory setup is described, then the materials used are listed, followed by a brief description of the experimental procedures and conditions at which the kinetic measurements were conducted.

2.1. Reactor and periphery

The reactor setup used in this work is presented in detail elsewhere.²¹ It consists of a laboratory tube reactor made of the stainless steel with an internal diameter of 12 mm, and a total length of 460 mm. The reactor is divided in four independent heating zones, each of which is surrounded by brass jaws equipped with heating cartridges (Horst GmbH) to set the

temperature at the reactor outer wall. The gas supply is regulated *via* mass flow controller (Bronkhorst High-Tech B.V.) by using proportional integral derivative control. The system pressure is set by using a mechanical pressure regulator (Emerson Electric Co.). A gas chromatograph G1530A (Agilent Technologies) was used to analyse the composition of the feed gas and product gas.

2.2. Materials

Commercial catalysts, *i.e.*, Cu/ZnO/Al₂O₃ (CZA) and γ -Al₂O₃ (Alfa Aesar) were used as hydrogenation catalyst for the methanol synthesis and methanol dehydration to DME, respectively. Relevant properties of the used catalysts are provided in Table 1. The catalysts were ground and sieved to a particle size between 250 and 500 μ m. To avoid hot spot formation, the catalytic bed was diluted with silicon carbide (SiC, Hausen Mineralien-großhandel GmbH) of the same size distribution.

The feed gases, carbon monoxide (CO, 99.97%), nitrogen (N₂, 99.9999%), hydrogen (H₂, 99.9999%) and a mixture carbon dioxide/nitrogen (CO₂/N₂, 50 : 50 \pm 1.0%) were purchased by Air Liquid Germany GmbH.

2.3. Kinetic measurements

Before performing the kinetic measurements, the CZA share of the catalytic bed was reduced at atmospheric pressure (5% H₂ in N₂, at temperatures between 393 and 513 K). Following the reduction procedure, the catalyst was conditioned until stable catalyst activity was achieved, in order to decouple the kinetic measurements from deactivation effects. The reduction and conditioning procedures are described in detail elsewhere¹⁷ and summarized in the ESI.† The kinetic measurements were performed at a pressure of 50 bar under variation of the CZA-to- γ -Al₂O₃ weight ratio (μ), temperature (T), space time (τ), and carbon oxide ratio (COR),

$$\text{COR} = \frac{y_{\text{CO}_2,\text{in}}}{y_{\text{CO}_2,\text{in}} + y_{\text{CO},\text{in}}} \times 100\% \quad (1)$$

Table 1 Selected properties of the commercial catalysts

Properties of the CZA catalyst ¹⁰	
Metal composition (Cu/Zn/Al)/wt%	64/29/6
Specific surface area (S_{BET})/m ² g ⁻¹	98
Pore volume/cm ³ g ⁻¹	0.332
Maximum pore diameter/nm	11
Pore size range/nm	5–26
Properties of the γ -Al ₂ O ₃ catalyst ³³	
Specific surface area (S_{BET})/m ² g ⁻¹	213
NH ₃ -TPD peak position in low and high temperature regions/K	512 and 624
Total acidity/mmol NH ₃ per g _{cat} (desorbed NH ₃ in NH ₃ -TPD)	0.37
Acidity in low and high temperature regions/mmol NH ₃ per g _{cat}	0.18 and 0.19

The experimental conditions as summarized in Table 2 were chosen in order to measure intrinsic kinetics *i.e.*, by minimizing heat and mass transport limitations. The total catalyst mass in all experiments was 2 g, while the mass of each catalyst was distributed in different ratios ($\mu = m_{\text{CZA}}/m_{\gamma\text{-Al}_2\text{O}_3}$). The mole fraction of H₂ in the feed ($y_{\text{H}_2,\text{in}}$) was set to 46.5% to avoid a stoichiometric limitation in all cases. The mole fraction of carbon oxides in the feed, *i.e.*, $y_{\text{CO}_2,\text{in}} = y_{\text{CO}_2,\text{in}} + y_{\text{CO},\text{in}}$ was at 15%, and the fraction of N₂ ($y_{\text{N}_2,\text{in}}$) was set accordingly to 38.5%. The concentrations used for the model parametrization were determined from the mean value of at least 4 chromatograms per operating point. Each set point was held for at least 3 hours enabling multiple readings, and confirmation of stability.

2.4. Estimation of model-specific parameters

The Matlab® (Version R2019a) built-in solver *ode45* was used to integrate the system of differential equations (Section 3.1) along the reactor axial coordinate. The model-specific parameters were fitted to experimental data using the nonlinear least-squares solver *lsqcurvefit* and the algorithm *trust-region-reflective*. The model-specific parameters were estimated such as to minimize the weighted sum of squared errors,

$$\text{SSE} = \sum_{n=1}^{\text{No. Exps}} w_n [y_n - f(x_n, \theta)]^2 \quad (2)$$

where y_i represent the response values (measured quantities), $f(x_n, \theta)$ the predicted values with the nonlinear model function, and x_n and θ are respectively the predictor values of observation n , and the model-specific parameters.

The parameter estimation took place based on the measured mole fractions of the components in the product gas, excluding water and methanol since it was not possible to detect these species accurately over the wide range of conditions shown in Table 2. Reported values for water and methanol correspond to those calculated based on the component balances (C, H and O balance). Additionally, experimental data for which the component balances exhibited a relative error higher than 8% were excluded from the parameter estimation ($w_n = 0$). Due to the strong influence of initial parameter values, and in order to avoid local optimality, the fitting procedure was iteratively repeated until the relative difference between the parameters obtained in two consecutive iterations was lower than 5%. The Matlab built-in function *nlparci* was used to calculate the 95% confidence intervals of the parameter estimates using the residuals and the Jacobian matrix of the fitted model, which are

both output arguments of *lsqcurvefit*. Additionally, correlation coefficients were computed using eqn (3),³⁴

$$\rho_{ij} = \frac{v_{ij}}{\sqrt{v_{i,i} v_{j,j}}} \quad (3)$$

Here, v_{ij} represents the elements of the covariance matrix of the parameters of the fitted model. The covariance matrix V_θ is calculated with the variance of the experimental fluctuations s^2 (assumed to be constant over all experiments) and the Jacobian matrix J by,

$$V_\theta = s^2(J^T J)^{-1} \quad (4)$$

Correlation coefficients $|\rho_{ij}| \geq 0.95$ are assessed to indicate a strong parameter correlation.³⁵

3. Mathematical model

In this section, the mathematical model consisting of the reactor model (balance equations) and the reaction kinetic model (rate expressions) is presented.

3.1. Reactor model

The change of the mole fraction of the components along the reactor's axial coordinate can be described by the balance equation of an ideal plug flow reactor (eqn (5)). This simplified form of the general material balance of a fixed-bed reactor is admissible for the characteristics of the lab-scale reactor, and the conditions at which it was operated. Isothermal operation was achieved by diluting the catalyst bed with silicon carbide (SiC), and diluting the feed gas with inert N₂. Temperature gradients did not exceed 2 K in any of the measurements. Hence, the assumption of isothermal operation applies and the energy balance can be omitted. All measurements took place under steady state conditions, which was verified experimentally. Furthermore, it was proven by the means of *a priori* criteria, that no significant influence of mass or heat transport processes took place, and that the assumption of plug flow applies. Finally, the pressure drop in the fixed bed was determined to be negligible by the means of correlations. Values to support the mentioned assumptions are reported in Table S1 in the ESI.† It can be concluded that the intrinsic reaction rates were measured in all experiments and that the reactor can be described by the balance equations of an ideal plug flow reactor. Furthermore, the volume contraction caused by reaction can be accounted for by eqn (6).

$$\frac{dy_i}{dz} = \frac{RTZ}{up} \left(R_i - y_i \sum_k^N R_k \right), \quad (5)$$

$$\frac{du}{dz} = \frac{RTZ}{p} \sum_i^N R_i. \quad (6)$$

In eqn (5) and (6), y_i is the mole fraction of component i , z represents the position in the axial coordinate, R is the universal gas constant in J mol⁻¹ K⁻¹, T is the temperature in K, p is the pressure in Pa, u is the gas velocity in m s⁻¹, ν_{ij} is the stoichiometric coefficient of component i in reaction j , and N is the number of components in the system. Z is the compressibility

Table 2 Conditions for kinetic measurements

Variable	Values
Temperature (T), K	503, 513, 523, 533
Space-time ^a (τ), kg _{cat} s m _{gas} ⁻³	240, 300, 400
Carbon oxide ratio (COR), %	20, 40, 60, 80
Catalyst ratio (μ), g _{CZA} g _{γ-Al₂O₃} ⁻¹	1, 2, 3, 5

^a At standard conditions: $p = 101\,325$ Pa, $T = 293.15$ K.

factor of the mixture, which takes into account possible deviations from the ideal gas behavior at the high pressure (50 bar) considered in our investigations. The Peng–Robinson equation of state (PR-EoS)³⁶ was chosen to calculate Z , since it has already been successfully applied to the system under consideration,^{21,37} and it provides accurate calculations for light gases, alcohols and hydrocarbons.³⁸ In addition, van der Waals mixing rules³⁶ were used to account for inter-molecule interactions. The molar rate of depletion or formation of component i due to chemical reaction (R_i in mol m⁻³ s⁻¹) is defined by:

$$R_i = \sum_j^J \vartheta_{ij} r_j^v, \quad (7)$$

with

$$r_j^v = (1 - \varepsilon_{\text{bed}}) \rho_{\text{cat},j} \xi_{\text{cat},j} r_j^m. \quad (8)$$

In the above equations, r_j^v and r_j^m are the volume and mass specific rates of reaction j in mol m³ s⁻¹ and mol kg⁻¹ s⁻¹, ε_{bed} is the porosity of the catalyst bed estimated to be 0.39, $\rho_{\text{cat},j}$ is the density of the catalyst that promotes reaction j , *i.e.*, the densities of the CZA and the γ -Al₂O₃ catalysts with the respective values of 1761.3 kg m⁻³ and 667.9 kg m⁻³, and J is the number of reactions. Finally, $\xi_{\text{cat},j}$ stands for the volume fraction of the catalyst that promotes reaction j calculated by,

$$\xi_{\text{CZA}} = \frac{V_{\text{CZA}}}{V_{\text{CZA}} + V_{\gamma\text{-Al}_2\text{O}_3} + V_{\text{SiC}}}, \quad (9)$$

$$\xi_{\gamma\text{-Al}_2\text{O}_3} = \frac{V_{\gamma\text{-Al}_2\text{O}_3}}{V_{\text{CZA}} + V_{\gamma\text{-Al}_2\text{O}_3} + V_{\text{SiC}}}. \quad (10)$$

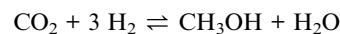
where V_{CZA} , $V_{\gamma\text{-Al}_2\text{O}_3}$ and V_{SiC} are the volumes of CZA, γ -Al₂O₃ and SiC respectively.

3.2. Reaction kinetic model

For the initial model discrimination, the available experimental data were simulated using eight different kinetic models from the open literature.^{15,21,22,30,31,39–41} Subsequently, the five models with the lower residual squared sum were parameterized to fit the data. Our previous model²¹ exhibited the best agreement with the experimental data acquired for this contribution, which can be attributed to similar operating conditions, and to the fact that in both contributions the same catalysts (same supplier), and pre-treatment procedures were employed. The mechanistic assumptions and model structure were chosen for fine-tuning, and the model structure that enabled the best fit is presented in the following. Further information on the initial model discrimination is presented in the ESI,[†] along with a compilation of the rate expressions and specific parameters of the tested models (Table S2[†]). The new estimated model parameters are presented in Section 4.2.1 followed by the statistical evaluation of the estimates.

The reaction network considered in this model consists of the CO₂ hydrogenation (reaction 1), the methanol dehydration to DME (reaction 2), and the water gas shift reaction (reaction 3). Reactions 1 and 3 are assumed to be promoted by the CZA catalyst, while reaction 2 is promoted by γ -Al₂O₃.

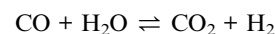
Reaction 1:



Reaction 2:



Reaction 3:



The reaction rate expressions were postulated based on the general Hougen–Watson formulation,

$$r = \frac{(\text{kinetic term})(\text{potential term})}{\text{adsorption term}}. \quad (11)$$

The kinetic term equals the rate constant of each reaction j (k_j). The potential term, describing the driving force of the reaction *i.e.*, the distance from thermodynamic equilibrium, is defined for each reaction j as follows,

$$\text{Potential term}_j = \prod_{i,j,v < 0} f_i^{|v_{ij}|} - \frac{1}{K_{f,j}} \prod_{i,j,v > 0} f_i^{|v_{ij}|}. \quad (12)$$

The adsorption term is generally defined by,

$$\text{Adsorption term} = \left(1 + \sum_i K_i f_i \right)^n. \quad (13)$$

It accounts for the inhibition caused by adsorbed species on the catalytically active surface, and hence it must be defined for each component of the catalyst mixture. The postulated model includes the adsorption of CO₂, CO and dissociated H₂ on the CZA (eqn (14)), whereas no adsorption on the dehydration catalyst was considered (eqn (15)). Furthermore, the adsorption term has a different influence on the rates of the CO₂ hydrogenation and the WGSR, with $n = 3$ and 1 respectively.^{21,29} In eqn (12) and (13), f_i is the fugacity of component i in bar, $K_{f,j}$ is the equilibrium constant of the same reaction, v_{ij} is the stoichiometric coefficient of component i in reaction j , and K_i is the adsorption constant of component i .

$$\text{Ads. term}_{\text{CZA}} = 1 + \sqrt{K_{\text{H}_2/\text{H}_2}} + K_{\text{CO}_2} f_{\text{CO}_2} + K_{\text{CO}} f_{\text{CO}} \quad (14)$$

$$\text{Ads. term}_{\gamma\text{-Al}_2\text{O}_3} = 1 \quad (15)$$

The resulting rate expressions for the three reactions are presented in eqn (16)–(18).

$$r_1^m = \frac{k_1 \left[f_{\text{CO}_2} f_{\text{H}_2}^3 - \frac{1}{K_{f,1}} f_{\text{MeOH}} f_{\text{H}_2\text{O}} \right]}{\left(1 + \sqrt{K_{\text{H}_2/\text{H}_2}} + K_{\text{CO}_2} f_{\text{CO}_2} + K_{\text{CO}} f_{\text{CO}} \right)^3} \quad (16)$$

$$r_2^m = k_2 \left[f_{\text{MeOH}}^2 - \frac{1}{K_{f,2}} f_{\text{DME}} f_{\text{H}_2\text{O}} \right] \quad (17)$$

$$r_3^m = \frac{k_3 \left[f_{\text{CO}} f_{\text{H}_2\text{O}} - \frac{1}{K_{f,3}} f_{\text{CO}_2} f_{\text{H}_2} \right]}{\left(1 + \sqrt{K_{\text{H}_2} f_{\text{H}_2}} + K_{\text{CO}_2} f_{\text{CO}_2} + K_{\text{CO}} f_{\text{CO}} \right)} \quad (18)$$

$$K_{f,j} = 10^{\left(\frac{A_j}{T} - B_j \right)} \quad (26)$$

The reaction rate and adsorption constants (k_j and K_i) are each calculated using modified Arrhenius and the van't Hoff equations (eqn (19) and (20)). This re-parameterization reduces the correlation between the frequency factor and the activation energy, as well as between the sticking coefficients and the enthalpy of adsorption.⁴² Other advantages of using re-parameterized expressions are lower computational costs and higher robustness in parameter estimation with the least squares algorithm.⁴³ These are particularly relevant for the fitting of large data sets, as used in this work.

$$k_j = \exp \left[k_{0,j}^* + E_{A,j}^* \left(\frac{T - T_R}{T} \right) \right] \quad (19)$$

$$K_i = \exp \left[K_i^* + \Delta H_{\text{ads},i}^* \left(\frac{T - T_R}{T} \right) \right] \quad (20)$$

The modified parameters are related to the parameters of the traditional Arrhenius equation according to eqn (21) and (22).³⁴

$$k_{0,j}^* = \ln(k_{0,j}) - \frac{E_{A,j}}{RT_R} \quad (21)$$

$$E_{A,j}^* = \frac{E_{A,j}}{RT_R} \quad (22)$$

the same applies to the van't Hoff equation as follows,

$$K_i^* = \ln(K_i) - \frac{\Delta H_{\text{ads},i}}{RT_R}, \quad (23)$$

$$\Delta H_{\text{ads},i}^* = \frac{\Delta H_{\text{ads},i}}{RT_R}. \quad (24)$$

The reference temperature (T_R) was calculated with eqn (25) based on the temperature of each experiment n .⁴⁴

$$T_R = \left(\frac{1}{\text{No. Exps}} \sum_n \frac{1}{T_n} \right)^{-1} \quad (25)$$

The equilibrium constants $K_{f,j}$ of each reaction j are calculated using eqn (26),⁴⁵ the temperature T in K, and the parameters in Table 3.

Table 3 Parameters for the calculation of eqn (26).²¹

Parameter	Reaction 1	Reaction 2	Reaction 3
A	3014.4029	1143.9494	2076.2131
B	10.3856	0.9925	2.0101

The equilibrium constants are dimensionless for reactions 2 and 3 (methanol dehydration to DME, and WGS), while $K_{f,1}$ (the equilibrium constant of CO_2 hydrogenation to methanol) has the units bar^{-2} , in accordance with the law of mass action.

For performance evaluation, the conversion of component i (X_i), and the carbon-normalized yield and selectivity of component i from CO_x (Y_i and S_i) were computed based using eqn (27)–(29), respectively.

$$X_i = \frac{n_{i,\text{in}} - n_{i,\text{out}}}{n_{i,\text{in}}} \quad (27)$$

$$Y_i = \frac{(n_{i,\text{out}} - n_{i,\text{in}}) \eta_{c,i}}{(n_{\text{CO}} + n_{\text{CO}_2})_{\text{in}}} \quad (28)$$

$$S_i = \frac{(n_{i,\text{out}} - n_{i,\text{in}}) \eta_{c,i}}{(n_{\text{CO}} + n_{\text{CO}_2})_{\text{in}} - (n_{\text{CO}} + n_{\text{CO}_2})_{\text{out}}} \quad (29)$$

In these equations, \dot{n}_i is the molar flow of component i , $\eta_{c,i}$ is the number of carbon atoms in the same component, and the subscripts “in” and “out” refer to the respective quantities at the reactor inlet and outlet.

4. Results and discussion

In this section, experimental results will be presented (Section 4.1), followed by the modelling results and mechanistic analysis (Section 4.2). Since most of the studies for the direct DME synthesis have been carried out with a catalyst weight ratio of one ($\mu = 1$), this catalyst ratio is treated here as the reference composition for the evaluation of experimental and simulations results. The results are presented for the highest space-time (at which the effects are more pronounced) unless otherwise stated.

4.1. Experimental results

This section presents an overview of the effects observed experimentally. To determine causality and for a comprehensive understanding of the phenomena, the reactions kinetics are studied and analyzed in Section 4.2 in the light of the derived kinetic model and further kinetic studies from the literature.

For an initial qualitative analysis of the experimental results, the measured conversion of CO_x (X_{CO_x}) and DME yield (Y_{DME}) are shown in Fig. 1 and 2 as a function of the temperature and the CZA-to- $\gamma\text{-Al}_2\text{O}_3$ ratio (μ) for the four investigated COR levels (20, 40, 60 and 80%). To create this graphical representation, the values between the experiments were calculated using low-pass interpolation with the Matlab® function *interp*. The maximal conversion attained for the different inlet feed

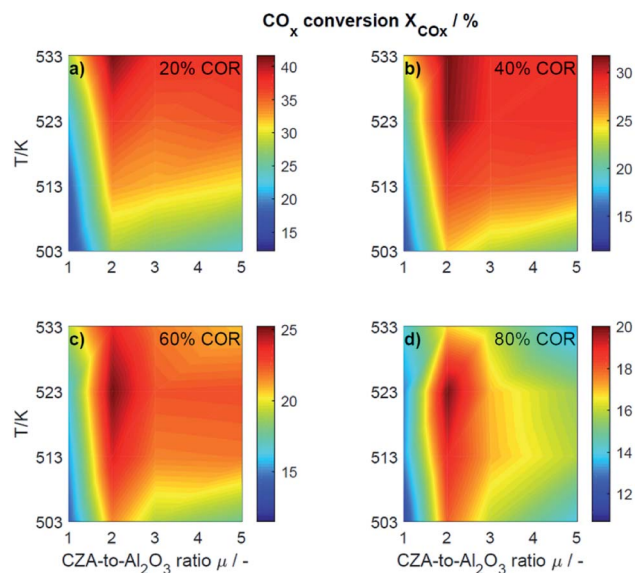


Fig. 1 Conversion of CO_x determined experimentally and plotted as a function of the temperature (T) and the CZA-to- $\gamma\text{-Al}_2\text{O}_3$ ratio (μ) for nominal CORs of (a) 20%, (b) 40%, (c) 60% and (d) 80%. Experimental conditions summarized in Table 2.

composition varies from 19.8% ($\text{COR} = 80\%$, $T = 523\text{ K}$, $\mu = 2$) to 42.6% ($\text{COR} = 20\%$, $T = 533\text{ K}$, $\mu = 2$). In general, low CORs, *i.e.*, low CO_2 contents in the feed, lead to higher conversions at all temperatures. The highest conversions were reached in all cases with $\mu = 2$, whereas the conversions attained with the reference catalyst bed composition ($\mu = 1$) are the lowest. Even at high temperatures relatively low conversions are attained with the reference $\mu = 1$ in comparison to those reached with the other catalyst beds. It is obvious that the temperature at

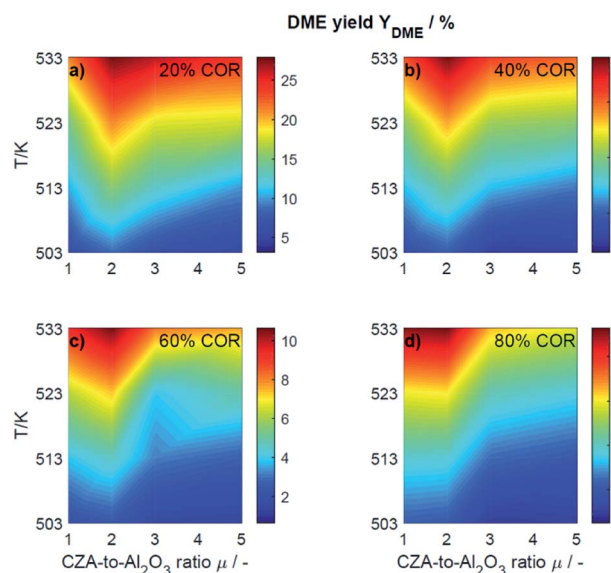


Fig. 2 Yield of DME determined experimentally and plotted as a function of the temperature (T) and the CZA-to- $\gamma\text{-Al}_2\text{O}_3$ ratio (μ) for nominal CORs of (a) 20%, (b) 40%, (c) 60% and (d) 80%. Experimental conditions summarized in Table 2.

which the maximal conversion was measured, decreases with increasing CORs.

The DME yield, displayed in Fig. 2, exhibits a strong temperature dependency. The maximal Y_{DME} varies between 4.6% ($\text{COR} = 80\%$, $T = 533\text{ K}$, $\mu = 2$) and 27.9% ($\text{COR} = 20\%$, $T = 533\text{ K}$, $\mu = 2$). Overall, lower CORs lead to higher yields of DME, and analogous to the conversion of CO_x , the highest yields were attained with a CZA-to- $\gamma\text{-Al}_2\text{O}_3$ ratio $\mu = 2$. The response surfaces are very similar for all CORs, however, it can be observed that with increasing COR, the region at which the highest yields are reached migrates towards the upper left corner *i.e.*, towards high temperatures and low μ . At 533 K and 20% COR for example, high yields are attained with all the catalyst beds, whereas at 80% COR, the yields reached at this temperature are high with μ up to two, and significantly lower with μ of three and higher.

To enable a quantitative analysis of the observed effects, representative results at the minimal and maximal temperature are investigated more in detail in the following. The CO_x conversion is depicted in Fig. 3 for the investigated CORs as a function of the CZA-to- $\gamma\text{-Al}_2\text{O}_3$ ratio, at the maximal and minimal temperature of 533 K and 503 K (Fig. 3a and b). At 533 K, the CO_x conversion increased for all measured feeds when increasing μ up to a value of 2. This effect was most pronounced for a COR of 20% where the relative enhancement of the conversion was of 47%. For a COR of 80% the relative enhancement amounted 19%. A further increase of the CZA-to- $\gamma\text{-Al}_2\text{O}_3$ ratio had a negative effect on the conversion compared to the conversion obtained with $\mu = 2$, but in all cases, the attained values were still higher than in the reference case ($\mu = 1$). The only exception to this observation was for $\text{COR} = 80\%$ and $\mu = 5$, where the conversion decreases from 14% ($\mu = 1$) to 13% ($\mu = 5$).

At a temperature of 503 K, the conversion of CO_x shown in Fig. 3b for all bed compositions and CORs is lower than for the corresponding values attained at 533 K, which can be attributed to the general dependency of the reaction rates on the temperature. For all CORs, a maximum at $\mu = 2$ was detected. With this CZA-to- $\gamma\text{-Al}_2\text{O}_3$ ratio, a relative conversion enhancement of 88% and 52% was obtained compared to $\mu = 1$ at the minimal and maximal COR levels of 20% and 80% respectively. Comparable to the observations made at 533 K, the effect of the catalyst bed composition on the conversion is more pronounced at lower CORs. Furthermore, it can be observed that with the reference

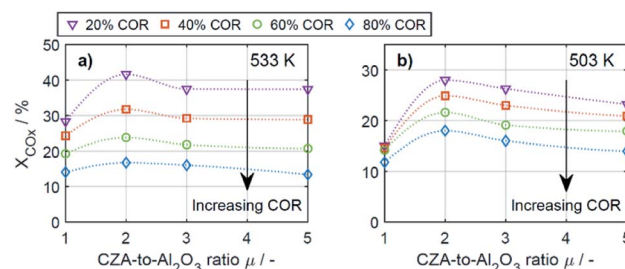


Fig. 3 CO_x conversion as a function of the CZA-to- $\gamma\text{-Al}_2\text{O}_3$ ratio (μ) for CORs from 20% to 80%. (a) $T = 533\text{ K}$ and (b) $T = 503\text{ K}$.

catalyst ratio $\mu = 1$, the attained CO_x conversion is at a close value of approx. 14% regardless of the CO_2 content in the inlet feed, in contrast to the other experiments with increasing CO_x conversion as the COR is decreased.

In general it was observed that decreasing amounts of CO_2 in the feed gas (*i.e.*, decreasing CORs) lead to higher conversions, and to more pronounced effects of the catalyst bed composition. The beneficial effect of low CO_2 concentration in the synthesis gas has been observed in other kinetic studies of both the methanol and the DME synthesis.^{14,15,26,46–48} Regarding the surface chemistry, low CO_2 concentration prevents sintering of the CZA catalyst, and promotes catalyst morphology that enhances the catalytic activity.^{48,49} From a thermodynamic perspective, high CO_2 feed concentration shifts the equilibrium of the WGSR towards the educts (H_2O and CO), resulting in increased water formation and subsequently in decrease of the methanol dehydration rate.^{14,15} This explanation is in accordance with our findings and is further confirmed by increased methanol selectivity at high CORs discussed in the following. In addition, we explain this effect on the basis of mechanistic considerations in Section 4.2.2.1.

In Fig. 4a–d the yields are shown for the minimal and maximal CORs 20% and 80%, and for the minimal and maximal temperatures 503 K and 533 K. Since the yield is calculated based on the reacted CO_x , and no other carbon-containing compounds were detected in a significant amount during the experiments, the yield is calculated only for methanol and DME. However, as discussed further in Section 4.2, CO and CO_2 formation was evidenced at some specific conditions.

At 533 K and a COR of 20% (Fig. 4a), the converted CO_x in the feed gas reacted to form mainly DME. In general, at this temperature and COR, an increased amount of the CZA catalyst led to a higher DME production than that attained with the reference catalyst bed ($\mu = 1$). The highest relative enhancement

of the DME yield was 30.3% with $\mu = 2$. A further increase of $\mu = 3$ and 5 also enhanced the yield of DME but to a lower extent (enhancement of 22.8% and 13.2% respectively compared to the yield attained with the reference $\mu = 1$). At the same temperature and a COR of 80% (Fig. 4b), the methanol yield was at least twice as high as that of DME. An increased μ did not increase the DME yield which amounts 4.6% at $\mu = 1$ and 2, and was lower otherwise. Comparing the results shown in Fig. 4a and b (and also Fig. S3a and b†), a shift of the selectivity from DME to methanol is observed when increasing the COR from 20 to 80%. The water concentration is low at high CO contents in the feed (water removal *via* WGSR), and high at a high level of CO_2 .¹⁴ Obviously, presence of water is thermodynamically unfavorable for the dehydration, explaining the observed methanol concentration at high CORs. This conclusion is supported by the mechanistic analysis provided in Section 4.2.2.1.

In Fig. 4c and d it is observable that for a temperature of 503 K, the yield of methanol is higher than that of DME for both COR levels. An enhancement of the DME yield compared to the reference case is still observable at a COR of 20% (38.2% and 4.3% with $\mu = 2$ and 3), whereas at 80% COR, an increase of the μ proved to be disadvantageous for the DME yield. The lowest DME yields were observed at 503 K, a COR of 80% and $\mu = 3$ and 5.

The catalytic activity of the CZA/ $\gamma\text{-Al}_2\text{O}_3$ system is a function of combined physicochemical characteristics such as Cu surface area, dispersion, and acidity.^{50–52} Furthermore, the setup of reaction conditions have also shown to be a key factor.²⁴ While the study of the catalysts properties was out of the scope of this work, a wide range of conditions was covered during the experimental program. The improvement observed by increasing the CZA-to- $\gamma\text{-Al}_2\text{O}_3$ ratio reveals that the number of required acid sites has already been significantly exceeded when equivalent catalysts masses are used.^{15,21} Therefore, an increase of the catalyst ratio leads to an overall enhancement of the synergetic effects of the direct DME synthesis *i.e.*, the faster methanol formation due to an increased amount of CZA catalyst has a positive effect on the methanol dehydration even though the amount of the catalyst that promotes this reaction is reduced. Overall, it was observed that the highest enhancement of the DME yield was attained at a CZA-to- $\gamma\text{-Al}_2\text{O}_3$ ratio of $\mu = 2$, and that higher ratios lead to a minor improvement, or even to a decrease of the DME production. Additionally, it was observed that the methanol yield increased with increasing CZA-to- $\gamma\text{-Al}_2\text{O}_3$ ratio at all conditions (Fig. 4a–d) as also described in other kinetic studies.^{15,24,50} Hence, the evidenced enhancement of the DME yield is associated to the higher conversion, *i.e.*, the conversion of CO_x increased more than the DME selectivity decreased, leading to higher DME yields than with the reference catalyst bed.

4.2. Modeling results

Predictive models able to make accurate predictions over a wide range of conditions are of considerable importance as a basis for model-based optimization and for the design of novel reactor concepts. The respective contribution of our work is a reaction kinetic model for direct DME synthesis suitable these

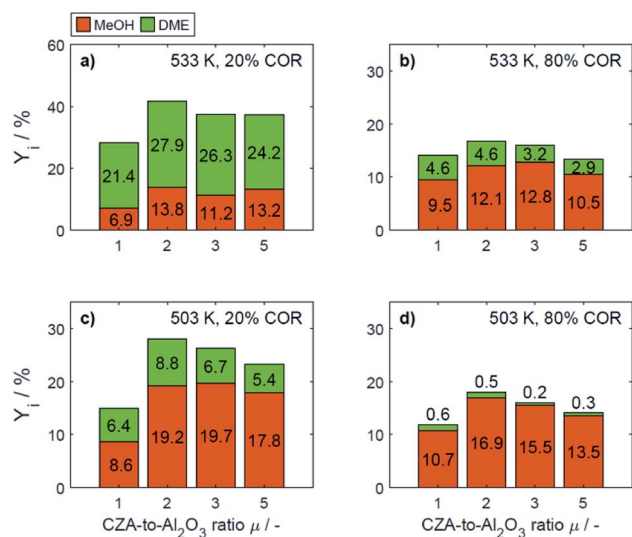


Fig. 4 Yield of methanol and DME at specific conditions: (a) 533 K, 20% COR, (b) 533 K, 80% COR, (c) 492 K, 20% COR and (d) 492 K, 80% COR.

purposes. In Section 4.2.1, the results of the parameter estimation are presented together with an analysis of the achieved goodness of fit and statistical significance of the parameter estimates. In Section 4.2.2, the phenomena experimentally observed (Section 4.1) are explained taking into account the derived kinetic model. In addition, we describe to what extent our findings are consistent with the results and new mechanistic insights of other studies.

4.2.1. Reaction kinetic model. In this section, the resulting kinetic model, *i.e.*, the parameter estimates and model evaluation are discussed. As mentioned briefly in Section 3.2, the presented model was the one that enabled the best fit of the experimental data within the entire range of conditions investigated in this work. The derived model chosen after a discrimination procedure agrees with the one derived from mechanistic assumptions by Lu *et al.*²⁹ and used in a previous work.²¹ It considers the linearly independent reactions CO₂ hydrogenation and WGSR, along with the methanol dehydration to DME. In agreement with the mentioned studies, including no adsorption term for the dehydration catalyst, and the adsorption of CO, CO₂ and dissociated H₂ on the CZA catalyst led to the best representation of the experimental data. Considering the adsorption of water and methanol as done in other kinetic studies of the direct DME synthesis^{15,30,53} worsen the quality of fit, and was therefore discounted from the model structure. The goodness of fit for CO, CO₂, H₂ and DME with the resulting model is represented by the parity diagrams in Fig. 5 with the measured quantities plotted against the numerically predicted ones. The model-specific parameters were estimated based on 186 experimental data points. The mean relative error between the predicted and measured molar fractions over all data amount to 2.7% for CO₂, 7.2% for CO, 1.0% for H₂, and 22.3% for DME. The deviation of the DME predictions is mostly attributed to an over-prediction of the data measured with $\mu = 5$. The data taken with this catalyst bed exhibits the lowest DME production and low DME mole fractions in the product gas as shown in Fig. 2. Hence, these measurements have a high signal-

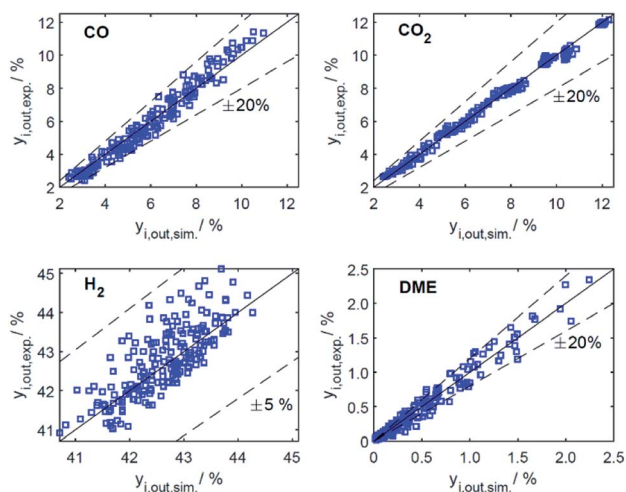


Fig. 5 Parity plots for mole percent of CO, CO₂, H₂ and DME in the product gas for all data (186 experiments).

Table 4 Estimated parameters in re-parameterized form according to eqn (19) and (20), and 95% confidence intervals

Reaction	k_{0j}^*	$E_{A,j}^*$
CO ₂ hydrogenation	3.19 (± 0.04) mol kg ⁻¹ s ⁻¹ bar ⁻⁴	7.60 (± 2.20)
MeOH dehydration	-5.72 (± 0.07) mol kg ⁻¹ s ⁻¹ bar ⁻²	24.58 (± 3.22)
WGSR	1.74 (± 0.11) mol kg ⁻¹ s ⁻¹ bar ⁻²	40.77 (± 4.96)

Adsorbate	K_i^*	$\Delta H_{ads,i}^*$
CO ₂	4.68 bar ⁻¹	-1.25
CO	-34.04 bar ⁻¹	-79.81
H ₂	7.13 bar ⁻¹	-5.04

to-noise ratio, and a lower measurement accuracy, to which the larger deviations can be attributed to. Nonetheless, the deviation of the DME predictions is considered acceptable, especially regarding the extensive range in which the experiments were measured. Furthermore, the predictions lie with a clear tendency and a weak scattering along the bisector ($y = x$), and no systematic deviations are identifiable for any of the species.

The resulting parameter estimates are shown in Table 4 along with the respective 95% confidence intervals. The adsorption parameters were fixed. Hence, no statistical information is available on these estimates. In regards to the rate constants, the confidence intervals demonstrate that all re-parameterized pre-exponential factors and activation energies are statistically significant. Moreover, the width of the confidence intervals is less than 13% of the respective estimates for five out of six parameters. The widest confidence interval was that of the re-parameterized activation energy of the CO₂ hydrogenation, with a width of 29% of the estimated value, which underlines the high statistical significance of the estimated kinetic parameters.

The reference temperature was calculated as $T_R = 517.43$ K using eqn (25) for the 186 experiments used for fitting.

Notice that $E_{A,j}^*$ and $\Delta H_{ads,i}^*$ are dimensionless according to eqn (22) and (24), and that k_{0j}^* is based on the mass of the catalyst that promotes each reaction, *i.e.*, CZA for the CO₂ hydrogenation and the WGSR, and γ -Al₂O₃ for the methanol dehydration to DME.

The adsorption constants K_i were calculated with eqn (20) at the different temperature levels to determine the influence of the adsorption of each species on the adsorption term (the reported value for H₂ corresponds to $\sqrt{K_{H_2}}$ according to eqn (14)). The calculated values are shown in Table 5. The CO adsorption has clearly the lowest adsorption constant, in agreement with

Table 5 Adsorption constants at different temperatures

	$T = 503$ K	$T = 513$ K	$T = 523$ K	$T = 533$ K
K_{CO_2}/bar^{-1}	111.9	109.2	106.6	104.1
K_{CO}/bar^{-1}	1.6×10^{-14}	3.2×10^{-15}	6.9×10^{-16}	1.6×10^{-16}
$\sqrt{K_{H_2}}/\text{bar}^{-0.5}$	37.9	36.0	34.3	32.8

Table 6 Binary correlation coefficients of parameter estimates

ρ_{ij}	$k_{0,1}^*$	$E_{A,1}^*$	$k_{0,2}^*$	$E_{A,2}^*$	$k_{0,3}^*$	$E_{A,3}^*$
$k_{0,1}^*$	1	-0.53	-0.83	0.40	-0.39	0.28
$E_{A,1}^*$		1	0.38	-0.85	0.31	-0.36
$k_{0,2}^*$			1	-0.44	-0.07	-0.11
$E_{A,2}^*$				1	-0.11	-0.03
$k_{0,3}^*$					1	-0.28
$E_{A,3}^*$						1

the studies of Lu *et al.*²⁹ and Delgado Otalvaro *et al.*²¹ where the same adsorption term was employed. The constant of CO₂ adsorption exhibited both in Delgado Otalvaro *et al.*²¹ and in the present work the highest value. This is also consistent with the investigations of Klier *et al.*,⁴⁷ where a strong CO₂ adsorption on the metallic catalyst was observed. All adsorption constants shown in Table 5 decrease with increasing temperature due to the exothermal nature of adsorption.

Binary correlation coefficients (ρ_{ij}) were computed to assess the correlation between the parameter estimates (Table 6). The absolute values of all the non-trivial correlations coefficients confirm that using the re-parameterized Arrhenius and van't Hoff equations (eqn (19) and (20)) led successfully to a weak correlation between the parameter estimates. In addition, the convergence time of the fitting was reduced by about 60% after applying re-parameterization.

4.2.2. Mechanistic analysis. Using the derived model, the proposed reaction mechanism is elucidated in the following based on representative results. The influence of the COR, the temperature, and the CZA-to- γ -Al₂O₃ ratio on the reactions rates is discussed, as well as the observed CO and CO₂ formation during reaction.

4.2.2.1 Effect of the COR. In Section 4.1 it has been shown that high conversions and yields of DME are attained at the lowest COR levels. This was observed at all conditions in the investigated operating range, although at differing extent. This is in accordance with former kinetic studies of the methanol,^{26,47,48} and DME synthesis^{14,15} which have shown that an optimal CO₂ feed concentration exists, at which both the methanol formation and subsequently the DME formation are favored, while exceeding this concentration leads to reduced conversions and yields. Sintering of Cu crystallites in the CZA catalyst takes place with CO/H₂ and CO₂/H₂ feeds due to Cu segregation from ZnO, and due to the presence of water respectively. However, sintering is prevented at the optimal CO₂ feed concentration.⁴⁸ Since we observed no optimal value for the COR within the investigated operating range, we conclude, in agreement with other studies,^{14,15,47,48} that the optimal value is probably less than or equal to 3%, which was the lowest CO₂ concentration considered in this work (at 20% COR).

To elucidate the effect of the COR on the reactions rates, these have been depicted in Fig. 6a–c at exemplary conditions for the minimal and maximal CORs of 20% and 80%. Additionally, the mole percentage profiles of water, methanol and

DME are displayed in Fig. 6d (Fig. S4 in the ESI† includes the profiles of CO and CO₂, which were left out here for better visualisation). It is shown that the rates of the three reactions, *i.e.*, CO₂ hydrogenation, methanol dehydration and WGSR, are higher at 20% COR than at 80% COR. This effect is straight forward for the WGSR where CO₂ is a product, and an increased product concentration shifts the equilibrium towards the educts according to the Le Chatelier's principle. For the CO₂ hydrogenation on the other hand, it may appear contradictory that the rate is lower at higher CORs since CO₂ is a reactant in this reaction. This has been attributed to several factors in the literature such as to the presence of water in high concentrations leading to sintering of the Cu particles,⁴⁸ to thermodynamic limitation of the methanol formation,⁵⁴ or to strong CO₂ adsorption on the metallic catalyst.⁴⁷ CO₂ adsorption is also believed to be important in our study, which is accounted for in the model by the strong influence of CO₂ concentration on the adsorption term (eqn (14) and Section 4.2.1), and by the considerable influence of the adsorption term on the CO₂ hydrogenation (eqn (16)). The strong influence of the adsorption term leads to an overall decrease of the reaction rate with increasing CO₂ in the feed, even though the potential term of the forward reaction is indeed higher at higher CORs.

The rate of the WGSR (Fig. 6c) takes on negative values at the reactor entrance at both CORs, indicating that the reverse water gas shift reaction (rWGSR) is faster than the WGSR at the inlet conditions. At 80% COR the rWGSR is particularly fast (high negative values, $\min. r_3^v = -3.7 \text{ mol m}^{-3} \text{ s}^{-1}$ at $z = 0$), which we attribute to the high concentrations of CO₂ and H₂ in the feed. Although a high hydrogen feed concentration is necessary to avoid the stoichiometric limitation of CO₂ hydrogenation to methanol, the high feed concentration of both, CO₂ and H₂, accelerates the rWGSR instead of the CO₂ hydrogenation as evidenced, leading to water and CO production.^{16,55} The

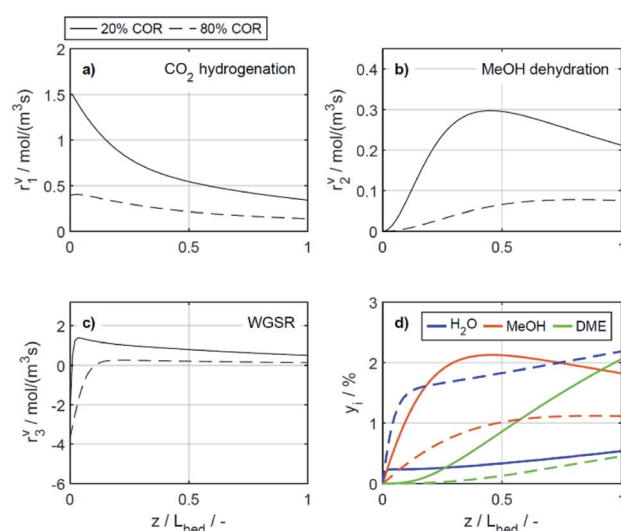


Fig. 6 Reaction rates (a) CO₂ hydrogenation, (b) MeOH dehydration, (c) WGSR and (d) mole percentage profiles of water, methanol and DME at $T = 533 \text{ K}$, $\mu = 2$. (—) Solid lines: 20% COR, (---) dashed lines: 80% COR.

simulations show that the rWGSr prevails over the WGSr for the initial 10% bed length, resulting in a pronounced increase of water concentration (Fig. 6d, blue dashed line). From a bed length beyond 10%, the water gas shift equilibrium (reaction 3) shifts to the right side and r_3^v takes on nearly constant positive values over the entire following bed length, accompanied by reduced overall water formation as water is partially consumed by the WGSr. The widely accepted mechanism of methanol formation by CO₂ hydrogenation over copper-based catalysts was disputed by Gaikwad *et al.*⁵⁶ It was shown by means of space-resolved experiments that the main carbon source for methanol formation from CO₂ rich feeds depends on the reaction conditions, in particular on the temperature. The authors concluded that at 533 K and CO₂/H₂ feeds, methanol formation takes place *via* CO hydrogenation formed by the rWGSr at the reactor inlet. Our simulation results are in accordance with that conclusion, *i.e.*, the rWGSr takes place at the reactor inlet, followed by the CO hydrogenation, in the model described by the WGSr and the subsequent CO₂ hydrogenation. We also believe that this explains the higher conversions and yields at high CO feed concentration. At this COR, the rWGSr prevails only at the reactor entrance (up to 0.8% reactor length), and the rate does not reach such high negative values (min. $r_3^v = -2.2 \text{ mol m}^{-3} \text{ s}^{-1}$ at $z = 0$). As a result, the water concentration at the reactor entrance rises steeply, but does not reach such a high level as at 80% COR. Although water has shown to limit the catalyst deactivation by coke deposition^{31,57} high water concentration in is indisputably detrimental for direct DME synthesis, especially when using $\gamma\text{-Al}_2\text{O}_3$ as the dehydration component.^{4,54} This underlines the importance of water removal, *e.g.*, by permselective membranes^{58,59} which could also be axially tailored to counteract the observed steep water increase at the reactor entrance shown here as well as in other kinetic studies.^{60,61}

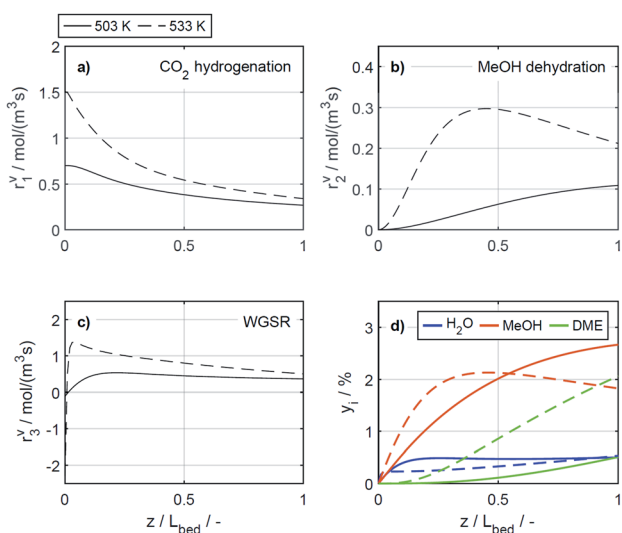


Fig. 7 Reaction rates (a) CO₂ hydrogenation, (b) MeOH dehydration, (c) WGSr and (d) mole percentage profiles of water, methanol and DME at $\mu = 2$ and COR = 20%. (—) Solid lines: $T = 503 \text{ K}$, (---) dashed lines: $T = 533 \text{ K}$.

Clearly, the methanol dehydration to DME is also affected strongly by the COR, as shown in Fig. 6b. At 20% COR the concentration of methanol is higher than the concentration of water for the largest portion of the reactor (solid lines in Fig. 6d). Conversely, at 80% COR the water concentration is higher than the concentration of methanol (dashed lines in Fig. 6d). Reduced methanol dehydration rate at high CORs has been explained in the literature by deactivation phenomena of the $\gamma\text{-Al}_2\text{O}_3$, and by a strong adsorption of methanol and/or water on the surface of the dehydration catalyst.^{14,28,30,62} In our experiments, no activity drop was observed and, as mentioned in Section 3.1, the model that enabled the best fit to the experimental data is based on the assumption that no adsorption on the dehydration catalyst takes place.^{21,29,54} Hence, the influence of the COR on the dehydration rate is accounted for by thermodynamics only. *I.e.*, considering the stoichiometry of the dehydration reaction it is clear that high methanol and low water concentrations as evidenced at 20% COR are thermodynamically favorable for DME formation, while low methanol and high water concentrations as exhibited at 80% COR are disadvantageous. As a result, the methanol dehydration is significantly slower at 80% COR than at 20% COR explaining the decreasing DME formation with increasing CORs observed experimentally (Fig. 2 and 4a, b).

4.2.2.2 Effect of the temperature. The reaction rates, and the mole fractions of DME, water and methanol are depicted in Fig. 7 at the minimal and maximal evaluated temperatures, *i.e.*, at 503 K and 533 K for a COR of 20%. Due to the general temperature dependence of the reaction rate constants, all reactions proceed faster at 533 K than at 503 K (Fig. 7a–c). In addition to the temperature dependence of the rate constants, the dependence of the adsorption rates is also relevant when assessing the influence of temperature based on the proposed model. Adsorption constants decrease with increasing temperatures due to the exothermal nature of adsorption processes (Table 5). Since the adsorption terms have an indirect proportional effect on the reaction rates (eqn (11)), the slower adsorption also contributes to the higher rates of the CO₂ hydrogenation and WGSr evidenced at higher temperatures.

A factor not considered by the model but potentially favoring methanol dehydration at elevated temperature is enhanced water desorption from the dehydration catalyst surface,⁶³ leading to an increased number of available active centres for the dehydration reaction. The effect of the temperature on the concentrations profiles is shown in Fig. 7d. Compared to 503 K (solid lines), at 533 K (dashed lines) the methanol concentration is higher for 55% of the reactor length, while the water concentration is lower for almost the entire reactor. Hence it is obvious that at 533 K, the driving force of the dehydration reaction is increased, leading to significantly higher DME concentrations and DME yields, as also determined experimentally (Fig. 4a and c). Furthermore, the concentration increase for DME is significantly higher than for methanol, confirming that higher temperatures have a positive effect on DME selectivity²⁴ (Fig. S2 and S3†).

In the study of Gaikwad *et al.*,⁵⁶ for methanol synthesis at 453, 533 and 613 K, the authors concluded that at 533 K the

main reaction mechanism takes place *via* rWGSR and CO hydrogenation, while at lower temperature, direct CO₂ hydrogenation is the dominant pathway. In Fig. 8, simulation results at the highest COR considered (80%) and at 503 and 533 K show that our lumped kinetic model is mechanistically sound according to these new insights. The respective reaction rates of the WGSR (Fig. 8c) are of particular interest: at 533 K, the phenomenon described in Section 4.2.2.1 takes place; *i.e.*, the rWGSR dominates at the reactor inlet, followed by both, WGSR and CO₂ hydrogenation, in combination representing a descriptor for CO hydrogenation; at 503 K, the WGSR rate is nearly zero and shows a nearly constant profile along the reactor length. This leads us to the conclusion that at 503 K, methanol formation takes place *via* direct CO₂ hydrogenation. From the findings of Gaikwad *et al.*,⁵⁶ it cannot be concluded exactly at which temperature the mechanism shifts, although from our findings it seems plausible that at 503 K, both reaction pathways are contributing.

4.2.2.3 Effect of the catalyst bed composition. There are several studies concerning the catalyst bed composition for the direct DME synthesis. A literature overview recently provided by Peinado *et al.*²⁴ summarizes that most studies have been performed for CO₂ lean feeds and, with high CZA proportions in the catalyst bed. Some of the studies cited state that the optimal catalyst bed composition consists of 50% CZA^{24,50,64} while other authors, like us, came to the conclusion that higher CZA-to-acid catalyst ratios are advantageous for the DME productivity.^{15,21,46} To demonstrate the influence of higher CZA-to- γ -Al₂O₃ ratios on the reaction rates, these are depicted in Fig. 9 for the reference CZA-to- γ -Al₂O₃ weight ratio $\mu = 1$, and for $\mu = 2$, which exhibited the best performance with regard to the DME yield in the experiments. The increased μ is clearly advantageous for all the reactions rates, as assumed in Section 4.1. The effect of the

catalyst bed composition is less pronounced than that of the COR and the temperature, and no significant changes on the shapes of the reaction rate profiles is observed. With regard to the concentration profiles, an increased μ leads to higher methanol and DME concentrations, whereas the concentration of water is virtually unchanged. Moreover, the relative increase in methanol concentration is higher than the relative increase in DME, indicating a decrease of the selectivity towards DME, consistent with experimental observations described in Section 4.1.

Table S3 in the ESI† provides an overview on studies with different CZA-to- γ -Al₂O₃ ratios. A direct comparison with other works regarding this variable is not comprehensively possible, due to the wide range of process parameters evaluated in literature studies,²⁴ and also due to more or less widespread catalyst properties, reactor types and configurations, and finally the respective methodology followed in each study. Commonly drawn conclusions in accordance with our work are as follows: (1) DME selectivity increases with decreasing CZA-to- γ -Al₂O₃ ratios when CO₂ is present in the feed.^{24,50} (2) However, decreasing CZA-to- γ -Al₂O₃ ratio especially below a value of 1, is detrimental for the DME production.^{15,24,64} (3) Hence, increased DME yield attained with increasing CZA-to- γ -Al₂O₃ ratios is attributed to a significant enhancement of the CO_x conversion, that makes up for the selectivity loss. Higher amounts of the CZA catalyst, evidently lead to higher rates of CO₂ hydrogenation and water gas shift reaction (Fig. 9a and c), which are both promoted by this catalyst. On the other hand, increased methanol formation and water depletion rates are contributing to methanol dehydration to DME. Hence, explaining the higher rate of the dehydration reaction (Fig. 9b), even though compared to the reference case ($\mu = 1$), the fraction of the dehydration catalyst at $\mu = 2$ is reduced. It should also be noted that most of the studies mentioned are experimental in scope. This emphasizes the general importance and necessity of

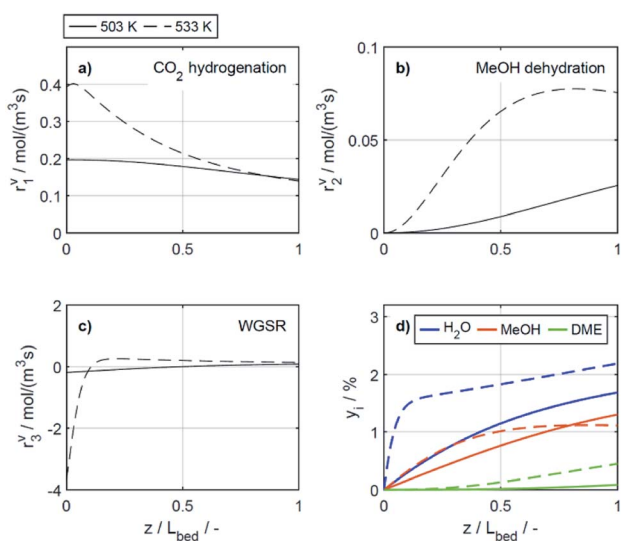


Fig. 8 Reaction rates (a) CO₂ hydrogenation, (b) MeOH dehydration, (c) WGSR and (d) mole percentage profiles of water, methanol and DME at $\mu = 2$ and COR = 80%. (—) Solid lines: $T = 503$ K, (---) dashed lines: $T = 533$ K.

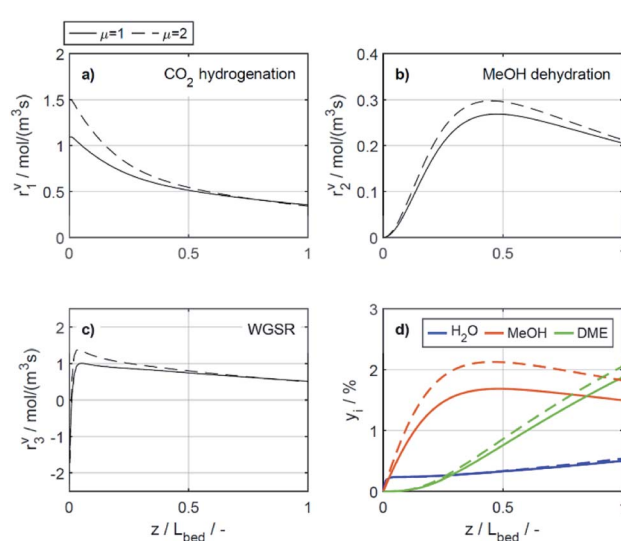


Fig. 9 Reaction rates (a) CO₂ hydrogenation, (b) MeOH dehydration, (c) WGSR and (d) mole percentage profiles of water, methanol and DME at $T = 533$ K, COR = 20%. (—) Solid lines: $\mu = 1$, (---) dashed lines: $\mu = 2$.

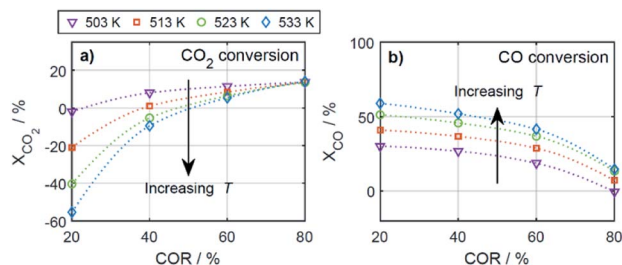


Fig. 10 CO₂ and CO conversion for all evaluated CORs and temperatures. $\mu = 2$.

models valid for a broader range of catalyst bed compositions (especially also for a wide range of CO₂/CO_x feed ratios) to enable model-based evaluation of optimization strategies and/or reactor designs under consideration of these variables.

4.2.2.4 CO₂ and CO formation during reaction. According to eqn (27), a negative conversion (X_i) indicates that the amount of the respective species i is higher at the reactor outlet than at the reactor inlet, *i.e.*, that the species was formed during reaction. Within the wide operational windows studied in this work, CO₂ and CO formation was observed at specific conditions.

As depicted in Fig. 10a, CO₂ formation was evidenced at high temperatures and low CORs. The highest CO₂ formation, *i.e.*, the lowest CO₂ conversion, was observed at 20% COR and 533 K. At these conditions, the WGSR is faster than the CO₂ hydrogenation for most of the reactor length. Hence, more CO₂ is produced than consumed, explaining the negative CO₂ conversions. Contrary to the results at higher temperatures, CO₂ formation does not take place at 503 K.

CO formation on the other hand, was evidenced at low temperatures and high CORs (Fig. 10b). The minimal CO conversion took place at 80% COR and 503 K, caused by a relatively late shift of the rWGSR to WGSR. At these conditions, the rWGSR prevailed over the WGSR for approx. half of the reactor length. The CO produced in the first half of the reactor, is not completely consumed in the second half, leading to the slight overall CO production shown in Fig. 10b. In agreement with the mechanistic analysis presented before, CO₂ and CO conversion show opposite trends, with the CO conversion increasing with temperature, as methanol formation takes place *via* CO hydrogenation.⁵⁶ CO conversion is also increasing with decreasing COR, due to WGSR that is favored at high CO feed concentration, and decreases respectively with increasing COR according to an increased participation of the rWGSR.

5. Summary and conclusions

The reaction kinetics of the direct DME synthesis over Cu/ZnO/Al₂O₃ (CZA) and γ -Al₂O₃ were investigated at high pressure (50 bar) in a temperature range between 503 and 533 K, CZA-to- γ -Al₂O₃ weight ratios from 1 to 5, space times from 240 to 400 kg_{cat} s m_{gas}⁻³, and carbon oxide ratios (CO₂/CO_x) from 20 to 80%. The successful fitting to these data resulted in the main contribution of this paper: a mechanistically sound reaction kinetic model with a particularly large range of validity. Due to

its wide validity range, the reaction kinetic model provided in this contribution is suitable aiming towards optimal reactor and/or process design, and optimization of novel technologies for the direct DME synthesis.

The influence of key process variables on reaction rates was examined in light of the derived model, and representative results were presented with the goal of determining causality and providing a comprehensive understanding of the observed phenomena. An increased CZA-to- γ -Al₂O₃ ratio was found to be favorable in terms of DME yield, although this reduced the amount of dehydrogenation catalyst. This is attributed to the synergistic effects of direct DME synthesis, *i.e.*, an increased methanol production rate also accelerates the dehydration of methanol to DME. With regard to the composition of the feed, a high CO content leads to an increased DME yield, since the water gas shift reaction and thus the water consumption in the system are accelerated. Conversely, a high CO₂ content leads to a significantly increased water concentration. This is due to a strong effect of reverse water gas shift at the reactor inlet, which increases with CO₂ content. Moreover, it was shown that increasing temperatures lead to higher DME yield and selectivity regardless of the feed composition. However, at high CO₂ content in the feed, the attainable enhancement by optimization of the reaction conditions might not lead to sufficiently high DME yields for the process to be economically feasible. Therefore, additional technical improvements are necessary to achieve a significant increase in overall performance. Possible technical improvements include water removal, novel reactor concepts such as membrane reactors or reactive distillation, as well as a customized product separation.

Conflicts of interest

There are no conflicts to declare.

Acknowledgements

This research was funded by the Helmholtz Association, Research Programme “Materials and Technologies for the Energy Transition (MTET)”, Topic 3 “Chemical Energy Carriers”.

Notes and references

- 1 N. Dahmen, J. Abeln, M. Eberhard, T. Kolb, H. Leibold, J. Sauer, D. Stapf and B. Zimmerlin, *Wiley Interdiscip. Rev.: Energy Environ.*, 2017, **6**, e236.
- 2 B. Niethammer, S. Wodarz, M. Betz, P. Haltenort, D. Oestreich, K. Hackbarth, U. Arnold, T. Otto and J. Sauer, *Chem. Ing. Tech.*, 2018, **90**, 99–112.
- 3 T. A. Semelsberger, R. L. Borup and H. L. Greene, *J. Power Sources*, 2006, **156**, 497–511.
- 4 Z. Azizi, M. Rezaeiemanesh, T. Tohidian and M. R. Rahimpour, *Chem. Eng. Process.*, 2014, **82**, 150–172.
- 5 H. G. Roh and C. S. Lee, in *Locomotives and Rail Road Transportation*, Springer Singapore, Singapore, 2017, pp. 113–128.

- 6 K. Alper, K. Tekin, S. Karagöz and A. J. Ragauskas, *Sustainable Energy Fuels*, 2020, **4**, 4390–4414.
- 7 W.-H. Chen, C.-L. Hsu and X.-D. Wang, *Energy*, 2016, **109**, 326–340.
- 8 L. Liu, Z. Lin, S. Lin, Y. Chen, L. Zhang, S. Chen, X. Zhang, J. Lin, Z. Zhang, S. Wan and Y. Wang, *J. Energy Chem.*, 2021, **58**, 564–572.
- 9 R. Ahmad, D. Schrempp, S. Behrens, J. Sauer, M. Döring and U. Arnold, *Fuel Process. Technol.*, 2014, **121**, 38–46.
- 10 S. Polierer, D. Guse, S. Wild, K. Herrera Delgado, T. N. Otto, T. A. Zevaco, M. Kind, J. Sauer, F. Studt and S. Pitter, *Catalysts*, 2020, **10**, 816.
- 11 F. Dalena, A. Senatore, A. Marino, A. Gordano, M. Basile and A. Basile, in *Methanol*, Elsevier, 2018, pp. 3–28.
- 12 K. Takeishi, *Biofuels*, 2010, **1**, 217–226.
- 13 A. Ateka, P. Pérez-Uriarte, M. Gamero, J. Ereña, A. T. Aguayo and J. Bilbao, *Energy*, 2017, **120**, 796–804.
- 14 K. L. Ng, D. Chadwick and B. A. Toseland, *Chem. Eng. Sci.*, 1999, **54**, 3587–3592.
- 15 R. Peláez, P. Marín and S. Ordóñez, *Fuel Process. Technol.*, 2017, **168**, 40–49.
- 16 S. P. Naik, T. Ryu, V. Bui, J. D. Miller, N. B. Drinnan and W. Zmierzczak, *Chem. Eng. J.*, 2011, **167**, 362–368.
- 17 S. Wild, S. Polierer, T. A. Zevaco, D. Guse, M. Kind, S. Pitter, K. Herrera Delgado and J. Sauer, *RSC Adv.*, 2021, **11**, 2556–2564.
- 18 E. Catizzzone, G. Bonura, M. Migliori, F. Frusteri and G. Giordano, *Molecules*, 2017, **23**, 31.
- 19 M. T. Luu, D. Milani, M. Wake and A. Abbas, *Chem. Eng. Sci.*, 2016, **149**, 143–155.
- 20 I. A. Kurzina, S. I. Reshetnikov, N. I. Karakchieva and L. N. Kurina, *Chem. Eng. J.*, 2017, **329**, 135–141.
- 21 N. Delgado Otalvaro, M. Kaiser, K. Herrera Delgado, S. Wild, J. Sauer and H. Freund, *React. Chem. Eng.*, 2020, **5**, 949–960.
- 22 C. P. Renk, *Die einstufige aus Synthesegas Dimethylether-Synthese Experimentelle und theoretische Betrachtungen zur einstufigen DME-Synthese mit Synthesegas aus der Flugstrom-Druckvergasung von Biomasse*, Forschungszentrum Karlsruhe GmbH, 2009.
- 23 K. Bizon, K. Skrzypek-Markiewicz and G. Continillo, *Catalysts*, 2020, **10**, 852.
- 24 C. Peinado, D. Liuzzi, M. Retuerto, J. Boon, M. A. Peña and S. Rojas, *Chem. Eng. J.*, 2020, **4**, 100039.
- 25 K. McBride, T. Turek and R. Güttel, *AIChE J.*, 2012, **58**, 3468–3473.
- 26 K. M. V. Bussche and G. F. Froment, *J. Catal.*, 1996, **161**, 1–10.
- 27 G. H. Graaf, E. J. Stamhuis and A. A. C. M. Beenackers, *Chem. Eng. Sci.*, 1988, **43**, 3185–3195.
- 28 G. Bercic and J. Levec, *Ind. Eng. Chem. Res.*, 1993, **32**, 2478–2484.
- 29 W. Z. Lu, L. H. Teng and W. De Xiao, *Chem. Eng. Sci.*, 2004, **59**, 5455–5464.
- 30 A. T. Aguayo, J. Ereña, D. Mier, J. M. Arandes, M. Olazar and J. Bilbao, *Ind. Eng. Chem. Res.*, 2007, **46**, 5522–5530.
- 31 J. Ereña, I. Sierra, A. T. Aguayo, A. Ateka, M. Olazar and J. Bilbao, *Chem. Eng. J.*, 2011, **174**, 660–667.
- 32 J. Park, H. S. Kim, W. B. Lee and M.-J. Park, *Catalysts*, 2020, **10**, 655.
- 33 Y. T. Kim, K.-D. Jung and E. D. Park, *Appl. Catal., A*, 2011, **393**, 275–287.
- 34 M. Schwaab and J. C. Pinto, *Chem. Eng. Sci.*, 2007, **62**, 2750–2764.
- 35 K. Toch, J. W. Thybaut and G. B. Marin, *AIChE J.*, 2015, **61**, 880–892.
- 36 D.-Y. Peng and D. B. Robinson, *Ind. Eng. Chem. Fundam.*, 1976, **15**, 59–64.
- 37 K. Ye, H. Freund and K. Sundmacher, *J. Chem. Thermodyn.*, 2011, **43**, 2002–2014.
- 38 A. Tripodi, M. Compagnoni, R. Martinazzo, G. Ramis and I. Rossetti, *Catalysts*, 2017, **7**, 159.
- 39 Y. I. Pyatnitskii, P. E. Strizhak and N. K. Lunev, *Theor. Exp. Chem.*, 2009, **45**, 325–330.
- 40 P. Ratamanalaya, S. Limtrakul, T. Vatanatham and P. Ramachandran, in *TICHe International Conference 2011*, vol. 2011, pp. ee014.1–ee014.5.
- 41 Z. Nie, H. Liu, D. Liu, W. Ying and D. Fang, *J. Nat. Gas Chem.*, 2005, **14**, 22–28.
- 42 A. K. Agarwal and M. L. Brisk, *Ind. Eng. Chem. Process Des. Dev.*, 1985, **24**, 203–207.
- 43 D. M. Espie and S. Macchietto, *Ind. Eng. Chem. Res.*, 1988, **27**, 2175–2179.
- 44 F. Vegliò, M. Trifoni, F. Pagnanelli and L. Toro, *Hydrometallurgy*, 2001, **60**, 167–179.
- 45 G. H. Graaf, P. J. J. M. Sijtsema, E. J. Stamhuis and E. Al, *Chem. Eng. Sci.*, 1986, **41**, 2883–2890.
- 46 A. Ateka, I. Sierra, J. Ereña, J. Bilbao and A. T. Aguayo, *Fuel Process. Technol.*, 2016, **152**, 34–45.
- 47 K. Klier, V. Chatikavanij, R. G. Herman and G. W. Simmons, *J. Catal.*, 1982, **74**, 343–360.
- 48 O. Martin, C. Mondelli, A. Cervellino, D. Ferri, D. Curulla-Ferré and J. Pérez-Ramírez, *Angew. Chem., Int. Ed.*, 2016, **55**, 11031–11036.
- 49 J. D. Grunwaldt, A. M. Molenbroek, N. Y. Topsøe, H. Topsøe and B. S. Clausen, *J. Catal.*, 2000, **194**, 452–460.
- 50 J. W. Bae, H. S. Potdar, S. H. Kang and K. W. Jun, *Energy Fuels*, 2008, **22**, 223–230.
- 51 J. Palomo, M. Á. Rodríguez-Cano, J. Rodríguez-Mirasol and T. Cordero, *Appl. Catal., B*, 2020, **270**, 118893.
- 52 A. García-Trenco and A. Martínez, *Appl. Catal., A*, 2012, **411–412**, 170–179.
- 53 I. Sierra, J. Ereña, A. T. Aguayo, M. Olazar and J. Bilbao, *Ind. Eng. Chem. Res.*, 2010, **49**, 481–489.
- 54 U. Mondal and G. D. Yadav, *J. CO₂ Util.*, 2019, **32**, 299–320.
- 55 M. P. Rohde, G. Schaub, S. Khajavi, J. C. Jansen and F. Kapteijn, *Microporous Mesoporous Mater.*, 2008, **115**, 123–136.
- 56 R. Gaikwad, H. Reymond, N. Phongprueksathat, P. Rudolf von Rohr and A. Urakawa, *Catal. Sci. Technol.*, 2020, **10**, 2763–2768.
- 57 A. T. Aguayo, J. Ereña, I. Sierra, M. Olazar and J. Bilbao, *Catal. Today*, 2005, **106**, 265–270.
- 58 N. Diban, A. M. Urtiaga, I. Ortiz, J. Ereña, J. Bilbao and A. T. Aguayo, *Ind. Eng. Chem. Res.*, 2014, **53**, 19479–19487.

Paper

- 59 I. Iliuta, F. Larachi and P. Fongarland, *Ind. Eng. Chem. Res.*, 2010, **49**, 6870–6877.
- 60 M. De Falco, M. Capocelli and G. Centi, *Chem. Eng. J.*, 2016, **294**, 400–409.
- 61 S. K. Wilkinson, L. G. A. Van de Water, B. Miller, M. J. H. Simmons, E. H. Stitt and M. J. Watson, *J. Catal.*, 2016, **337**, 208–220.
- 62 M. Mollavali, F. Yaripour, H. Atashi and S. Sahebdehfar, *Ind. Eng. Chem. Res.*, 2008, **47**, 3265–3273.
- 63 V. Sanchez Escribano, G. Garbarino, E. Finocchio and G. Busca, *Top. Catal.*, 2017, **60**, 1554–1564.
- 64 J. Abu-Dahrieh, D. Rooney, A. Goguet and Y. Saih, *Chem. Eng. J.*, 2012, **203**, 201–211.

ARTICLE

Electronic Supplementary Information

Kinetics of Direct DME Synthesis from CO₂ rich syngas under variation of the CZA-to-γ-Al₂O₃ ratio of a mixed catalyst bed

Nirvana Delgado Otalvaro,^a Gerardo Sogne,^a Karla Herrera Delgado,^{*a} Stefan Wild,^a Stephan Pitter^a and Jörg Sauer^a

S1. Reduction procedure and conditioning

Before performing the kinetic measurements, the CZA share of the catalytic bed was activated at atmospheric pressure with a volume flow of 300 ml min⁻¹ containing 5% of H₂ and 95% of N₂. The system was heated from 373 to 473 K at a heating rate of 20 K h⁻¹. This temperature was hold for one hour, followed by further heating to 513 K at a heating rate of 12 K h⁻¹. Finally, the H₂ concentration in the gas flow was increased to 50%, maintaining the same total flow rate for an additional hour. Posterior to the catalyst reduction, the operating conditions 300 ml min⁻¹, 503 K, 20% COR and 50 bar, were set to allow the catalyst system to run in. This operating point was maintained and the concentration of the product gas was monitored until a steady state of the catalyst system could be assumed (between 12 and 20 h time on stream).

S2. A priori Criteria.

Table S1. Calculated criteria for the verification of assumptions.

Phenomena to be neglected	Criteria	Equation	Calculated Value*
Outer mass transfer	Mears ¹	$\eta Da_{II} = \frac{r_{j,eff}}{\beta_i c_i} < \frac{0.05}{ n }$	0.0182
Inner mass transfer	Weisz-Prater ²	$\psi = \frac{(r_{j,eff} l_c^2) n + 1}{D_{i,eff} c_{i,s} 2} < 0.15$	9.30E-06
Outer heat transfer	Mears ¹	$\frac{ \Delta H_R r_{j,eff} R E_A}{\lambda T R T} < 0.15$	0.0008
Inner heat transfer	Anderson ³	$\frac{ \Delta H_R r_{j,eff} r_{kat}^2 E_A}{\lambda T_s R T} < 0.75$	0.0397
Radial Gradients	d/D-ratio ⁴	$24 < \frac{d_{tube}}{d_{particle}} < 48$	24
Non-Isothermal operation	Rule of Thumb	$\Delta T = T_{max} - T_{min}$	2
Axial dispersion	Bodenstein Number ⁵	$Bo = \frac{u_0 L}{D_{ax}} > 100$	481
Pressure drop	$\Delta p/L$ Zhavoronkov Correlation ⁶	$\frac{\Delta p_{max}}{p} \sim 0$	5.0 E-08

*for the worst-case scenario

^a Karlsruhe Institute of Technology (KIT), Hermann-von-Helmholtz-Platz 1, D-76344 Eggenstein-Leopoldshafen, Germany. E-mail: karla.herrera@kit.edu.
Tel: +49 721 608 28631

S3. Model Discrimination.

For the initial model discrimination, the available experimental data were first simulated using eight different kinetic models from the open literature^{7–14}. The sum of the squared errors between the measured and predicted composition of the product gas was calculated for each model and depicted in Fig. S1. In this figure, the models are named after the first author.

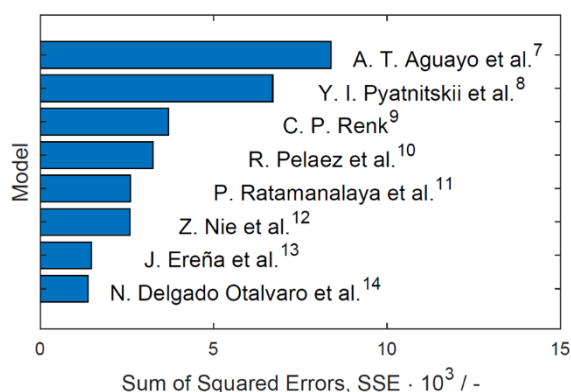


Figure S1. Total sum of squared errors for the implemented models

After this initial screening, the five models with the lower residual squared sum were parametrized to fit the experimental data. The model by Delgado Otalvaro et al.¹⁴ agreed best with the available experimental data. Hence, the model structure and respective mechanistic assumptions were chosen for fine-tuning. To enable a direct comparison of the tested models and parameters, these have been compiled in Table S2. Additionally, the mean relative error between the predictions with the different models, and the experiments for each species i (RE_i) is also given. RE_i is calculated by:

$$RE_i = 100\% \frac{1}{No. Exps} \sum_{n=1}^{No. Exps} \frac{|y_{i,out,measured,n} - y_{i,out,predicted,n}|}{y_{i,out,measured,n}}$$

The indices of the reaction rates, and rate constants in Table S2 correspond to the following reactions:

1. $\text{CO}_2 + 3 \text{H}_2 \rightleftharpoons \text{CH}_3\text{OH} + \text{H}_2\text{O}$
2. $2 \text{CH}_3\text{OH} \rightleftharpoons \text{CH}_3\text{OCH}_3 + \text{H}_2\text{O}$
3. $\text{CO} + \text{H}_2\text{O} \rightleftharpoons \text{CO}_2 + \text{H}_2$
4. $\text{CO} + 2 \text{H}_2 \rightleftharpoons \text{CH}_3\text{OH}$
5. $n\text{CO} + (2n + 1)\text{H}_2 \rightleftharpoons \text{C}_n\text{H}_{2n+2} + n\text{H}_2\text{O}$

Table S2. Compilation of tested reaction kinetic models with the respective specific parameters, and resulting relative error for each species.

Model	Rate expressions	Model specific parameter	RE/%
N. Delgado Otalvaro ¹⁴	$r_1 = k_1 \frac{\left(f_{\text{CO}_2} f_{\text{H}_2}^3 - \frac{f_{\text{H}_2\text{O}} f_{\text{CH}_3\text{OH}}}{K_{f,1}}\right) [(1 - \varepsilon_{\text{bed}}) \rho_{\text{CZA}} \xi_{\text{CZA}}]}{\left(1 + K_{\text{CO}_2} f_{\text{CO}_2} + K_{\text{CO}} f_{\text{CO}} + \sqrt{K_{\text{H}_2} f_{\text{H}_2}}\right)^3}$ $r_2 = k_2 \left(f_{\text{CH}_3\text{OH}}^2 - \frac{f_{\text{DME}} f_{\text{H}_2\text{O}}}{K_{f,2}}\right) [(1 - \varepsilon_{\text{bed}}) \rho_{\text{ALOX}} \xi_{\text{ALOX}}]$ $r_3 = k_3 \frac{\left(f_{\text{H}_2\text{O}} - \frac{f_{\text{CO}_2} f_{\text{H}_2}}{K_{f,3}}\right) [(1 - \varepsilon_{\text{bed}}) \rho_{\text{CZA}} \xi_{\text{CZA}}]}{1 + K_{\text{CO}_2} f_{\text{CO}_2} + K_{\text{CO}} f_{\text{CO}} + \sqrt{K_{\text{H}_2} f_{\text{H}_2}}}$	$k_1 = \exp(-6.94) \exp\left[-\frac{21.81}{R T_R} \left(\frac{T_R}{T} - 1\right)\right]$ $k_2 = \exp(-2.07) \exp\left[-\frac{42.77}{R T_R} \left(\frac{T_R}{T} - 1\right)\right]$ $k_3 = \exp(-2.75) \exp\left[-\frac{10.82}{R T_R} \left(\frac{T_R}{T} - 1\right)\right]$ $K_{\text{CO}} = \exp(-15.32) \exp\left[\frac{14.03}{R T_R} \left(\frac{T_R}{T} - 1\right)\right]$ $K_{\text{CO}_2} = \exp(-0.57) \exp\left[-\frac{0}{R T_R} \left(\frac{T_R}{T} - 1\right)\right]$ $K_{\text{H}_2} = \exp(-19.51) \exp\left[\frac{14.68}{R T_R} \left(\frac{T_R}{T} - 1\right)\right]$ $[r_j] = \text{mol m}^{-3} \text{s}^{-1}$	CO 9.7 CO2 7.1 H2 1.5 DME 54.5
J. Ereña ¹³	$r_2 = k_2 \left(f_{\text{CH}_3\text{OH}}^2 - \frac{f_{\text{DME}} f_{\text{H}_2\text{O}}}{K_2}\right)$	$k_2 = 3.41 \cdot 10^{-3} \exp\left(-\frac{63.5}{R} \left(\frac{1}{T} - \frac{1}{548}\right)\right)$	CO 11.3

	$r_3 = k_3 \left(f_{\text{CO}} f_{\text{H}_2\text{O}} - \frac{f_{\text{CO}_2} f_{\text{H}_2}}{K_3} \right)$ $r_4 = k_4 \frac{\left(f_{\text{H}_2}^2 f_{\text{CO}} - \frac{f_{\text{CH}_3\text{OH}}}{K_4} \right) r_{\text{CH}_3\text{OH}}}{\left(1 + K_{\text{H}_2\text{O}} f_{\text{H}_2\text{O}} + K_{\text{CO}_2} f_{\text{CO}_2} \right)}$ $r_5 = k_5 \frac{\left(f_{\text{CO}} f_{\text{H}_2}^3 - \frac{f_{\text{HC}} f_{\text{H}_2\text{O}}}{K_5} \right)}{\left(1 + K_{\text{H}_2\text{O}} f_{\text{H}_2\text{O}} + K_{\text{CO}_2} f_{\text{CO}_2} \right)}$	k_3 : not given $k_4 = 2.4 \cdot 10^{-5} \exp\left(-\frac{90.0}{R} \left(\frac{1}{T} - \frac{1}{548}\right)\right)$ $k_5 = 1.23 \cdot 10^{-7} \exp\left(-\frac{9.9}{R} \left(\frac{1}{T} - \frac{1}{548}\right)\right)$ $K_{\text{H}_2\text{O}} = 2.67 \cdot 10^{-3} \exp\left(\frac{384.8}{R} \left(\frac{1}{T} - \frac{1}{548}\right)\right)$ $K_{\text{CO}_2} = 1.13 \cdot 10^{-3} \exp\left(\frac{43.4}{R} \left(\frac{1}{T} - \frac{1}{548}\right)\right)$ $[k_2] = \text{mol}_{\text{DME}} (\text{mol}_c)^{-1} \text{g}_{\text{cat}}^{-1} \text{h}^{-1} \text{bar}^{-2}$ $[k_4] = \text{mol}_{\text{CH}_3\text{OH}} (\text{mol}_c)^{-1} \text{g}_{\text{cat}}^{-1} \text{h}^{-1} \text{bar}^{-3}$ $[k_5] = \text{mol}_{\text{HC}} (\text{mol}_c)^{-1} \text{g}_{\text{cat}}^{-1} \text{h}^{-1} \text{bar}^{-4}$ $[E_a] = \text{kJ mol}^{-1}$ $[\Delta H_{\text{ads}}] = \text{kJ mol}^{-1}$ $[K_i] = \text{bar}^{-1}$	CO2 7.6 H2 1.6 DME 62.8
Z. Nie ¹²	$r_1 = k_1 \frac{f_{\text{CO}_2} f_{\text{H}_2}^3 \left(1 - \frac{f_{\text{CH}_3\text{OH}} f_{\text{H}_2\text{O}}}{K_{f_1} f_{\text{CO}_2} f_{\text{H}_2}^3} \right)}{\left(1 + K_{\text{CO}} f_{\text{CO}} + K_{\text{CO}_2} f_{\text{CO}_2} + K_{\text{H}_2} f_{\text{H}_2} \right)^4}$ $r_2 = k_2 \frac{f_{\text{CH}_3\text{OH}} \left(1 - \frac{f_{\text{DME}} f_{\text{H}_2\text{O}}}{K_{f_2} f_{\text{CH}_3\text{OH}}^2} \right)}{\left(1 + \sqrt{K_{\text{CH}_3\text{OH}}} f_{\text{CH}_3\text{OH}} \right)^2}$ $r_4 = k_4 \frac{f_{\text{CO}} f_{\text{H}_2}^2 \left(1 - \frac{f_{\text{CH}_3\text{OH}}}{K_{f_4} f_{\text{CO}} f_{\text{H}_2}^2} \right)}{\left(1 + K_{\text{CO}} f_{\text{CO}} + K_{\text{CO}_2} f_{\text{CO}_2} + K_{\text{H}_2} f_{\text{H}_2} \right)^3}$	$k_1 = 5.059 \cdot 10^3 \exp\left(-\frac{67515}{R T}\right)$ $k_2 = 1.602 \cdot 10^3 \exp\left(-\frac{43473}{R T}\right)$ $k_4 = 7.380 \cdot 10^3 \exp\left(-\frac{54307}{R T}\right)$ $K_{\text{CO}} = 3.934 \cdot 10^{-6} \exp\left(\frac{37373}{R T}\right)$ $K_{\text{CO}_2} = 1.858 \cdot 10^{-6} \exp\left(\frac{53795}{R T}\right)$ $K_{\text{H}_2} = 0.6716 \exp\left(-\frac{6476}{R T}\right)$ $K_{\text{CH}_3\text{OH}} = 3.480 \cdot 10^{-6} \exp\left(\frac{54689}{R T}\right)$ $[r_j] = \text{ml g}^{-1} \text{h}^{-1}$	CO 36.5 CO2 10.6 H2 6.7 DME 100
P. Ratamana laya ¹¹	$r_2 = k_2 \frac{\left(p_{\text{CH}_3\text{OH}}^2 - \frac{p_{\text{DME}} p_{\text{H}_2\text{O}}}{K_{\text{eq}_2}} \right)}{\left(1 + \sqrt{K_{\text{CH}_3\text{OH}}} p_{\text{CH}_3\text{OH}} + K_{\text{H}_2\text{O}} p_{\text{H}_2\text{O}} \right)^2}$ $r_3 = k_3 \frac{\left(p_{\text{CO}} p_{\text{H}_2\text{O}} - \frac{p_{\text{CO}_2} p_{\text{H}_2}}{K_{\text{eq}_3}} \right)}{\left(1 + K_{\text{CO}} p_{\text{CO}} + K_{\text{H}_2\text{O}} p_{\text{H}_2\text{O}} + K_{\text{CO}_2} p_{\text{CO}_2} + \sqrt{K_{\text{H}_2}} p_{\text{H}_2} \right)^2}$ $r_4 = k_4 \frac{\left(p_{\text{CO}} p_{\text{H}_2}^2 - \frac{p_{\text{CH}_3\text{OH}}}{K_{\text{eq}_4}} \right)}{\left(1 + K_{\text{CO}} p_{\text{CO}} + \sqrt{K_{\text{H}_2}} p_{\text{H}_2} + K_{\text{CH}_3\text{OH}} p_{\text{CH}_3\text{OH}} \right)^3}$	$k_2 = 1.69 \cdot 10^8 \exp\left(-\frac{69787}{R T}\right)$ $k_3 = 1202.8 \exp\left(-\frac{20437}{R T}\right)$ $k_4 = 40.498 \exp\left(-\frac{18203}{R T}\right)$ $K_{\text{CH}_3\text{OH}} = 0.9535 \exp\left(\frac{16243}{R T}\right)$ $K_{\text{H}_2\text{O}} = 6.992 \exp\left(\frac{26452}{R T}\right)$ $K_{\text{CO}} = 4.49 \cdot 10^{-7} \exp\left(\frac{60528}{R T}\right)$ $K_{\text{CO}_2} = 1.092 \cdot 10^{-7} \exp\left(\frac{66924}{R T}\right)$ $K_{\text{H}_2} = 0.2487 \exp\left(\frac{30961}{R T}\right)$ $[K_i] = \text{bar}^{-1}$	CO 36.1 CO2 10.7 H2 6.7 DME 100
R. Pelaez ¹⁰	$r_1 = \frac{k_1}{\left(1 + K_{\text{H}_2\text{O}} f_{\text{H}_2\text{O}} \right)^3} \left(f_{\text{CO}_2} f_{\text{H}_2} - \frac{f_{\text{CH}_3\text{OH}} f_{\text{H}_2\text{O}}}{K_{\text{eq}_1} f_{\text{H}_2}^2} \right)$ $r_2 = k_2 \left(f_{\text{CH}_3\text{OH}}^2 - \frac{f_{\text{DME}} f_{\text{H}_2\text{O}}}{K_{\text{eq}_2}} \right)$ $r_3 = k_3 \left(f_{\text{CO}} f_{\text{H}_2\text{O}} - \frac{f_{\text{CO}_2} f_{\text{H}_2}}{K_{\text{eq}_3}} \right)$ $r_4 = \frac{k_4}{\left(1 + K_{\text{H}_2\text{O}} f_{\text{H}_2\text{O}} \right)^3} \left(f_{\text{CO}} f_{\text{H}_2} - \frac{f_{\text{CH}_3\text{OH}}}{K_{\text{eq}_4} f_{\text{H}_2}} \right)$	Equation for temperature dependency of the rate or adsorption constants is not given. Parameter estimates: $k_{1,\text{at } 523 \text{ K}} = 2.55 \cdot 10^{-3} \text{ mol kg}_{\text{cat}}^{-1} \text{ s}^{-1} \text{bar}^{-2}$ $E_{a,1} = 3.8 \text{ kJ/mol}$ $k_{2,\text{at } 523 \text{ K}} = 8.13 \text{ mol kg}_{\text{cat}}^{-1} \text{ s}^{-1} \text{bar}^{-2}$ k_3 : not given (r_3 at equilibrium) $k_{4,\text{at } 523 \text{ K}} = 6.43 \cdot 10^{-7} \text{ mol kg}_{\text{cat}}^{-1} \text{ s}^{-1} \text{bar}^{-2}$ $E_{a,4} = 171.8 \text{ kJ/mol}$ $K_{\text{H}_2\text{O}} = 19 \text{ bar}^{-1}$	CO 25.8 CO2 13.2 H2 6.4 DME 99.5

C. P. Renk ⁹	$r_2 = k_2 c_{\text{CH}_3\text{OH}}^{1,1} - k_{2'} c_{\text{DME}}^{1,2} c_{\text{H}_2\text{O}}$ $r_3 = k_3 c_{\text{CO}}^{0,2} c_{\text{H}_2\text{O}}^{1,3} - k_{3'} c_{\text{H}_2}^{0,4} c_{\text{CO}_2}^{0,2}$ $r_4 = k_4 c_{\text{H}_2} c_{\text{CO}}^{0,5} - k_{4'} c_{\text{CH}_3\text{OH}}^{2,4}$	$k_2 = 5.1 \cdot 10^1 \exp\left(-\frac{0}{RT}\right)$ $k_{2'} = 8.6 \cdot 10^6 \exp\left(-\frac{31}{RT}\right)$ $k_3 = 1.5 \cdot 10^4 \exp\left(-\frac{0.2}{RT}\right)$ $k_{3'} = 2.6 \cdot 10^9 \exp\left(-\frac{107}{RT}\right)$ $k_4 = 1.4 \cdot 10^{13} \exp\left(-\frac{138}{RT}\right)$ $k_{4'} = 1.1 \cdot 10^{11} \exp\left(-\frac{44}{RT}\right)$ $[E_a] = \text{kJ mol}^{-1}$ $[k_j] = [k_{j'}] = \text{ml g}^{-1} \text{s}^{-1} \text{ml}^{n-1} \text{mol}^{1-n}$	CO 26.8 CO2 12.4 H2 7.6 DME 100
Y. I. Pyatnitskii ⁸	$r_1 = k_1 \frac{p_{\text{CO}_2} p_{\text{H}_2} \left(1 - \frac{p_{\text{H}_2\text{O}} p_{\text{CH}_3\text{OH}}}{K_1 p_{\text{H}_2}^3 p_{\text{CO}_2}}\right)}{\left(1 + a_3 \frac{p_{\text{H}_2\text{O}}}{p_{\text{H}_2}} + a_1 \sqrt{p_{\text{H}_2}} + a_2 p_{\text{H}_2\text{O}}\right)^3}$ $r_2 = k_2 \frac{p_{\text{CH}_3\text{OH}} \left(1 - \frac{p_{\text{DME}} p_{\text{H}_2\text{O}}}{K_2 p_{\text{CH}_3\text{OH}}^2}\right)}{1 + K_{\text{CH}_3\text{OH}} p_{\text{CH}_3\text{OH}} + \frac{p_{\text{H}_2\text{O}}}{K_{\text{H}_2\text{O}}}}$ $r_3 = -k_3 \frac{p_{\text{CO}_2} \left(1 - K_3 \frac{p_{\text{H}_2\text{O}} p_{\text{CO}}}{p_{\text{H}_2} p_{\text{CO}_2}}\right)}{1 + a_3 \frac{p_{\text{H}_2\text{O}}}{p_{\text{H}_2}} + a_1 \sqrt{p_{\text{H}_2}} + a_2 p_{\text{H}_2\text{O}}}$	$k_1 = 0.00107 \exp\left(\frac{4414}{T}\right)$ $k_2 = 2.82 \cdot 10^6 \exp\left(-\frac{6938}{T}\right)$ $k_3 = 1.22 \cdot 10^7 \exp\left(-\frac{11398}{T}\right)$ $a_1 = 0.499 \exp\left(\frac{2068}{T}\right)$ $a_2 = 6.62 \cdot 10^{-11} \exp\left(\frac{14928}{T}\right)$ $a_3 = 3453.38$ $K_{\text{CH}_3\text{OH}} = 2.20 \cdot 10^{-5} \exp\left(\frac{7738}{T}\right)$ $K_{\text{H}_2\text{O}} = 0.051 \exp\left(\frac{626}{T}\right)$ $[a_1] = \text{bar}^{-0.5}, [a_2] = \text{bar}^{-1}$ $[a_3] = -$ $[k_1] = \text{mol g}^{-1} \text{s}^{-1} \text{bar}^{-2}$ $[k_2] = \text{mol}_{\text{DME}} \text{g}^{-1} \text{h}^{-1} \text{bar}^{-1}$ $[k_3] = \text{mol g}^{-1} \text{s}^{-1} \text{bar}^{-1}$ $[K_{\text{CH}_3\text{OH}}] = \text{bar}^{-1}, [K_{\text{H}_2\text{O}}] = \text{bar}$	CO 26.6 CO2 18.4 H2 7.3 DME 98.5
A. T. Aguayo ⁷ (Model 1)	$r_2 = k_2 \left(f_{\text{CH}_3\text{OH}}^2 - \frac{f_{\text{DME}} f_{\text{H}_2\text{O}}}{K_2}\right)$ $r_3 = k_3 \left(f_{\text{CO}} f_{\text{H}_2\text{O}} - \frac{f_{\text{CO}_2} f_{\text{H}_2}}{K_3}\right)$ $r_4 = k_4 \left(f_{\text{CO}} f_{\text{H}_2}^2 - \frac{f_{\text{CH}_3\text{OH}}}{K_4}\right)$ $r_5 = k_5 \left(f_{\text{CO}} f_{\text{H}_2}^3 - \frac{f_{\text{HC}} f_{\text{H}_2\text{O}}}{K_5}\right)$	$k_2 = 1.44 \exp\left(-\frac{80.64}{R} \left(\frac{1}{T} - \frac{1}{548}\right)\right)$ $k_3 \text{ not given } (r_3 \text{ in equilibrium})$ $k_4 = 1.91 \cdot 10^{-6} \exp\left(-\frac{11.3}{R} \left(\frac{1}{T} - \frac{1}{548}\right)\right)$ $k_5 = 2.04 \cdot 10^{-7} \exp\left(-\frac{15.92}{R} \left(\frac{1}{T} - \frac{1}{548}\right)\right)$ $[E_a] = \text{kcal mol}^{-1}$ $[k_2] = \text{mol}_{\text{DME}} (\text{mol}_{\text{H}_2})^{-1} \text{g}_{\text{cat}}^{-1} \text{h}^{-1} \text{bar}^{-2}$ $[k_4] = \text{mol}_{\text{CH}_3\text{OH}} (\text{mol}_{\text{H}_2})^{-1} \text{g}_{\text{cat}}^{-1} \text{h}^{-1} \text{bar}^{-3}$ $[k_5] = \text{mol}_{\text{HC}} (\text{mol}_{\text{H}_2})^{-1} \text{g}_{\text{cat}}^{-1} \text{h}^{-1} \text{bar}^{-4}$	CO 35.7 CO2 9.9 H2 7.3 DME 127.2

S4. Selectivity

The selectivity towards DME is displayed here in Figs. S2 and S3 complementary to Figs. 1, 2 and 4 of the manuscript.

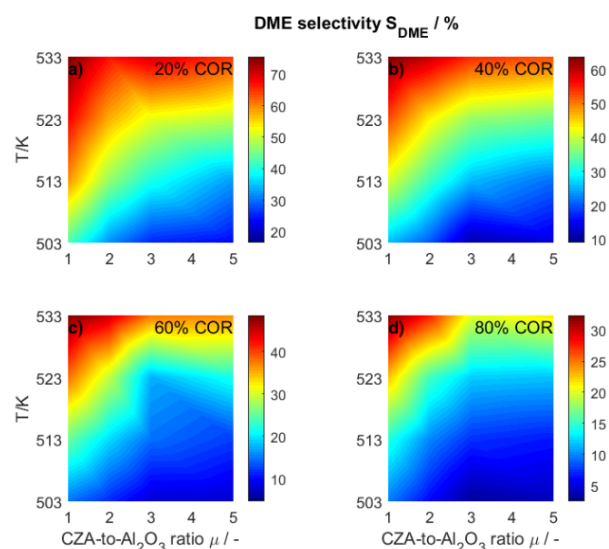


Figure S2. DME selectivity determined experimentally and plotted as a function of the temperature (T) and the CZA-to- γ - Al_2O_3 ratio (μ) for CORs of **a)** 20% **b)** 40% **c)** 60% **d)** 80%. Experimental conditions summarized in Table 1.

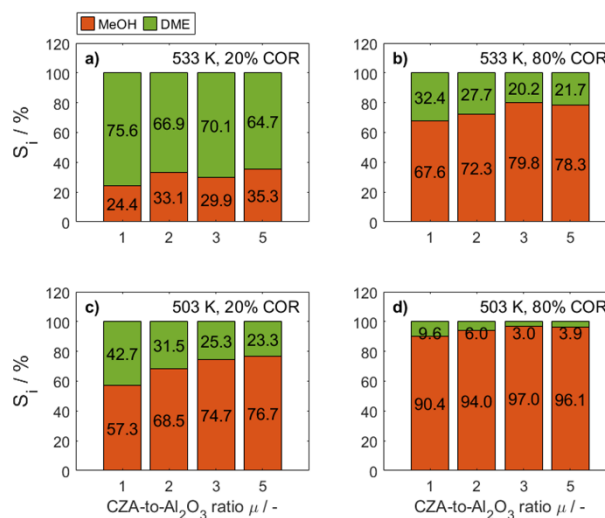


Figure S3. Selectivity of methanol and DME at specific conditions: **a)** 533 K, 20% COR, **b)** 533 K, 80% COR, **c)** 492 K, 20% COR **d)** 492 K, 80% COR

S5. Mole percentage profiles including CO and CO₂

The concentration profiles of CO and CO₂ are shown here for the sake of completeness.

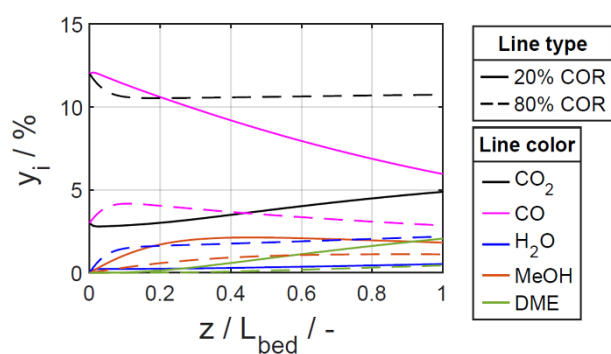


Figure S4. Mole percentage profiles of CO, CO₂, water, methanol and DME at $T=533$ K, $\mu=2$.

(—) Solid lines: 20% COR, (---) Dashed lines: 80% COR

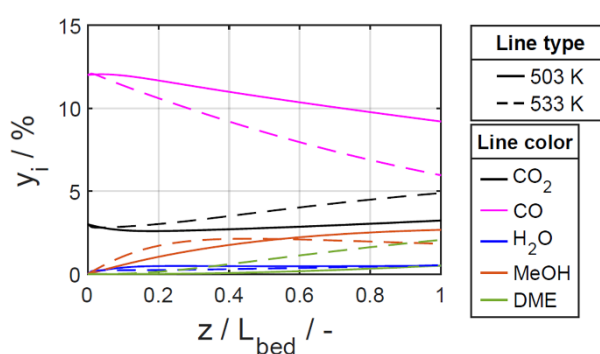


Figure S5. Mole percentage profiles of CO, CO₂, water, methanol and DME at $\mu=2$ and COR=20%.

(—) Solid lines: $T=503$ K, (---) Dashed lines: $T=533$ K

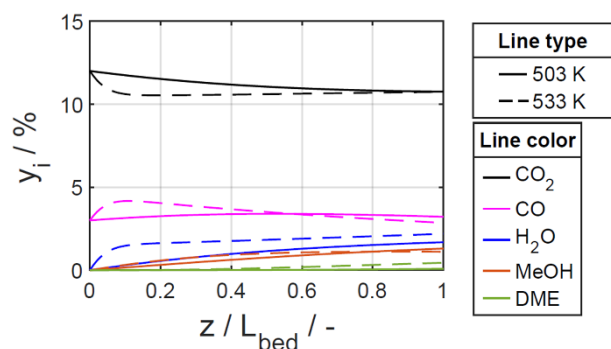


Figure S6. Mole percentage profiles of CO, CO₂, water, methanol and DME at $\mu=2$ and COR=80%.

(—) Solid lines: $T=503$ K, (---) Dashed lines: $T=533$ K

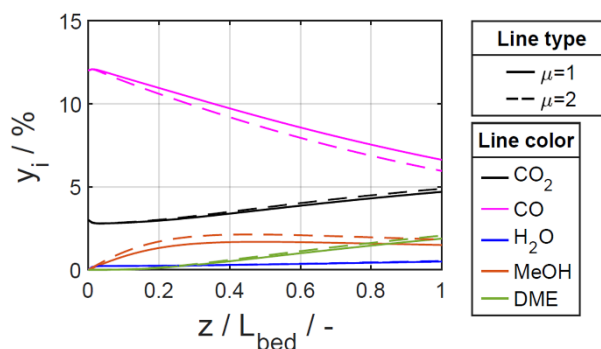


Figure S7. Mole percentage profiles of CO, CO₂, water, methanol and DME at $T=533$ K, COR=20%.

(—) Solid lines: $\mu=1$, (---) Dashed lines: $\mu=2$

S6. Overview of selected studies conducted at different CZA-to- γ -Al₂O₃ ratios

Table S3. Overview of selected studies conducted at different CZA-to- γ -Al₂O₃ ratios

Study - named after first author	Catalyst system and properties	Feed, conditions, reactor,* catalyst particle size	Optimal catalyst bed composition**
R. Pelaez et al. ¹⁰	- CZA: CHEMPACK S_{BET} : 76.6 m ² g ⁻¹ Pore volume: 0.257 cm ³ g ⁻¹ - γ -Al ₂ O ₃ : BASF S_{BET} : 239.9 m ² g ⁻¹ Pore volume: 0.545 cm ³ g ⁻¹	CO/CO ₂ /H ₂ 250-270 °C, 30 bar, 0.067-0.244 kgh/Nm ³ 100-250 μ m CZA/ γ -Al ₂ O ₃ : 70/30, 85/15, 92.5/7.5%	CZA/ γ -Al ₂ O ₃ : 92.5/7.5% regarding CO conversion and DME yield
N. Delgado Otalvaro et al. ¹⁴	Commercial CZA/ γ -Al ₂ O ₃	CO/CO ₂ /H ₂ /Inert 220-260 °C, 50 bar, 200-700 Nml/min, 250-500 μ m (model-based optimization)	65.5% CZA, 34.5% γ -Al ₂ O ₃ (v.) without dilution. Regarding conversion of CO _x and DME yield
K. L. Ng et al. ¹⁵	- CZA - γ -Al ₂ O ₃ : Norton Chemicals Co.	CO/CO ₂ /H ₂ /He, 250 °C, 50 bar, 27500 h ⁻¹ , Gradientless, internal-recycle-type reactor, stacked catalysts, 250-500 μ m, CZA/ γ -Al ₂ O ₃ : 1/0, 1/0.5, 1/1, 1/2	CZA/ γ -Al ₂ O ₃ : 1/2 regarding DME yield***
C. Peinado et al. ¹⁶	-CZA: Katalco 51-8 - γ -Al ₂ O ₃ : Alfa Aesar bimodal S_{BET} : 220-280 m ² g ⁻¹	CO/CO ₂ /H ₂ , 270-290 °C, 25-50 bar, 5000-7500 h ⁻¹ , 250-300 μ m, CZA/ γ -Al ₂ O ₃ : 90/10, 50/50, 10/90	CZA/ γ -Al ₂ O ₃ : 50/50 regarding DME productivity
J. W. Bae et al. ¹⁷	- CZA: prod. in-house CuO/ZnO/Al ₂ O ₃ =50/40/10 - γ -Al ₂ O ₃ : prod. in-house S_{BET} : 437.8 m ² g ⁻¹	CO/CO ₂ /H ₂ : 41/21/38 v. %, 250 °C, 40 bar, 11000 h ⁻¹ Pellet form hybrid catalyst CZA/ γ -Al ₂ O ₃ : 1, 3, 5	CZA/ γ -Al ₂ O ₃ : 1 Regarding the DME selectivity CZA/ γ -Al ₂ O ₃ : 5 Regarding the CO conversion
J. Abu-Dahrieh et al. ¹⁸	-CZA: prod. in-house CuO/ZnO/Al ₂ O ₃ =60/30/10 S_{BET} : 56.9 m ² g ⁻¹ pore size: 1.05 nm	CO/CO ₂ /H ₂ /Ar: 31/4/62/3 v. %, 200-260 °C, 20 bar, 2400 ml g ⁻¹ h ⁻¹ , 250-425 μ m,	CZA/ γ -Al ₂ O ₃ : 1 and CZA/HZSM-5: 3 regarding the DME yield

	- NH4ZSM-5, HZSM-5 and γ -Al ₂ O ₃ γ -Al ₂ O ₃ : prod. in-house, S _{BET} : 117 m ² g ⁻¹ , Pore size = 1.035 nm	admixed catalyst, CZA/ γ -Al ₂ O ₃ : 1, 2, 3	
A. Ateka et al. ¹⁹	Comparison of different commercial and in-house made catalyst systems - CuO–ZnO–ZrO ₂ , CuO–ZnO–MnO, and CuO/ZnO/Al ₂ O ₃ CZA: S _{BET} : 24 m ² g ⁻¹ , Pore volume: 0.081 cm ³ g ⁻¹ Cu dispersion: 5.2% - SAPO-18 and γ -Al ₂ O ₃ SAPO-18: S _{BET} : 480 m ² g ⁻¹ , Pore volume: 0.39 cm ³ g ⁻¹ Total acidity: 0.42 mmol _{NH₃} /g _{cat}	CO/CO ₂ /H ₂ , 275 °C, 30 bar, 3.7 g h (mol _C) ⁻¹ , 125–500 μ m, Bifunctional catalysts CZA/SAPO-18: 1, 2, 5, 10	CZA/SAPO-18: 2 regarding yield and selectivity of DME for CO ₂ free feeds (H ₂ /CO=3)

* The reactor type is a fixed bed tubular reactor, with mechanically mixed catalyst bed unless otherwise stated

** percentages and ratios in weight, unless otherwise stated

*** In this study the mass of CZA was held constant while the mass of γ -Al₂O₃ was increased to achieve a higher γ -Al₂O₃-to-CZA ratio. Hence, the γ -Al₂O₃-to-CZA ratio leading to the highest performance was the case at which the total catalyst mass was also the highest.


Notes and references

- 1 D. Mears, *J. Catal.*, 1971, **20**, 127–131.
- 2 P. B. Weisz and C. D. Prater, in *Advances in Catalysis*, eds. W. G. Frankenburg, V. I. Komarewsky and E. K. Rideal, Academic Press, 1954, pp. 143–196.
- 3 J. B. Anderson, *Chem. Eng. Sci.*, 1963, **18**, 147–148.
- 4 J. Pérez-Ramírez, *Catal. Today*, 2000, **60**, 93–109.
- 5 M. Baerns, A. Behr, A. Brehm, J. Gmehling, H. Hofmann and U. Onken, *Technische chemie*, John Wiley & Sons, 2013.
- 6 T. Zeiser, Friedrich-Alexander-Universität Erlangen-Nürnberg, 2008.
- 7 A. T. Aguayo, J. Ereña, D. Mier, J. M. Arandes, M. Olazar and J. Bilbao, *Ind. Eng. Chem. Res.*, 2007, **46**, 5522–5530.
- 8 Y. I. Pyatnitskii, P. E. Strizhak and N. K. Lunev, *Theor. Exp. Chem.*, 2009, **45**, 325–330.
- 9 C. P. Renk, Forschungszentrum Karlsruhe GmbH, 2009.
- 10 R. Peláez, P. Marín and S. Ordóñez, *Fuel Process. Technol.*, 2017, **168**, 40–49.
- 11 P. Ratamanalaya, S. Limtrakul, T. Vatanatham and P. Ramachandran, in *TICHe International Conference 2011*, 2011, p. ee014.1-ee014.5.
- 12 Z. Nie, H. Liu, D. Liu, W. Ying and D. Fang, *J. Nat. Gas Chem.*, 2005, **14**, 22–28.
- 13 J. Ereña, I. Sierra, A. T. Aguayo, A. Ateka, M. Olazar and J. Bilbao, *Chem. Eng. J.*, 2011, **174**, 660–667.
- 14 N. Delgado Otalvaro, M. Kaiser, K. Herrera Delgado, S. Wild, J. Sauer and H. Freund, *React. Chem. Eng.*, 2020, **5**, 949–960.
- 15 K. L. Ng, D. Chadwick and B. A. Toseland, *Chem. Eng. Sci.*, 1999, **54**, 3587–3592.
- 16 C. Peinado, D. Liuzzi, M. Retuerto, J. Boon, M. A. Peña and S. Rojas, *Chem. Eng. J. Adv.*, 2020, **4**, 100039.
- 17 J. W. Bae, H. S. Potdar, S. H. Kang and K. W. Jun, *Energy and Fuels*, 2008, **22**, 223–230.
- 18 J. Abu-Dahrieh, D. Rooney, A. Goguet and Y. Saih, *Chem. Eng. J.*, 2012, **203**, 201–211.
- 19 A. Ateka, I. Sierra, J. Ereña, J. Bilbao and A. T. Aguayo, *Fuel Process. Technol.*, 2016, **152**, 34–45.

Modeling the Direct Synthesis of Dimethyl Ether using Artificial Neural Networks

Nirvana Delgado Otalvaro, Pembe Gül Bilir, Karla Herrera Delgado*, Stephan Pitter, and Jörg Sauer

DOI: 10.1002/cite.202000226

 This is an open access article under the terms of the Creative Commons Attribution License, which permits use, distribution and reproduction in any medium, provided the original work is properly cited.



Supporting Information
available online

Artificial neural networks (ANNs) are designed and implemented to model the direct synthesis of dimethyl ether (DME) from syngas over a commercial catalyst system. The predictive power of the ANNs is assessed by comparison with the predictions of a lumped model parameterized to fit the same data used for ANN training. The ANN training converges much faster than the parameter estimation of the lumped model, and the predictions show a higher degree of accuracy under all conditions. Furthermore, the simulations show that the ANN predictions are also accurate even at some conditions beyond the validity range.

Keywords: Artificial neural network, Dimethyl ether, Kinetics, Modeling

Received: October 28, 2020; *revised:* January 14, 2021; *accepted:* February 05, 2021

1 Introduction

Using artificial neural networks (ANNs) is the most widespread machine learning approach for modeling complex phenomena due to their simple formulation, flexibility and robustness [1, 2]. ANNs have proven to be suitable for creating predictive models for chemical engineering processes and several applications have been subject of research in the last decades such as the evaluation and modeling of complex kinetic data [3–6], catalyst design [7, 8], soft sensing [1, 9], advanced process control [10], and others [11]. Studies regarding the application of ANNs for the synthesis of dimethyl ether (DME) have been reported, e.g., for the screening of additives [7, 8], the optimization of temperature profiles in a temperature gradient reactor [12], and the modeling of the single process steps [13, 14]. Furthermore, ANNs have been used for predicting the performance of the liquid phase direct synthesis of DME over CuO/ZnO/Al₂O₃ and H-ZSM-5 catalysts [9]. In this work, we used ANNs to model the direct synthesis of DME from CO₂-rich synthesis gas over a mixed catalyst bed of commercial CuO/ZnO/Al₂O₃ (CZA) and γ -Al₂O₃ catalysts at high pressure. DME is of general interest due to its potential for chemical energy storage, making it a promising key compound in power to fuel technologies [15–20]. However, the detailed reaction mechanism of this system is still controversial [21]. One of the main difficulties for modeling the direct DME synthesis concerns changes in the catalyst during time on stream. It has been shown that the catalytic active state of CZA

dynamically adjusts to the process conditions [22, 23], particularly at high CO₂ contents in the synthesis gas feed [24]. In addition, water formation not only influences the active centers of CZA, but also those on the solid acid dehydration component (i.e., γ -Al₂O₃) [25, 26]. Morphological and structural changes induced by certain operating conditions or interactions with reactants, intermediates or products make it almost impossible to correlate a vast array of experiments at different working conditions using a simple kinetic model [27].

The ANNs used to model the direct synthesis of DME map the input-output relationships in intrinsic kinetic data taken over a wide range of operating conditions and inlet feed compositions. The ANNs applied are fully connected multi-layer feedforward networks trained by supervised learning. A brief summary of the theoretical background regarding the design and training of ANNs, is provided in the Supporting Information (SI). For the ANN design, several back-propagation training algorithms as well as different activation functions and network architectures have been tested. Additionally, a data partitioning scheme is pre-

Nirvana Delgado Otalvaro, Pembe Gül Bilir,
Dr. Karla Herrera Delgado, Dr. Stephan Pitter,
Prof. Dr.-Ing. Jörg Sauer
karla.herrera@kit.edu
Karlsruhe Institute of Technology, Institute of Catalysis Research
and Technology, Hermann-von-Helmholtz-Platz, 76344 Eggen-
stein-Leopoldshafen, Germany.m

sented, which enables the data division for training and testing in an automated fashion. We conduct simulations within and beyond the model's validity range to shed light on the ANN's predictive ability in both operational windows, and report on the ability of simple ANNs in modeling this system in comparison to that of a lumped kinetic model fitted to the same data.

2 Data and Methodology for the ANN's Design

Shallow feedforward ANNs (ANNs with one hidden layer) were designed and implemented in Matlab[®] software R2018a v9.4.0. The experimental kinetic data used for training and testing were acquired and published in a previous work [28]. The used data set consists of 180 experiments carried out in a fixed bed reactor at 50 bar using a 1:1 mechanical mixture of a commercial CZA catalysts and γ -Al₂O₃. The syngas composition, the temperature (T) and the total gas flow ($\dot{V}_{N,in}$) were varied during the experiments as summarized in Tab. 1, while the hydrogen amount in the feed gas was determined for each experiment according to Eq. (1). The remaining fraction of the feed gas consisted of a mixture of the inert gases argon and nitrogen.

$$y_{H_2,in} = 2.3(y_{CO,in} + y_{CO_2,in}) + y_{CO_2,in} \quad (1)$$

Table 1. Conditions of kinetic data taken from Delgado Otavaro et al. [28]

Parameter	Value
T [K]	493, 503, 513, 523, 533
$\dot{V}_{N,in}$ [slpm] ^{a)}	0.2, 0.3, 0.4, 0.5, 0.6, 0.7
$y_{CO_2,in}$ [%]	1, 3
$y_{CO,in}$ [%]	4, 8, 15

a) Standard liter per minute, $T = 0^\circ\text{C}$ and $p = 1.01325$ bar

The ANNs were trained to predict the mole fraction of the main species (CO, CO₂, H₂ and DME) in the product gas based on the composition of the syngas ($y_{CO,in}$, $y_{CO_2,in}$, $y_{H_2,in}$) and the varied operating conditions. Hence, the input vector (x) and target vector (y) are summarized as follows:

$$x^T = [y_{CO,in}, y_{CO_2,in}, y_{H_2,in}, T, \dot{V}_{N,in}] \quad (2)$$

and

$$y^T = [y_{CO,out}, y_{CO_2,out}, y_{H_2,out}, y_{DME,out}] \quad (3)$$

For the design of ANNs the network architecture, i.e., the number of neurons in the hidden layer, as well as a suitable activation function of these neurons and a training algorithm must be determined. Since there is no generally

accepted theoretical basis to address these questions, answers are obtained empirically. For this purpose, various network architectures and multiple functions were screened and analyzed concerning the resulting accuracy and convergence time (refer to SI for further details on the evaluated algorithms). The assessment was carried out in regard to the mean squared error (MSE) and the convergence time. For this initial screening, the experimental input data were divided randomly into three data subsets: training, validation and test data containing 70 %, 15 % and 15 % of the experimental data, respectively. The validation subset was used for training to improve generalization through early stopping, except in the case of Bayesian regularization where generalization is achieved by regularization and no validation subset is required [29, 30]. The randomized data classification was constant for all trials conducted in this initial screening to ensure that the same samples were used in all cases, thus, excluding any influence of the data division from the preliminary results.

After determining the most appropriate functions several networks were trained using the pseudo-random two-stage data-partitioning scheme presented in Sect. 3.1. The error function on the test data was considered the determining factor for selecting the best network. Since this data set is completely independent of the training routine, the error on these data is a sufficient indicator of both the prediction accuracy and the generalization of the network.

Posterior to the training and network selection, simulations were performed with the selected network. The responses of the ANN were evaluated in comparison to a lumped kinetic model parametrized to the same experimental data used for the ANN training. The parameters of the lumped model were fitted to kinetic data measured in the absence of transport limitations. The assumptions of steady state, isothermal and isobaric operation, negligible gradients in radial direction and negligible backmixing effects apply. Therefore, only the effects of chemical reaction and thermodynamic equilibria are included in this model. However, since the lumped kinetic model is based on balance equations and partially on knowledge of the reaction mechanism, it is expected to deliver better predictions than the ANN when extrapolated.

The adjusted coefficient of determination R_{adj}^2 was computed as a measure of the goodness of fit (Eq. (4)). Different from the coefficient of determination R^2 (Eq. (5)), R_{adj}^2 takes the number of degrees of freedom of each model into consideration, hence, providing an unbiased basis for the comparison of two different model structures.

$$R_{adj}^2 = 1 - \frac{(1 - R^2)(N - 1)}{N - p} \quad (4)$$

$$R^2 = 1 - \frac{\sum_{n=1}^N (y_{n,out} - \hat{y}_{n,out})^2}{\sum_{n=1}^N (y_{n,out} - \bar{y}_{out})^2} \quad (5)$$

In Eqs. (4) and (5), N is the total number of experiments, and p is the number of model parameters. $\hat{y}_{n,out}$ and $y_{n,out}$ are the predicted and measured mole fraction of an arbitrary component in the product gas for experiment n , and \bar{y}_{out} is the mean value of the measured mole fraction over all experiments.

3 Results and Discussion

3.1 Network Design and Training

During the initial screening the activation and training functions available in Matlab[®] were changed systematically in order to find the most suitable function for the available data. The screening showed that the piecewise linear functions (ReLU, satlin, tribas and satlins) perform poorly compared to the nonlinear functions (radbasn, elliotsig, tansig, softmax and logsig). The best performance was obtained with the widely used logarithmic sigmoid function logsig (refer to Fig. S5 in the SI). When evaluating the training functions no convergence was achieved in any of the run trials with the algorithms Gradient Descent (gd) and Gradient Descent with Momentum (gdm). On the other hand, the Jacobian backpropagation methods Levenberg-Marquardt (lm) and Bayesian regularization (br) provide more accurate predictions than the gradient descent algorithms (cgp, scg, rp, bfg, cgb and cgf). Between lm and br, the lowest MSE and fastest convergence was achieved with br (Fig. S6). This Matlab[®] training function is based on the Bayesian interpolation frame proposed by MacKay [31] which is advantageous for problems where the data set is limited since no validation subset is required [29]. Furthermore, Bayesian regularization calculates and trains only the number of parameters necessary to minimize the target function (effective number of parameters) [32,33]. As a result, fewer parameters are used than are available reducing the model sensitivity to the network architecture, as long as the minimum number of neurons is provided. Based on these advantages and the empirically obtained results, Bayesian regularization was selected for the network design.

The proposed data division and training procedure is illustrated in Fig. 1. In the first stage of data division, the samples were randomly assigned to two subsets: “Design Data” and “Test Data A”. In the second stage, the “Design Data” subset containing 90 % of the samples was divided into “Train Data”, which is used to calculate weights and biases, and “Test Data B” used to compare different models within the framework of Bayesian regularization (without a validation subset). Afterwards, the multi-start strategy was applied by restarting the training procedure from different initial parameter values 100 times. This procedure, labeled as (1) in Fig. 1, screens the parameter space in order to generate different solutions of the optimization problem, and thus, to overcome possible local optimality. After completion, the second stage of data partitioning is repeated to

train the networks based on a different data division (label (2) in Fig. 1). All trained networks and training records were stored in a 100 by 100 array for the subsequent network selection. Finally, the “Test Data A” subset, which contains 10 % of the original samples, was used to provide an unbiased assessment of the network performance on separate data, and thus, of its generalization ability. Thereby, the ANN with the lowest error on these data exhibits the best generalization to the independent data set and was chosen as the most suitable network. A random division is advantageous for the problem at hand considering the multidimensionality of the input space. The presented scheme allows data partitioning in an automated fashion and increases the adaptability of the proposed modeling routine to new data sets of different structures. Furthermore, the model requirements, i.e., high accuracy, fast convergence and good generalization, are fulfilled.

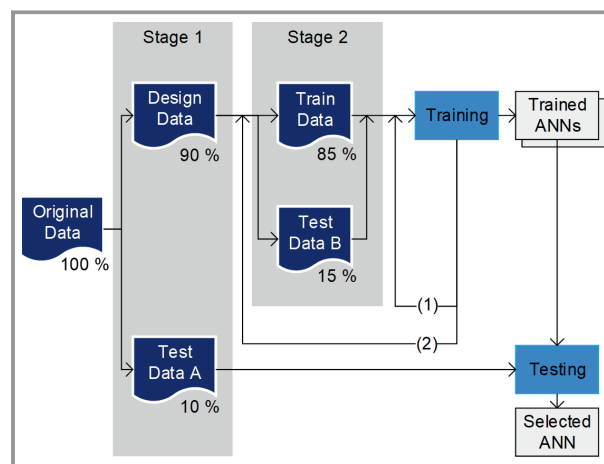


Figure 1. Data division scheme and training strategy.

The training strategy was conducted for networks with up to 15 neurons in the hidden layer. This screening showed that five hidden neurons provide enough complexity for the network to adapt sufficiently to the available data set. Therefore, the network with a 5-5-4 architecture (5 input, 5 hidden and 4 output neurons, Fig. S8) was selected. This structure ensures a sufficient number of parameters to avoid underfitting, while the problem of overfitting is prevented by training the network with Bayesian regularization. The resulting ANN is shown schematically in the SI, where also the parameters of the ANN and further training results are given.

The proposed approach is applicable when modeling with ANNs due to their remarkably fast convergence. For the chosen architecture, the time elapsed after the training of 10 000 networks was 7.9 min (refer to the SI). In contrast, the parametrization of the lumped kinetic model to the same data takes approximately 3.5 h using the same CPU (on windows 10 Pro (64-bit) operating system with i5 processor and 8 GB RAM).

3.2 Evaluation of the Selected ANN

Simulations were performed to evaluate the predictive ability of the selected network. Fig. 2 shows parity plots itemized for the main components in the system displaying the agreement between the measured and predicted concentrations in the product gas for all experiments. Clearly, the model is capable of simulating the observed trends accurately. For all components, the simulated points are evenly distributed around the $y = x$ line, indicating that there are no pronounced systematic deviations between model predictions and experimental data.

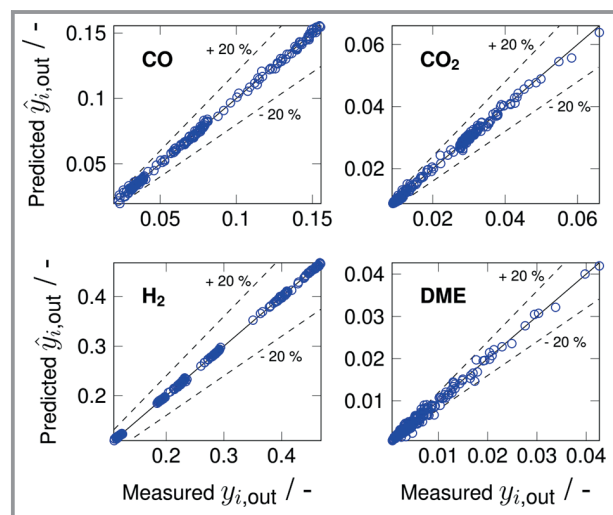


Figure 2. Parity plots for concentrations in the product gas.

We attribute the observed goodness of fit to the fact that appropriate activation and training functions were chosen as well as a network architecture that provides sufficient model complexity and flexibility for modeling. Additionally, the proposed data partitioning scheme proved to be effective in enabling the model to gain insight into the underlying phenomena with the available data.

The mean relative error (RE) over all inlet compositions is shown in Fig. 3 against the temperature and the inlet volume flow. Clearly, the ANN shows a higher predictive accuracy than the lumped kinetic model for all species in the entire experimentally covered operating window. This is caused by the flexibility and higher dimensionality of the ANN and its superior capacity to adapt to the data. The RE of CO, CO₂ and H₂ over all data lies below 3% (2%, 2.9% and 0.4%, respectively), while the RE of DME amounts to 11%. Both response surfaces for DME follow the same trend, with the prediction error decreasing with increasing temperature. At low temperatures, the low reaction rates lead to overall low conversion and yield. Hence, resulting in small DME amounts in the product gas and thus in a reduced measuring accuracy [28]. Therefore, the deviations of both models can be mainly attributed to experimental measurement uncertainties. Additionally, the fact that the ANN

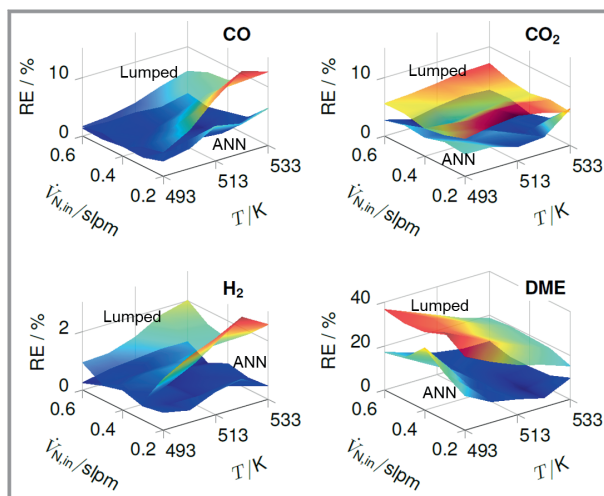


Figure 3. Mean relative error (RE) of prediction for the lumped model and ANN over all data.

did not adapt to the measured values, although the network has sufficient flexibility, is an indication that overfitting was successfully avoided and the data were not simply stored by the network, but the input-output relationships were effectively identified. The adjusted coefficients of determination reported in Tab. 2 highlight the suitability of both models and confirm the better adjustment of the ANN to the experimental data especially for the fractions of DME and CO₂.

Table 2. Adjusted coefficients of determination.

R_{adj}^2	$\hat{y}_{H_2,out}$	$\hat{y}_{CO,out}$	$\hat{y}_{CO_2,out}$	$\hat{y}_{DME,out}$
ANN model	0.999	0.998	0.994	0.984
Lumped model	0.998	0.992	0.984	0.943

In order to determine if the trained ANN is suitable as a non-linear regression tool, the ANN's generalization ability and its suitability to make predictions on unseen data have to be tested. For this purpose, additional simulations were performed for unobserved data within and beyond the model's validity range. The lumped model published in our previous work [28] is employed for a comparative analysis of the ANN's predictions. Since both models were fitted to the same experimental data, these are valid in the same range of conditions, thus, providing a sufficient basis for comparison. In the following, representative results are presented that illustrate and compare the responses of both models. Additional simulation results are given in the SI.

In Fig. 4, the experimental values are sorted arbitrarily in ascending order and depicted along with the superimposed confidence intervals of both fits at a significance level of 95%. It can be observed that the confidence intervals of the ANN predictions are narrower than the confidence interval of the lumped model. It is obvious, in particular for the fractions of DME and CO₂, that the respective confidence

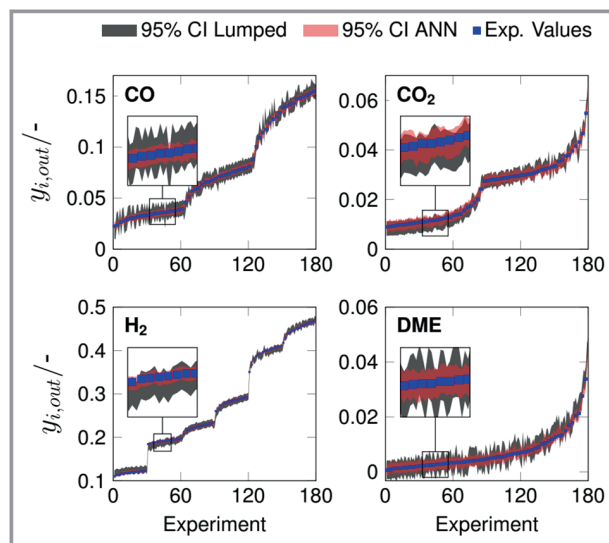


Figure 4. Measured concentrations in the product gas and 95 % confidence intervals (CI) of the ANN and lumped model. For clarity, only every third experimental data point is shown.

intervals of both models are wider in the low concentration range. This is in accordance with the presumption made before in this section that low concentrations of DME are subject to an increased measurement uncertainty, which also explains why this effect is not observable for the fractions of CO or H₂ where the confidence intervals appear to be of the same order of magnitude in the entire operating window.

Fig. 5 displays simulation and experimental results in the temperature range between 453 K and 573 K. The range where both models are formally valid (between 493 K and 533 K) is marked in gray for better visualization.

The predictions of the ANN within the model's validity range are slightly closer to the experimental values than the predictions obtained with the lumped kinetic model, consistent with the previous discussion. Since the phenomena in this range are dominated by reaction kinetics, the effects observed under these conditions can be explained by the temperature dependence of the reaction rate, described by the Arrhenius equation. With increasing temperature, the fraction of DME and CO₂ in the effluent increases, while the fraction of CO and H₂ decreases. The fact that CO₂ behaves as a product can be attributed to the water-gas shift reaction, which is promoted by the CZA catalyst and, in the evaluated range, is faster than the CO₂ hydrogenation. With regards to the total gas flow, it is observed that at decreasing values, the fraction of CO and H₂ at the reactor outlet decreases as well, while the fraction of DME and CO₂ increases. These results can be explained by the inverse relationship between the total gas flow with residence time and gas load, that lead to higher conversion and product yield. Furthermore, the consistency of this effect throughout the entire investigated gas flow range can be attributed to a constant selectivity towards DME. A detailed description of the

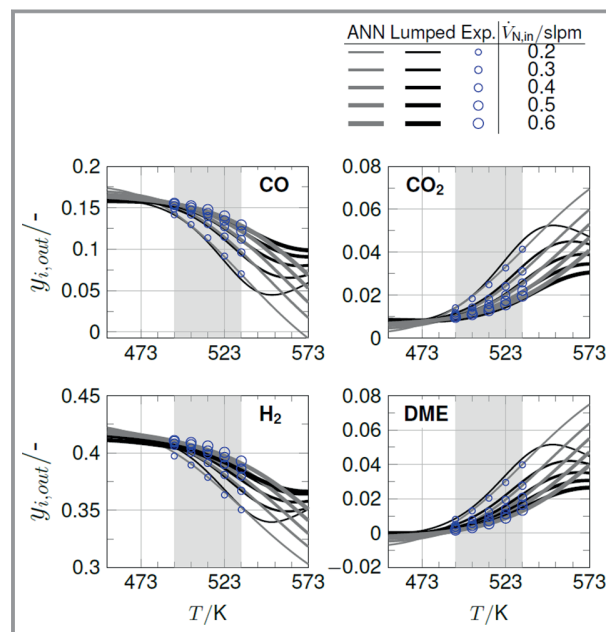


Figure 5. Components mole fraction in the product gas. Gray area marks the range covered experimentally. Feed: 16.1 % CO, 0.8 % CO₂, 42.3 % H₂, 40.8 % inert gas (Ar and N₂). $p = 50$ bar.

observed phenomena can be found elsewhere [28]. Model predictions in this operational range demonstrate the high level of agreement between the simulated and measured values, also showing a smooth mapping and the ANN's ability to generalize and make predictions for unseen data within the model's validity range.

Unexpectedly, the predictions of the lumped model and the ANN at temperatures below 493 K are similar although the ANN was not trained in this temperature range. Both models indicate that at low temperatures the reaction rates are too low to achieve high conversion. Hence, the concentrations of all components are close to the respective values in the feed gas. There are no additional constraints in the ANN's structure that prevent negative concentrations to be computed (in the lumped kinetic model, this effect is prevented inherently by the balance equations). Thus, at low temperatures some negative values are predicted. However, for DME and CO₂, progressions do not decrease steeply into the negative quadrant with decreasing temperatures. Instead, all values in this temperature range are close to zero. Similar good prediction accuracy despite extrapolation was observed for most but not all feed compositions and components (refer to SI, Fig. S9 to S13). Therefore, although the underlying model is able to extrapolate accurately for most conditions in this range, the quality of the predictions cannot be guaranteed in all cases. The predictions for temperatures above 533 K provide valuable insights into the phenomena comprised by the models. As the main chemical reactions involved in the DME synthesis are exothermic, high temperatures are kinetically favorable, but thermodynamically unfavorable. This trade-off of

exothermic reactions is reflected by a change in the slope of the concentration profile and is taken into account in the lumped kinetic model by the equilibrium constants in the rate expressions. However, since the kinetic data were measured at conditions at which the influence of the equilibrium is minor (kinetic regime), the ANN has no information about the characteristics of this phenomenon, causing the predictions of both models to diverge at high temperatures. With increasing temperature, the concentration profiles predicted with ANN follow the observed trend in the experimentally covered range, i.e., increasing for DME and CO₂, and decreasing for H₂ and CO, while the concentration profiles computed with the lumped kinetic model exhibit the expected points of inflection. Similarly, predictions for low flow rates at which mass transport limitation occurs can be expected to be inaccurate because the model was parameterized to fit intrinsic kinetic data, i.e., in an operating range with negligible influence of mass and heat transport.

4 Summary and Conclusions

In this paper ANNs were used to model the direct synthesis of DME from syngas over a commercial dual catalyst system at high pressure. The exact mechanism of this process is not yet fully understood, and modeling has so far only been possible in limited operating windows. The networks used in this study are shallow, feedforward and fully connected. It was demonstrated that the logarithmic sigmoid function is most applicable for the problem at hand, and that a higher accuracy is obtained when applying training algorithms that use Jacobian backpropagation, particularly Bayesian regularization. A pseudo-random data division scheme allowing data partitioning in an automated fashion was presented. The training was conducted for ANNs of different structures and five hidden neurons proved to provide sufficient model complexity to map the available data. The network with the best performance on unseen data was selected and its predictive ability was assessed by comparison with experimental data and with predictions of a lumped kinetic model parametrized to fit the same database. In summary, it was observed that the ANNs are remarkably fast, very flexible and exhibit a superior adaptability to the experimental data than the lumped kinetic model while still providing a comparable interpolation ability.

Moreover, accuracy of the model predictions outside the experimentally covered parameter range was also evaluated. When the model was extrapolated towards lower reaction rates, i.e., lower temperatures and higher flow rates, the ANN was able to deliver accurate predictions and to describe the single-stage DME synthesis systemically for most components and inlet feeds. This indicates that extrapolations of the model may be admissible for operating conditions at which the phenomena covered by the underlying model takes place. However, it is not possible to predict

deviations prior to training. Extrapolations of the ANN towards higher reaction rates, on the other hand, lead as expected to divergent predictions, as overlapping effects occur (e.g., thermodynamic limitation of exothermic reactions at high temperatures) which, at the current stage of development, cannot be reflected by the ANN that was trained to fit data taken in the operational window dominated only by reaction kinetics.

Our findings underline the suitability of the ANN to act as a predictive tool for Brownfield applications such as soft sensing, real-time optimization, online control, predictive maintenance and others, where models with high flexibility and adaptability, the capacity to map complex nonlinear relationships as well as fast convergence and low computational cost are required. Furthermore, we conclude that ANNs have the potential to be used for modeling the direct DME synthesis in an even wider range of operation where the relationship between input and output variables is ambiguous and modeling under mechanistic assumptions was not yet possible. The presented data partitioning and training methodology can be applied for this purpose with simple requirements: the input-output relationships to be modeled must be measurable and enough data must be available for parameter discrimination, i.e., for the training of the network. One possible application is the modeling of catalyst deactivation as a function of the time on stream and/or the conditions to which the catalyst system is exposed to. Regardless of the catalyst system, most kinetic studies of the direct DME synthesis are carried out under steady state conditions, due to the highly dynamic behavior of the catalysts which makes the mechanistic modeling in a wide range of conditions very challenging. However, if the required data are available, the modeling with the proposed methodology can be easily adapted to new state variables that need to be considered.

Supporting Information

Supporting Information for this article can be found under DOI: <https://doi.org/10.1002/cite.202000226>.

This research was funded by the Helmholtz Association, Research Programme “Storage and Cross-linked Infrastructures”, Topic “Synthetic Hydrocarbons”. Open access funding enabled and organized by Projekt DEAL.

Symbols used

N	[-]	total number of experiments
p	[bar]	pressure
R^2	[-]	adjusted coefficient of determination
R^{2adj}	[-]	coefficient of determination
T	[K]	temperature

$\dot{V}_{N,in}$	[slpm]	total gas flow at standard conditions, standard liter per minute, $T = 0^\circ\text{C}$ and $p = 1.01325\text{ bar}$
y	[-]	measured mole fraction
\hat{y}	[-]	predicted mole fraction

Sub- and Superscripts

in	quantity at reactor inlet
n	experiment index
out	quantity at reactor outlet
T	transpose of a matrix or vector

Abbreviations

ANN	artificial neural network
br	Bayesian regularization
CI	confidence interval
CZA	CuO/ZnO/Al ₂ O ₃
DME	dimethyl ether
lm	Levenberg-Marquardt
MSE	mean squared error
RE	relative error

References

- J. Mohd Ali, M. A. Hussain, M. O. Tade, J. Zhang, *Expert Syst. Appl.* **2015**, *42* (14), 5915–5931. DOI: <https://doi.org/10.1016/j.eswa.2015.03.023>
- M. Negnevitsky, *Artificial Intelligence: A Guide to Intelligent Systems*, Pearson education, London **2005**.
- V. Goncalves, K. M. Honório, A. B. F. da Silv, in *Artificial Neural Networks – Architectures and Applications* (Ed: K. Suzuki), IntechOpen, London **2013**, 203–223. DOI: <https://doi.org/10.5772/51275>
- F. Amato, J. L. González-Hernández, J. Havel, *Talanta* **2012**, *93*, 72–78. DOI: <https://doi.org/10.1016/j.talanta.2012.01.044>
- M. Shiva, H. Atashi, F. Tabrizi, A. Mirzaei, A. Zare, *Fuel Process. Technol.* **2013**, *106*, 631–640. DOI: <https://doi.org/10.1016/j.fuproc.2012.09.056>
- S. Sunphorka, B. Chalermisinsuwan, P. Piumsomboon, *Fuel* **2017**, *193*, 142–158. DOI: <https://doi.org/10.1016/j.fuel.2016.12.046>
- K. Omata, Sutarto, M. Hashimoto, G. Ishiguro, Y. Watanabe, T. Umegaki, M. Yamada, *Ind. Eng. Chem. Res.* **2006**, *45* (14), 4905–4910. DOI: <https://doi.org/10.1021/ie050640g>
- K. Omata, Sutarto, M. Hashimoto, G. Ishiguro, Y. Watanabe, T. Umegaki, M. Yamada, *Ind. Eng. Chem. Res.* **2005**, *44* (2), 296–301. DOI: <https://doi.org/10.1021/ie049302q>
- G. R. Moradi, F. Parvizian, *Can. J. Chem. Eng.* **2011**, *89* (5), 1266–1273. DOI: <https://doi.org/10.1002/cjce.20558>
- J. Appel, C. Colombo, U. Dätwyler, Y. Chen, N. Kerimoglu, *Chimia* **2016**, *70* (9), 621–627. DOI: <https://doi.org/10.2533/chimia.2016.621>
- H. Z. Li, Z. Liu, Z., *Catalysts* **2017**, *7* (10), 306. DOI: <https://doi.org/10.3390/catal7100306>
- K. Omata, T. Ozaki, T. Umegaki, Y. Watanabe, N. Nukui, M. Yamada, *Energy Fuels* **2003**, *17* (4), 836–841. DOI: <https://doi.org/10.1021/ef0202438>
- P. Valeh-e-Sheyda, F. Yaripour, G. Moradi, M. Saber, *Ind. Eng. Chem. Res.* **2010**, *49* (10), 4620–4626. DOI: <https://doi.org/10.1021/ie9020705>
- S. Alamolhoda, M. Kazemeini, A. Zaherian, M. R. Zakerinasab, *J. Ind. Eng. Chem.* **2012**, *18* (6), 2059–2068. DOI: <https://doi.org/10.1016/j.jiec.2012.05.027>
- M. Stiefel, R. Ahmad, U. Arnold, M. Döring, *Fuel Process. Technol.* **2011**, *92* (8), 1466–1474. DOI: <https://doi.org/10.1016/j.fuproc.2011.03.007>
- E. Catizzzone, G. Bonura, M. Migliori, F. Frusteri, G. Giordano, *Molecules* **2017**, *23* (1), 1–28. DOI: <https://doi.org/10.3390/molecules23010031>
- M. Gentzen, W. Habicht, D. E. Doronkin, J.-D. Grunwaldt, J. Sauer, S. Behrens, *Catal. Sci. Technol.* **2016**, *6*, 1054–1063. DOI: <https://doi.org/10.1039/C5CY01043H>
- N. Dahmen, U. Arnold, N. Djordjevic, T. Henrich, T. Kolb, H. Leibold, J. Sauer, *J. Supercrit. Fluids* **2015**, *96*, 124–132. DOI: <https://doi.org/10.1016/j.supflu.2014.09.031>
- U. Mondal, G. D. Yadav, *J. CO₂ Util.* **2019**, *32*, 299–320. DOI: <https://doi.org/10.1016/j.jcou.2019.02.003>
- U. Mondal, G. D. Yadav, *J. CO₂ Util.* **2019**, *32*, 321–338. DOI: <https://doi.org/10.1016/j.jcou.2019.02.006>
- J. Park, H. S. Kim, W. B. Lee, M.-J. Park, *Catalysts* **2020**, *10* (10), 655. DOI: <https://doi.org/10.3390/catal10060655>
- R. Schlögl, *Angew. Chem., Int. Ed.* **2015**, *54* (11), 3465–3520. DOI: <https://doi.org/10.1002/anie.201410738>
- S. Kuld, M. Thorhauge, H. Falsig, C. F. Elkjær, S. Helveg, I. Chorkendorff, J. Sehested, *Science* **2016**, *352* (6288), 969–974.
- J.-D. Grunwaldt, A. M. Molenbroek, N. Y. Topsøe, H. Topsøe, B. S. Clausen, *J. Catal.* **2000**, *194* (2), 452–460. DOI: <https://doi.org/10.1006/jcat.2000.2930>
- F. Frusteri, M. Migliori, C. Cannilla, L. Frusteri, E. Catizzzone, A. Aloise, G. Giordano, G. Bonura, *J. CO₂ Util.* **2017**, *18*, 353–361.
- A. I. Osman, J. K. Abu-Dahrieh, D. W. Rooney, S. A. Halawy, M. A. Mohamed, A. Abdelkader, *Appl. Catal., B* **2012**, *127*, 307–315. DOI: <https://doi.org/10.1016/j.apcatb.2012.08.033>
- K. F. Kalz, R. Kraehnert, M. Dvoyashkin, R. Dittmeyer, R. Gläser, U. Krewer, K. Reuter, J.-D. Grunwaldt, *ChemCatChem* **2017**, *9*, 17–29. DOI: <https://doi.org/10.1002/cctc.201600996>
- N. Delgado Otalvaro, M. Kaiser, K. Herrera Delgado, S. Wild, J. Sauer, H. Freund, *React. Chem. Eng.* **2020**, *5*, 949–960. DOI: <https://doi.org/10.1039/d0re00041h>
- Z. S. H. Chan, H. W. Ngan, A. B. Rad, A. K. David, N. Kasabov, *Neurocomputing* **2006**, *70* (1), 409–419. DOI: <https://doi.org/10.1016/j.neucom.2005.12.131>
- D. J. C. Mackay, *Network: Comput. Neural Syst.* **1995**, *6*, 469–505. DOI: https://doi.org/10.1088/0954-898X_6_3_011
- D. J. C. MacKay, *Neural Comput.* **1992**, *4*, 415–447. DOI: https://doi.org/10.1007/978-94-017-2219-3_3
- F. Burden, D. Winkler, in *Artificial Neural Networks: Methods and Applications* (Ed: D. J. Livingstone), Humana Press, Totowa, NJ **2009**. DOI: <https://doi.org/10.1007/978-1-60327-101-1>
- H. Okut, Bayesian Regularized Neural Networks for Small n Big p Data, in *Artificial Neural Networks – Models and Applications* (Ed: J. L. Garcia Rosa), IntechOpen, London **2016**. DOI: <https://doi.org/10.5772/63256>
- S. Zendeheboudi, N. Rezaei, A. Lohi, *Appl. Energy* **2018**, *228*, 2539–2566. DOI: <https://doi.org/10.1016/j.apenergy.2018.06.051>
- I. A. Basheer, M. Hajmeer, *J. Microbiol. Methods* **2000**, *43* (1), 3–31. DOI: [https://doi.org/10.1016/S0167-7012\(00\)00201-3](https://doi.org/10.1016/S0167-7012(00)00201-3)
- K. Hornik, M. Stinchcombe, H. White, *Neural Networks* **1989**, *2* (5), 359–366. DOI: [https://doi.org/10.1016/0893-6080\(89\)90020-8](https://doi.org/10.1016/0893-6080(89)90020-8)

- [37] G. Cybenko, *Math. Control Signals Syst.* **1989**, *2*, 303–314. DOI: <https://doi.org/10.1007/BF02551274>
- [38] K. Hornik, *Neural Networks* **1991**, *4* (2), 251–257. DOI: [https://doi.org/10.1016/0893-6080\(91\)90009-T](https://doi.org/10.1016/0893-6080(91)90009-T)
- [39] M. H. Beale, M. T. Hagan, H. B. Demuth, *Neural Network Toolbox TM User's Guide R2013b*, The Mathworks Inc, 7th ed., The MathWorks, Inc. **2013**.
- [40] A. A. Hameed, B. Karlik, M. S. Salman, *Knowledge-Based Syst.* **2016**, *114*, 79–87. DOI: <https://doi.org/10.1016/j.knosys.2016.10.001>
- [41] B. Sharma, P. Venugopalan, *IOSR J. Comput. Eng.* **2014**, *16* (1), 31–35. DOI: <https://doi.org/10.9790/0661-16123135>
- [42] H. Yonaba, F. Anctil, V. Fortin, *J. Hydrol. Eng.* **2010**, *15* (4), 275–283. DOI: [https://doi.org/10.1061/\(ASCE\)HE.1943-5584.0000188](https://doi.org/10.1061/(ASCE)HE.1943-5584.0000188)
- [43] <https://uk.mathworks.com/help/deeplearning/ug/choose-a-multilayer-neural-network-training-function.html>, (Accessed on April 24, 2020)
- [44] J. E. Dennis, R. B. Schnabel, *Numerical Methods for Unconstrained Optimization and Nonlinear Equations*, Society for Industrial and Applied Mathematics, Philadelphia, PA **1996**. DOI: <https://doi.org/10.1137/1.9781611971200>
- [45] P. E. Gill, W. Murray, M. H. Wright, *Practical Optimization*, Academic Press, London **1981**. DOI: <https://doi.org/10.1002/nme.1620180612>
- [46] M. J. D. Powell, *Math. Program.* **1977**, *12*, 241–254. DOI: <https://doi.org/10.1007/BF01593790>
- [47] E. M. L. Beale, in *Numerical Methods for Nonlinear Optimization* (Ed: F. A. Lootsma), Academic Press, London **1972**, 39–43.
- [48] L. E. Scales, *Introduction to Non-Linear Optimization*, Macmillan International Higher Education in Computer Science Series, Palgrave Macmillan, London **1985**.
- [49] D. W. Marquardt, *J. Soc. Ind. Appl. Math.* **1963**, *11* (2), 431–441. DOI: <https://doi.org/10.1137/0111030>
- [50] M. T. Hagan, M. B. Menhaj, *IEEE Trans. Neural Networks* **1994**, *5* (6), 989–993. DOI: <https://doi.org/10.1109/72.329697>
- [51] R. Battiti, *Neural Comput.* **1992**, *4* (2), 141–166. DOI: <https://doi.org/10.1162/neco.1992.4.2.141>
- [52] M. Riedmiller, H. Braun, in *IEEE International Conference on Neural Networks*, San Francisco, USA, **1993**, *4*, 586–591. DOI: <https://doi.org/10.1109/ICNN.1993.298623>
- [53] M. F. Møller, *Neural Networks* **1993**, *6* (4), 525–533. DOI: [https://doi.org/10.1016/S0893-6080\(05\)80056-5](https://doi.org/10.1016/S0893-6080(05)80056-5)

Supporting Information

Modeling the Direct Synthesis of Dimethyl Ether using Artificial Neural Networks

Nirvana Delgado Otalvaro¹, Pembe Gül Bilir¹, Dr. Karla Herrera Delgado*¹, Dr. Stephan Pitter¹, and Prof. Dr-Ing. Jörg Sauer¹

DOI: 10.1002/cite.202000226

Author affiliations

¹Karlsruhe Institute of Technology, Institute of Catalysis Research and Technology, Hermann-von-Helmholtz-Platz, DE-76344 Eggenstein-Leopoldshafen, Germany.
Email corresponding author: karla.herrera@kit.edu

1 Introduction

Artificial Neural Networks - Key Design Parameters and Modeling

Features and Functional Principles. ANNs are a mathematical portrayal of the human neural system. Similar to the biological system, ANNs consist of interconnected neurons that are responsible for the processing and forwarding of data. There is an extensive number of ANN types that can be classified based on their application, topology, connection pattern and the applied learning method as depicted in Fig. S1.

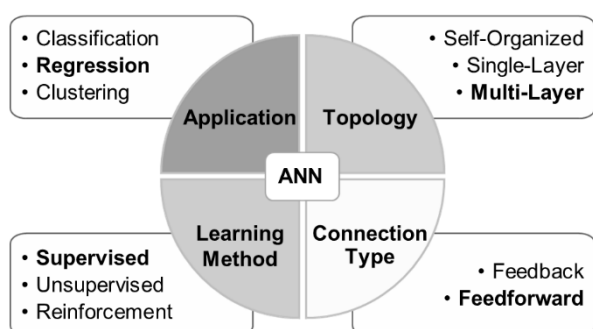


Figure S1. Classification of artificial neural networks (modified according to Sohrab Zendehboudi et al. [34]).

The ANNs relevant for this contribution are multilayer, feedforward networks used for function evaluation (i.e., nonlinear regression) and trained by supervised learning method.

In multilayer feedforward networks, the elementary units (neurons) are organized into layers, as depicted in Fig. S2. There is one input layer containing the input signals and one output layer containing all output signals of the network. Additionally, they may also have

one or more hidden layers located between input and output. These networks are known as “shallow” or “deep” ANNs respectively. Moreover, the “feedforward” connection type between neurons indicates that information is transferred unidirectionally from the input to the output layer.

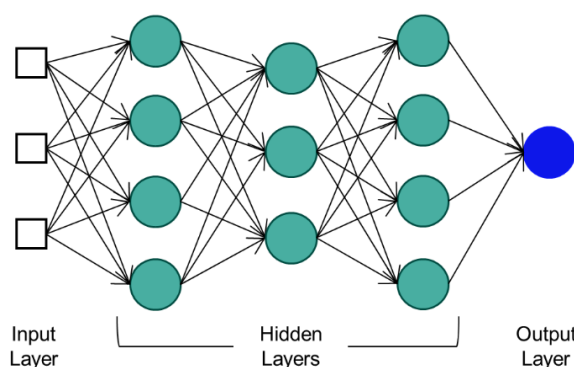


Figure S2. Structure of a multilayer feedforward artificial neural network.

The functional principle of an artificial neuron is shown in Fig. S3. The input signals x_i are multiplied with connections weights w_i that define the influence of the respective input data on the neuron’s output signal. The net input n of the neuron is the sum of all weighted input signals and the bias b , which represents the neuron’s threshold. If this threshold is exceeded, the neuron will be activated, i.e., an output signal y will be produced. The neural output signal is calculated using the activation function $f(n)$ that transforms the input of the neuron e.g., introducing nonlinearities. This output signal is then transferred to the next artificial neuron [34, 35].

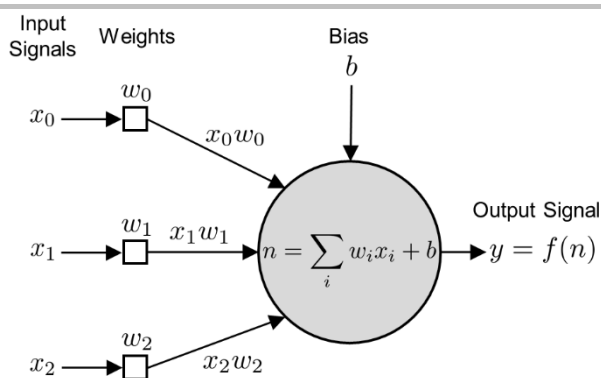


Figure S3. Functionality of an artificial neuron.

The number of neurons in the input and output layers is constraint by the scenario under consideration, while the number of hidden layers and hidden neurons must be determined by the designer based on trial-and-error or using rules-of-thumb [35, 1]. Clearly, an increasing number of hidden layers would lead to an increasing number of parameters. In some cases, a large network can be favorable for the model prediction accuracy. However, too many hidden layers can also lead to an excessive information processing capacity, and thus to the memorization of the training samples (overfitting). On the other hand, an insufficient number of parameters can result in poor forecasting abilities of the network. One approach for choosing the network structure is provided by the universal approximation theorem [36, 37]. This theorem states that a network with at least one hidden layer and nonlinear hidden neurons would be capable of approximating any continuous function in a closed and bounded domain. Therefore, this type of network can be applied universally for function approximation when theoretical models are not available [35, 38].

Furthermore, “supervised learning” refers to the learning method in which the available dataset contains information about the inputs (i.e., the composition of the participating chemical species and the operating conditions) and the desired output data or targets (i.e., the measured composition of the gaseous products). The network “learns” by systematically changing the network parameters in order to minimize the error between predictions and targets. The “training” of a multilayer network, i.e., the estimation of the parameters (weights and biases) that adapt the predictions to the available data, is conducted using numerical optimization algorithms. These may use the gradient of the error function with respect to the network parameters or the Jacobian matrix of the errors [39]. Both the gradients and the Jacobian matrix can be calculated using the

backpropagation algorithm as follows: First, the output signals of the network are calculated using the input data and the initial values of the network’s parameters. Afterwards, an error function is calculated (e.g., sum of squared errors) using the training data. The computed error is subsequently (back) propagated through the network using the chain rule of calculus to determine the error caused by each parameter. The weights and biases are adjusted accordingly and the previous steps are repeated iteratively in order to minimize the value of the calculated error function [35, 40, 41].

Generalization. One of the most relevant features of ANNs is their ability to generalize. A good generalization implies that the model did not merely memorized the training examples, but that it can make reliable predictions on unseen data as well. Three of the numerous approaches to improve generalization are relevant in our contribution: growing, regularization and early stopping.

When growing is applied, the size of the network is systematically increased until adequate performance is achieved. This technique aims to find the simplest (smallest) network architecture that will provide just enough complexity to fit the data while avoiding overfitting.

In contrast, regularization suppresses the model complexity by restricting, not the number, but the magnitude of the network parameters. Typically, the error function is given by the mean squared error (MSE),

$$\text{MSE} = \frac{1}{N} \sum_{i=1}^N (\hat{y}_i - y_i)^2, \quad (\text{S1})$$

where \hat{y} represents the targets, y the network predictions and N the total number of training samples. In regularization, this function is modified by adding the sum of square weights and biases given by

$$\text{MSW} = \frac{1}{n} \sum_{j=1}^n w_j^2. \quad (\text{S2})$$

The modified error function then takes the form

$$E = (1 - \gamma) \text{MSE} + \gamma \text{MSW}, \quad (\text{S3})$$

where γ is the performance ratio. Using this expression as the regularization objective function, both the prediction errors and the network parameters are minimized simultaneously during training, thus, attaining a smooth network response and good generalization.

Furthermore, early stopping involves the monitoring of the training progress to determine when the training must be terminated. For this, the available data must be divided into at least two subsets: training and validation data. The training data are used to compute the gradients or the Jacobian matrix necessary to update the values of the network parameters. On the other hand, the validation data are used to monitor the generalization ability of the network at each training step as illustrated in Fig. S4. Throughout the course of training, the training error will decrease since the parameters are being updated to fit these data. Similarly, the validation error decreases with each step until the network begins to memorize the training data resulting in poor performance on the validation subset. The training is terminated when the validation error starts to rise, and the parameter vector at the point with the lowest validation error is selected as the optimal parameter set [35, 29].

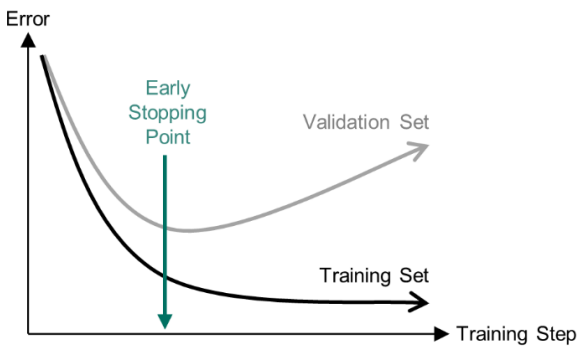


Figure S4. Schematic representation of early stopping.

An additional data set for testing can be used to assess the model's generalization ability and for model selection. This data set should only be used after the training procedure has been completed to ensure an unbiased assessment.

2 Data and Methodology for the ANN's Design

Activation Function. The nonlinear activation functions listed in Tab. S1 were used in the hidden neurons to include the known nonlinearities of the kinetic data in the model and to increase computational flexibility, while linear neurons were used in the output layer. While testing the listed activation functions, the remaining design parameters were kept constant at the default values in MATLAB®, namely the Levenberg-Marquardt training algorithm and 10 neurons in the hidden layer.

Table S1. Tested activation functions [39, 42].

Abbr.	Name of Function	Equation
elliotsig	Elliot Symmetric Sigmoid	$f(n) = \frac{n}{1 + n }$
logsig	Logarithmic Sigmoid	$f(n) = \frac{1}{1 + e^{-n}}$
poslin	Positive Linear	$f(n) = \begin{cases} 0, & n \leq 0 \\ n, & n > 0 \end{cases}$
radbasn	Normalized Radial Basis	$f(n) = \frac{e^{-n^2}}{\sum e^{-n^2}}$
satlin	Saturating Linear	$f(n) = \begin{cases} 0, & n \leq 0 \\ n, & 0 < n < 1 \\ 1, & n \geq 1 \end{cases}$
satlins	Symmetric Saturating Linear	$f(n) = \begin{cases} -1, & n \leq -1 \\ n, & -1 < n < 1 \\ 1, & n \geq 1 \end{cases}$
softmax	Softmax	$f(n) = \frac{e^n}{\sum e^n}$
tansig	Hyperbolic Tangent Sigmoid	$f(n) = \frac{2}{1 + e^{-2n}} - 1$
tribas	Triangular Basis	$f(n) = \begin{cases} 0, & n \leq -1 \\ 1 - n , & -1 < n < 1 \\ 0, & n \geq 1 \end{cases}$

Training Algorithm. There are several algorithms for training ANNs with backpropagation. Here, the functions listed in Tab. S2 were applied using the logarithmic sigmoid activation function (logsig). Relevant bibliographic information on the training algorithms is also provided.

Table S2. Tested training algorithms [43]

Abbr.	Algorithm	References
bfg	BFGS Quasi-Newton	[44, 45]
br	Bayesian Regularization	[29, 30, 32]
cgb	Conjugate Gradient with Powell/Beale Restarts	[46, 47]
cgf	Fletcher-Powell Conjugate Gradient	[39, 48]
cgp	Polak-Ribiere Conjugate Gradient	[39, 48]
gd	Gradient Descent	[39]
gdm	Gradient Descent with Momentum	[39]
gdx	Variable Learning Rate Gradient Descent	[39]
lm	Levenberg-Marquardt	[39, 49, 50]
oss	One Step Secant	[51]
rp	Resilient Backpropagation	[52]
scg	Scaled Conjugate Gradient	[53]

3 Results and Discussion

3.1. Network Design and Training

Activation Function. Fig. S5 displays the mean squared error values of all activation functions tested and the training time required for one ANN. The performance of all nonlinear activation functions is very similar. The lowest MSE was obtained with the widely used logarithmic sigmoid function.

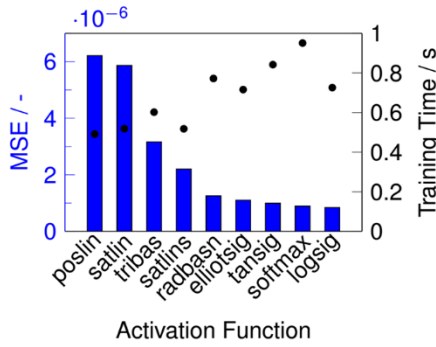


Figure S5. MSE and training time with the tested activation functions.

Training Algorithm. The performance of the tested training algorithms is outlined in Fig. S6. The algorithms gd and gdm were left out since no convergence was achieved in any of the run trials. The lowest MSE was obtained with the algorithms that apply Jacobian backpropagation i.e., lm and br. The time required for the training of one ANN with these function was 0.97 s and 0.67 s respectively.

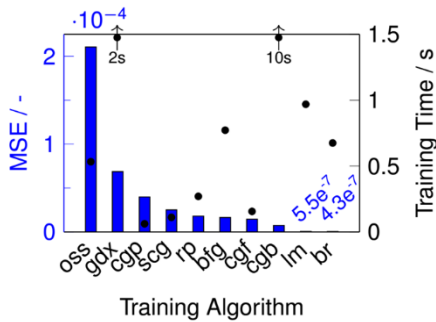


Figure S6. MSE and training time with the tested training algorithms.

Network Architecture. To find an appropriate ANN size, shallow networks with up to 15 hidden neurons were tested. The training time shown in Fig. S7 refers to the time required to train and test 10000 networks with the described training strategy (Fig. 1 in the manuscript). A network with five hidden neurons delivers a satisfactory fit for all components (highest mean relative error over all data was 11% for DME).

The training with this architecture was completed in 7.9 minutes.

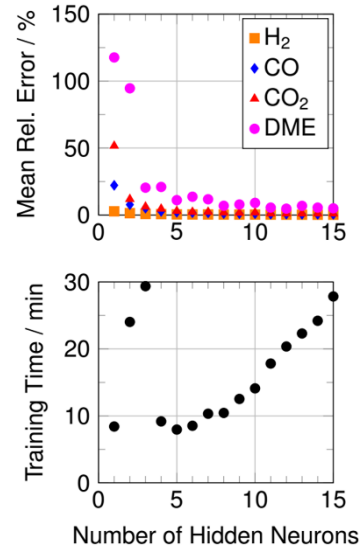


Figure S7. Mean relative error of prediction for each species and training time of 10000 networks for different sizes of the hidden layer.

The resulting ANN is illustrated schematically in Fig. S8.

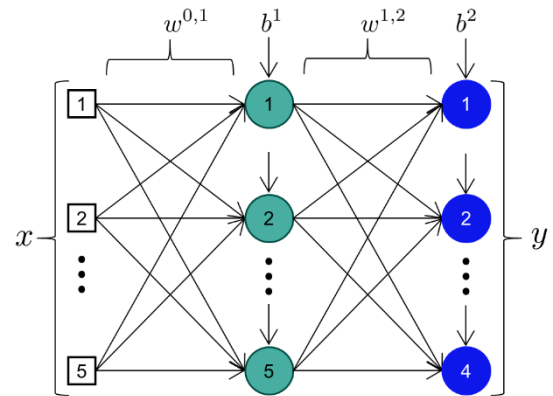


Figure S8. Schematic representation of selected network architecture.

The matrices $w^{0,1}$ and $w^{1,2}$ contain the connection weights between input and hidden layer, and between hidden and output layer respectively. The biases of the hidden and output neurons are contained in the vectors b^1 and b^2 .

$$w^{0,1} = \begin{bmatrix} -0,598 & -3,355 & 1,252 & 0,680 & 0,823 \\ 0,273 & 17,103 & -14,004 & -0,248 & -0,077 \\ 0,056 & 0,499 & -2,861 & -0,075 & -0,033 \\ 0,549 & 5,560 & -0,982 & -1,001 & -1,375 \\ 0,069 & 10,954 & -8,966 & 0,576 & -0,022 \end{bmatrix}$$

$$b^{1,T} = [2,865 \quad -1,339 \quad -0,282 \quad -3,556 \quad -2,025]$$

$$w^{1,2} = \begin{bmatrix} 1,038 & -0,990 & -1,992 & 0,249 & 1,817 \\ 4,583 & -4,413 & -2,297 & 1,267 & 5,526 \\ -3,856 & 5,226 & 0,080 & -1,070 & -5,563 \\ -6,733 & 4,573 & 0,197 & -1,890 & -5,701 \end{bmatrix}$$

$$b^{2,T} = [-0,208 \quad -3,315 \quad 2,765 \quad 5,580]$$

3.2 Evaluation of the Selected ANN

Fig. 5 in the manuscript displays simulation and experimental results in the temperature range between 180 °C and 300 °C. Complementary to this diagram, Figs. S9 to S13 show the results for the remaining inlet feed compositions. The pressure is in all cases $p=50$ bar.

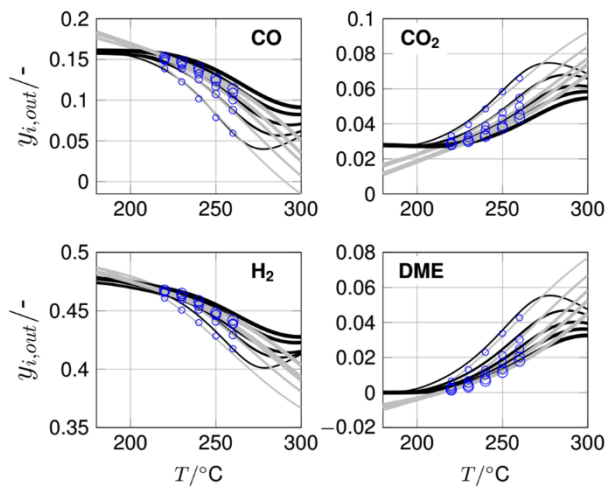


Figure S9. Components mole fraction in the product gas. Feed: 16.1 % CO, 2.8 % CO₂, 48.8 % H₂, 32.3 % inert gas (Ar and N₂).

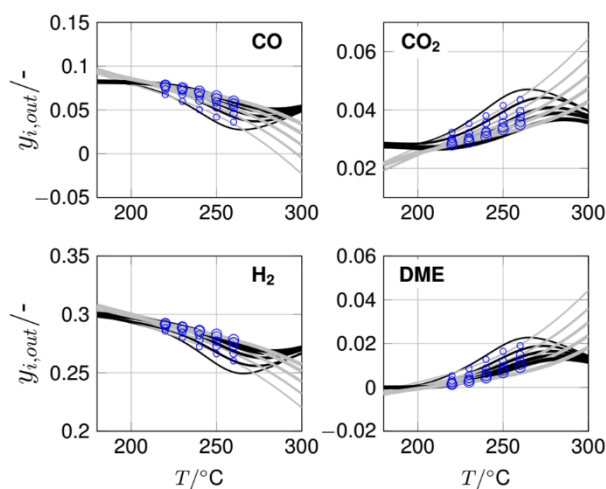


Figure S10. Components mole fraction in the product gas. Feed: 8.4 % CO, 2.9 % CO₂, 30.3 % H₂, 58.4 % inert gas (Ar and N₂).

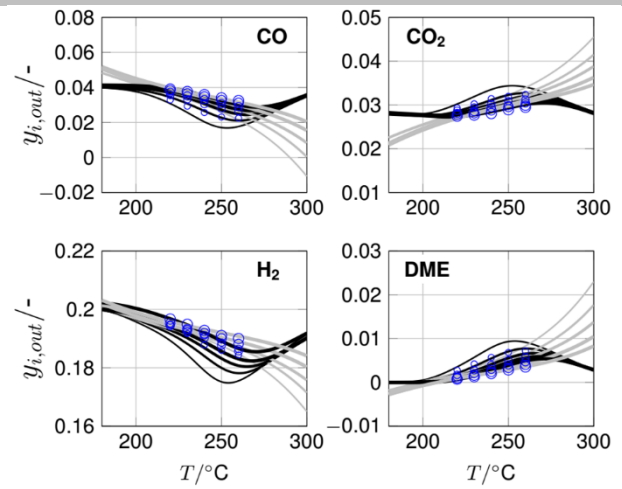


Figure S11. Components mole fraction in the product gas. Feed: 4.1 % CO, 2.9 % CO₂, 20.3 % H₂, 72.7 % inert gas (Ar and N₂).

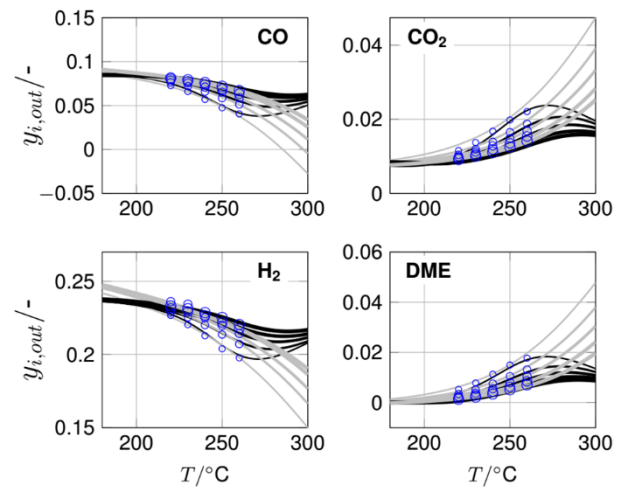


Figure S12. Components mole fraction in the product gas. Feed: 8.6 % CO, 0.8 % CO₂, 24.0 % H₂, 66.6 % inert gas (Ar and N₂).

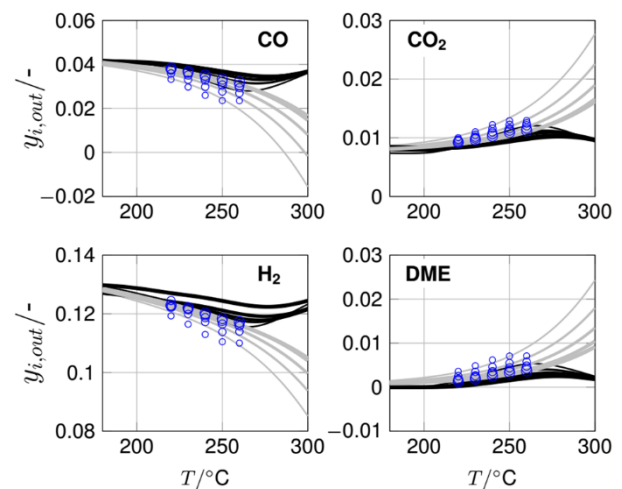


Figure S13. Components mole fraction in the product gas. Feed: 4.3 % CO, 0.8 % CO₂, 13.1 % H₂, 81.8 % inert gas (Ar and N₂).

Article

Kinetics of the Direct DME Synthesis: State of the Art and Comprehensive Comparison of Semi-Mechanistic, Data-Based and Hybrid Modeling Approaches

Nirvana Delgado Otalvaro , Pembe Gül Bilir , Karla Herrera Delgado * , Stephan Pitter  and Jörg Sauer 

Institute of Catalysis Research and Technology (IKFT), Karlsruhe Institute of Technology (KIT), Hermann-von-Helmholtz-Platz 1, 76344 Eggenstein-Leopoldshafen, Germany; nirvana.delgado@kit.edu (N.D.O.); pembe-guel.bilir@student.kit.edu (P.G.B.); stephan.pitter@kit.edu (S.P.); j.sauer@kit.edu (J.S.)

* Correspondence: karla.herrera@kit.edu; Tel.: +49-721-608-28631

Abstract: Hybrid kinetic models represent a promising alternative to describe and evaluate the effect of multiple variables in the performance of complex chemical processes, since they combine system knowledge and extrapolability of the (semi-)mechanistic models in a wide range of reaction conditions with the adaptability and fast convergence of data-based approaches (e.g., artificial neural networks—ANNs). For the first time, a hybrid kinetic model for the direct DME synthesis was developed consisting of a reactor model, i.e., balance equations, and an ANN for the reaction kinetics. The accuracy, computational time, interpolation and extrapolation ability of the new hybrid model were compared to those of a lumped and a data-based model with the same validity range, using both simulations and experiments. The convergence of parameter estimation and simulations with the hybrid model is much faster than with the lumped model, and the predictions show a greater degree of accuracy within the models' validity range. A satisfactory dimension and range extrapolation was reached when the extrapolated variable was included in the knowledge module of the model. This feature is particularly dependent on the network architecture and phenomena covered by the underlying model, and less on the experimental conditions evaluated during model development.

Keywords: hybrid modeling; reaction kinetics; dimethyl ether



Citation: Delgado Otalvaro, N.; Bilir, P.G.; Herrera Delgado, K.; Pitter, S.; Sauer, J. Kinetics of the Direct DME Synthesis: State of the Art and Comprehensive Comparison of Semi-Mechanistic, Data-Based and Hybrid Modeling Approaches. *Catalysts* **2022**, *12*, 347. <https://doi.org/10.3390/catal12030347>

Academic Editors: Enrico Catizzone and Ana Palčić

Received: 7 February 2022

Accepted: 12 March 2022

Published: 18 March 2022

Publisher's Note: MDPI stays neutral with regard to jurisdictional claims in published maps and institutional affiliations.



Copyright: © 2022 by the authors. Licensee MDPI, Basel, Switzerland. This article is an open access article distributed under the terms and conditions of the Creative Commons Attribution (CC BY) license (<https://creativecommons.org/licenses/by/4.0/>).

1. Introduction

Dimethyl ether (DME) is an important chemical that can be used as an intermediate for the production of CO₂-neutral base products, as coolant or propellant, and as a diesel substitute or fuel additive [1–3]. A promising alternative to the state-of-the-art two-step DME production is the direct or one-step synthesis in a single reactor over dual catalyst systems [4–6]. This process has been demonstrated at pilot scale and it is currently under further development [1,7,8], for which reliable predictive models are essential. However, the detailed reaction mechanism of the direct DME synthesis has not yet been fully understood [9] and its modeling is challenging. Reasons for this are, for example, variable structural changes of the metallic catalyst depending on the reaction conditions [10], the variation of the dominant pathway of the methanol synthesis [11], as well as the deactivation of the dehydration catalyst, e.g., by acidity loss due to H⁺/Cu²⁺ ion exchange, especially in the case of zeolite-based systems, and the sintering of the metallic catalyst in the presence of high water concentrations [12–14].

Several semi-mechanistic or lumped models that enable the modeling of the system in a specific operational range have been developed [15–26]. However, due to the mentioned difficulties, semi-mechanistic models for the direct DME synthesis are difficult to fit in a wide range of conditions. This is where the potential of machine learning approaches to extract and predict input–output relationships in large data sets comes into play. These methods, especially artificial neural networks (ANNs), have been used successfully in

various areas of the chemical industry, mostly as predictive tools [27–30]. One of the general drawbacks of ANNs is that their predictions are only reliable in the range in which the training data were measured and extrapolation is only possible in a slightly extended range [31]. However, unlike semi-mechanistic models, ANNs can be easily adapted to large amounts of multidimensional data in broad operational windows [30,31].

Models that combine the features of both (semi-)mechanistic and data-based approaches represent a promising alternative for modeling the behavior of chemical reactors [32]. However, recent studies have highlighted that the adoption of machine learning approaches is still limited for chemical processes [27,33,34]. An extensive literature search on models for direct DME synthesis revealed that most models are semi-mechanistic, while only a few are data-based, and none of the models are hybrid in nature (Section 2). Therefore, in addition to providing a timely overview of the available models for direct DME synthesis, a main objective of this work is to establish an initial hybrid model for this system and to comprehensively compare the different types of models (Section 3). Simulation results obtained with the hybrid model are compared to those obtained with a semi-mechanistic and a data-based model that have the same range of validity, which enables an evaluation of the structural differences between the model types. Based on similar works [35–37], it is expected that the hybrid model provides a higher accuracy than the lumped model, while exhibiting an increased extrapolation capability compared with the data-based one. These hypotheses are evaluated in a quantitative manner in Section 4. In this section, critical model features such as accuracy, computational burden, interpolation and extrapolation ability are tested, using both simulations and experiments.

2. Available Models for the Direct Synthesis of DME—An Overview

In this section, an overview of kinetic models for the direct synthesis of DME over the commercial catalyst system with CuO/ZnO/Al₂O₃ (CZA) and γ -Al₂O₃ is presented.

2.1. Semi-Mechanistic (Lumped) Models

In the semi-mechanistic modeling approach, assumptions about the reaction mechanism are made and experimental data are used to determine the reaction kinetic parameters. Therefore, the influence of relevant operating conditions on the DME direct synthesis is the focus of numerous current research projects. Overviews are given, for example, by Z. Azizi et al. [4] and U. Mondal and G. D. Yadav [38].

The ranges evaluated in available modeling studies [15–26] are presented in Figure 1 for process variables that are particularly relevant for reaction kinetics, i.e., the temperature, pressure, the CZA-to- γ -Al₂O₃ weight ratio (μ , Equation (1)), the carbon oxide ratio (COR, Equation (2)) and the stoichiometric number (SN, Equation (3)).

$$\mu = \frac{m_{\text{CZA}}}{m_{\gamma\text{-Al}_2\text{O}_3}} \quad (1)$$

$$\text{COR} = 100\% \frac{y_{\text{CO}_2,\text{in}}}{y_{\text{CO}_2,\text{in}} + y_{\text{CO},\text{in}}} \quad (2)$$

$$\text{SN} = \frac{y_{\text{H}_2,\text{in}} - y_{\text{CO}_2,\text{in}}}{y_{\text{CO},\text{in}} + y_{\text{CO}_2,\text{in}}} \quad (3)$$

The overlapping of the ranges is obvious and explained by the constraints inherent to the system under consideration. For example, the maximal temperature is defined based on the thermal stability of the catalysts, so as to avoid sintering of CZA except, of course, for studies where deactivation phenomena are investigated [18,20]. The lowest temperature, on the other hand, is typically chosen under consideration of the other process variables so as to have measurements in a range where the catalyst is active, and the signal-to-noise ratio is high. In the summarized studies, temperatures from 473 to 623 K have been evaluated (Figure 1a).

Since the process exhibits volume contraction, an increase in pressure has a positive effect on the process performance according to LeChatelier's law [39]. However, the maximal pressure is limited due to high investment costs and necessary safety measures. At lab scale, the pressure range is often constrained by the experimental rig. As shown in Figure 1b, some studies [15,17,21,26] are conducted at 50 bar, which is the typical industrial operational pressure for methanol synthesis, while others evaluate a pressure range instead of a constant pressure level [18–20,22,24,25]. Overall, the summarized publications cover a pressure range from 9 to 72 bar.

As depicted in Figure 1c, the CZA-to- γ - Al_2O_3 weight ratio (μ) was chosen to be equal to or higher than the one in most studies, since it has been demonstrated that an increased fraction of methanol catalyst is beneficial for the overall process [15,16,40]. The optimal catalyst bed composition has been shown to be a function of the operating conditions [15,16] and the composition of syngas, especially regarding the CO_2 amount in the feed [17].

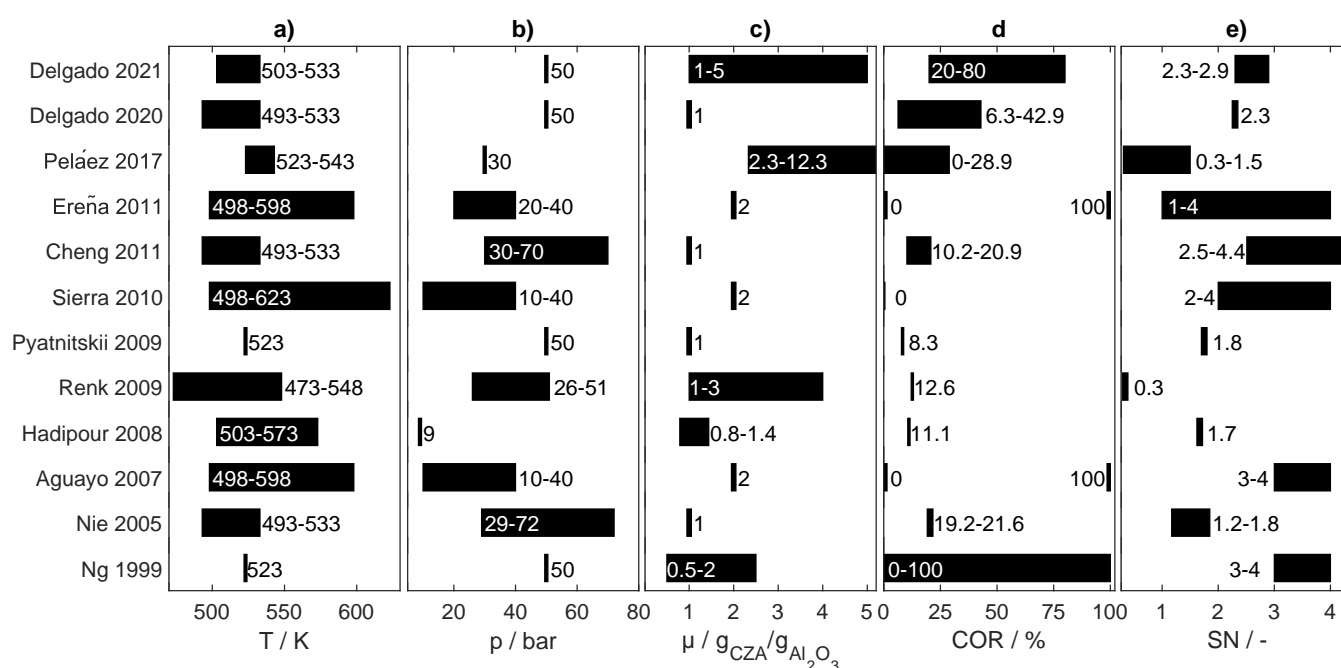


Figure 1. Overview of lumped models' validity ranges regarding (a) temperature (b) pressure (c) CZA-to- γ - Al_2O_3 weight ratio μ (d) carbon oxide ratio COR and (e) stoichiometric number SN. Models [15–26] named after first author and year of publication.

In terms of the feed gas composition, instead of a simple listing of this heterogeneous information reported by different authors, an unambiguous characterization was conducted using the COR and SN in order to enable the comparison of the models.

The relevance of the COR lies in the high influence of the CO_2 content in the syngas on the process performance: High CO_2 levels in the feed have been shown to promote water formation and to reduce the attainable product yield [14,41,42]. However, kinetic models valid in a wide COR range are useful for process design and optimization, as interest in CO_2 utilization grows in the industry [43]. The wide pattern in Figure 1d illustrates that the influence of CO_2 has become increasingly important in recent years and is essential in current kinetic studies.

The SN is relevant in terms of the different hydrogen requirements for methanol production via CO or CO_2 hydrogenation. This is because, due to the different syngas production technologies, the H_2 content in the syngas is known to vary over a wide range [44], and adjustment of the H_2 content in the feed gas is not always economically feasible due to the lack of sustainable H_2 sources [45,46]. As shown in Figure 1e, a large range of SN is covered by the presented kinetic studies. However, a closer look in each publication reveals

that in most cases, the effect of this variable was not evaluated systematically. Clearly, operating conditions for kinetic studies are chosen with consideration of the concurrent effects on the other process variables. For example, if the system is operated at low pressure, higher temperatures and low dilutions are required to achieve product concentrations that can be measured accurately. As a consequence, optimal conditions found in these studies are often local optima within the validity range of each model or experimental range. For example, Pelaez et al. [16] observed an increasing yield of DME with an increasing CZA fraction up to 92.5 wt.%, at a pressure of 30 bar and no CO₂ in the feed. In contrast, in our previous investigations [17] conducted at 50 bar and high CO₂ contents in the feed, an optimal catalyst bed composition was observed at approximately 66 wt.%. Hence, aiming towards the global optimization of the direct DME synthesis, a further systematic evaluation of process variables and their simultaneous effects is still necessary. However, in addition to the aforementioned process variables, many other factors play a significant role, such as the dynamic behavior of the catalysts, the reactor and its configuration, the composition of the CZA catalyst, the heat removal concept, etc. Therefore, in terms of time and resources, a comprehensive exploration of the state space is probably only feasible using models that have enough flexibility to evaluate larger operational ranges and number of process variables.

2.2. Data-Based Models

Artificial neural networks (ANNs) are one of the most powerful machine learning approaches for modeling [29,47,48], and as universal approximators, these can approximate nearly any continuous function in a bounded domain [49,50]. An essential step of this modeling approach is answering the design questions for ANNs, e.g., which activation functions are appropriate for the problem at hand, and how many layers and neurons are required to achieve sufficient model complexity [31]. The performance of the networks is typically evaluated based on the prediction accuracy and the convergence time, which have been shown to be remarkable, and superior in comparison to that of traditional (semi-)mechanistic models [32,51–53]. Further advantages of this modeling approach, is that no prior knowledge of the chemistry and physics of the system to be described is required and the high adaptability of ANNs to different structures and sizes of data sets [32,47,54]. Unlike semi-mechanistic models, ANNs (and, in general, machine learning approaches) have not been widely used for the modeling of the direct DME synthesis. Studies conducted for this process or for the single steps are summarized in the following.

In a previous work [51], we applied ANNs for the modeling of the direct synthesis of DME over the commercial catalyst system CZA/ γ -Al₂O₃ using data that had previously been used for the parametrization of a lumped model. ANNs could be trained successfully even with the limited amount of data. The trained ANN exhibited a fast convergence, and a high adaptability to the experimental data. Moradi et al. [52] analyzed the use of ANNs for modeling the single-step DME synthesis over a bifunctional CZA-H-ZSM-5 catalyst. The authors successfully trained an ANN to predict the CO conversion, as well as the DME selectivity and yield. Between 2003 and 2009, Omata et al. also conducted simulations of single-step DME synthesis using ANNs. Unlike Delgado Otalvaro et al. and Moradi et al., they used ANNs aiming at the maximization of the CO conversion by optimizing the temperature profile in the reactor [55,56] and by identifying effective additives for the CZA/ γ -Al₂O₃ catalyst based on the physicochemical properties of the elements [57].

Additionally, studies using ANNs have been conducted for the single steps of the direct synthesis [53,58–61]. For example, Svitnic et al. [58] used ANNs for the prediction of by-product formation in the methanol synthesis from syngas, based on data from a pilot plant. Moreover, since the methanol dehydration to DME proceeds without any relevant side reactions, its rate is directly proportional to the rate of depletion and/or formation and it can be measured directly. This advantage of the methanol dehydration to DME was used by Valeh-E-Sheyda et al. [59] and Alamohada et al. [53] who used kinetic data and ANNs for the data-based modeling of the kinetics of this reaction.

2.3. Hybrid Models

To the best of our knowledge, hybrid models have not been yet applied to the direct DME synthesis. However, some hybrid models have been derived for the individual steps of this process. Zahedi et al. [62] used a hybrid model for the modeling of the CO₂ hydrogenation to methanol. In their work, the authors applied a mechanistic, a data-based and a hybrid modeling approach and demonstrated the superior performance of the hybrid model regarding accuracy and computational effort. Potočnik et al. [63] used a kinetic model from the literature to predict the methanol production rate as a function of the pressure, temperature and the partial pressure of the main species in the system. ANNs were used in combination with this model as an error-corrector, enhancing the prediction accuracy in the range where experimental data were available. Alavi et al. [64] derived a mechanistic and a hybrid model for the methanol dehydration to DME. Here, an ANN was trained using data from a white-box model to predict the global reaction rate and it was integrated in the balance equations. The hybrid model was simpler and 20 times faster than the mechanistic model.

These studies show the potential of hybrid modeling for related systems. The second part of this contribution is devoted to the derivation of the first hybrid model for the direct DME synthesis.

3. Models' Structures, Modeling and Experimental Methodology

For the comparative study aimed in this work, the observed discrepancies between model predictions must be only attributable to the models' structural differences. Hence, these must be valid in the same range of conditions. In this section, the models' structures are presented in order to identify crucial differences. The lumped and the data-based models are described first in Sections 3.1 and 3.2, since elements from these types are necessary for the development of the hybrid model. The mathematical structure of the latter is subsequently introduced in Section 3.3. The results obtained with the hybrid model and the comparative analysis between the different model types is given in Section 4.

The structure of the models relevant in this work, i.e., the lumped, hybrid and data-based models, is shown schematically in Figure 2. The lumped and the hybrid model both consist of a reaction kinetic model for the calculation of the reaction rates and a reactor model based on the balance equations for the laboratory reactor. The mole fraction profiles $y_i(z)$ of the different species in the system are calculated by integration of the differential equations. With the data-based model, on the other hand, the mole fractions are predicted directly using ANNs.

The color spectrum in Figure 2 represents the level of information required for the different types of modeling; the darker the color, the less system knowledge is necessary. The ANNs, for example, are predictors based on training data, i.e., black box models. The reactor model for the tube reactor is characterized as white box since it is derived based on the species and the total mass balance. In contrast, the lumped and the hybrid model are both characterized as gray box. The lumped model is the model with the greatest knowledge content among the three, because the balance equations are generally valid and the rate expressions are based on mechanistic assumptions and thermodynamic considerations. It is considered a gray box model since the parameters of the Arrhenius and Van't Hoff equations are estimated to fit experimental data. Comparably, the hybrid model is also considered a gray box model, since it involves knowledge and data-based elements in its structure.

In this contribution, a hybrid model for the direct DME synthesis is derived and presented. Since this is the first model of this type for the DME synthesis, its assessment has been made based on validation experiments and comparison with a semi-mechanistic model [15] and a data-based model [51].

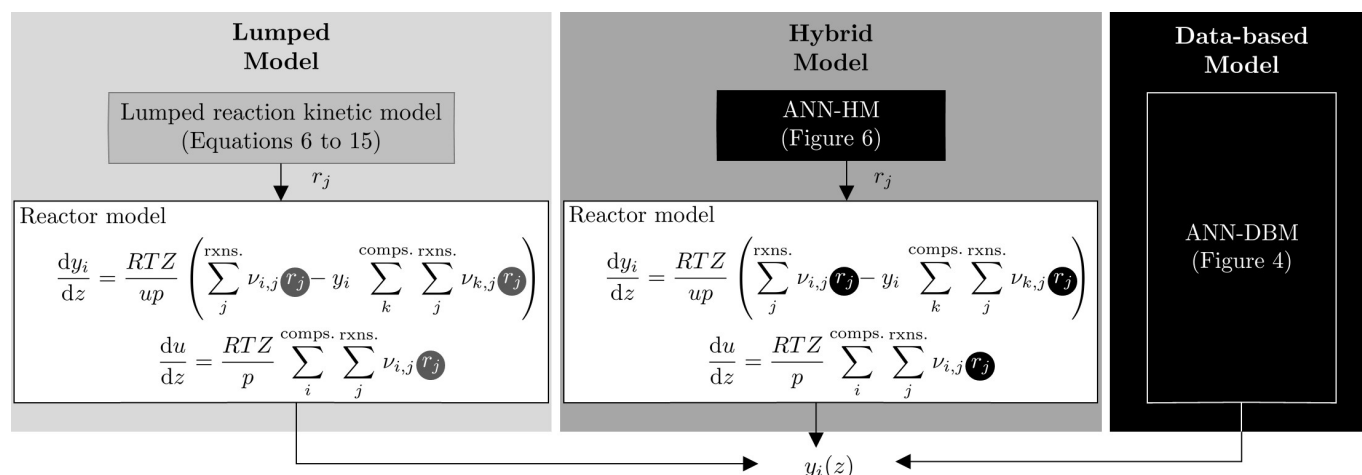


Figure 2. Schematic representation of the lumped, hybrid and data-based models relevant for this work.

3.1. Lumped Model

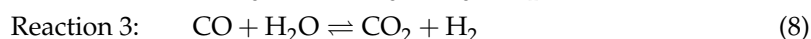
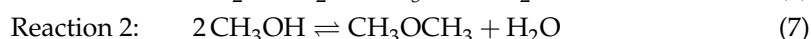
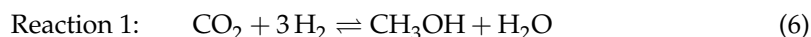
The lumped model was developed and validated in detail in a previous work [15]. It consists of balance equations and a lumped reaction kinetic model parametrized to fit intrinsic kinetic data. Equation (4) describes the change of the molar fraction of species i (y_i) along the axial coordinate (z). Equation (5) accounts for the drop of the gas velocity u due to the reaction-induced volume contraction.

$$\frac{dy_i}{dz} = \frac{RTZ}{up} \left(\sum_j^{rxns.} \nu_{i,j} r_j - y_i \sum_k^{comps. rxns.} \sum_j \nu_{k,j} r_j^v \right) \quad (4)$$

$$\frac{du}{dz} = \frac{RTZ}{p} \sum_i^{comps. rxns.} \sum_j \nu_{i,j} r_j^v \quad (5)$$

In Equations (4) and (5), y_i is the molar fraction of component i , R is the universal gas constant in $\text{J mol}^{-1} \text{K}^{-1}$, T is the temperature in K, Z is the mixture's compressibility factor calculated with the Peng–Robinson equation of state (PR-EoS) [65], u is the gas velocity in m s^{-1} , p is the pressure in Pa, $\nu_{i,j}$ is the stoichiometric coefficient of species i in reaction j . The abbreviations “Nr” and “Nc” refer to the number of reactions and components, respectively. Finally, r_j^v is the volume-specific rate of reaction j in $\text{mol m}^{-3} \text{s}^{-1}$ which is defined by the reaction kinetic model described in the following.

The reaction kinetic model is based on the mechanistic study of Lu et al. [66] considering the CO_2 hydrogenation to methanol, the methanol dehydration to DME and the water gas shift reaction (WGSR) (Equations (6)–(8)). Other possible reactions such as CO_2 methanation were not included because no other products were detected at significant concentrations during the kinetic experiments.



The respective reaction rates in mol kg⁻¹ s⁻¹ are calculated with Equations (9)–(11).

$$r_1 = k_1 \frac{\left(f_{\text{CO}_2} f_{\text{H}_2}^3 - \frac{f_{\text{H}_2\text{O}} f_{\text{CH}_3\text{OH}}}{K_{f,1}} \right)}{\left(1 + K_{\text{CO}_2} f_{\text{CO}_2} + K_{\text{CO}} f_{\text{CO}} + \sqrt{K_{\text{H}_2} f_{\text{H}_2}} \right)^3} \quad (9)$$

$$r_2 = k_2 \left(f_{\text{CH}_3\text{OH}}^2 - \frac{f_{\text{DME}} f_{\text{H}_2\text{O}}}{K_{f,2}} \right) \quad (10)$$

$$r_3 = k_3 \frac{\left(f_{\text{H}_2\text{O}} - \frac{f_{\text{CO}_2} f_{\text{H}_2}}{K_{f,3} f_{\text{CO}}} \right)}{1 + K_{\text{CO}_2} f_{\text{CO}_2} + K_{\text{CO}} f_{\text{CO}} + \sqrt{K_{\text{H}_2} f_{\text{H}_2}}} \quad (11)$$

Finally, r_j^v is given by

$$r_j^v = \begin{cases} r_j [(1 - \epsilon) \rho_{\text{CZA}} \zeta_{\text{CZA}}], & j = 1 \vee j = 3 \\ r_j [(1 - \epsilon) \rho_{\gamma\text{-Al}_2\text{O}_3} \zeta_{\gamma\text{-Al}_2\text{O}_3}], & j = 2. \end{cases} \quad (12)$$

In Equations (9)–(12), f_i is the fugacity of component i in bar, calculated using the fugacity coefficients obtained from the PR-EoS, ϵ is the catalyst bed void fraction, ρ_{CZA} and $\rho_{\gamma\text{-Al}_2\text{O}_3}$ are the CZA and $\gamma\text{-Al}_2\text{O}_3$ densities, and ζ_{CZA} and $\zeta_{\gamma\text{-Al}_2\text{O}_3}$ are the respective volume fractions in the catalyst bed. The equilibrium constants ($K_{f,j}$) are calculated with Equation (13), whereas the reaction rate and adsorption constants (k_j and K_i) are defined by the reparametrized Arrhenius and Van 't Hoff equations (Equations (14) and (15)) for a reference temperature T_R of 503 K.

$$K_{f,j} = 10^{\left(\frac{A_j}{T} - B_j \right)} \quad (13)$$

$$k_j = k_{j,T_R} \exp \left[-E_{A,j,n} \left(\frac{T_R}{T} - 1 \right) \right], \quad \text{with } E_{A,j,n} = \frac{E_{A,j}}{T_R R} \quad (14)$$

$$K_i = K_{i,T_R} \exp \left[-\Delta H_{i,n} \left(\frac{T_R}{T} - 1 \right) \right], \quad \text{with } \Delta H_{i,n} = \frac{\Delta H_i}{T_R R}. \quad (15)$$

The model-specific parameters for Equations (13)–(15) (A_j , B_j , k_{j,T_R} , $E_{A,j,n}$, K_{i,T_R} and $\Delta H_{i,n}$) are provided in Table 1.

Table 1. Model-specific parameters for the lumped model [15].

Reaction	Equation (13)		Equation (14)		Adsorbate	Equation (15)	
	A	B	ln(k_{T_R})	$E_{A,n}$		ln(K_{T_R})	$\Delta H_{ads,n}$
1	3014.4029	10.3857	−6.94	21.81	CO	−15.32	−14.03
2	1143.9494	0.9925	−2.07	42.77	CO ₂	−0.57	0
3	2076.2131	2.0101	−2.75	10.82	H ₂	−19.51	−14.68

These parameters were determined based on intrinsic kinetic data acquired in a fixed bed reactor at a pressure of 50 bar under variation of the temperature, the feed composition ($y_{\text{CO},in}$, $y_{\text{CO}_2,in}$, $y_{\text{H}_2,in}$) and the total gas flow, as summarized in Table 2. The catalyst bed consisted of mechanically mixed CZA and $\gamma\text{-Al}_2\text{O}_3$ catalysts in a 1:1 mass ratio for a total catalyst mass of 2 g.

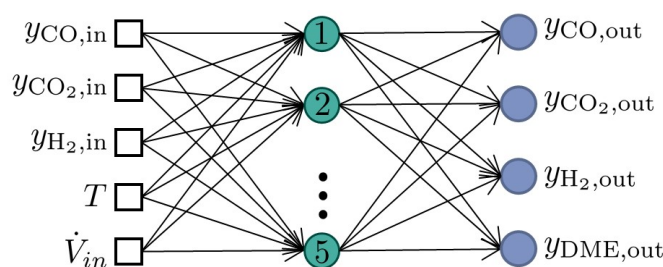
Table 2. Conditions for kinetic measurements [15].

Param.	Value	Unit
T	220, 230, 240, 250, 260	$^{\circ}\text{C}$
\dot{V}_{in}	0.2, 0.3, 0.4, 0.5, 0.6, 0.7	slpm *
$y_{\text{CO}_2,\text{in}}$	0, 1, 3	%
$y_{\text{CO},\text{in}}$	4, 8, 15	%
$y_{\text{H}_2,\text{in}}$	$y_{\text{H}_2,\text{in}} = 2.3(y_{\text{CO},\text{in}} + y_{\text{CO}_2,\text{in}}) + y_{\text{CO}_2,\text{in}}$	%

* Standard liters per minute, $T = 0^{\circ}\text{C}$ and $p = 1.01325$ bar.

3.2. Data-Based Model and ANN Training Strategy

The data-based model derived and evaluated in a previous work [51] consists of an ANN trained to predict the concentration of CO, CO₂, H₂ and DME in the product gas based on the composition of the feed gas ($y_{\text{CO},\text{in}}$, $y_{\text{CO}_2,\text{in}}$ and $y_{\text{H}_2,\text{in}}$), the total gas flow \dot{V}_{in} and the temperature (Figure 3). In this configuration, the ANN replaces both the reactor and the reaction kinetic model. The model was trained using the same data used for the parameter estimation of the lumped kinetic model (Table 2) and, hence, it has the same validity range.

**Figure 3.** Representation of the data-based model. Adapted from N. Delgado Otalvaro et al. [51].

The data division and training strategy used for the data-based model is also relevant to this work [51]. The ANN of the data-based model (ANN-DBM) and the one of the hybrid model (ANN-HM) are predictors of different quantities and are trained using different data structures (Section 3.3). However, the data division and training methodology presented in our previous work [51] is automatic and adaptable to multidimensional data sets of different sizes and structures, and thus used in this work for the design of the ANN-HM. As depicted in Figure 4, the data division is conducted in two stages. In Stage 1, the data samples are divided into two subsets, one for the design and training of the networks (Design Data), and one for the posterior network selection based on separate data (Test Data A). In Stage 2, the design data are again divided into two subsets, the Train Data subset used in the backpropagation framework [67] to determine the network's parameters (weights and biases), and the Test Data B subset used in the framework of Bayesian regularization [68] to test the trained networks without a validation subset. The training is conducted iteratively under variation of the start parameter values (label (1)) to avoid local optimality, and of the data division of the design data (label (2)). The Test Data B subset is not used directly to determine the network's parameters, however, since the data in this subset are used for model selection, it introduces a certain bias in the model. To guarantee that the network with the best generalization, i.e., with the best performance on independent data samples, is chosen, Test Data A are used for the final network selection.

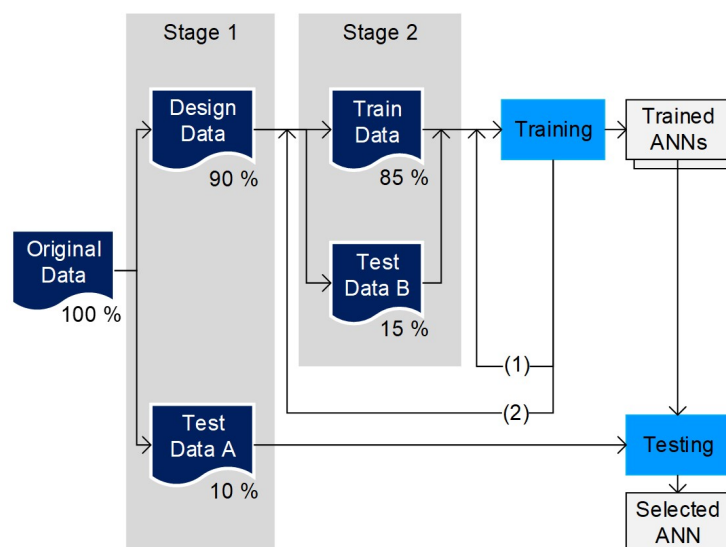


Figure 4. Data division scheme and training strategy. Taken from N. Delgado Otalvaro et al. [51].

3.3. Hybrid Model

As depicted in Figure 2, the hybrid model consists of two parts: a reactor model and an ANN. The reactor model is the same that is used in the lumped model (Equations (4) and (5)). These are generally valid and constitute the “knowledge module” of the hybrid model. The ANN embedded within the framework of the ordinary differential equations, is used for the calculation of the reaction rates (r_j), and replaces the reaction kinetic model. Clearly, the ANN of the data-based model is not suitable for the calculation of the rates, since this ANN is trained to predict the product gas composition. In the following sections, the design of the ANN as a predictor of the rates for the hybrid model (ANN-HM) is described.

3.3.1. Architecture

Comparable to the architecture of the ANN-DBM, the ANN-HM is also shallow (one single hidden layer with a finite number of hidden neurons) and feedforward (unidirectional information flow from input to output), as depicted in Figure 5. The new ANN-HM is trained to replace the reaction kinetic model, i.e., to predict the reaction rates along the axial coordinate z . Hence, the target vector y contains three elements, one representing the rate of each reaction (Equations (6)–(8)), as follows,

$$y = [r_1, r_2, r_3]_z. \quad (16)$$

The rates are calculated as a function of the temperature and the mole fractions of each species in the system. The input vector is thus defined by

$$x = [y_{\text{CO}}, y_{\text{CO}_2}, y_{\text{H}_2}, y_{\text{H}_2\text{O}}, y_{\text{MeOH}}, y_{\text{DME}}, y_{\text{Ar}}, y_{\text{N}_2}, T]_z. \quad (17)$$

The elements in Equations (16) and (17) correspond to the values at different positions of the axial coordinate z . Since all experiments were conducted under isothermal conditions, the temperature is constant along the reactor length L_{bed} and Equation (18) applies.

$$T|_z = T, \forall z \in [0, L_{\text{bed}}]. \quad (18)$$

Other process variables that are considered to be constant in the axial domain and over all data points, such as the catalyst distribution and pressure, are not included explicitly in the model. Furthermore, the proposed structure is one of innumerable possibilities for the design of the ANN-HM, and additional input variables can be included in the network to consider further phenomena if the respective data is available. For example, including the

time on stream (ToS) in the input vector and data samples measured at different ToS during the ANN training would enable to consider the effect of activity loss on the reactions rates.

While the number of input and output neurons is constrained by the input and output variables (Equations (16) and (17)), the number of neurons in the hidden layer has to be determined empirically. For the selection of an appropriate number of hidden neurons (HN), architectures with up to 30 HN were tested. The best ANN was selected based on the prediction accuracy on “unseen” data, using a mean relative error of 5% over all samples in Test Data A (Figure 4).

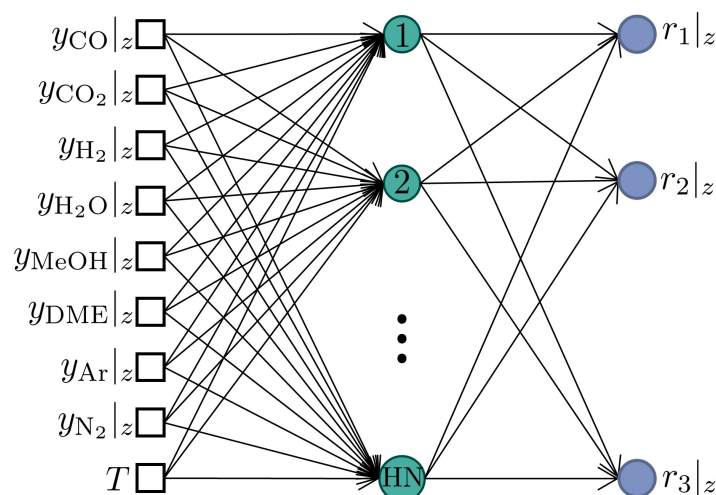


Figure 5. Schematic representation of ANN’s architecture for the hybrid model (ANN-HM).

The remaining network’s characteristics are chosen to be the same as in the data-based model in order to ensure comparability of the models. Hence, the logarithmic sigmoid and the positive linear functions were used as the activation function in the hidden and output neurons, respectively. The sigmoid function serves to map the known nonlinearities in the system. Bayesian regularization was chosen as the training algorithm. This method proposed by McKay [68] aims to avoid overfitting by training only the number of parameters necessary to minimize the objective function, instead of all parameters available. Thus, the model sensibility to the network architecture is reduced and overfitting can be avoided.

3.3.2. Training Data

For a comparative study of the models, possible biases must be excluded to ensure that the prediction discrepancies are caused only by the structural differences between the model types. For the comparison of the lumped and the data-based model, this was achieved by training/parametrizing both models with the same experimental data. In the case of the hybrid model, the ANNs act as a predictor for the reaction rates, which are not metrologically accessible from integral experiments where the measurable variable is the composition of the product gas ($y_{i,out}$). Therefore, to generate training data for the ANN-HM, simulations are performed with the lumped model under the conditions of the experiments to which the lumped and data-based models were fitted (Table 2). The axial domain is discretized as shown in Figure 6, using different mesh refinements with 5, 10, 15, 50 and 100 uniformly distributed elements, and the reaction rates at the nodal points are used for training.

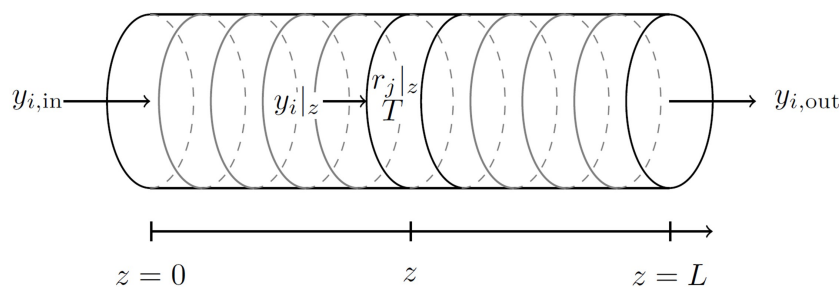


Figure 6. Schematic representation of the axial domain discretization, exemplary for 10 uniformly distributed elements.

3.4. Experimental Equipment and Procedures

New experiments were conducted with the same laboratory setup used for the measurement of the kinetic data for model development. These experiments were performed to validate the simulation results obtained during extrapolation analysis in Section 4.3. The reactor used for the experiments is a plug flow tube reactor made of stainless steel. It has a length of 460 mm and an internal diameter of 12 mm. For heating purposes, the reactor outer wall is enclosed by four brass jaws with heating cartridges (Horst GmbH, Lorsch, Germany). The pressure of the reactor is regulated manually with a mechanical pressure regulator (Emerson Automation Solutions, Langenfeld, Germany) and mass flow controller (Bronkhorst High-Tech B.V., AK Ruurlo, The Netherlands) are used to regulate the gas flow into the reactor. A Fourier-transform infrared spectrometer (FTIR, Gaset Technologies GmbH, Germany) and a gas chromatograph (GC, Agilent Technologies Deutschland GmbH, Waldbronn, Germany) were used to quantitatively analyze the feed and product gases. Further details on the reactor setup and analytics are described in previous works [15,17].

The syngas used for the experiments consisted of the feed gases hydrogen (H_2 , 99.9999%), carbon monoxide (CO , 99.97%), a mixture of carbon dioxide and nitrogen (CO_2/N_2 , 20:80 \pm 1.0%), as well as nitrogen (N_2 , 99.9999%). The gases were purchased by Air Liquide Deutschland GmbH., Ludwigshafen, Germany. A 1:1 mechanical mixture of the commercial catalysts $\text{CuO}/\text{ZnO}/\text{Al}_2\text{O}_3$ (CZA) and $\gamma\text{-Al}_2\text{O}_3$ (Alfa Aesar, Kandel, Germany) was used. The size distribution of the catalyst particles lay between 250 μm and 500 μm . Silicon carbide (SiC, Hausen Mineraliengroßhandel GmbH, Germany) with the same particle size distribution was mechanically mixed with the commercial catalysts in order to avoid the formation of hot spots in the catalytic bed.

Before starting the experimental measurements, the catalyst was reduced using 5% H_2 in N_2 at atmospheric pressure and temperatures between 363 K and 513 K. After that, the catalysts were conditioned and the measured species concentrations were monitored based on a reference experimental point to check for any loss of activity. After a stable catalytic activity was achieved, any deactivation of the catalysts could be ruled out. Additional information on the catalyst conditioning and deactivation can be found in the ESI.

4. Hybrid Model Results

In this chapter, the results of the ANN-HM training are presented first, followed by the evaluation of the models performance and interpolation ability. Subsequently, a comparative analysis of the predictions of the three different model types is conducted and complemented with the experimental validation of simulation results.

4.1. ANN-HM Training Results

In the absence of an established systematic approach, determining the appropriate number of hidden neurons (HNs) is one of the major challenges in modeling with ANNs. If the number of HN is too low, the forecasting ability of the model is limited, and the input-output relationships in the data might not be represented accurately. If the number of HN is too high, overfitting might occur. In this case, the model can learn the data

noise or “memorize” the training data, and the error on the test data, which is not used during training, typically begins to rise [31,47]. In Figure 7, two error measures, namely, the mean squared error (Figure 7a) and the mean relative error (Figure 7b) are shown as a function of the number of HNs. It is observed that as the number of HNs increases, the prediction accuracy also increases, which can be attributed to the increasing number of parameters and model complexity. Additionally, in the evaluated range with up to 30 HNs, the error on the test data set also decreased with increasing complexity (Figure 7b), which indicates that overfitting was suppressed effectively. Another observation from this figure is that the error on the training and test data sets is of the same order of magnitude, which is also an indication of the successful avoidance of overfitting. We attribute this to the training algorithm based on Bayesian regularization, which has proven to be effective for this purpose [51,68–70].

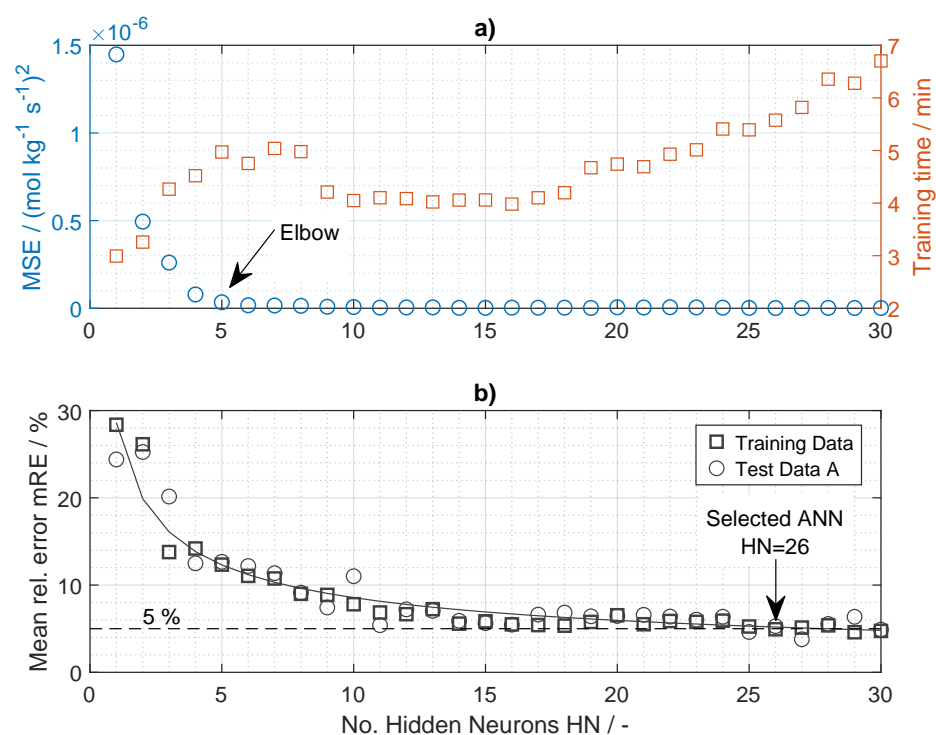


Figure 7. Training results for different architectures of the ANN-HM. (a) Mean squared error (MSE) and training time (b) mean relative error (mRE) on training and testing data sets.

Approaches for network selection include empirical correlations [71–73] or graphical methods. One approach is the elbow method, where a loss function, e.g., the mean squared error (MSE) between targets and model outputs is plotted against the number of hidden neurons, and the optimal network is determined based on the inflection point (elbow) of the curve [74]. According to this theory, the optimal number of HN is approx. 4 or 5 (see Figure 7a). On the other hand, the mean relative error of prediction (depicted in Figure 7b) shows that 5 HNs do not provide enough model complexity to achieve the targeted prediction accuracy. A $\text{mRE} \leq 5\%$ is achieved with networks with more than 25 HNs. Based on this and, most importantly, on the model performance regarding extrapolation (further discussion in Section 4.3) the ANN with 26 HN was chosen for the further analysis. A schematic representation of the resulting network as well as the model-specific parameters are provided in the Supplementary Material.

The time required to train 10,000 ANNs (with 100 schemes for the division of design data and 100 set of start parameter values as described in Section 3.2) is also plotted in Figure 7a. Overall, the training time increases with the number of parameters. However,

even at the highest number of parameters tested (with $HN = 30$), the training time remained below 7 min. Considering that the training of the data-based model and the parameter estimation for the lumped kinetic model required approximately 7.9 min and 3.5 h, respectively [51], the computational burden can be assessed as remarkably low, as expected from related studies [32,62,64].

4.2. Hybrid Model Performance and Interpolation Ability

After integration of the selected ANN-HM into the differential equation framework, the predictions of the hybrid model can be evaluated in comparison with the experimental values and the predictions of the other models. First, the successful implementation of the hybrid model is validated by comparison with experimental data. The mean relative error between the experiments and the predictions of the lumped and the hybrid model are shown in Table 3. The high similarity between the deviations of both models from experimental data is explained by the fact the ANN-HM was trained with reaction rates calculated with the lumped model, and shows the high level of accuracy obtained with the hybrid approach. Similarly to the computational burden, the accuracy of hybrid models has been previously investigated in related studies [62,64,75] which show, in agreement with our results, the remarkable performance of this model type.

Table 3. Mean relative errors (mRE) between the experiments and the predictions of the lumped and hybrid model.

Model	mRE $y_{H_2,out}$	mRE $y_{CO,out}$	mRE $y_{CO_2,out}$	mRE $y_{DME,out}$
Lumped	1.49%	5.49%	6.02%	28.89%
Hybrid	1.49%	5.45%	6.08%	28.36%

The interpolation ability of the hybrid model was also evaluated, and no difficulties were observed. This is shown for an exemplary feed gas composition in Figure 8 (further examples are given in the Supplementary Material). In this figure, the mole fractions of H_2 , CO, CO_2 and DME predicted with the hybrid model within the temperature and total gas flow ranges are shown. At increasing temperatures, the reaction rates also increase, leading to higher product concentration (DME and CO_2) and lower concentration of the educts CO and H_2 at the reactor outlet. Similarly, a decreasing total gas flow leads to longer residence times, which affects the outlet concentrations in the same way as increasing temperatures. These expected trends and also smooth gradients are observed over the response surfaces for all species. A further illustration of the interpolation ability of the hybrid model can be observed in Figures 11 and 12 between the dashed lines that represent the models' range of validity. In this range, the predictions of the hybrid and the lumped models are almost identical and the predictions of the data-based model are comparable to those of the other two models, but show a slightly better agreement with the experiments.

Another relevant feature between the different model types is the convergence time. To provide a quantitative comparison, simulations were conducted with the three models for all the operating points in the data base (on Windows 10 Pro (64-bit) operating system with i5 processor and 8GB RAM). The time required by each model to simulate the 180 operating points was:

- Data-Based: 0.0798 s;
- Hybrid: 4.2432 s;
- Lumped: 16.4095 s.

The superiority of the data-based model regarding the convergence time is obvious, and although the hybrid model is slower than the data-based one, the former is still approximately four times faster than the lumped model.

The convergence time is of special interest when the models are used for optimization purposes and large number of simulations have to be conducted to screen the state space.

A further characteristic relevant for optimization is the extrapolation ability of the models, which is evaluated in the following section.

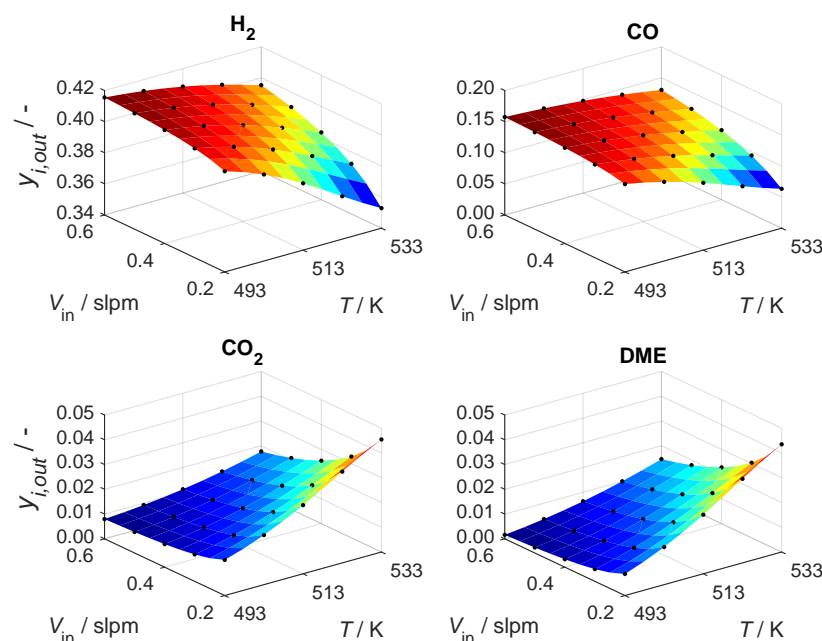


Figure 8. Surface response for the hybrid model predictions of the mole fractions of H_2 , CO , CO_2 , and DME within the validity range of the temperature and total gas flow. The black points represent the conditions at which the data for model development were measured. Feed composition: 42.33% H_2 , 16.14% CO , 0.82% CO_2 . Pressure 50 bar. CZA-to- γ - Al_2O_3 -ratio $\mu = 1$. ANN-HM with 26 HNs.

4.3. Models' Extrapolation Ability

The following sections are dedicated to the evaluation of the models' predictive ability outside the range of validity, i.e., the extrapolation ability. For this purpose, two types of extrapolation are evaluated—dimension and range extrapolation. Dimension extrapolation refers to the extrapolation of a variable that was kept constant during the experiments for model development. Range extrapolation, on the other hand, refers to the evaluation of a variable outside the range screened during these experiments [76]. The pressure and the catalyst bed composition are used here as exemplary variables to evaluate the dimension extrapolation (Section 4.3.1). Range extrapolation is analyzed based on the temperature in Section 4.3.2. Experimental values used for validation of the simulations at extrapolated conditions are reported in the Supplementary Material.

4.3.1. Dimension Extrapolation

Since all the experimental data used for the parametrization of the hybrid model were acquired at constant pressure and catalyst bed composition ($p = 50$ bar and CZA-to- γ - Al_2O_3 mass ratio $\mu = 1$), these variables are suitable for the evaluation of the hybrid model regarding dimension extrapolation.

The pressure was evaluated in a range between 40 and 60 bar by means of experiments and simulations. The data-based model was not used for this analysis since the structure of the ANN-DBM, which only takes the concentration of the syngas, the temperature and the total gas flow into account, does not allow simulations at other pressure levels (refer to ANN structure, Figure 3).

At 50 bar, the deviation between the experiments for model development and for validation show a very good agreement, with a maximal deviation of 4.5%. Furthermore, the validation experiments show the expected behavior, i.e., with increasing pressure, the product gas concentration of the educts decreases and that of the products increases (Figure 9). Due to the volume contraction of the methanol synthesis from CO_2 (Equation (6)),

the rate of this reaction is favored by high pressures. Hence, from the thermodynamic perspective, the pressure has always a positive effect on the overall process performance. This effect is reflected by the lumped model for all species in the entirety of the evaluated pressure range. The average deviations between the experiments and the predictions of the lumped model lie by 2.1% for H₂, 1.5% for CO, 6.9% for CO₂ and 12.6% for DME within the prediction accuracy of the model, confirming the high fidelity of the semi-mechanistic model approach. The concentration profiles obtained with the hybrid model, on the other hand, are nearly constant over all evaluated pressures at the value predicted for 50 bar. Similar to the ANN-DBM, the structure of the ANN-HM does not allow the variation of the pressure (Figure 5) since all the training data was measured at only one pressure level. Thus, the pressure dependency of the reaction rates is not considered by the hybrid model and dimension extrapolation regarding this variable is not possible.

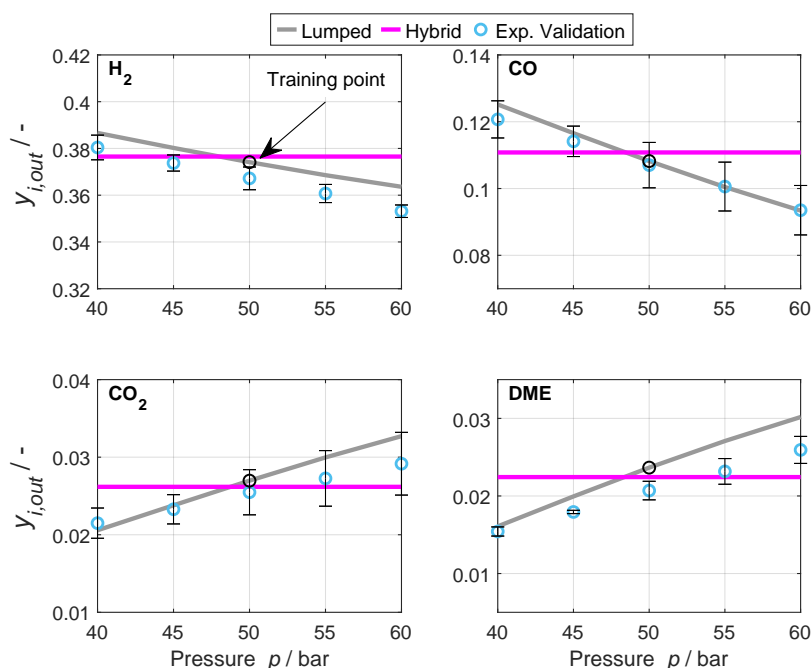


Figure 9. Experimental validation of dimensional extrapolation of the pressure. Feed composition: 42.3% H₂, 16.1% CO, 0.82% CO₂. Total gas flow 0.4 slpm. Temperature 533 K. CZA-to- γ -Al₂O₃-ratio $\mu = 1$. ANN-HM with 26 HNs.

The catalyst bed composition μ is also suitable for testing the dimension extrapolation of the hybrid model, since all the experiments for model development were measured with $\mu = 1$. Unlike the pressure, μ does not have a direct influence on the reaction rates, and hence extrapolating this variable does not imply the extrapolation of the ANN-HM. Therefore, better extrapolation results are expected. For this analysis, μ was varied from 0 to 5 and simulations with the lumped and hybrid model were conducted. Representative results are shown in Figure 10.

With the lumped model, an increasing conversion of CO_x and yield of DME with increasing μ is predicted, and the values at the highest μ display a high proximity to the values at equilibrium. This behavior is attributed to the synergy of the direct synthesis, where the equilibrium of the methanol synthesis is shifted towards the products by methanol consumption through the dehydration to DME. With an increasing μ , methanol is produced faster, which boosts the methanol dehydration reaction and overcompensates for the decreased amount of dehydration catalyst [15].

The conversion and yield predicted by the selected hybrid model (ANN-HM with 26 HN) show a remarkably good agreement with the predictions of the lumped kinetic model over the entirety of the extrapolated range. The predictions of the lumped and the

hybrid model overlap from μ up to 1, and proceed with a very similar trend. Although the deviation between the models' predictions increases as the distance from the training point $\mu = 1$ becomes larger, the predictions are thermodynamic consistent, and very similar over the whole evaluated range (e.g., at $\mu = 5$, $X_{\text{CO}_x} = 58.7$ and 55% with the lumped and the hybrid model, respectively).

The predictions of hybrid models with ANN-HM with 5 and 28 HNs are shown in Figure 10a,c to illustrate the importance of considering the model's extrapolation ability during the network selection. Both models displayed a relatively good performance on the training data in Section 4.1. This is also evident in Figure 10a,c, where the conversion and yield profiles predicted by all hybrid models overlap near the training point. However, the hybrid models with 5 and 28 HN clearly lack the ability to extrapolate. The predictions of these models do not follow the expected trend, nor do they respect the laws of thermodynamics. This illustrates one of the major drawbacks of data-based and/or hybrid approaches. Both models delivered a good performance on the training data and exhibited a good interpolation ability. However, it is not possible to predict the quality of the forecasts beyond the range where these models were trained, since the predictions at extrapolated conditions (especially regarding dimension extrapolation) are only dependent on the mathematical structure of the network, without an explainable phenomenological reason.

As mentioned in Section 3.3.2, different mesh refinements of the axial domain were tested during the generation of training data. Figure 10b,d show the CO_x conversion and DME yield at mesh refinements with 5, 10 and 15 axially distributed elements. Evidently, the mesh refinement with five elements does not provide enough data for training, leading to poor extrapolation capability of the hybrid model. With 15 elements, on the other hand, no relevant improvement of the network generalization is achieved and the predictions almost entirely overlap with those obtained with 10 axial elements. Similarly, no improvement was achieved with mesh refinements with 50 and 100 elements, however, the training time increased noticeably with the large number of data samples.

In this section, it was shown that the data-based models (ANN-DBM and ANN-HM) lack in extrapolation ability, while the hybrid model could be extrapolated successfully in a large range when the extrapolation variable was not in the data-based module of the hybrid structure and the extrapolation ability was taken into account during model development. This requires knowledge of the system and/or of the expected trends, and is only relevant if extrapolation is relevant for the aimed application of the hybrid model.

4.3.2. Range Extrapolation

Range extrapolation refers to the evaluation of a variable that was varied during model development, outside the range in which that variation occurred [76]. For the evaluation of this extrapolation case, experiments and simulations with the three models were conducted at temperatures between 453 and 573 K at two different total gas flow rates. Initially, the results at a total gas flow of 0.2 slpm are shown and discussed, followed by results at 0.6 slpm. The hybrid model with ANN-HM with 26 HNs was used here, as it was the only model that delivered good extrapolation ability for the catalyst bed composition. Equivalent results with other architectures of the ANN-HM are given in the Supplementary Material.

Figure 11 shows the predictions of the three models as well as the experiments used for model development (conducted in a previous work [15]) and validation for a total gas flow of 0.2 slpm. Additionally, the molar fractions at equilibrium calculated with the RGGibbs reactor in Aspen Plus are displayed, along with the models' validity range which is enclosed by the dashed lines.

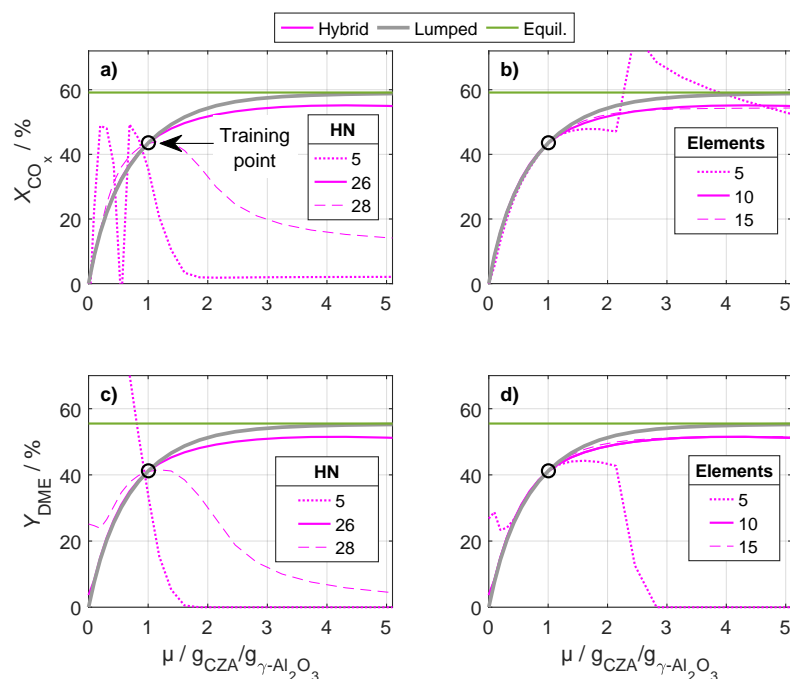


Figure 10. Dimension extrapolation of the catalyst bed composition. The plots show (a) the CO_x conversion calculated with the lumped model and with the hybrid models consisting of various HN, (b) the CO_x conversion at various mesh refinements, (c) the DME yield calculated with the lumped model and hybrid models consisting of various HN as well as (d) the DME yield at different mesh refinements. The results are plotted against μ , ranging from 0 to 5. Feed composition: 48.42% H_2 , 16.07% CO , 2.81% CO_2 . Total gas flow 0.2 slpm. Temperature 533 K. Pressure 50 bar.

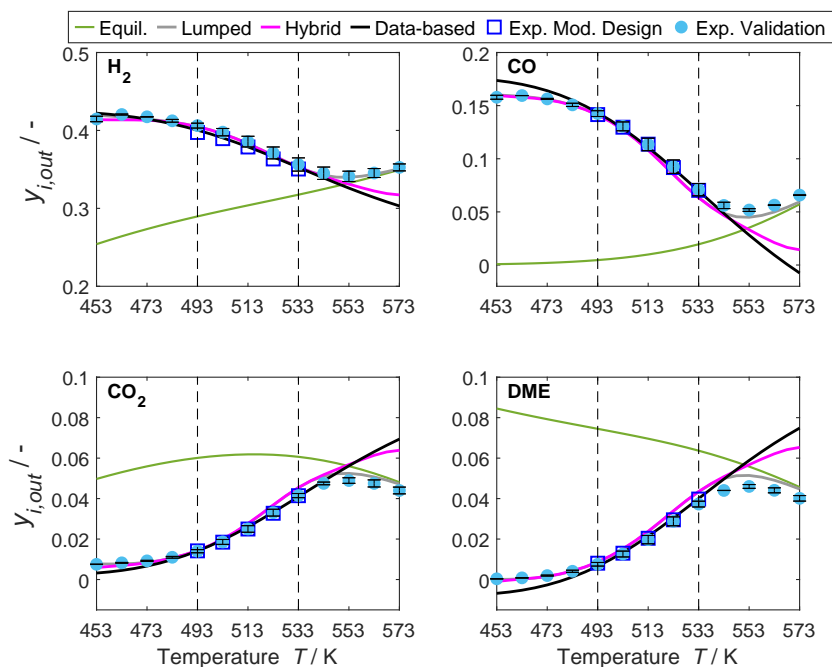


Figure 11. Evaluation of range extrapolation by comparison of models' predictions and experimental results beyond the models' validity range for temperature. Feed composition: 42.3% H_2 , 16.1% CO , 0.82% CO_2 . Total gas flow 0.2 slpm. Pressure 50 bar. CZA-to- $\gamma\text{-Al}_2\text{O}_3$ -ratio $\mu = 1$. ANN-HM with 26 HNs.

The experiments for experimental validation were conducted in the same reactor in which the kinetic measurements for model development were performed. Additionally, the same catalyst reduction and conditioning procedure were followed. As a result, the experiments from our previous work [15] could be verified, and the experiments in the temperature range between 493 and 533 K overlap with a low relative deviation of maximal 6.6% (max. mRE between experiments for model development and experiments for validation).

Bellow 493 K, the predictions of the hybrid and the lumped models are virtually identical. The predictions of the data-based model slightly differ, however, the correct and expected tendency is observable. At low temperatures, the rate of the reactions is low and almost no conversion takes place. Hence, the concentration of each species should be equal to the concentration in the feed gas, i.e., 42.3% H₂, 16.1% CO, 0.82% CO₂ and 0% DME. The hybrid model predicts this behavior correctly and the predictions do not deviate from those of the lumped model, although the model was not explicitly trained in this range. This can be explained by the fact that the phenomena that play a significant role in this temperature range are the same as in the range where the model was trained. The influence of the thermodynamic equilibrium is low compared to that of the reaction kinetics as it can be inferred from the distance to the values in equilibrium. Similarly, *a priori* criteria confirmed that no mass or heat transport limitations take place (refer to ESI). Hence, it can be concluded that, although the rate of reactions is low, the reaction kinetics control the process performance also in this temperature range and the performance can be described correctly by the hybrid model which was trained to predict this phenomenon. In addition, the hybrid model yields physically reasonable results and the predicted concentrations remain above 0 for all conditions, unlike the predictions of the data-based model, which also assume negative values.

Above 533 K, the predictions of the three models diverge. At increasing temperature levels, the influence of the thermodynamic equilibrium also increases, as the concentrations become closer to those at equilibrium. The rates of reversible exothermic reactions increase initially due to the positive influence of the temperature, but decrease at the proximity of the thermodynamic equilibrium when the back-reaction is favored. At the temperature at which thermodynamics prevails over reaction kinetics, an inflection point occurs, as can be clearly observed in the predictions of the lumped model (gray lines). The concentration of the educts, in this case CO and H₂, then rises and that of the products DME and CO₂ decreases as the reaction rates decrease. This can be predicted by the lumped model successfully due to the Hougen–Watson formulation of the rate expressions (Equations (9)–(11)), which accounts for the effect of the proximity to the thermodynamic equilibrium on the rates by the means of the equilibrium constants ($K_{f,j}$). The predictions of the data-based model do not show any inflection point and the concentration profiles follow the same trend as in the range of validity. This indicates that the data-based model only reflects the effect of the temperature on the reaction rate, but not the effect of the proximity to the thermodynamic equilibrium. In this temperature range, the hybrid model predictions lie between the predictions of the data-based and the lumped model in all cases. The molar fraction profiles flatten with increasing temperature, but a clear inflection point is not evident in the evaluated range. Unlike the lumped model, the hybrid approach attains knowledge about phenomena affecting the reaction rates only from data. Hence, since most operational points in the training data set were measured at conditions at which reaction kinetics prevail and thermodynamic equilibrium has a negligible effect, the hybrid model does not have enough information about the effects the equilibrium can have on the rates and on the process performance. The measured values at temperatures above 533 K showed that the lumped model exhibits the highest accuracy, especially in terms of the shape of the curve with a clearly visible inflection point.

Equivalent results measured or simulated are shown in Figure 12 for a total gas flow of 0.6 slpm. The residence time for this gas low rate is shorter than at 0.2 slpm, and lower conversions are attained. Therefore, the distance to thermodynamic equilibrium is larger

which, according to the discussion above, leads to the observed higher prediction accuracy. At this gas flow rate, the simulations of the three models are very similar in the whole temperature range. A slight difference is noticed at temperatures above 553 K, where the predictions of the data-based model diverge. However, the predictions of the lumped and the hybrid model remain superimposed with a maximal relative deviation of 3% (computed for CO₂ at 573 K). This confirms that the reason for the model discrepancy is the influence of the thermodynamic equilibrium which becomes more relevant at higher temperatures, and indicates that the extrapolation limits of data-based and hybrid models do not strictly depend on the evaluated range of conditions, but more on the effects considered by the underlying models.

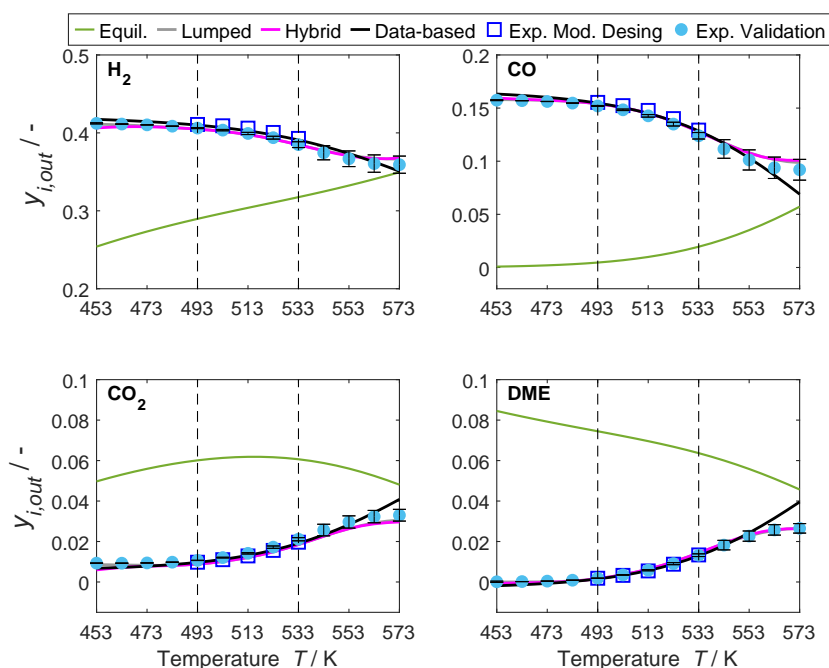


Figure 12. Evaluation of range extrapolation by comparison of models' predictions and experimental results beyond the models' validity range for temperature. Feed composition: 42.3% H₂, 16.1% CO, 0.82% CO₂. Total gas flow 0.6 slpm. Pressure 50 bar. CZA-to- γ -Al₂O₃-ratio $\mu = 1$. ANN-HM with 26 HNs. Predictions of the lumped and hybrid model overlap over the entire temperature range.

5. Summary and Conclusions

The first part of this work provides a timely overview of the models available for the direct DME synthesis. It has been shown that most of the available models for the direct DME synthesis are semi-mechanistic, i.e., based on mechanistic assumptions. Since these models are only valid in a limited operational range, special attention was paid to the validity of each of the semi-mechanistic models, which were compared graphically to enable a fast overview of the investigated ranges in each work. Additionally, works where data-based models were used for the direct DME synthesis have been summarized. No hybrid model could be found in the open literature for this system.

The second part of this paper deals with the implementation and evaluation of a hybrid model for the direct DME synthesis, aiming to identify and evaluate specific advantages and disadvantages of hybrid modeling approaches for this system. The developed hybrid model displayed a high level of accuracy and good interpolation ability over the entirety of the validity range. Additionally, it exhibited a low computational burden, e.g., the training of this model was approximately 30 times faster than the parametrization of a lumped model, and simulations compiled almost 4 times faster on the same CPU. These results are broadly consistent with studies in the open literature and confirmed expected outcomes regarding accuracy and computational effort.

As one of the main concerns about hybrid models, the extrapolation ability has been put to test and the predictions of a semi-mechanistic and a data-based model, as well as experiments, have been used for the evaluation of the hybrid model performance. Based on exemplary variables (pressure, catalyst bed composition and temperature), it has been shown that dimension extrapolation, i.e., extrapolation of a variable that was kept constant during model development, was not possible when this variable directly affects the data-based module of the hybrid model. For example, simulations and experiments show that the effect of the pressure on the reaction rates could not be considered by the ANN, which was trained at one pressure level only. In contrast, a good extrapolation ability in a broad range was achieved when the extrapolated variable was in the knowledge-module of the hybrid model. As an example, it is shown that the extrapolation of the CZA-to- γ -Al₂O₃ weight ratio was possible and delivered qualitatively accurate results in the broad range between ratios of zero to five, although all experiments used for model development were conducted with a ratio of one. A suitable ANN architecture proved to be essential for the accuracy of predictions at extrapolated conditions. Range extrapolation, i.e., the evaluation of a variable outside the range where it was screened during model development, was possible, although in a limited range. It could be concluded that the limit for extrapolation is defined by the phenomena the underlying models can map, which depends strongly on the network architecture, instead of the range defined by conditions evaluated experimentally during model development.

Since there is currently no theoretical framework for network selection, and broadly used rules of thumbs failed to deliver a suitable network in our study, the best network was chosen manually based on simulations results. Clearly, this represents a major drawback when a large number of network architectures must be tested, which limits the transferability of the presented results. Based on the gained insights, we conclude that the hybrid modeling approach could be best applied when large data sets in wide operational windows are available, and the input–output relationships between the data are not yet fully understood. This way, the advantages of the hybrid model (i.e., high accuracy and low computation effort) could be exploited to fill knowledge gaps, while avoiding extrapolation. Specifically for direct DME synthesis, one application with high potential for immediate use is to expand the model scope using the numerous lumped kinetic models available in the literature. These are valid in different operating windows and can be used to generate reaction kinetics data, analogous to the procedure followed in this work. After the training of ANNs with these data and integration of these ANNs in the hybrid model structure, the expected outcome is a model that enables cross-evaluation of multiple process variables such as different catalysts, reactor types and reaction conditions throughout nearly the entire relevant operating window.

Supplementary Materials: The following are available online at <https://www.mdpi.com/article/10.3390/catal12030347/s1>, Figure S1: Schematic representation of the ANN-HM. Figure S2: Surface response for the hybrid model predictions of the mole fractions of H₂, CO, CO₂ and DME within the validity range of the temperature and total gas flow. Feed composition: 48.0% H₂, 16.11% CO, 2.88% CO₂. Pressure 50 bar. CZA-to- γ -Al₂O₃-ratio $\mu = 1$. ANN-HM with 26 HNs. Figure S3: Surface response for the hybrid model predictions of the mole fractions of H₂, CO, CO₂ and DME within the validity range of the temperature and total gas flow. Feed composition: 13.05% H₂, 4.10% CO, 0.86% CO₂. Pressure 50 bar. CZA-to- γ -Al₂O₃-ratio $\mu = 1$. ANN-HM with 26 HNs. Figure S4: Range extrapolation of the temperature. Nominal feed composition: 42.3% H₂, 16.1% CO, 0.82% CO₂. Total gas flow 0.2 slpm. Pressure 50 bar. CZA-to- γ -Al₂O₃-ratio $\mu = 1$. ANN-HM with 5 HNs. Figure S5: Range extrapolation of the temperature. Nominal feed composition: 42.3% H₂, 16.1% CO, 0.82% CO₂. Total gas flow 0.6 slpm. Pressure 50 bar. CZA-to- γ -Al₂O₃-ratio $\mu = 1$. ANN-HM with 5 HNs. Figure S6: Range extrapolation of the temperature. Nominal feed composition: 42.3% H₂, 16.1% CO, 0.82% CO₂. Total gas flow 0.2 slpm. Pressure 50 bar. CZA-to- γ -Al₂O₃-ratio $\mu = 1$. ANN-HM with 28 HNs. Figure S7: Range extrapolation of the temperature. Nominal feed composition: 42.3% H₂, 16.1% CO, 0.82% CO₂. Total gas flow 0.6 slpm. Pressure 50 bar. CZA-to- γ -Al₂O₃-ratio $\mu = 1$. ANN-HM with 28 HNs. Figure S8: CO_x-conversion (X_{CO_x}) as a function of the Time-On-Stream (ToS) for a

reference operating point measured at 513 K, 50 bar and 7599.5 h^{-1} and a feed of 38.2% H_2 , 15.2% CO , 1.0% CO_2 , 45.7% N_2 . Table S1: Model specific parameters of the ANN-HM with 5 HNs. Connection weights of the input and hidden layer, biases of the hidden layer. Table S2: Model specific parameters of the ANN-HM with 5 HNs. Connection weights of the hidden and output layer, biases of the output layer. Table S3: Model specific parameters of the chosen ANN-HM with 26 HNs. Connection weights of the input and hidden layer, biases of the hidden layer. Table S4: Model specific parameters of the chosen ANN-HM with 26 HNs. Connection weights of the hidden and output layer, biases of the output layer. Table S5: Model specific parameters of the ANN-HM with 28 HNs. Connection weights of the input and hidden layer, biases of the hidden layer. Table S6: Model specific parameters of the ANN-HM with 28 HNs. Connection weights of the hidden and output layer, biases of the output layer. Table S7: Calculated a priori criteria for determination of transport limitations (Reference [77] are cited in Table S7). Table S8: Experimental values measured for validation of simulation results at extrapolated conditions. The catalyst bed consisted of 1.007 g CZA, 0.9996 g $\gamma\text{-Al}_2\text{O}_3$, 9.98 g SiC, and it was 7.8 cm long.

Author Contributions: Conceptualization, N.D.O., K.H.D. and J.S.; methodology, N.D.O.; software, N.D.O.; validation, N.D.O., P.G.B. and K.H.D.; formal analysis, N.D.O. and P.G.B.; investigation, N.D.O. and P.G.B.; resources, K.H.D., S.P. and J.S.; data curation, N.D.O. and P.G.B.; writing—original draft preparation, N.D.O.; writing—review and editing, N.D.O., P.G.B., K.H.D., S.P. and J.S.; visualization, N.D.O. and P.G.B.; supervision, K.H.D., S.P. and J.S.; project administration, K.H.D., S.P. and J.S.; funding acquisition, K.H.D., S.P. and J.S. All authors have read and agreed to the published version of the manuscript.

Funding: This research was funded by Helmholtz Association (Research Program “Storage and Cross-linked Infrastructures”, Topic “Synthetic Hydrocarbons”).

Institutional Review Board Statement: Not applicable.

Informed Consent Statement: Not applicable.

Data Availability Statement: Not applicable.

Acknowledgments: The authors would like to thank Siegbert Johnsen for the technical support, Linus Janning for valuable discussions and support, and Katharina Stoll for proofreading the manuscript.

Conflicts of Interest: The authors declare no conflict of interest. The funders had no role in the design of the study; in the collection, analyses, or interpretation of data; in the writing of the manuscript, or in the decision to publish the results.

References

1. Dahmen, N.; Arnold, U.; Djordjevic, N.; Henrich, T.; Kolb, T.; Leibold, H.; Sauer, J. High pressure in synthetic fuels production. *J. Supercrit. Fluids* **2015**, *96*, 124–132. [CrossRef]
2. Niethammer, B.; Wodarz, S.; Betz, M.; Haltenort, P.; Oestreich, D.; Hackbarth, K.; Arnold, U.; Otto, T.; Sauer, J. Alternative Liquid Fuels from Renewable Resources. *Chem. Ing. Tech.* **2018**, *90*, 99–112. [CrossRef]
3. Semelsberger, T.A.; Borup, R.L.; Greene, H.L. Dimethyl ether (DME) as an alternative fuel. *J. Power Sources* **2006**, *156*, 497–511. [CrossRef]
4. Azizi, Z.; Rezaeimanesh, M.; Tohidian, T.; Rahimpour, M.R. Dimethyl ether: A review of technologies and production challenges. *Chem. Eng. Process. Process Intensif.* **2014**, *82*, 150–172. [CrossRef]
5. Zhu, Y.; Wang, S.; Ge, X.; Liu, Q.; Luo, Z.; Cen, K. Experimental study of improved two step synthesis for DME production. *Fuel Process. Technol.* **2010**, *91*, 424–429. [CrossRef]
6. Polierer, S.; Guse, D.; Wild, S.; Herrera Delgado, K.; Otto, T.N.; Zevaco, T.A.; Kind, M.; Sauer, J.; Studt, F.; Pitter, S. Enhanced Direct Dimethyl Ether Synthesis from CO_2 -Rich Syngas with Cu/ZnO/ZrO₂ Catalysts Prepared by Continuous Co-Precipitation. *Catalysts* **2020**, *10*, 816. [CrossRef]
7. Joint News Release: BASF and Lutianhua Plan to Pilot a New Production Process that Significantly Reduces CO_2 Emissions. 2019. Available online: <https://www.basf.com/global/en/media/news-releases/2019/06/p-19-249.html> (accessed on 1 April 2021).
8. Wang, Z.; He, T.; Li, J.; Wu, J.; Qin, J.; Liu, G.; Han, D.; Zi, Z.; Li, Z.; Wu, J. Design and operation of a pilot plant for biomass to liquid fuels by integrating gasification, DME synthesis and DME to gasoline. *Fuel* **2016**, *186*, 587–596. [CrossRef]
9. Park, J.; Kim, H.S.; Lee, W.B.; Park, M.J. Trends and Outlook of Computational Chemistry and Microkinetic Modeling for Catalytic Synthesis of Methanol and DME. *Catalysts* **2020**, *10*, 655. [CrossRef]
10. Grunwaldt, J.D.; Molenbroek, A.M.; Topsøe, N.Y.; Topsøe, H.; Clausen, B.S. In situ investigations of structural changes in Cu/ZnO catalysts. *J. Catal.* **2000**, *194*, 452–460. [CrossRef]

11. Gaikwad, R.; Reymond, H.; Phongprueksathat, N.; Rudolf von Rohr, P.; Urakawa, A. From CO or CO₂?: Space-resolved insights into high-pressure CO₂ hydrogenation to methanol over Cu/ZnO/Al₂O₃. *Catal. Sci. Technol.* **2020**, *10*, 2763–2768. [CrossRef]
12. Martin, O.; Mondelli, C.; Cervellino, A.; Ferri, D.; Curulla-Ferré, D.; Pérez-Ramírez, J. Operando Synchrotron X-ray Powder Diffraction and Modulated-Excitation Infrared Spectroscopy Elucidate the CO₂ Promotion on a Commercial Methanol Synthesis Catalyst. *Angew. Chem. Int. Ed.* **2016**, *55*, 11031–11036. [CrossRef] [PubMed]
13. Miletto, I.; Catizzone, E.; Bonura, G.; Ivaldi, C.; Migliori, M.; Gianotti, E.; Marchese, L.; Frusteri, F.; Giordano, G. In situ FT-IR characterization of CuZnZr/ferrierite hybrid catalysts for one-pot CO₂-to-DME conversion. *Materials* **2018**, *11*, 2275. [CrossRef] [PubMed]
14. Chen, W.H.; Hsu, C.L.; Wang, X.D. Thermodynamic approach and comparison of two-step and single step DME (dimethyl ether) syntheses with carbon dioxide utilization. *Energy* **2016**, *109*, 326–340. [CrossRef]
15. Delgado Otalvaro, N.; Kaiser, M.; Herrera Delgado, K.; Wild, S.; Sauer, J.; Freund, H. Optimization of the direct synthesis of dimethyl ether from CO₂ rich synthesis gas: Closing the loop between experimental investigations and model-based reactor design. *React. Chem. Eng.* **2020**, *5*, 949–960. [CrossRef]
16. Peláez, R.; Marín, P.; Ordóñez, S. Direct synthesis of dimethyl ether from syngas over mechanical mixtures of CuO/ZnO/Al₂O₃ and Γ -Al₂O₃: Process optimization and kinetic modelling. *Fuel Process. Technol.* **2017**, *168*, 40–49. [CrossRef]
17. Delgado Otalvaro, N.; Sogne, G.; Herrera Delgado, K.; Wild, S.; Pitter, S.; Sauer, J. Kinetics of the direct DME synthesis from CO₂ rich syngas under variation of the CZA-to- γ -Al₂O₃ ratio of a mixed catalyst bed. *RSC Adv.* **2021**, *11*, 24556–24569. [CrossRef]
18. Ereña, J.; Sierra, I.; Aguayo, A.T.; Ateka, A.; Olazar, M.; Bilbao, J. Kinetic modelling of dimethyl ether synthesis from (H₂+CO₂) by considering catalyst deactivation. *Chem. Eng. J.* **2011**, *174*, 660–667. [CrossRef]
19. Cheng, C.; Zhang, H.; Ying, W.; Fang, D. Intrinsic kinetics of one-step dimethyl ether synthesis from hydrogen-rich synthesis gas over bi-functional catalyst. *Korean J. Chem. Eng.* **2011**, *28*, 1511–1517. [CrossRef]
20. Sierra, I.; Ereña, J.; Aguayo, A.T.; Olazar, M.; Bilbao, J. Deactivation kinetics for direct dimethyl ether synthesis on a CuO-ZnO-Al₂O₃/ γ -Al₂O₃ Catalyst. *Ind. Eng. Chem. Res.* **2010**, *49*, 481–489. [CrossRef]
21. Pyatnitskii, Y.I.; Strizhak, P.E.; Lunev, N.K. Kinetic modeling for the conversion of synthesis gas to dimethyl ether on a mixed Cu-ZnO-Al₂O₃ catalyst with γ -Al₂O₃. *Theor. Exp. Chem.* **2009**, *45*, 325–330. [CrossRef]
22. Renk, C.P. Die Einstufige Dimethylether-Synthese aus Synthesegas: Experimentelle und Theoretische Betrachtungen zur Einstufigen DME-Synthese mit Synthesegas aus der Flugstrom-Druckvergasung von Biomasse. Ph.D. Thesis, 2009. Available online: <https://publikationen.bibliothek.kit.edu/1000012461/3815570> (accessed on 31 October 2009).
23. Hadipour, A.; Sohrabi, M. Synthesis of some bifunctional catalysts and determination of kinetic parameters for direct conversion of syngas to dimethyl ether. *Chem. Eng. J.* **2008**, *137*, 294–301. [CrossRef]
24. Aguayo, A.T.; Ereña, J.; Mier, D.; Arandes, J.M.; Olazar, M.; Bilbao, J. Kinetic Modeling of Dimethyl Ether Synthesis in a Single Step on a CuO/ZnO/Al₂O₃/ Γ -Al₂O₃ Catalyst. *Ind. Eng. Chem. Res.* **2007**, *46*, 5522–5530. [CrossRef]
25. Nie, Z.; Liu, H.; Liu, D.; Ying, W.; Fang, D. Intrinsic kinetics of dimethyl ether synthesis from syngas. *J. Nat. Gas Chem.* **2005**, *14*, 22–28. [CrossRef]
26. Ng, K.L.; Chadwick, D.; Toseland, B.A. Kinetics and modelling of dimethyl ether synthesis from synthesis gas. *Chem. Eng. Sci.* **1999**, *54*, 3587–3592. [CrossRef]
27. Strieth-Kalthoff, F.; Sandfort, F.; Segler, M.H.S.; Glorius, F. Machine learning the ropes: Principles, applications and directions in synthetic chemistry. *Chem. Soc. Rev.* **2020**, *49*, 6154–6168. [CrossRef]
28. Jha, S.K.; Bilalovic, J.; Jha, A.; Patel, N.; Zhang, H. Renewable energy: Present research and future scope of Artificial Intelligence. *Renew. Sustain. Energy Rev.* **2017**, *77*, 297–317. [CrossRef]
29. Li, H.; Zhang, Z.; Liu, Z. Application of Artificial Neural Networks for Catalysis: A Review. *Catalysts* **2017**, *7*, 306. [CrossRef]
30. Goncalves, V.; Maria, K.; da Silv, A.B.F. Applications of Artificial Neural Networks in Chemical Problems. In *Artificial Neural Networks—Architectures and Applications*; Suzuki, K., Ed.; InTech: London, UK, 2013; Chapter 10, pp. 203–223. [CrossRef]
31. Basheer, I.; Hajmeer, M. Artificial neural networks: Fundamentals, computing, design, and application. *J. Microbiol. Methods* **2000**, *43*, 3–31. [CrossRef]
32. Zendejboudi, S.; Rezaei, N.; Lohi, A. Applications of hybrid models in chemical, petroleum, and energy systems: A systematic review. *Appl. Energy* **2018**, *228*, 2539–2566. [CrossRef]
33. Sansana, J.; Joswiak, M.N.; Castillo, I.; Wang, Z.; Rendall, R.; Chiang, L.H.; Reis, M.S. Recent trends on hybrid modeling for Industry 4.0. *Comput. Chem. Eng.* **2021**, *151*, 107365. [CrossRef]
34. Hein, J.E. Machine learning made easy for optimizing chemical reactions. *Nature* **2021**, *590*, 40–41. [CrossRef] [PubMed]
35. von Stosch, M.; Oliveira, R.; Peres, J.; Feyo de Azevedo, S. Hybrid semi-parametric modeling in process systems engineering: Past, present and future. *Comput. Chem. Eng.* **2014**, *60*, 86–101. [CrossRef]
36. McBride, K.; Sundmacher, K. Overview of Surrogate Modeling in Chemical Process Engineering. *Chem. Ing. Tech.* **2019**, *91*, 228–239. [CrossRef]
37. Chen, L.; Hontoir, Y.; Huang, D.; Zhang, J.; Morris, A. Combining first principles with black-box techniques for reaction systems. *Control Eng. Pract.* **2004**, *12*, 819–826. [CrossRef]
38. Mondal, U.; Yadav, G.D. Perspective of dimethyl ether as fuel: Part I. Catalysis. *J. CO₂ Util.* **2019**, *32*, 299–320. [CrossRef]
39. Behr, A.; Agar, D.W.; Jörissen, J.; Vorholt, A.J. *Einführung in Die Technische Chemie*, 2nd ed.; Springer: Berlin, Germany, 2016.

40. Aguayo, A.T.; Ereña, J.; Sierra, I.; Olazar, M.; Bilbao, J. Deactivation and regeneration of hybrid catalysts in the single-step synthesis of dimethyl ether from syngas and CO₂. *Catal. Today* **2005**, *106*, 265–270. [[CrossRef](#)]
41. Ateka, A.; Pérez-Uriarte, P.; Gamero, M.; Ereña, J.; Aguayo, A.T.; Bilbao, J. A comparative thermodynamic study on the CO₂ conversion in the synthesis of methanol and of DME. *Energy* **2017**, *120*, 796–804. [[CrossRef](#)]
42. Luu, M.T.; Milani, D.; Wake, M.; Abbas, A. Analysis of di-methyl ether production routes: Process performance evaluations at various syngas compositions. *Chem. Eng. Sci.* **2016**, *149*, 143–155. [[CrossRef](#)]
43. Catizzone, E.; Bonura, G.; Migliori, M.; Frusteri, F.; Giordano, G. CO₂ Recycling to Dimethyl Ether: State-of-the-Art and Perspectives. *Molecules* **2017**, *23*, 31. [[CrossRef](#)]
44. Nestler, F.; Krüger, M.; Full, J.; Hadrich, M.J.; White, R.J.; Schaadt, A. Methanol Synthesis—Industrial Challenges within a Changing Raw Material Landscape. *Chem. Ing. Tech.* **2018**, *90*, 1409–1418. [[CrossRef](#)]
45. Centi, G.; Perathoner, S. Opportunities and prospects in the chemical recycling of carbon dioxide to fuels. *Catal. Today* **2009**, *148*, 191–205. [[CrossRef](#)]
46. Dalena, F.; Senatore, A.; Marino, A.; Gordano, A.; Basile, M.; Basile, A. Methanol Production and Applications: An Overview. In *Methanol*; Elsevier: Amsterdam, The Netherlands, 2018; pp. 3–28. [[CrossRef](#)]
47. Mohd Ali, J.; Hussain, M.A.; Tade, M.O.; Zhang, J. Artificial Intelligence techniques applied as estimator in chemical process systems—A literature survey. *Expert Syst. Appl.* **2015**, *42*, 5915–5931. [[CrossRef](#)]
48. Panerati, J.; Schnellmann, M.A.; Patience, C.; Beltrame, G.; Patience, G.S. Experimental methods in chemical engineering: Artificial neural networks—ANNs. *Can. J. Chem. Eng.* **2019**, *97*, 2372–2382. [[CrossRef](#)]
49. Cybenko, G. Mathematics of Control, Signals, and Systems Approximation by Superpositions of a Sigmoidal Function. *Math. Control Signals Syst.* **1989**, *2*, 303–314. [[CrossRef](#)]
50. Hornik, K.; Stinchcombe, M.; White, H. Multilayer Feedforward Networks are Universal Approximators. *Neural Netw.* **1989**, *2*, 359–366. [[CrossRef](#)]
51. Delgado Ojalvario, N.; Bilir, P.G.; Herrera Delgado, K.; Pitter, S.; Sauer, J. Modeling the Direct Synthesis of Dimethyl Ether using Artificial Neural Networks. *Chem. Ing. Tech.* **2021**, *93*, 754–761. [[CrossRef](#)]
52. Moradi, G.R.; Parvizian, F. An expert model for estimation of the performance of direct dimethyl ether synthesis from synthesis gas. *Can. J. Chem. Eng.* **2011**, *89*, 1266–1273. [[CrossRef](#)]
53. Alamolhoda, S.; Kazemeini, M.; Zaherian, A.; Zakerinasab, M.R. Reaction kinetics determination and neural networks modeling of methanol dehydration over nano γ -Al₂O₃ catalyst. *J. Ind. Eng. Chem.* **2012**, *18*, 2059–2068. [[CrossRef](#)]
54. Blanco, M.; Coello, J.; Iturriaga, H.; Maspocho, S.; Redón, M. Artificial Neural Networks for Multicomponent Kinetic Determinations. *Anal. Chem.* **1995**, *67*, 4477–4483. [[CrossRef](#)]
55. Omata, K.; Ozaki, T.; Umegaki, T.; Watanabe, Y.; Nukui, N.; Yamada, M. Optimization of the temperature profile of a temperature gradient reactor for DME synthesis using a simple genetic algorithm assisted by a neural network. *Energy Fuels* **2003**, *17*, 836–841. [[CrossRef](#)]
56. Omata, K.; Hashimoto, M.; Sutarto; Yamada, M. Artificial neural network and grid search aided optimization of temperature profile of temperature gradient reactor for dimethyl ether synthesis from syngas. *Ind. Eng. Chem. Res.* **2009**, *48*, 844–849. [[CrossRef](#)]
57. Omata, K.; Sutarto; Hashimoto, M.; Ishiguro, G.; Watanabe, Y.; Umegaki, T.; Yamada, M. Design and development of Cu-Zn oxide catalyst for direct dimethyl ether synthesis using an artificial neural network and physicochemical properties of elements. *Ind. Eng. Chem. Res.* **2006**, *45*, 4905–4910. [[CrossRef](#)]
58. Svitnic, T.; Do, N.T.Q.; Schuhmann, T.; Renner, T.; Haag, S.; Örs, E. Data-driven approach for predictive modeling of by-product formation in methanol synthesis. In Proceedings of the 30th European Symposium on Computer Aided Process Engineering, Milan, Italy, 24–27 May 2020; pp. 505–510. [[CrossRef](#)]
59. Valeh-E-Sheyda, P.; Yaripour, F.; Moradi, G.; Saber, M. Application of artificial neural networks for estimation of the reaction rate in methanol dehydration. *Ind. Eng. Chem. Res.* **2010**, *49*, 4620–4626. [[CrossRef](#)]
60. Ye, J. Artificial neural network modeling of methanol production from syngas. *Pet. Sci. Technol.* **2019**, *37*, 629–632. [[CrossRef](#)]
61. Din, I.U.; Shaharun, M.S.; Naeem, A.; Alotaibi, M.A.; Alharthi, A.I.; Nasir, Q. CO₂ Conversion to Methanol over Novel Carbon Nanofiber-Based Cu/ZrO₂ Catalysts—A Kinetics Study. *Catalysts* **2020**, *10*, 567. [[CrossRef](#)]
62. Zahedi, G.; Elkamel, A.; Lohi, A.; Jahanmiri, A.; Rahimpor, M.R. Hybrid artificial neural network—First principle model formulation for the unsteady state simulation and analysis of a packed bed reactor for CO₂ hydrogenation to methanol. *Chem. Eng. J.* **2005**, *115*, 113–120. [[CrossRef](#)]
63. Potočník, P.; Grabec, I.; Šetinc, M.; Levec, J. Neural net based hybrid modeling of the methanol synthesis process. *Neural Process. Lett.* **2000**, *11*, 219–228. [[CrossRef](#)]
64. Alavi, M.; Jazayeri-Rad, H.; Behbahani, R.M. Optimizing the Feed Conditions in a Dimethyl Ether Production Process To Maximize Methanol Conversion Using a Hybrid First Principle Neural Network Approach. *Chem. Eng. Commun.* **2014**, *201*, 650–673. [[CrossRef](#)]
65. Peng, D.Y.; Robinson, D.B. A new two-constant equation of state. *Ind. Eng. Chem. Fundam.* **1976**, *15*, 59–64. [[CrossRef](#)]
66. Lu, W.Z.; Teng, L.H.; Xiao, W.D. Simulation and experiment study of dimethyl ether synthesis from syngas in a fluidized-bed reactor. *Chem. Eng. Sci.* **2004**, *59*, 5455–5464. [[CrossRef](#)]

67. Hameed, A.A.; Karlik, B.; Salman, M.S. Back-propagation algorithm with variable adaptive momentum. *Knowl.-Based Syst.* **2016**, *114*, 79–87. [[CrossRef](#)]
68. MacKay, D.J.C. Bayesian Interpolation. *Neural Comput.* **1992**, *4*, 415–447. [[CrossRef](#)]
69. Okut, H. Bayesian Regularized Neural Networks for Small n Big p Data. In *Artificial Neural Networks—Models and Applications*; InTech: London, UK, 2016; Chapter 2. [[CrossRef](#)]
70. Burden, F.; Winkler, D. Bayesian Regularization of Neural Networks. *Methods Mol. Biol.* **2009**, *458*, 23–42. [[CrossRef](#)]
71. Kalogirou, S.A.; Bojic, M. Artificial neural networks for the prediction of the energy consumption of a passive solar building. *Energy* **2000**, *25*, 479–491. [[CrossRef](#)]
72. Lachtermacher, G.; Fuller, J.D. Back propagation in time-series forecasting. *J. Forecast.* **1995**, *14*, 381–393. [[CrossRef](#)]
73. Jadid, M.N.; Fairbairn, D.R. Neural-network applications in predicting moment-curvature parameters from experimental data. *Eng. Appl. Artif. Intell.* **1996**, *9*, 309–319. [[CrossRef](#)]
74. Amato, F.; González-Hernández, J.L.; Havel, J. Artificial neural networks combined with experimental design: A “soft” approach for chemical kinetics. *Talanta* **2012**, *93*, 72–78. [[CrossRef](#)]
75. Zahedi, G.; Lohi, A.; Mahdi, K. Hybrid modeling of ethylene to ethylene oxide heterogeneous reactor. *Fuel Process. Technol.* **2011**, *92*, 1725–1732. [[CrossRef](#)]
76. Van Can, H.J.L.; Te Braake, H.A.B.; Dubbelman, S.; Hellinga, C.; Luyben, K.C.A.M.; Heijnen, J.J. Understanding and applying the extrapolation properties of serial gray-box models. *AIChE J.* **1998**, *44*, 1071–1089. [[CrossRef](#)]
77. Pérez-Ramírez, J.; Berger, R.J.; Mul, G.; Kapteijn, F.; Moulijn, J.A. Six-flow reactor technology a review on fast catalyst screening and kinetic studies. *Catal. Today* **2000**, *60*, 93–109. [[CrossRef](#)]

Supplementary Materials: Kinetics of the direct DME synthesis: state of the art and comprehensive comparison of semi-mechanistic, data-based and hybrid modeling approaches

Nirvana Delgado Otalvaro ¹, Pembe Gül Bilir ¹, Karla Herrera Delgado ^{1*}, Stephan Pitter ¹ and Jörg Sauer ¹

1. Model specific parameters of the ANN-HM

The model specific parameters of the ANN-HMs discussed in the manuscript (ANN-HM with 5, 26 and 28 HNs) are given in this section. Specifically, these are the connection weights between the input and the hidden layer ($W_{i,h}$) and between the hidden and the output layer ($W_{h,o}$), as well as the biases of the hidden and outputs neurons (b_h and b_o) as shown in Figure S1.

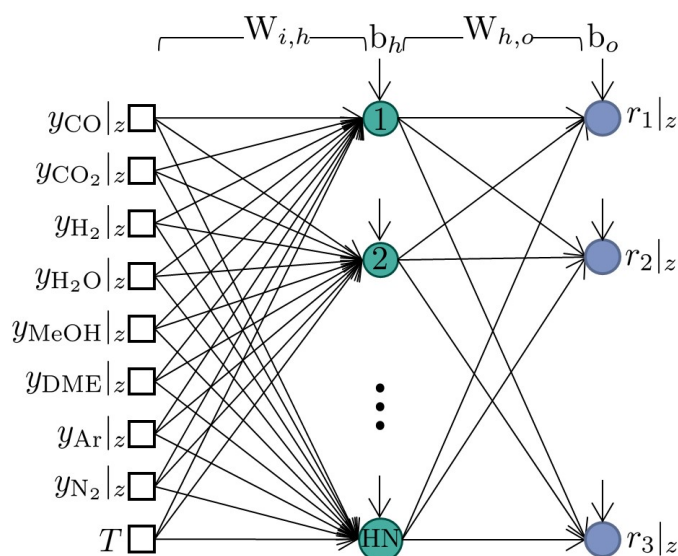


Figure S1. Schematic representation of the ANN-HM.

Table 1: Model specific parameters of the ANN-HM with 5 HNs. Connection weights of the input and hidden layer, biases of the hidden layer.

$W_{i,h}$										b_h
-0.60114	0.14025	-0.63213	0.80736	0.08968	-0.04125	-0.27108	0.00641	-0.43090		3.10519
-1.14673	0.65526	1.31330	1.05803	0.01463	-0.00635	-0.26234	0.05774	-0.44970		3.95600
-3.02931	-0.02462	-3.53521	0.79813	0.04093	19.72959	-3.39553	-0.23304	-1.22452		20.09301
3.98021	-5.89989	0.18136	-1.04395	-0.77207	-0.14084	0.37947	0.21915	0.88733		-7.69831
2.60925	0.85926	2.62343	0.47530	-1.60951	-18.55797	3.14491	0.16885	1.05177		-19.56385

Table 2: Model specific parameters of the ANN-HM with 5 HNs. Connection weights of the hidden and output layer, biases of the output layer.

$W_{h,o}^{-1}$			b_o
-14.986096	-16.498396	-14.484296	2.8317
4.86557018	5.96789325	4.68863279	10.1015
6.23236401	-0.5675959	-0.8749624	10.0811
-11.948762	-13.012473	-11.014278	
8.14194045	0.55032097	-1.1746633	

Table 3: Model specific parameters of the chosen ANN-HM with 26 HNs. Connection weights of the input and hidden layer, biases of the hidden layer.

$W_{i,h}$										b_h
0.26106	0.12391	0.82471	0.33482	-0.72017	-0.16497	-0.19633	-0.32429	0.86960	-0.36237	
0.19960	0.28507	-1.86320	0.22985	-0.67681	-1.02954	0.16398	0.11994	0.36954	-1.43625	
-1.16703	-1.23930	1.94422	0.56587	0.49974	0.16683	1.36101	0.10762	0.45637	-1.66672	
0.20960	0.84537	0.24244	0.16916	2.68825	-2.82029	0.66726	-0.00679	2.02909	-4.48702	
0.09335	0.43959	-0.34136	0.30138	-0.16581	-0.58593	-0.26262	-0.07968	-1.58115	0.47128	
0.00205	0.06033	-0.14307	-0.04459	0.11140	-0.40748	0.06257	-0.22526	0.28571	-0.02085	
0.16260	0.45512	2.20344	-0.94117	-0.25011	-0.46153	0.34534	-0.03916	0.32684	-2.61076	
-0.24824	-0.39428	0.83872	-0.18088	0.37006	-0.00575	0.06836	0.20577	-1.22799	1.04678	
0.06642	0.20981	0.64012	0.33408	-0.77574	-1.37976	0.24136	-0.16015	0.97653	-1.36315	
-0.22450	-0.46566	-0.82017	-0.21527	1.06934	0.04703	-0.35663	0.05209	-1.94161	3.53783	
0.35660	0.70139	-0.16036	-0.35555	0.14775	0.37536	0.00984	0.08682	1.31660	-2.49721	
-0.56388	-0.14535	0.24360	0.31073	-0.98601	-0.13431	0.77766	0.02603	0.25057	-1.83903	
-0.79324	1.26824	1.96136	-1.87042	0.29754	0.27066	0.87333	0.10029	1.36528	-2.69636	
0.85912	1.50609	-2.13724	-0.40449	-0.68632	-0.33117	-1.34989	-0.21578	-0.16249	2.31635	
1.18093	0.13571	-2.43287	-0.26083	0.13894	-0.98120	-0.62123	-0.01411	0.16473	-0.56915	
0.13604	0.99348	-0.45484	-0.78550	-0.55885	-1.27551	0.17066	0.31817	0.22216	-1.61553	
0.21975	0.25746	-1.96152	0.22746	-0.90822	0.80587	-0.28249	-0.00652	-1.18703	0.06408	
0.46520	0.10702	0.07642	0.22147	0.77300	0.61035	-0.50695	-0.01416	0.11848	0.16956	
0.25148	0.94812	-0.01635	-0.31923	-0.37376	-0.26056	-0.16762	0.11647	-0.40989	-1.07456	
0.65769	0.69521	-0.14171	-0.00214	0.16558	0.92229	-0.69206	-0.32748	-0.59464	-0.22123	
0.47396	-0.10615	0.40137	0.06801	0.67045	0.12422	-0.72975	-0.20161	-1.00531	2.23222	
0.27067	-0.45266	-1.49560	-0.23085	0.80500	-0.47034	0.42334	0.07572	0.62688	-2.28619	
-0.30719	-0.34633	0.06663	1.04917	0.81328	0.10817	0.47108	-0.04857	1.04581	-1.57837	
0.57060	0.64921	-1.08245	-0.15155	-0.39120	0.14038	-0.56275	-0.03471	-0.73006	0.16251	
0.19670	-0.23625	-0.58807	0.57185	-0.11151	0.01358	-0.15972	0.04672	0.66813	0.32134	
0.12129	-0.23764	-2.28032	1.35823	-0.28722	-0.20917	-0.11084	-0.00218	-0.25148	0.02584	

Table 4: Model specific parameters of the chosen ANN-HM with 26 HNs. Connection weights of the hidden and output layer, biases of the output layer.

	$\mathbf{W}_{h,o}^{-1}$		\mathbf{b}_o
0.6009	-0.1806	0.2787	-0.2325
-1.5689	0.0367	1.3037	-0.8352
0.5055	1.0450	1.8062	-0.4410
-0.2549	4.9671	0.2776	
-0.9679	0.4391	0.1689	
-0.5245	-0.2991	-0.3791	
1.4918	-0.1403	1.6442	
-0.5030	-1.7649	-0.2364	
-0.4736	-2.2558	-0.4178	
-1.6924	2.0570	0.3809	
2.9428	1.3525	0.0294	
0.7372	0.6209	-1.2581	
-2.6214	-1.4086	0.8564	
0.2751	1.0030	2.0603	
1.5861	2.0752	0.7404	
2.0191	0.6807	-0.0775	
0.3512	-1.8184	-0.0947	
-0.0987	0.2139	1.2012	
-2.3025	-1.8966	-1.4302	
0.4858	0.0648	-0.4688	
1.6234	0.2751	-0.5682	
-1.1198	-2.5540	-2.5515	
-1.5483	-1.0474	-1.0012	
-1.1105	-1.1005	-0.8157	
0.1349	-0.3539	-1.0865	
1.1528	-0.0161	-0.9238	

Table 5: Model specific parameters of the ANN-HM with 28 HNs. Connection weights of the input and hidden layer, biases of the hidden layer.

$W_{i,h}$									b_h
0.46664	0.28557	0.43946	-0.00902	-0.16684	0.54786	-0.43955	0.21328	-0.19793	-0.16975
0.60392	0.25781	-0.59811	-1.10325	-0.45429	0.44810	-0.66461	-0.11598	0.98309	1.48690
0.07021	-0.02014	0.00078	0.01422	0.72290	-0.30191	-0.02811	0.14087	0.04316	-0.13027
-0.65256	-0.60885	-0.01501	-0.47318	0.50558	-0.77336	0.62161	0.16996	0.63660	0.93549
-0.19340	0.37544	-1.33623	0.05289	-0.24590	0.51843	-0.46170	-0.06380	-1.95280	2.33584
-0.12152	-0.18302	-1.03475	0.82643	0.44755	0.75689	0.47722	-0.03124	1.65909	-2.46539
0.04288	0.29545	0.68057	-0.10564	0.35736	-0.67963	-0.00200	-0.39468	0.95627	-0.38664
-0.56356	0.67832	2.15088	-0.97097	2.05435	-0.92779	0.52143	0.00043	1.51639	-0.88890
-0.57398	-0.33225	-0.48717	0.55994	-0.00700	1.28148	0.26237	-0.00604	-0.04937	0.32635
0.48020	-0.09632	1.15148	0.49759	-0.08547	1.44197	-0.99544	-0.29592	-0.29415	2.49784
-0.49102	-0.47841	0.52580	-0.25073	0.55789	-0.56585	0.53654	0.08371	0.09385	-0.09893
-0.18325	-0.13461	0.47380	-0.18808	0.43415	-0.08744	0.13086	0.05678	0.17174	0.11998
-0.06853	0.28728	0.73074	-0.53532	0.24692	-0.38353	-0.01040	-0.14186	-0.69265	0.32885
-0.24823	-0.48929	0.60280	-0.27136	1.18187	-1.33482	-0.17447	-0.01340	-1.50596	3.43600
-0.75584	-0.31503	1.63727	0.08533	1.34722	-0.20588	0.42242	-0.18111	0.90560	0.94341
-1.28804	-0.83502	-1.31090	-0.65176	-0.91017	-1.24448	1.05639	0.28885	-0.59850	1.50718
-0.44566	-0.36471	1.78173	-0.59253	0.53608	0.07252	0.27134	-0.01676	0.84184	0.93740
0.73352	-0.90533	-1.51640	2.18375	0.16292	-1.12499	-0.88997	-0.03892	-1.02122	2.41060
1.49650	1.85872	-2.08273	-2.02300	0.28420	-0.19405	-2.46870	-0.23513	-0.77545	6.15865
-0.44727	-0.36909	-0.31667	-0.18004	-0.21224	1.43467	0.19270	-0.01945	0.35410	0.54217
-0.17363	-0.40172	0.07947	0.27894	-0.19348	-0.23665	0.17962	0.07693	0.10611	0.02526
-0.07722	0.60267	-1.06913	-0.95967	0.15029	-0.05226	0.62780	0.02814	0.57058	-3.35825
-0.86457	0.74219	3.77944	-1.28672	0.87443	-0.04660	0.54564	0.00464	0.77024	-0.37002
-0.57021	-0.43266	-1.12872	0.23752	-0.51371	-0.83880	0.80082	0.27356	0.13021	-1.04363
-0.22845	0.49498	1.06860	-0.88429	0.87760	0.09871	0.36785	-0.10285	1.83416	-1.25260
0.09510	-0.11401	0.15330	0.24541	0.33723	-0.14926	-0.07379	0.13185	-0.16622	0.02456
0.49600	0.60806	-1.44494	-0.91344	-0.63084	-0.42098	-0.15879	0.11993	0.01247	-0.91623
0.25459	-0.19486	-0.00958	0.53563	0.49777	-0.08896	-0.23045	-0.21662	-0.94394	0.13169

Table 6: Model specific parameters of the ANN-HM with 28 HNs. Connection weights of the hidden and output layer, biases of the output layer.

$\mathbf{W}_{h,o}^{-1}$			\mathbf{b}_o
0.04726	-0.79667	0.43343	0.1063
-1.19233	-0.88727	0.03829	-0.6298
-0.69891	-0.61537	-0.24272	-0.4188
1.02313	1.75151	0.62214	
-1.01982	-1.59516	-0.84936	
-1.76369	-1.66547	-1.24119	
-0.25505	-1.44239	0.32571	
-1.59085	2.50186	0.09647	
-0.49080	0.93114	1.42095	
1.28131	0.54790	-0.37088	
0.28152	-1.14893	-0.84685	
0.13544	-0.88629	0.25524	
-1.00940	-0.10411	1.01269	
-3.10077	1.21421	0.07743	
1.35216	1.63563	-0.66500	
-1.00380	-1.34031	0.03127	
-0.13046	1.07453	1.51489	
2.51110	0.87342	-2.01953	
0.93582	1.24484	2.61213	
-0.03322	-1.04785	-1.38058	
0.18938	-0.40356	-0.61202	
0.13238	-1.13961	-2.50424	
0.15077	-3.01093	-0.01719	
-0.51431	-1.25468	-0.09573	
1.28006	-0.24813	-0.14723	
-0.35293	-0.46369	-0.09210	
2.32963	1.98265	-0.13629	
-0.50319	-0.76767	-0.46772	

2. Supplementary figures

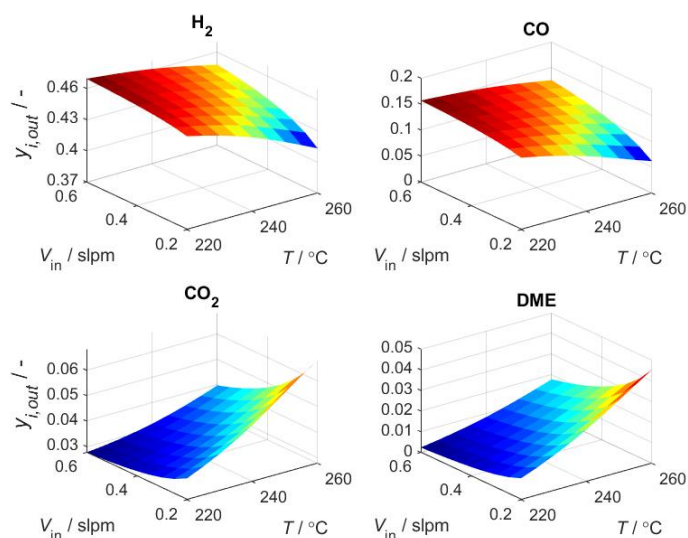


Figure S2. Surface response for the hybrid model predictions of the mole fractions of H_2 , CO, CO_2 and DME within the validity range of the temperature and total gas flow. Feed composition: 48.0 % H_2 , 16.11 % CO, 2.88 % CO_2 . Pressure 50 bar. CZA-to- γ - Al_2O_3 -ratio $\mu = 1$. ANN-HM with 26 HNs.

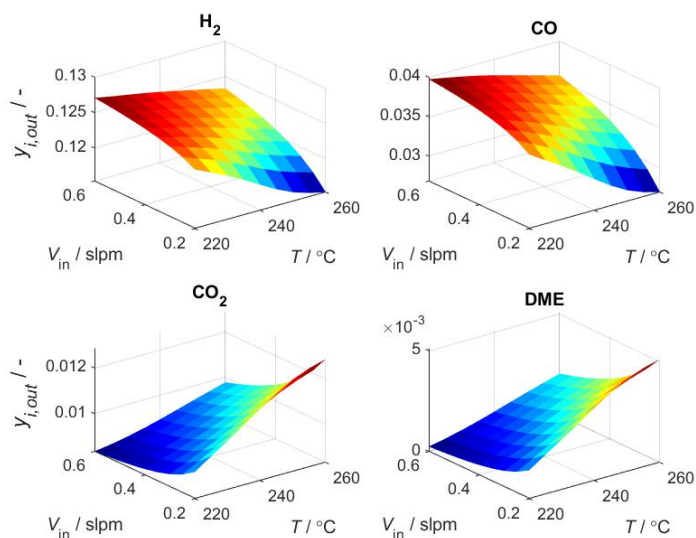


Figure S3. Surface response for the hybrid model predictions of the mole fractions of H_2 , CO, CO_2 and DME within the validity range of the temperature and total gas flow. Feed composition: 13.05 % H_2 , 4.10 % CO, 0.86 % CO_2 . Pressure 50 bar. CZA-to- γ - Al_2O_3 -ratio $\mu = 1$. ANN-HM with 26 HNs.

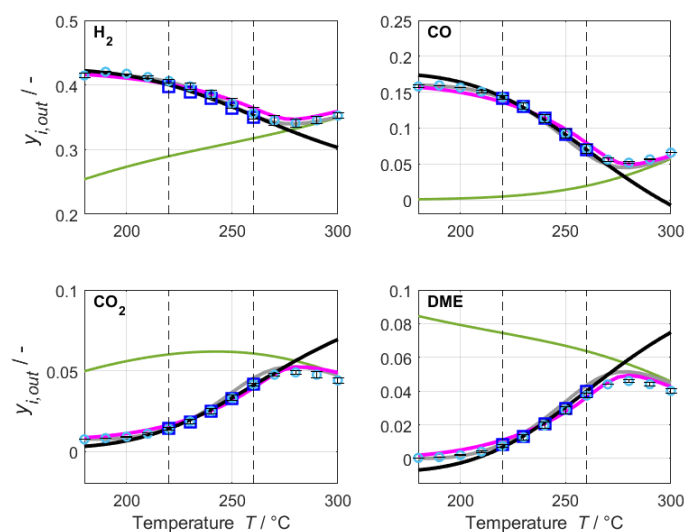


Figure S4. Range extrapolation of the temperature. Nominal feed composition: 42.3 % H_2 , 16.1 % CO , 0.82 % CO_2 . Total gas flow 0.2 slpm. Pressure 50 bar. CZA-to- $\gamma\text{-Al}_2\text{O}_3$ -ratio $\mu = 1$. ANN-HM with 5 HNs.

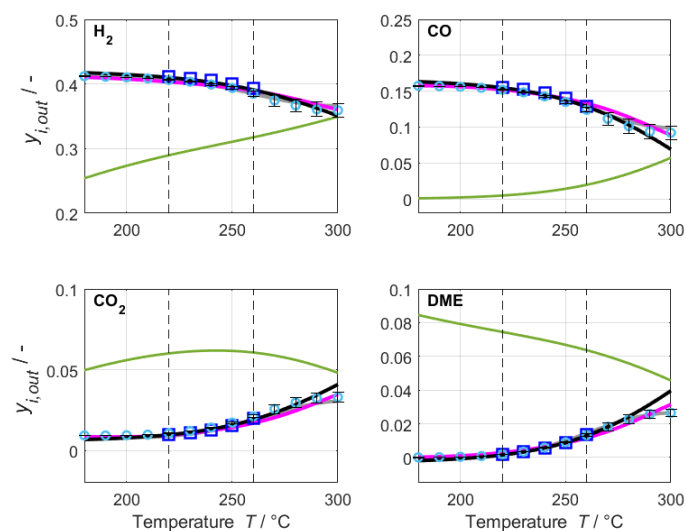


Figure S5. Range extrapolation of the temperature. Nominal feed composition: 42.3 % H_2 , 16.1 % CO , 0.82 % CO_2 . Total gas flow 0.6 slpm. Pressure 50 bar. CZA-to- $\gamma\text{-Al}_2\text{O}_3$ -ratio $\mu = 1$. ANN-HM with 5 HNs.

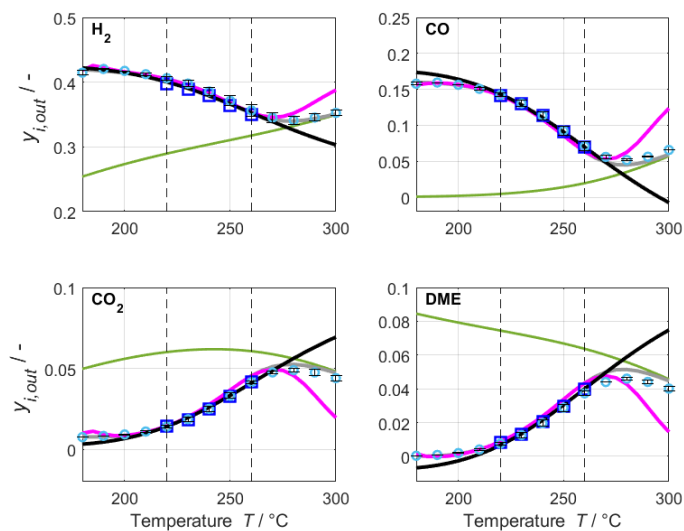


Figure S6. Range extrapolation of the temperature. Nominal feed composition: 42.3 % H_2 , 16.1 % CO , 0.82 % CO_2 . Total gas flow 0.2 slpm. Pressure 50 bar. CZA-to- $\gamma\text{-Al}_2\text{O}_3$ -ratio $\mu = 1$. ANN-HM with 28 HNs.

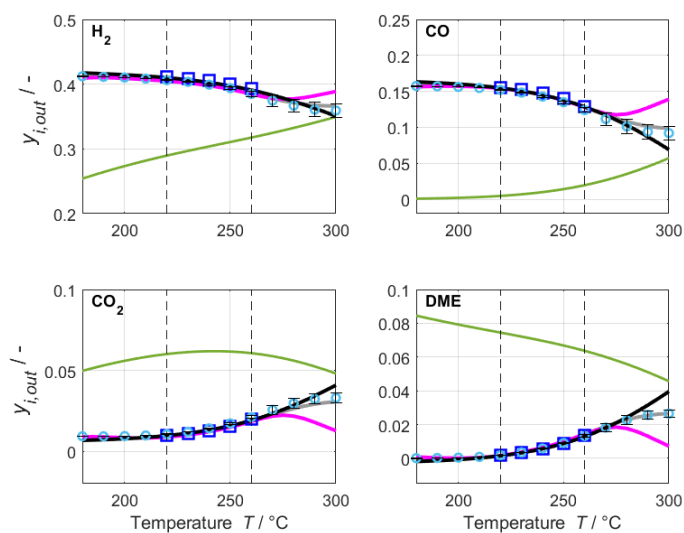


Figure S7. Range extrapolation of the temperature. Nominal feed composition: 42.3 % H_2 , 16.1 % CO , 0.82 % CO_2 . Total gas flow 0.6 slpm. Pressure 50 bar. CZA-to- $\gamma\text{-Al}_2\text{O}_3$ -ratio $\mu = 1$. ANN-HM with 28 HNs.

3. A priori criteria for the determination of mass and heat transport limitations

A priori criteria were employed for ruling out mass and heat transport limitations. These criteria were calculated for temperatures between 180-300 °C and total gas flows between 0.15-0.8 slpm. The values calculated for the worst case scenarios are give in Table 7 for each reaction, and show that mass and heat transport limitations do not play a significant role at the evaluated operating conditions.

Table 7: Calculated a priori criteria for determination of transport limitations.

Phenomenon	Equation [1]	Max. Calculated Value
Outer mass transfer	$\frac{r_{j,eff} n }{a'k_f c_b} < 0.05$	For reaction 1: $3.29 \cdot 10^{-5}$ For reaction 2: $2.09 \cdot 10^{-5}$ For reaction 3: $5.74 \cdot 10^{-5}$
Outer heat transfer	$\frac{E_A}{RT_b} \left \frac{-\Delta H_R}{hT_b} \right \frac{r_{j,eff}}{a'} < 0.05$	For reaction 1: $4.75 \cdot 10^{-4}$ For reaction 2: $3.09 \cdot 10^{-4}$ For reaction 3: $4.97 \cdot 10^{-4}$
Inner mass transfer	$\frac{r_{j,eff} L^2 (n+1)}{D_{eff} c_s} < 0.15$	For reaction 1: $4.62 \cdot 10^{-4}$ For reaction 2: $2.93 \cdot 10^{-4}$ For reaction 3: $8.06 \cdot 10^{-4}$
Inner heat transfer	$\frac{E_A}{RT_b} \left \frac{-\Delta H_R}{\lambda_{eff,p} T_b} \right r_{j,eff} L^2 < 0.1$	For reaction 1: $4.28 \cdot 10^{-5}$ For reaction 2: $2.78 \cdot 10^{-5}$ For reaction 3: $4.48 \cdot 10^{-5}$

4. Experimental values

The experimental values measured for validation of the simulation results at extrapolated conditions are given in Table 8.

5. Catalyst conditioning and deactivation

Figure S8 shows the CO_x-conversion (X_{CO_x}) as a function of the Time-On-Stream (ToS) for a reference operating point measured at 513 K, 50 bar and 7599.5 h⁻¹ and a feed of 38.2 % H₂, 15.2 % CO, 1.0 % CO₂, 45.7 % N₂. Within the first 25 hours the reaction conditions were left constant at 513 K, 50 bar and 7599.5 h⁻¹. After that, the conditions were varied dynamically between 453-573 K, 40-60 bar and 2849.8-15199.0 h⁻¹. After 129 hours the experiments for model validation at 453-573 K, 40-60 bar as well as 2849.8-15199.0 h⁻¹ were taken. Between the ToS of 129 and 160 hours, where the experiments were conducted, the X_{CO_x} remains stable with a relative deviation of 10 % between the minimal and maximal measured X_{CO_x} .

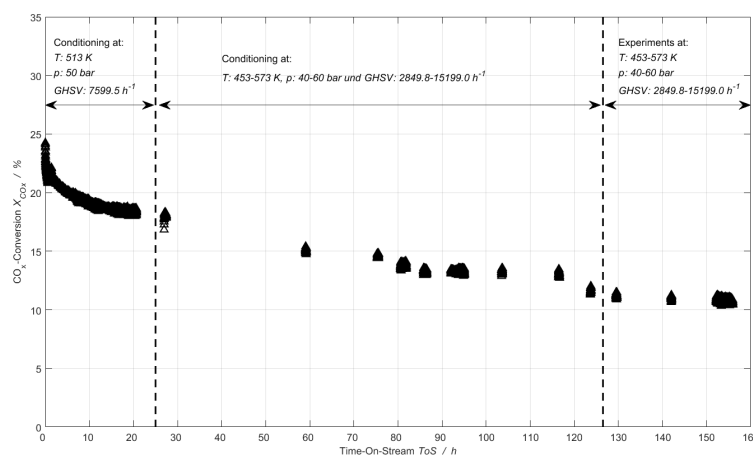


Figure S8. The CO_x-conversion (X_{CO_x}) as a function of the Time-On-Stream (ToS) for a reference operating point measured at 513 K, 50 bar and 7599.5 h⁻¹ and a feed of 38.2 % H₂, 15.2 % CO, 1.0 % CO₂, 45.7 % N₂.

Table 8: Experimental values measured for validation of simulation results at extrapolated conditions. The catalyst bed consisted of 1.007g CZA, 0.9996 g γ -Al₂O₃, 9.98 g SiC, and it was 7.8 cm long.

$y_{i,in}$				Conditions				$y_{i,out}$								Standard Deviation $y_{i,out}$							
H ₂ %	CO %	CO ₂ %	N ₂ %	T °C	\dot{V}_{in} slpm	P bar	H ₂ %	CO %	H ₂ O %	CO ₂ %	MeOH %	DME %	N ₂ %	H ₂ %	CO %	H ₂ O %	CO ₂ %	MeOH %	DME %	N ₂ %			
37.7	15.2	0.8	46.2	180	0.20	50	41.47	15.79	0.09	0.75	0.16	0.04	41.71	0.35	0.19	0.01	0.01	0.01	0.00	0.53			
37.7	15.2	0.8	46.2	190	0.20	50	42.04	15.95	0.10	0.83	0.23	0.08	40.77	0.07	0.00	0.01	0.02	0.03	0.01	0.14			
37.7	15.2	0.8	46.2	200	0.20	50	41.75	15.63	0.10	0.92	0.32	0.20	41.09	0.02	0.05	0.01	0.03	0.06	0.02	0.05			
37.7	15.2	0.8	46.2	210	0.20	50	41.23	15.07	0.11	1.10	0.38	0.41	41.70	0.18	0.15	0.01	0.04	0.08	0.05	0.14			
37.7	15.2	0.8	46.2	220	0.20	50	40.62	14.25	0.12	1.40	0.43	0.75	42.43	0.31	0.27	0.02	0.08	0.09	0.09	0.31			
37.7	15.2	0.8	46.2	230	0.20	50	39.78	13.05	0.17	1.86	0.47	1.26	43.42	0.47	0.42	0.03	0.12	0.08	0.14	0.51			
37.7	15.2	0.8	46.2	240	0.20	50	38.56	11.35	0.23	2.50	0.52	1.97	44.86	0.69	0.59	0.04	0.16	0.06	0.21	0.81			
37.7	15.2	0.8	46.2	250	0.20	50	37.11	9.26	0.28	3.30	0.57	2.88	46.61	0.76	0.63	0.01	0.17	0.03	0.22	0.97			
37.7	15.2	0.8	46.2	260	0.20	50	35.63	7.09	0.28	4.15	0.59	3.73	48.53	0.85	0.58	0.01	0.10	0.01	0.14	1.16			
37.7	15.2	0.8	46.2	270	0.20	50	34.51	5.61	0.27	4.75	0.58	4.40	49.89	0.79	0.30	0.00	0.07	0.00	0.00	1.16			
37.7	15.2	0.8	46.2	280	0.20	50	34.11	5.17	0.26	4.89	0.56	4.60	50.40	0.66	0.13	0.01	0.14	0.00	0.09	1.01			
37.7	15.2	0.8	46.2	290	0.20	50	34.53	5.63	0.27	4.75	0.54	4.41	49.86	0.57	0.03	0.02	0.17	0.00	0.12	0.89			
37.7	15.2	0.8	46.2	300	0.20	50	35.26	6.58	0.29	4.40	0.51	4.01	48.96	0.45	0.02	0.00	0.17	0.00	0.14	0.72			
37.5	14.9	1.0	46.7	180	0.60	50	41.22	15.74	0.07	0.93	0.09	0.01	41.93	0.07	0.04	0.03	0.00	0.07	0.03	0.02			
37.5	14.9	1.0	46.7	190	0.60	50	41.13	15.70	0.09	0.93	0.13	0.02	42.00	0.02	0.01	0.01	0.00	0.01	0.00	0.04			
37.5	14.9	1.0	46.7	200	0.60	50	41.03	15.62	0.11	0.94	0.18	0.04	42.08	0.02	0.01	0.00	0.00	0.01	0.00	0.03			
37.5	14.9	1.0	46.7	210	0.60	50	40.86	15.47	0.11	0.98	0.23	0.09	42.26	0.01	0.00	0.00	0.00	0.02	0.00	0.00			
37.5	14.9	1.0	46.7	220	0.60	50	40.62	15.20	0.12	1.07	0.26	0.19	42.55	0.07	0.04	0.00	0.01	0.02	0.00	0.08			
37.5	14.9	1.0	46.7	230	0.60	50	40.35	14.84	0.13	1.20	0.28	0.35	42.85	0.09	0.07	0.00	0.02	0.03	0.01	0.09			
37.5	14.9	1.0	46.7	240	0.60	50	39.93	14.27	0.13	1.42	0.27	0.58	43.40	0.14	0.12	0.00	0.03	0.01	0.03	0.18			
37.5	14.9	1.0	46.7	250	0.60	50	39.38	13.49	0.16	1.72	0.28	0.91	44.06	0.18	0.18	0.01	0.06	0.01	0.05	0.25			
37.5	14.9	1.0	46.7	260	0.60	50	38.49	12.39	0.22	2.11	0.31	1.32	45.15	0.37	0.30	0.03	0.08	0.02	0.07	0.52			
37.5	14.9	1.0	46.7	270	0.60	50	37.45	11.15	0.27	2.57	0.34	1.82	46.40	0.91	0.88	0.03	0.29	0.04	0.24	1.19			
37.5	14.9	1.0	46.7	280	0.60	50	36.68	10.12	0.36	2.97	0.38	2.27	47.23	1.01	0.95	0.03	0.30	0.04	0.25	1.33			
37.5	14.9	1.0	46.7	290	0.60	50	36.06	9.38	0.38	3.23	0.40	2.57	47.97	1.11	1.01	0.01	0.31	0.04	0.26	1.51			
37.5	14.9	1.0	46.7	300	0.60	50	35.92	9.20	0.39	3.30	0.40	2.65	48.14	1.10	0.98	0.01	0.29	0.04	0.23	1.51			
38.2	15.2	1.0	45.7	260	0.40	40	38.04	12.07	0.23	2.15	0.25	1.54	44.33	0.53	0.56	0.03	0.20	0.05	0.06	1.79			
38.2	15.2	1.0	45.7	260	0.40	45	37.38	11.41	0.24	2.33	0.31	1.79	45.00	0.35	0.46	0.02	0.19	0.06	0.02	1.64			
38.2	15.2	1.0	45.7	260	0.40	50	36.72	10.70	0.29	2.55	0.39	2.07	45.65	0.49	0.68	0.01	0.29	0.09	0.12	1.81			
38.2	15.2	1.0	45.7	260	0.40	55	36.07	10.06	0.31	2.73	0.47	2.32	46.25	0.39	0.73	0.03	0.36	0.14	0.17	1.71			
38.2	15.2	1.0	45.7	260	0.40	60	35.31	9.35	0.29	2.92	0.55	2.59	46.78	0.27	0.74	0.01	0.40	0.15	0.17	1.82			

References

1. Pérez-Ramírez, J.; Berger, R.J.; Mul, G.; Kapteijn, F.; Moulijn, J.A. Six-flow reactor technology a review on fast catalyst screening and kinetic studies. *Catalysis Today* **2000**, *60*, 93–109. doi:10.1016/S0920-5861(00)00321-7.